A Suborbital Payload for Soft X-ray Spectroscopy of Extended Sources

by

Phillip Henry Howard Oakley

B.A., Astrophysics, University of California, Berkeley, 2004

M.S., Astrophysics, University of Colorado, Boulder, 2007

A thesis submitted to the

Faculty of the Graduate School of the

University of Colorado in partial fulfillment

of the requirements for the degree of

Doctor of Philosophy

Department of Astrophysical and Planetary Sciences

2011

This thesis entitled:
A Suborbital Payload for Soft X-ray Spectroscopy of Extended Sources
written by Phillip Henry Howard Oakley
has been approved for the Department of Astrophysical and Planetary Sciences

Prof. Webster Cash

Prof. Randall McEntaffer

Prof. Andrew Hamilton

Research Associate Steve Osterman

Prof. Daniel Scheeres

Date

The final copy of this thesis has been examined by the signatories, and we find that both the content and the form meet acceptable presentation standards of scholarly work in the above mentioned discipline.

Oakley, Phillip Henry Howard (Ph.D., Astrophysical and Planetary Sciences)

A Suborbital Payload for Soft X-ray Spectroscopy of Extended Sources

Thesis directed by Prof. Webster Cash

This thesis details the intent, design and results of an X-ray suborbital rocket payload whose scientific target was the Cygnus Loop Supernova Remnant. The payload consists of wire grid collimators, off-plane gratings arrays and gaseous electron multiplier (GEM) detectors. The system was designed for measurements in the 17-107 Å bandpass with a resolution up to ~ 60 $(\lambda/\Delta\lambda)$. This instrument was christened the Extended X-ray Off-plane Spectrometer (EXOS) and was launched on a Terrier-Black Brant rocket on November 13th, 2009 from White Sands Missile Range and obtained 340 seconds of useable scientific data. The emission is dominated by O VII and O VIII, including the He-like O VII triplet at ~ 22 Å. Another feature at ~ 45 Å is composed primarily of Si XI and Si XII. The best-fit model to this spectrum is an equilibrium plasma model at a temperature of $\log(T) = 6.4$ (0.23 keV).

Dedication

An expert is a man who has made all the mistakes which can be made, in a very narrow field.

Neils Bohr

Acknowledgements

I owe a debt of gratitude to many individuals for their contributions to this project.

Thank you Web for your endless optimism, trust and for giving me the chance to prove myself. Thank you Randy, for setting such a high standard in both competence and character that I can only hope to live up to.

I'd like to thank NASA for their support of the sounding rocket program. The Wallops and White Sands Missile Range teams were critical towards the success of this project. I'd particularly like to thank Shane Thompson, Brian Banks and Charlie Kupelian for showing me the ropes and getting me through launch in one piece, Bill Payne for your patience, dedication and perseverance (even through great physical pain), and Rick Nelson for your kindness and impressive ability to schedule our launch.

Thanks to Sensor Sciences for your help with the GEMs, Heidi and everyone at Luxel for your assistance with the windows, Proportion-Air for debugging my gas system, the Hodgsons and JILA machine shop for cutting my metal, Toru Tamagawa for your assistance with our GEM plates and Charlie Zabel for your infinite kindness and assistance with our gas system.

Everyone at CASA deserves my thanks: Sarah for making such a great logo, Bobby for your Solidworks assistance and (more importantly) friendship, Joel and all the undergrads for your help, Ann for all your work and design help, Ted for everything you did with the electronics (I'll never forget about that converter) and for understanding how painful that work was, Nico for the late night company and your superhuman bench-press strength, and of course to Ben and Mike - your dedication and friendship meant so much to me.

Finally, I owe everything to my family for their support: to Kura for your warm greetings, to Mike for your unwavering support, to my parents for your infinite trust, enthusiasm and patience - I owe so much of who I am today to your example, and to Annie for your kindness, love and sacrifice - thank you for everything.

Contents

Chapter

Tables

Table

Figures

Figure

Chapter 1

Introduction

1.1 Supernova Remnants

Supernovae are among the most important and interesting events in our galaxy. They play a major role in the structural, compositional, and energy evolution of the interstellar medium (ISM). These events are one of the primary sources for metal creation in the ISM. Additionally, their interaction with the ISM influences the energy balance of the host galaxy through the creation of hot ionized gas.

The remnant formed by the blast wave of ejected material traveling into the ISM evolves over the span of millions of years in 4 main stages: ejecta-dominated expansion, adiabatic expansion, radiative cooling and disappearance. Details of these stages are presented below assuming a convenient standard of a spherically symmetric blast evolving into a homogenous medium. As we will see later this is not the exact case for the Cygnus Loop, yet it is still useful to examine the most basic case prior to complications.

1.1.1 Ejecta-Dominated Stage (free expansion)

The initial explosion produces a blast wave traveling at $\sim 10^4$ km/s with an energy of $\sim 10^{51}$ ergs (Chevalier 1977). This stage lasts until the swept-up matter is approximately equal to the initial mass of the ejecta. Assuming a constant density this happens when:

$$\frac{4}{3}\pi R^3 n_\circ \mu m_H = M_\circ \tag{1.1}$$

where M_o is the ejected mass. This gives a radius of:

$$R = \left(\frac{3M_\circ}{4\pi n_\circ \mu m_H}\right)^{\frac{1}{3}} \tag{1.2}$$

Scaling from convenient values gives the following:

$$R = 2.1 \ (\mu)^{-1/3} \left(\frac{n_\circ}{1 \text{ cm}^{-3}}\right)^{-1/3} \left(\frac{M_\circ}{1 \ M_\odot}\right)^{1/3} \quad \text{pc} \tag{1.3}$$

The time it takes to acquire this much material can be deduced with similar ease:

$$\begin{aligned} t \sim \frac{R}{v_\circ} &= 208.9 \ (\mu)^{-1/3} \left(\frac{n_\circ}{1 \text{ cm}^{-3}}\right)^{-1/3} \left(\frac{M_\circ}{1 \ M_\odot}\right)^{5/6} \left(\frac{E}{10^{51} \text{ erg}}\right)^{-1/2} \text{yr} && (1.4) \\ &= 208.9 \ (\mu)^{-1/3} \left(\frac{n_\circ}{1 \text{ cm}^{-3}}\right)^{-1/3} \left(\frac{M_\circ}{1 \ M_\odot}\right)^{1/3} \left(\frac{v_\circ}{10^9 \text{ cm/s}}\right)^{-1} \text{yr} && (1.5) \end{aligned}$$

where μ is the mean atomic weight and n_o the number density.

Assuming this phase is energy conserving we have an ending velocity of $v = v_\circ/\sqrt{2} \sim 7 \cdot 10^3$ km/s. The ejecta is traveling at a much higher velocity than the local ISM sound velocity of ~ 10 km/s and thus a shock wave is formed at the front of the ejecta. This deceleration process also produces an inward, or reverse, shock that reheats the interior material and typically causes X-ray emission at a higher temperature than at the forward moving blast wave. Despite its name this shock initially travels outward, but at a slower pace than the forward shock.

1.1.2 Adiabatic Stage (Sedov-Taylor)

Eventually the collected material is equal to or more massive than the original ejecta mass. During this stage the collisional ionization rate is much greater than the recombination rate, so little radiative cooling occurs. This stage is called the adiabatic stage, the Sedov-Taylor stage or the nonradiative stage.

A conceptual understanding of the remnant's behavior can be obtained using simple dimensional analysis. Taking the basic equations of:

$$E_o = \frac{1}{2}Mv^2 \tag{1.6}$$

$$M = \frac{4}{3}\pi R^3 n_H m_H \tag{1.7}$$

$$v \sim \frac{R}{t} \tag{1.8}$$

we find a qualitative equation of how the remnant will act over time in Equations 1.10 and 1.11.

$$E_o = \left(\frac{2}{3}\pi n_H m_H\right)\left(\frac{R^5}{t^2}\right) \tag{1.9}$$

$$R(t) = \left(\frac{3E_o}{2\pi n_H m_H}\right)^{\frac{1}{5}} t^{\frac{2}{5}} \tag{1.10}$$

$$v = \frac{\delta r}{\delta t} = \left(\frac{2}{5}\right)\left(\frac{3E_o}{2\pi n_H m_H}\right)^{\frac{1}{5}} t^{-\frac{3}{5}} \tag{1.11}$$

Scaling from convenient values gives us:

$$R \sim 1.6 \left(\frac{E_o}{10^{51}}\right)^{\frac{1}{5}} \left(\frac{n_H}{1}\right)^{-\frac{1}{5}} \left(\frac{t}{100 \text{ years}}\right)^{\frac{2}{5}} \text{ pc} \tag{1.12}$$

$$v \sim 6223 \left(\frac{E_o}{10^{51}}\right)^{\frac{1}{5}} \left(\frac{n_H}{1}\right)^{-\frac{1}{5}} \left(\frac{t}{100 \text{ years}}\right)^{-\frac{3}{5}} \text{ km/s} \tag{1.13}$$

The end of this stage occurs at $v \sim 100$ km/s. This gives typical values of: $R \sim 25$ pc and $t \sim$100,000 years. These values are for order of magnitude reference only. Various things can greatly influence this evolution including: magnetic fields, density variations (e.g. cavity explosions), etc.

1.1.3 Radiative Stage (Snowplow)

During this stage the temperature of the remnant has cooled to $\sim 10^6$ K and atoms can efficiently cool via radiative recombination. This stage is often called either the radiative stage or snowplow stage. Now that sufficient energy is being radiated away, one can no longer treat the kinematics as a constant energy problem. Using simple momentum conservation and dimensional analysis, one can derive order of magnitude estimations for length, mass and time scales:

$$M_1 v_1 = M_2 v_2 \tag{1.14}$$

$$M_2 = \frac{M_1 v_1}{10\mathrm{km/s}} \qquad (\sim 10^5 M_\odot) \tag{1.15}$$

$$R = \left(\frac{3 \times 10^5 M_\odot}{4\pi n_H m_H}\right)^{\frac{1}{3}} \qquad (\sim 50 \text{ pc}) \tag{1.16}$$

$$t \sim \frac{R}{v} \qquad (\sim 10^6 \text{ years}) \tag{1.17}$$

This phase lasts until the velocity reaches the ambient ISM velocity, which is ~ 10 km/s. At this point the remnant becomes indistinguishable from the local ISM, leaving behind only a hot ,less dense cavity.

Again, by doing some simple dimensional analysis we can derive relationships between radius, velocity and time to determine how the remnant is evolving compared to the previous stage.

$$\begin{aligned} p_o &= Mv && (1.18) \\ M &= \frac{4}{3}\pi R^3 n_H m_H && (1.19) \\ v &\sim \frac{R}{t} && (1.20) \\ p_o &\approx \left(\frac{4}{3}\pi n_H m_H\right)\left(\frac{R^4}{t}\right) && (1.21) \end{aligned}$$

$$R \approx \left(\frac{3p_o}{4\pi n_H m_H}\right)^{\frac{1}{4}} t^{\frac{1}{4}} \tag{1.22}$$

$$v = \frac{dr}{dt} \approx \left(\frac{1}{4}\right)\left(\frac{3p_o}{4\pi n_H m_H}\right)^{\frac{1}{4}} t^{-\frac{3}{4}} \tag{1.23}$$

Equations 1.22 and 1.23 provide a qualitative relationship of how the remnant is evolving over time during the snowplow phase. As a remnant enters the snowplow phase it will become substantially slower (Equation 1.23 versus 1.11). Thus simple observations detailing how fast the remnant is expanding, combined with decent distance measurements can reveal a great deal about the remnant's age and behavior.

Typical (i.e. order of magnitude estimates) values for the end of each phase are shown in Table 1.1 for velocity, mass, radius and time.

Table 1.1 Typical parameters of shock waves in different phases. All values (except the initial column) are final values, valid at the end of that particular phase. These values are meant for order of magnitude estimates only.

	Initial	When $M_\circ = M_{swept}$	Adiabatic Phase (until $v \approx 100$ km/s)	Radiative phase (until $v = v_{turb} \approx 10$ km/s)
v	10^4 km/s	7×10^3 km/s	100 km/s	10 km/s
M	$M_\circ$	$2M_\circ$	$10^4 M_\circ$	$10^5 M_\circ$
R	0	1pc	25 pc	50 pc
t	0	100 years	10^5 years	10^6 years

1.1.4 Disappearance Stage

In this last phase, the expanding shell becomes slower and fainter and its velocity becomes indistinguishable from the random motion of the ISM ($\sim$ 10 km/s). The remnant will become indistinguishable from the surrounding ISM. It is quite likely that a significant amount of diffuse galactic X-ray emission is due to remnants that have effectively merged with the ISM.

1.2 X-ray Emission from Supernova Remnants

Supernova remnants generally emit X-rays from three main sources. The first source is the shock heated ISM that forms a shell around the remnant's perimeter. The second is the ejecta (which will be reheated by the reverse shock). The third source of X-rays is from the central compact object. This discussion focuses on the first two sources. Emission from these regions is generally modeled as a thermal plasma. Given the abundance levels of elements, a temperature, interaction cross sections, etc., the ratio of ionization states and the likelihood of various transitions are calculated. From this list of expected transition strengths, a theoretical spectrum can be modeled. Several models have been created using similar techniques, but with different line lists and emission calculations. Below is a brief description of some of the difficulties with these models.

The forward shock wave will heat the ambient ISM up to the shock temperature T_s, which is typically $\sim 10^6 - 10^7$ K initially. As the blast wave gathers more material, it accelerates this matter to the blast velocity. Kinetic energy (up to T_s) is quickly transferred to the thermal motions of the ions through collisionless shocks. As the ions are much more massive, they are heated to a higher temperature than the electrons. Thus the ions and electrons are in a temperature non-equilibrium, or non-equipartition, state. The electron's temperature is one of the more uncertain parameters of plasma models and likely trails the ion temperature (Hamilton et al. 1983). The electrons are thought to be heated up by either Coulomb collisions or through collisionless shocks by plasma instabilities or turbulence (McKee 1974). Assuming the former, the shock temperature can be calculated as:

$$kT_s = \frac{2(\gamma - 1)}{(\gamma + 1)^2} \mu m_H v_s^2 = \frac{3}{16} \mu m_H v_s^2 \tag{1.24}$$

Spitzer (1962) calculates the equipartition time between electrons and ions as:

$$t_{equ} = 5.87 \frac{A_e^{1/2}}{\epsilon n_e ln\Lambda} T_s^{3/2} (\theta_e + \epsilon\theta_i)^{3/2} \tag{1.25}$$

where A_e is the electron mass (in amu), $\epsilon \equiv m_E/m_i$, Λ the Coulomb logarithm, $\theta_e \equiv T_e/T_s$ and $\theta_i \equiv T_i/T_s$.

Masai (1994) show that the electron temperature can be shown to follow the scaling relationship:

$$T_e \propto (n_e\ t\ T_s)^{2/5} \propto n_e^{2/5}\ t^{2/5}\ v_s^{4/5} \tag{1.26}$$

He shows that electrons can be heated to a few keV fairly quickly (a few $10^2 - 10^3$ years), and that assuming $T_e = T_i$ is not grossly in error.

A different theory, proposed by McKee (1974) suggests that electrons will acquire energy in collisionless shocks at high Mach numbers by means of plasma instabilities or turbulence. Their model would quickly produce equipartition of electron and ion temperatures. Some evidence for this exists, as X-ray observations of young SNRs show electrons heated to several keV, a much higher value than expected without equipartition and suggestive that $T_e \sim T_i$ (Bleeker 1990). However Hughes et al. (1998) find that, in modeling of LMC SNRs, models without collisionless heating were in stronger agreement. Thus the extent of electron heating in the blast wave is one of the most uncertain parameters in X-ray modeling. Until this issue is settled, it is difficult to predict the importance of non-equipartion effects in a middle aged supernova remnant.

The ISM material is typically in a neutral state prior to being shocked, though this is not necessarily the case for a cavity explosion such as the Cygnus Loop. This gas is then in a ionizing state as the rate of ionization far exceeds the rate of recombination. Thus the ionization state is initially lower than would be expected for a gas in a collisional ionization equilibrium (CIE) state at a electron temperature of T_e. This is due to both the age of the remnant being less than the age required to reach an equilibrium state and because the shock is continuously sweeping up new, neutral material (Hamilton et al. 1983). Assuming a state of CIE would therefore underestimate the flux from lower ionization states at a given temperature.

Observations of many of the young ($<$ 2000 years old) historical remnants have recently shown a different nature of X-ray emission. First confirmed in SN 1006, this emission is dominated by continuum rather than emission lines (Koyama et al. 1995). This continuum is generally fit with a power-law that is steeper than that seen in Radio emission (Reynolds & Keohane 1999). However the emission mechanism is the same in both Radio and X-ray: synchrotron radiation. This emission is produced from electrons spiraling along magnetic field lines. As the shock front hits the ISM, magnetic field lines are likely compressed, and electrons can be accelerated to non-thermal velocities. The resultant spectrum is a featureless continuum.

1.3 The Cygnus Loop

Below is a brief description of previous observations taken on the Cygnus Loop SNR. These observations are organized by bandpass for convenience.

1.3.1 Radio Observations

A 1420 MHz image taken by Moffat (1971) using the Cambridge Half-mile Telescope shows that Radio emission is roughly coincident with optical emission (Figure 1.1). A ridge of Radio emission of width $\sim 5'$ is seen along a shell-like shape. This is taken to be a region where the blast wave has compressed the ISM and thus the magnetic field lines. Here electrons can cycle around the magnetic field lines increasing their energy beyond what one would expect from thermalized electrons. This electron motion also causes synchrotron emission. He also finds a fractional polarization of $\sim 25\%$ in the Southern region. This was later confirmed by Kundu & Becker (1972), who estimated the magnetic field strength in the shell to be B $\sim 10\mu$G. Using the Very Large Array (VLA), Straka et al. (1986) find good agreement between the spatial distributions of optical (especially Hα) and Radio emission in the northeastern edge (Figure 1.1). They also note a decrease in Radio emission interior to the bright Hα filaments, but where optical [O I] emission is strong. This is surprising as the lifetime of relativistic electrons is expected to be significantly longer than the time to cool shocked [O I] producing gas.

Observations using the Synthesis Telescope at the Dominion Radio Astrophysical Observatory (Leahy et al. 1997) confirm distinct polarization between the northern and southern portions of the remnant. The north shows only a few areas of polarized emission (with a mean of 2.4% over the northern rim) contrasting the substantial polarized emission from southern regions. Furthermore they find that the brighter regions of X-ray emission in the north are anti-correlated with percent polarization. They suggest that because the north has higher electron density (based on the brighter X-ray emission) it likely has sufficient thermal electrons mixed in with synchrotron electrons to depolarize most of the emission.

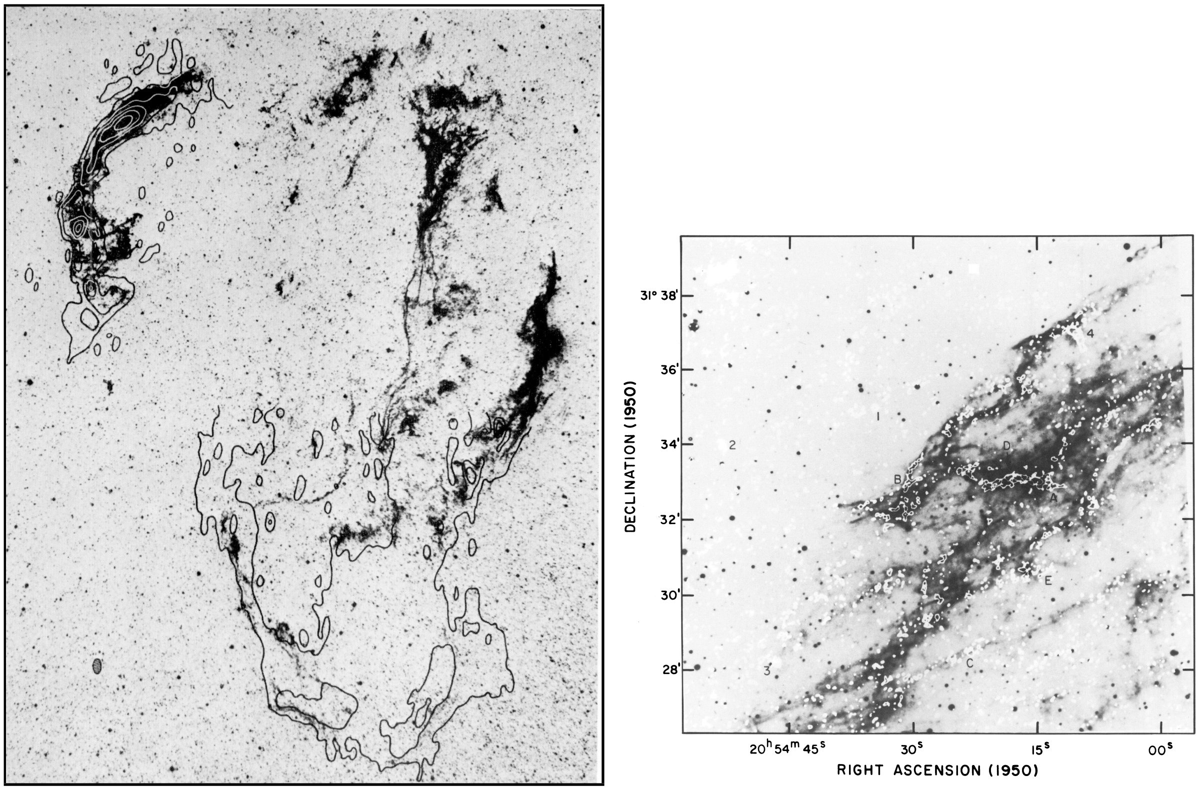

Figure 1.1 Comparison of Radio and Optical emission from the Cygnus Loop. **Left** - Radio contours (1420 MHz) of the entire remnant overlaid onto an image of optical emission. **Right** - Radio contours overlaid on a [S II] image in the northeast corner of the Cygnus Loop from Straka et al. (1986). The authors state that the [S II] emission traces Hα emission extremely well.

A comprehensive spectroscopic study shows significant spectral variations over the Cygnus Loop (Leahy & Roger 1998). Using observations taken at 408 MHz, 1420 MHz and 2695 MHz, they examined 15 regions for comparison, two of which are presented in Figure 1.2. They find a surprising variety in the spectral index between regions ranging from 0.11 to 0.59 over the 408 MHz - 2695 MHz bandpass. This type of spectral variation over a remnant is rare and generally weak. This diversity could provide clues toward the remnant's interaction with the interstellar medium. Further investigation by Uyaniker et al. (2004) found a full remnant integrated spectral index of $\alpha = -0.5 \pm 0.06$ (Figure 1.3), typical of the majority of SNRs and indicative of a compression ratio of $\rho_1/\rho_0 \sim 4$. This spectrum shows no evidence of a spectral break at high frequencies. They find spectral index variations with an upper limit of $\Delta\alpha = 0.2$, with the Southern region dominating at lower frequencies while the flatter filaments elsewhere are strongest at higher frequencies. However they admit that it is uncertain how much of the spectral variations are due to calibration uncertainties, unresolved background sources and limitations inherent when comparing data from multiple telescopes. Their image taken at 1420 MHz is shown in Figure 1.4.

Observations of the HI 21cm line by Leahy (2002) suggest that the remnant is located between two blister regions with the main northern body on the near side and the southern extension on the far side. They define a blister region as an incomplete cavity in the ISM created by wind and ionization action of a star or group of stars located on one side of a dense cloud. This forms a curved wall along the dense cloud, while the other side (with low density) allows essentially free outflow. A competing theory by Uyaniker et al. (2002) is that the remnant is in fact two separate SNRs. Using the Effelsberg 100-m telescope at 2695 MHz they find significant differences in the north and south including: Radio morphology, polarization intensity, magnetic field orientation, steeper Radio spectral index changes in the South (implying less compression and thus a different acceleration mechanism), differences in optical, X-ray and infrared emission as well as the possible discovery of a stellar remnant located in the center of the Southern shell (Miyata et al. 2001). However, this possible stellar remnant was later shown to likely be a V = 12.6 mag G star (Kaplan et al. 2006), thus eliminating its possible progenitor status.

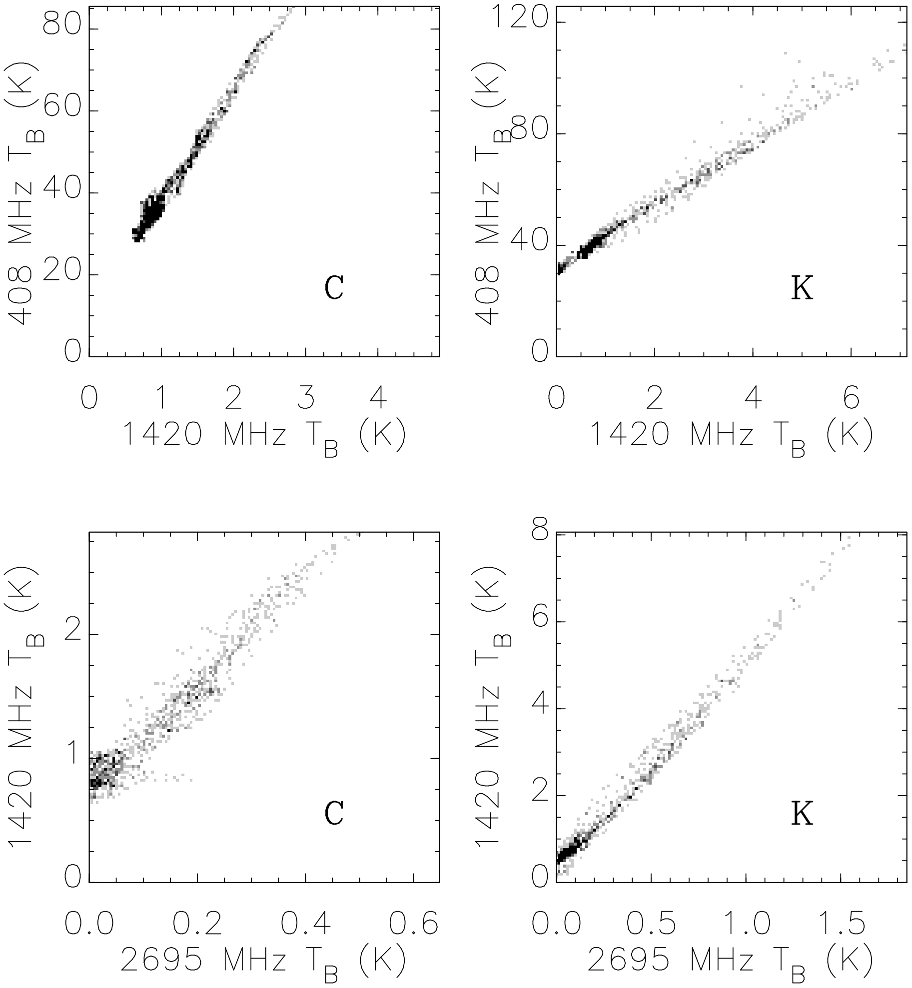

Figure 1.2 408-1420 and 1420-2695 MHz T-T plots for a region in the east-northeast rim (region K) and Southeast rim (region C) showing large differences in spectral index, particularly between 408-1420 MHz.

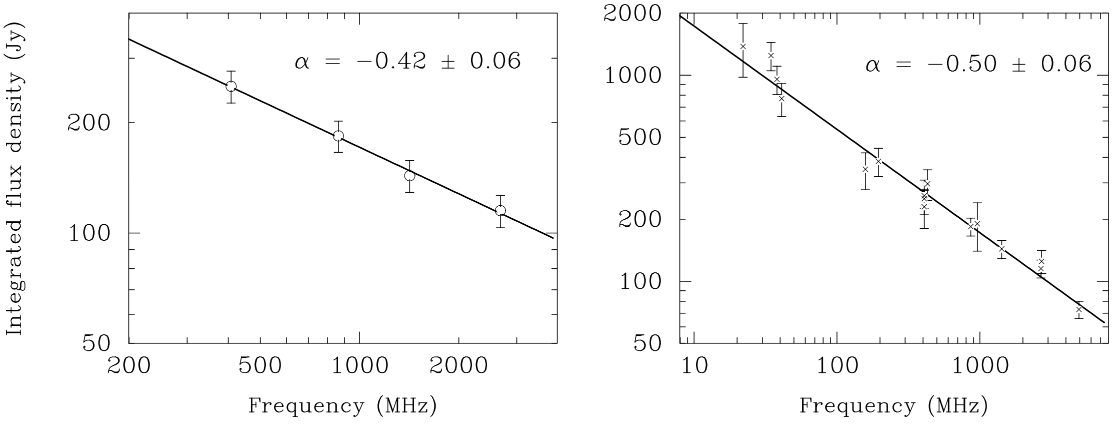

Figure 1.3 Integrated Radio spectra of the Cygnus Loop. **Left** - Results only from Uyaniker et al. (2004). **Right** - Results including previous studies.

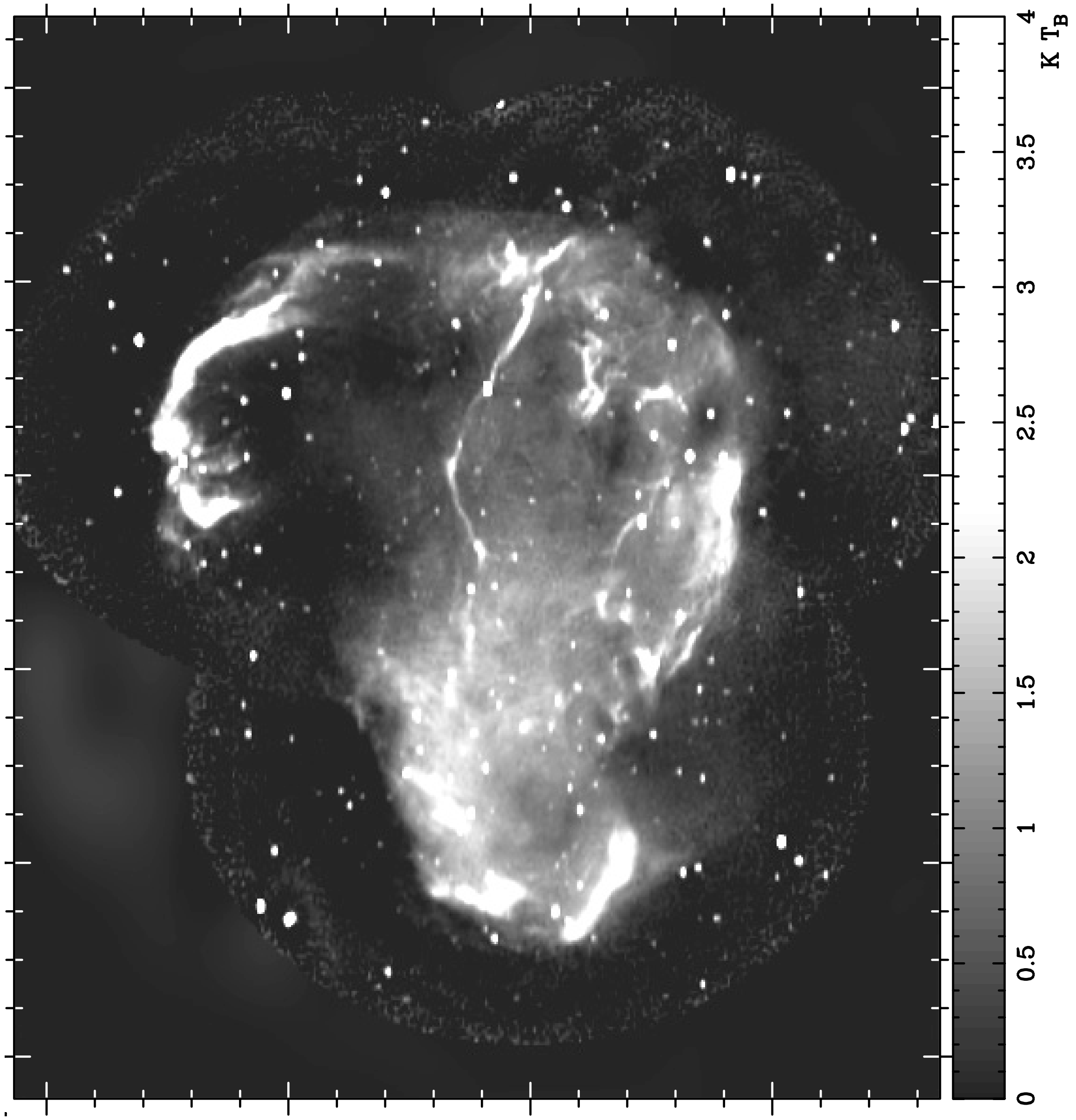

Figure 1.4 Image of the Cygnus Loop taken at 1420 MHz (Uyaniker et al. 2004). The angular HPBW is 1’ x 2’ (EW x NS).

1.3.2 Infrared Observations

Using the Infrared Astronomical Satellite (IRAS) at 12, 25, 60 and 100 µm Braun & Strom (1986) map emission from shock-heated dust in the Cygnus Loop. They find coincident emission with that in optical and X-ray maps (Figure 1.5). By calculating the energy of the remnant they find that if the pre-SNR environment was at a constant mean density, then the implied initial energy is a factor of ~ 4 larger than for other SNR (of both types). To resolve this excess energy they suggest that the pre-SNR environment was a shell geometry where the supernova takes place in the reduced density cavity. This yields fully consistent energy results. This also explains the complicated morphology of the remnant, as it is the result of remnant's interaction with several interconnected stellar bubbles.

Observations at 2µm show emission from vibrationally excited H_2 that is displaced ahead of the optical shock-excited filaments by $40'' - 160''$ in some locations (Graham et al. (1991a), Graham et al. (1991b)). UV fluorescence and X-ray heating as explanations are eliminated based on the broadness of the lines. With UV pumping, one would expect line widths to be reflective of the velocity dispersion of the cloud, and this was not observed. They suggest instead a magnetic shock precursor which gradually compresses the magnetic field ahead of the incoming shock. In their model, ion-magnetosonic waves travel faster than the shock and will heat and compress the preshock gas prior to the shock front arrival. This explains the more outward emission of H_2 in comparison to the shock front.

Observations by Arendt et al. (1992) show that the IR emission is well correlated with X-ray and optical emission. They decompose the IR emission into two distinct components, one correlated with the X-ray shell, and another with the optical filaments. The emission correlated with the X-ray shell is from collissionally heated dust with a temperature ~ 31 K and modelling work suggests a difficiency of grain radii below ~ 150 Å . The IR emission correlated with optical filaments is also at ~ 30 K heated by either collisional or radiative heating within the filaments.

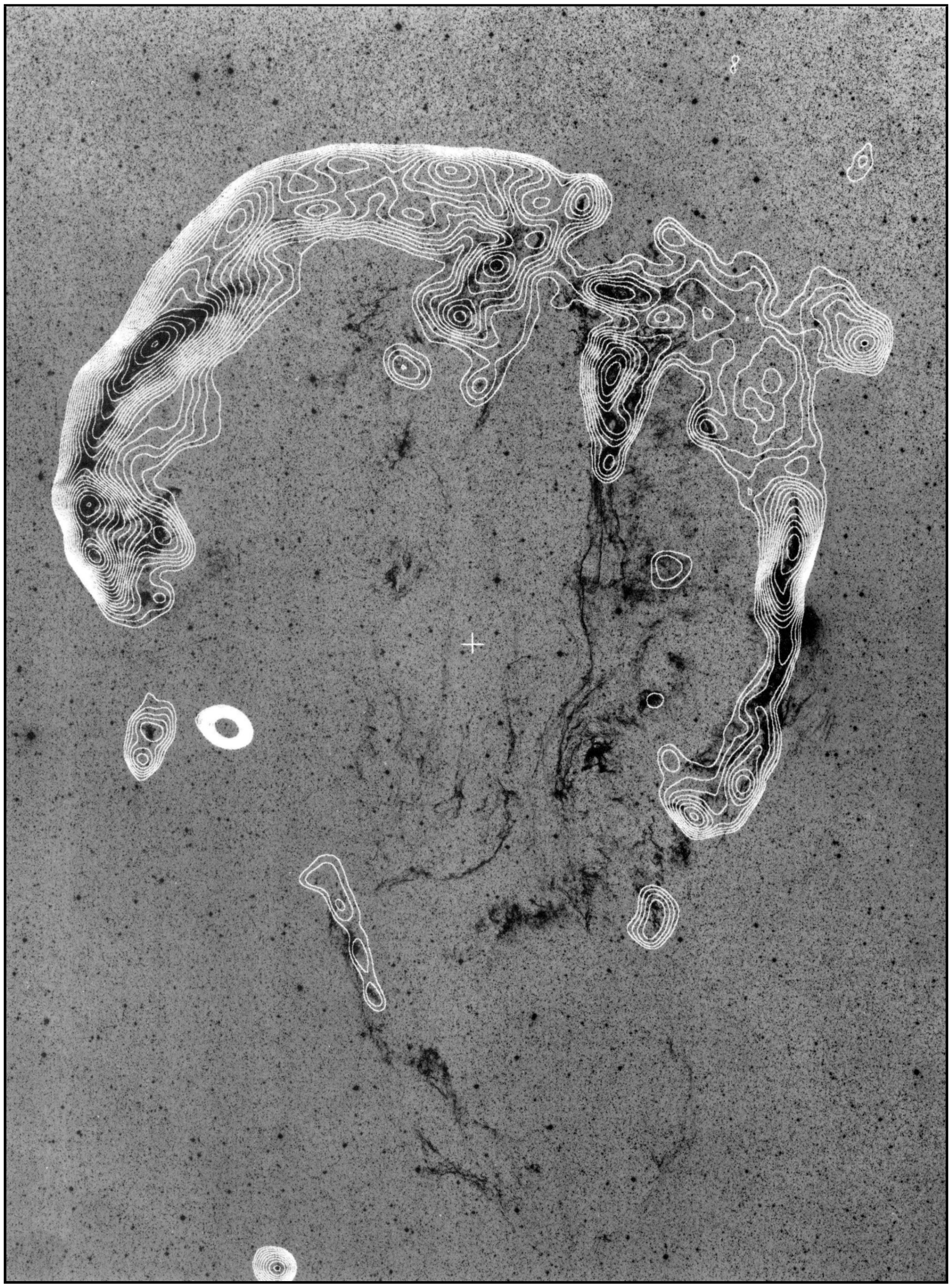

Figure 1.5 Contours of 60 μm dust emission from the Cygnus Loop overlaid on an optical image (Braun & Strom 1986).

1.3.3 Optical/ Ultraviolet Observations

Radial velocity studies in the optical by Minkowski (1958) found typical velocities of ∼100 km/s from the inner to outer radius of the remnant. Combined with an average proper motion of .03″/year leads to the calculation of a 770 pc distance to the Cygnus Loop (often referred to as the Veil Nebula in optical). Morphologically these filaments are thought to be sheets of gas seen edge-on (Greidanus & Strom (1992), Hester & Cox (1986)). The complex filamentary structure is due to slight density variations in the pre-shock density (Raymond et al. 1988). This low velocity supported the idea of an older (and thus slower) remnant in the radiative phase (Section 1.1.3) of development. However, Kirshner & Taylor (1976) find higher radial velocities in the range of +200 to -300 km/s using a scanning Fabry-Perot interferometer in low surface brightness regions. It is possible that the slower velocities measured before were due to slower shocks propagating in denser regions. This would explain their coincidence with high surface brightness features. The finding of a faint filament (Figure 1.6) traveling significantly ahead of the bright slow shock and emitting only in hydrogen Balmer (in the 4500 - 6900 Å bandpass) supports the fast shock idea (Raymond et al. 1980). These types of filaments are known as Balmer dominated or non-radiative filaments and are found exterior to the radiative regions due to their higher velocities. Given the velocities involved, it is likely the fast blast wave is traveling into a low density ($\sim 0.1 - 1$ cm^{-3}) inter-cloud region, while the slow waves are traveling within much denser ($\sim 1 - 10$ cm^{-3}) interstellar clouds. These lower density regions experience higher velocity shocks in addition to higher post-schock temperatures, causing the observed X-ray and coronal-line emissions. If these high velocity shocks encounter a partially neutral gas (sometimes referred to as the atomic shell around the SNR), the collisionless shock can excite the hydrogren atoms, permitting narrow Balmer photons with line profile widths corresponding to preshock temperatures. Additionally, shock-heated protons can recombine via charge exchange and emit Balmer lines after collisional excitations causing broad profiles corresponding to post-shock temperatures (Fesen & Itoh 1985).

Observations at the Palomar Observatory by Hester et al. (1994) produced a beautiful high-resolution Hα image in the northeast limb of the Cygnus Loop (Figure 1.6). Comparison of this image to previous images gives them a proper motion of $\sim 2''$ over the last 30 years. Combined with an estimated 200 km/s velocity gives them a distance of $\sim$ 700 pc. Further observations of Hα over the western and eastern limbs reveal several asymmetries in the Loop (Shull & Hippelein 1991). The shocked material on the near side of the SN is faster and fainter than that on the far side. The measured radial velocities range from -262 km/s on the near side to +92 km/s on the far side. This supports the idea of the progenitor evolving into a density discontinuity in the ISM. The progenitor created an asymmetric cavity due to this density discontinuity. Now the near side of the SNR is still expanding quickly into the low density gas, while the far half has encountered the higher density ISM and has thus been slowed down and begun emitting more brightly. These measurements put the Cygnus Loop at 600 pc. Using the Hubble Space Telescope, Blair et al. (1999), analyzed the proper motion of a single nonradiative filament in Hα over the last 44 years and deduce a distance of 440^{+130}_{-100} pc. This gives the remnant a physical size of 21.5 x 27 pc.

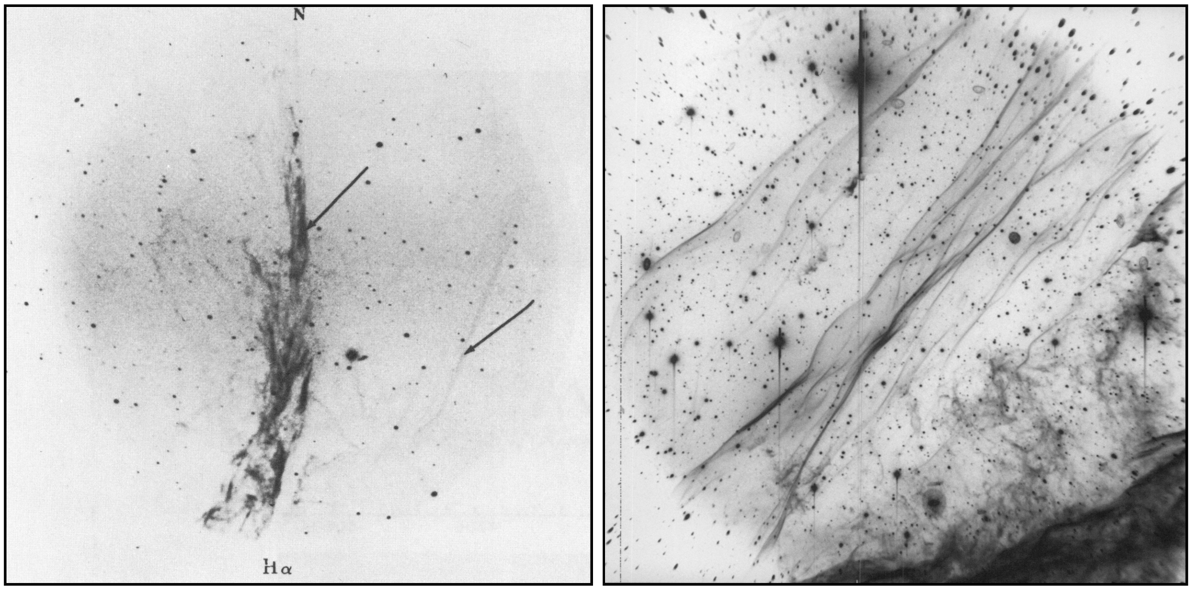

Figure 1.6 **Left** - Hα image of the NW part of the Cygnus Loop. The left arrow represents a bright filament also visible in [O III], while the right arrow represents a filament that does not emit in [O III]. This filament is thought to be a faster shock traveling ahead of the slower, bright shock behind it (Raymond et al. 1980). The image diameter is $\sim 17'$. **Right** - Hα image of the NE limb of the Cygnus Loop (Hester et al. 1994).

In another observation of Hα by Fesen et al. (1992) at Kitt Peak several conceptual shock behaviors are illustrated. This observation is a classic example of Balmer-dominated shocks, denser cloud structures, gas stripping and reverse shock emission. See the Figure 1.7 caption for details. By examining the northeastern Balmer-dominated limb, Hester et al. (1994) find that the limb may be decelerating rather quickly. This is consistent with the theory of a cavity explosion, where the blast wave has relatively recently begun to interact with the denser cavity wall. They also find that the narrow component of the Hα line has a line profile of surprising width (~ 33 km/s), corresponding to a preshock temperature of $\sim 25,000$K. They suggest this heating could be due to fast neutrals overtaking the shock wave or by cosmic rays.

Observations by Woodgate et al. (1974), Ballet (1989) and Sauvageot & Decourchelle (1995) detect lines of [Fe X] at 6374 Å and [Fe XIV] at 5303 Å in a strong X-ray emitting region of the Cygnus Loop. Typically supernova remnants that emit thermal X-rays also emit optical coronal lines, thus this finding supports the thermal nature of soft X-rays.

Levenson & Graham (2001) produce a false color image (Figure 1.8) in Hα, [S II] and [O III]. In this image the [O III] emission is immediately behind the shock front, indicating relatively fast shocks ($v_s \sim 170$ km/s) in the high density ($n \sim 15$ cm^{-3}) cloud.

Ultraviolet spectra taken by Benvenuti et al. (1980), Contini & Shaviv (1982) found depletion of several elements: C, N, O, Si, S and Fe with respect to cosmic abundances. Using the Hopkins Ultraviolet Telescope, Blair et al. (1991) take a detailed spectrum of a newly discovered fast radiative shock (≥ 150 km/s). They find strong emission in C III, N III and O VI as well as many fainter lines. Using the B5 band on the Ultraviolet Imaging Telescope (UIT) aboard the Space Shuttle, Danforth et al. (2000) find general agreement with Hα emission in nonradiative filaments, and agreement with [O III] emission in radiative filaments. This suggests that the emission in this bandpass arises at similar excitation energies, such as C IV.

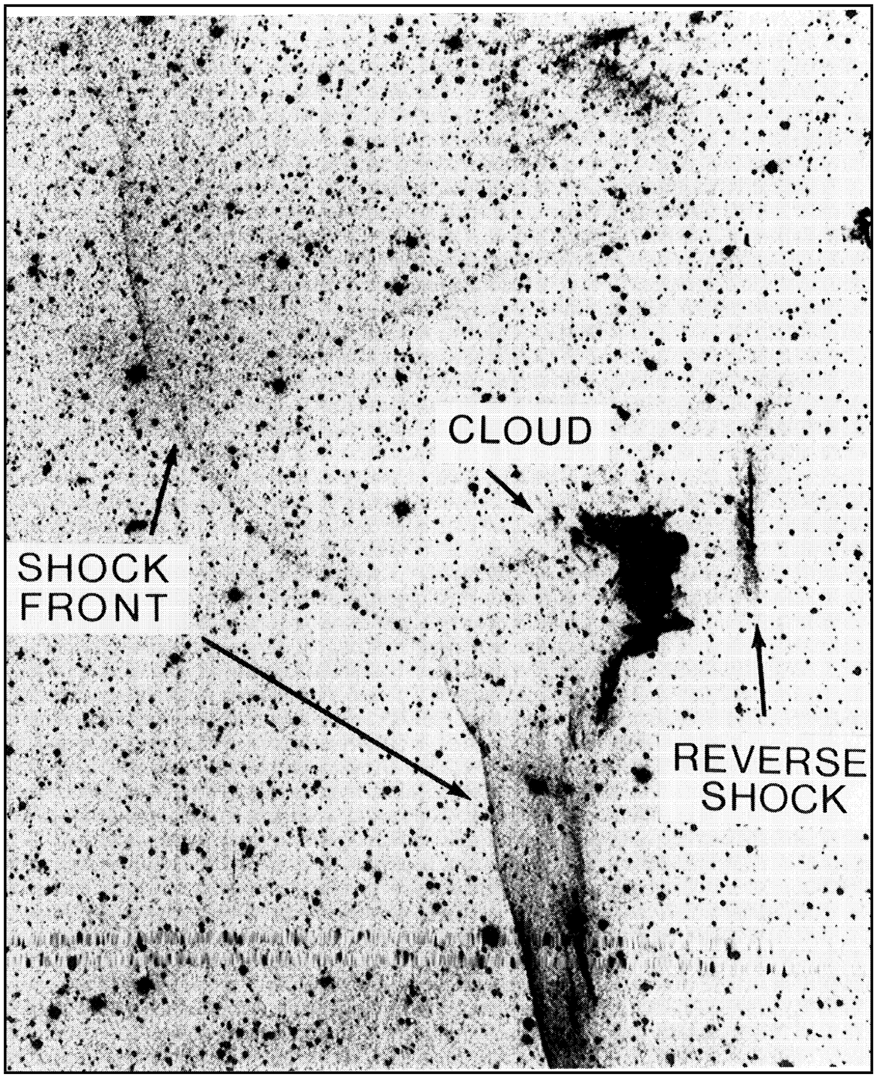

Figure 1.7 Hα image taken along the eastern side of the Cygnus Loop (Fesen et al. 1992). Here the foremost blast wave (traveling leftwards) is moving quickly ($\geq$ 200 km/s) and is rather faint due to the low density of the local ISM. Sometime recently (4.1 x 10^3 years ago based upon the $7.8'$ separation from the forward shock), the shock wave interacted with the cloud structure located behind the lower shock front. This cloud is $2'$ x $4'$ in angular size, 0.5 pc in physical size, a preshock density of 1-10 cm^{-3}, and a mass of $0.01 - 0.1 M_{\odot}$. As the shock hits this cloud, several items of interest occur. Due to the higher density, the cloud will begin to glow brightly in comparison to the Balmer-dominated shocks. This emission will be not just in Hα, but likely in other forbidden lines such as [O III]. This interaction will also generate a reverse shock that will reheat the interior material and cause bright emission particularly in the X-ray bandpass. This reverse shock is traveling at $\sim$ 180 km/s. The lower forward shock front is in the process of stripping away gas from the cloud. This suggests that the cloud has a lower density surface region, likely a warm partially ionized envelope that is being stolen by the shock front. The morphology of the forward shock fronts is due in part to cloud diffraction as the main cloud, as well as the smaller cloud in the northwestern corner of the image, modify the shape of the shock.

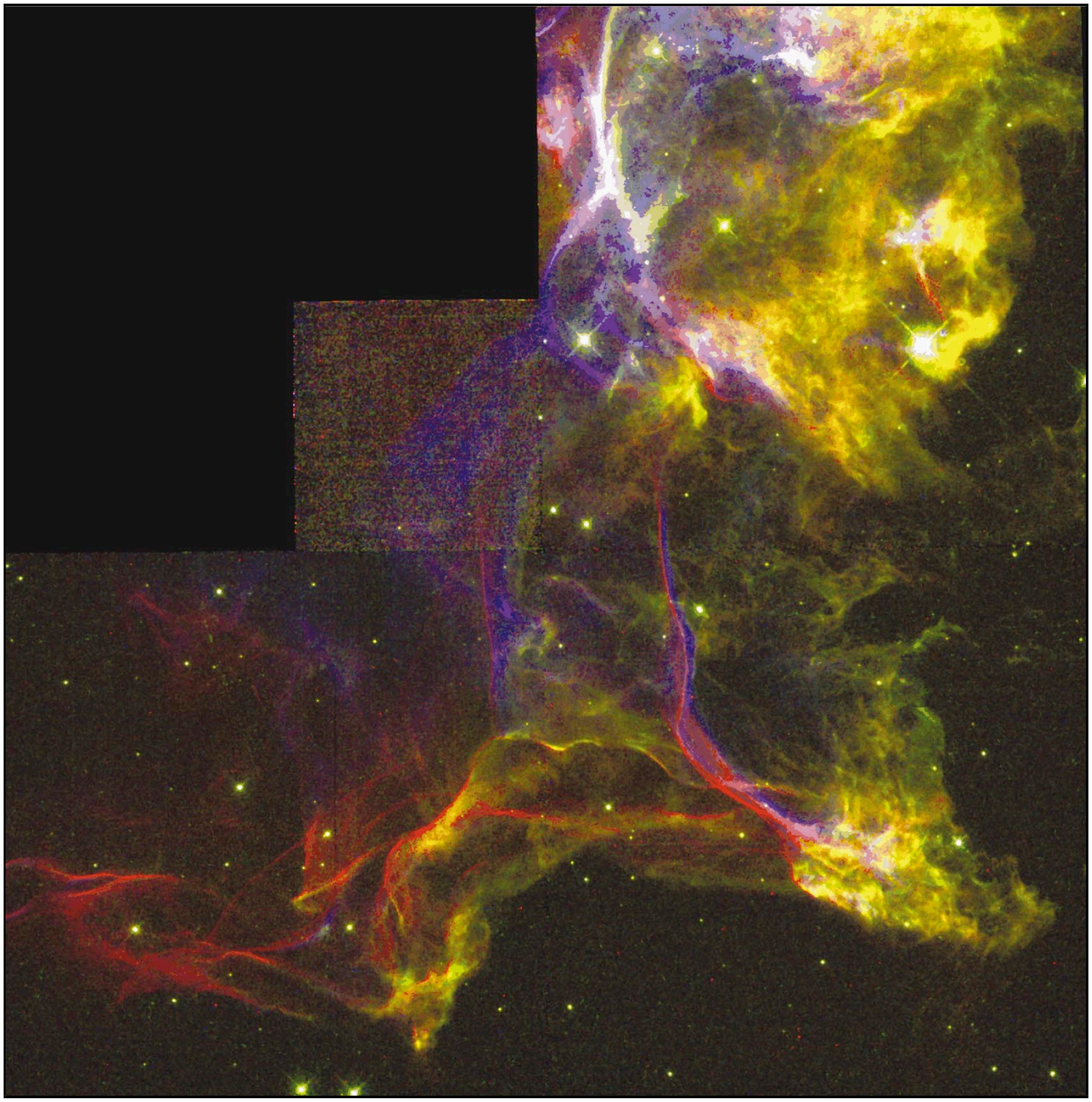

Figure 1.8 False color image in the Southeast corner of the Cygnus Loop (Levenson & Graham 2001). Color scheme is: Hα in red, [S II] in green, [O III] in blue. Yellow marks radiative cooling zones, while red is nonradiative Balmer-filaments.

1.3.4 X-ray Observations

One of the most comprehensive imaging studies of the Cygnus Loop is shown in Figure 1.9 (Levenson et al. (1997), Levenson et al. (1998)). The X-ray emission indicates a global shock velocity of a few hundred km/s, while the optical emission comes from denser regions of the ISM that decelerate the blast wave. The general correlation between the two indicates that this is a relatively new occurrence. This supports the cavity-explosion theory where the blast wave has only recently encountered the cavity wall rather than the original thought of a gradual evolution into the radiative phase. Around most of the perimeter of the Loop, Balmer-dominated filaments are emitting in Hα, marking the boundary of neutral material and just exterior to the limb-brightened X-rays. The continuity and smoothness of these filaments indicates that the medium in which they propagate is rather uniform, and of density $n \sim 0.1$ cm^{-3}. These filaments have an estimated age of ~ 1000 years. An additional observation by Levenson et al. (1999) utilized the ROSAT Position Sensitive Proportional Counter and obtained images of the entire loop at 0.25 keV and 1.25 keV (Figure 1.10).

A study by Aschenbach & Leahy (1999) compared X-ray images from ROSAT with Radio images from the Dominion Radio Astrophysical Observatory (DRAO). Figure 1.11 shows how these images compare. The result is fairly unclear. The most general difference is that the X-ray emission is significantly brighter in the north, while the Radio emits more strongly in the south. There are significant differences in the distribution of X-ray and Radio emission. However, several filaments show features in both bandpasses. The authors also complete a comparison of X-ray and Radio emission at the outer shock. The result (Figure 1.12) shows that the mean difference of the emission's radial location on the circumference is consistent with zero, but can vary with typical spreads of $\sim \pm 2'$.

One of the better high resolution spectra obtained in the 1/4 keV band was obtained by Vedder et al. (1986). Using the Focal Plane Crystal Spectrometer on the Einstein Observatory the authors scanned a small portion of the Cynus Loop and observed emission from O VII, O VIII and

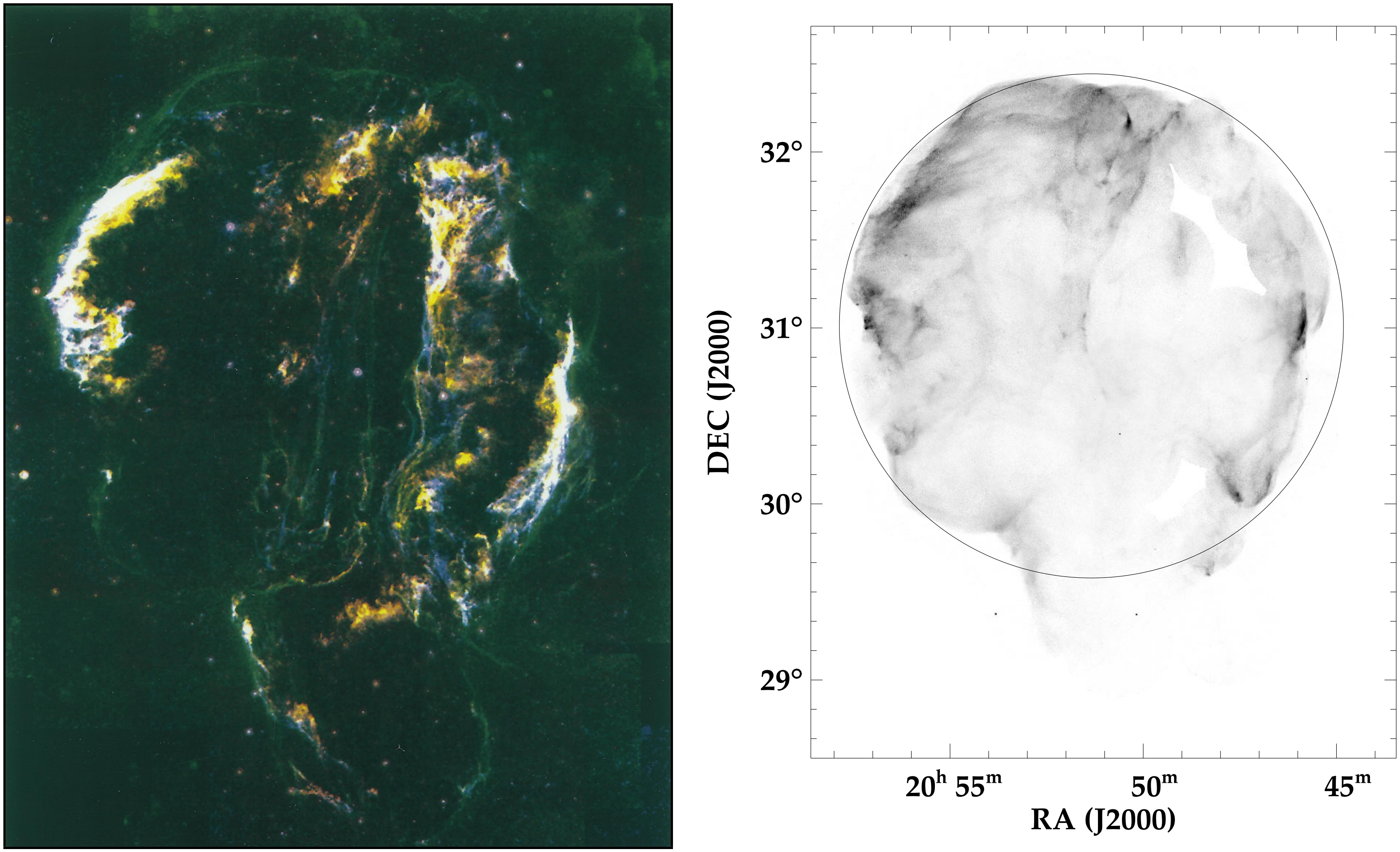

Figure 1.9 **Left** - Optical image showing Hα (green), [S II] (red) and [O III] (blue). Blends of Hα and [S II] are yellow, [O III] and [S II] are magenta and Hα and [O III] are cyan. **Right** - ROSAT HRI map of the Cygnus Loop in soft X-rays. The circle is the best fit circle to the blast wave edge defined by Balmer-dominated filaments emitting in Hα. Both images are from Levenson et al. (1998).

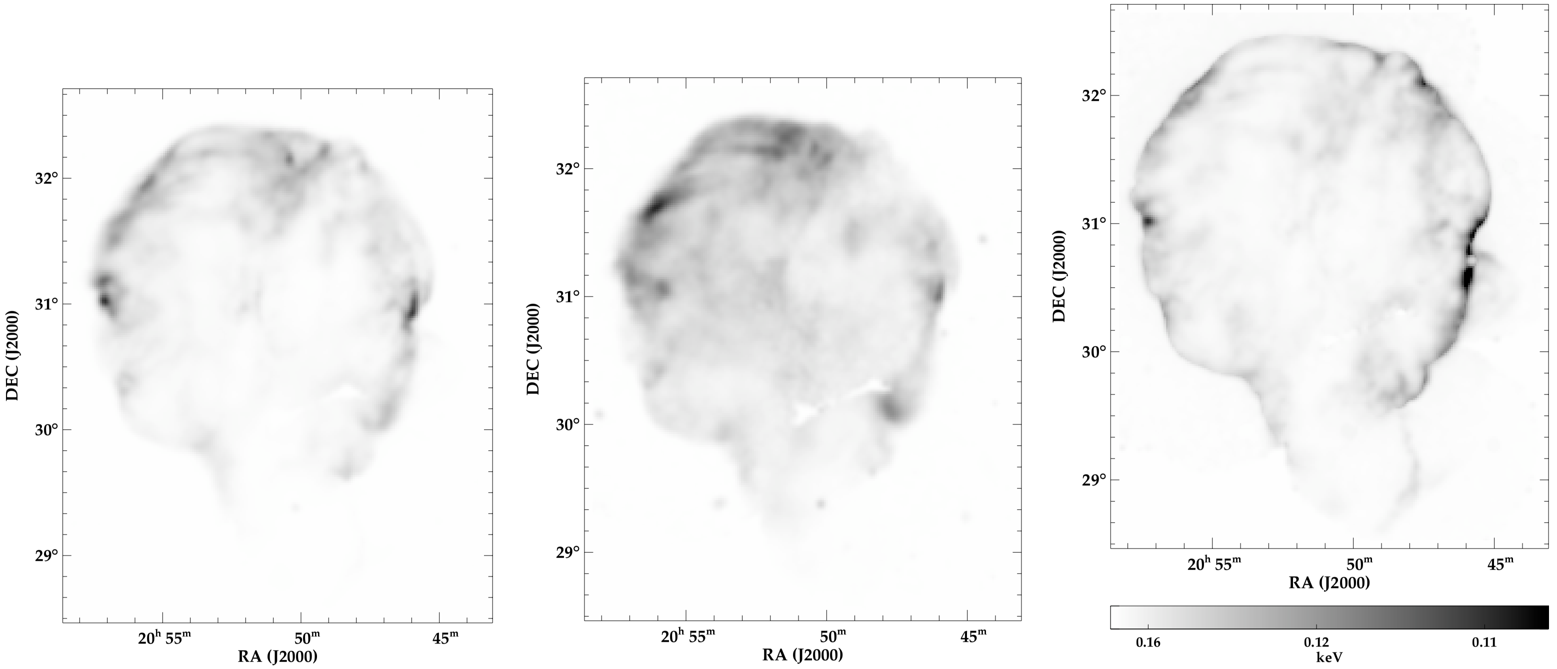

Figure 1.10 **Left** - ROSAT image at 0.25 keV. **Center** - ROSAT image at 1.25 keV. **Right** - Softness map of the Cygnus Loop. Corresponding temperature of a Raymond-Smith thermal plasma model is shown on the bottom.

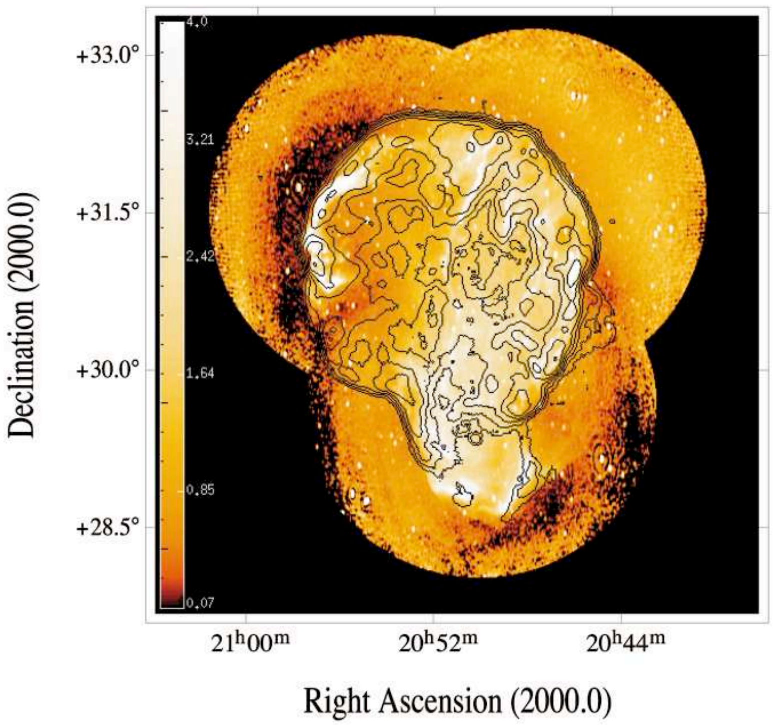

Figure 1.11 Radio brightness (in Kelvin) displayed in a logarithmic color scale overlayed with contours from the ROSAT .08-.41 keV map.

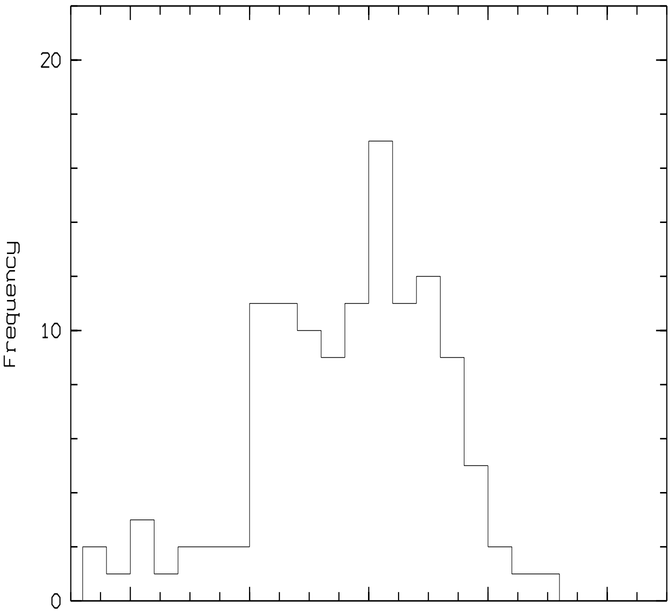

Figure 1.12 Histogram of offsets between the Radio edge and X-ray edge. The mean is 7″ and the FWHM is 3.6′.

Ne IX. The spectrum is shown in Figure 1.13. This spectrum is very useful as it can resolve the helium like triplet lines of O VII. By calculating the ratio of forbidden to resonance line emission leads to a determination of the likelihood of CIE conditions. Creating He-like ions in an excited state can occur via three main processes: collisional excitations, inner-shell ionizations of Li-like ions and recombination of H-like ions. If the plasma is ionizing, the relative H-like population is smaller than that of He-like ions, so the contribution of recombining H-like to He-like ions is small. Because the recombination process favors the forbidden triplet level, the forbidden to resonance ratio is reduced in a non-equilibriun (ionizing) state. For equilibrium plasmas between $10^6 - 10^7$ K, this ratio should be $\sim 0.6 - 1.0$. Because there is little to no forbidden line emission, this strongly suggests that the portion of the Cygnus Loop observed is not in ionization equilibrium.

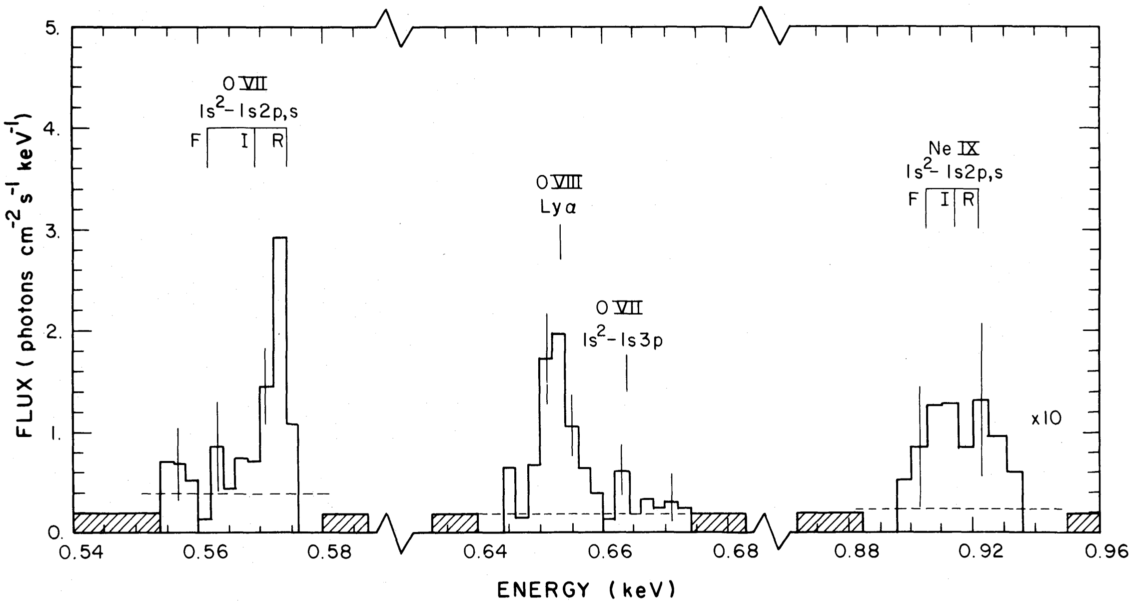

Figure 1.13 Soft X-ray spectrum obtained with the FPCS. The neon lines have been multiplied by a factor of 10. The dashed line marks the background level.

Using the Chandra ACIS CCD, Levenson et al. (2002) examine spectra from 4 small ($1' \times 15''$) regions (Figure 1.14). Their spectral fits (Figure 1.15) utilize equilibrium plasma models and find no evidence of nonequilibrium conditions. The find a temperature of kT = 0.03 keV best fits the X-rays at the shock front. Interior to the shock front, they find that the reflected shock has heated the material and is emitting with a kT $\sim$ 0.2 keV. The regions are best fit with absorbing column densities of $4.7 - 24 \times 10^{20}$ cm^{-2} and about half the solar abundance of oxygen. However these fits are fairly low quality, producing $\chi^2_\nu = 1.4 - 2.6$. Observations of the southwest limb using the same instrument show significant spectral variations in the region (Leahy 2004). These variations seem to be due to compositional, temperature and column density variations. Of the 21 sub-regions examined all were best fit with a VMEKAL model with kT = 0.174 - .207 keV. The Ne/O and Fe/O ratio are nearly constant in all the spectra, a further indication that the elements all originated in a single supernova. Given the ratios this was most likely a type II SN with $\sim 11 - 20 M_\odot$.

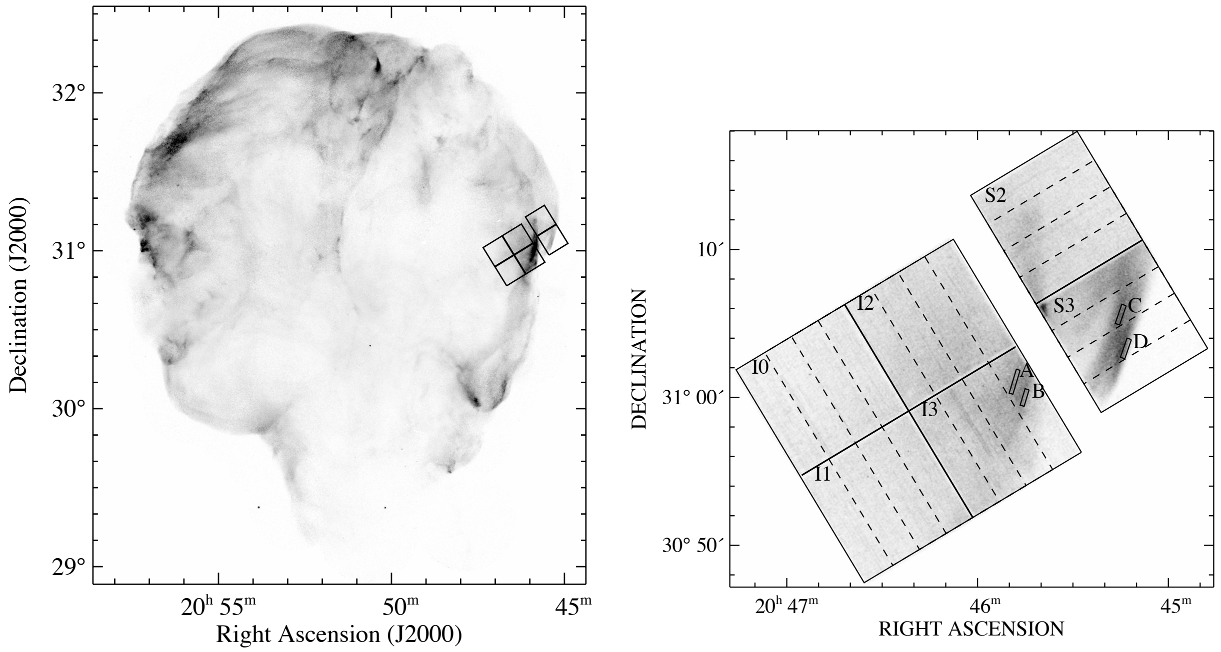

Figure 1.14 **Left** - Field of view of the Chandra ACIS instrument superimposed on the ROSAT HRI image of the full Cygnus Loop. **Right** - Magnified view of the 6 CCD chips. The rectangles are approximately 1' x 15" and are labelled for further spectral analysis.

Observations by Miyata et al. (2007) using Suzaku show different results. Using the energy resolution of the CCDs on Suzaku's XIS instrument, they obtain a spectrum of the northeastern limb of the Cygnus Loop (Figure 1.16). This spectrum (Figure 1.17) shows the strongest emission in lines of O VII and O VIII. The gap at $\sim$ 300 eV is due to the absorption edge of C used in the XRT thermal shield and the optical blocking filter of XIS. They note that there is significant emission below this edge in the 1/4 keV bandpass. Figure 1.18 shows several narrow band images of

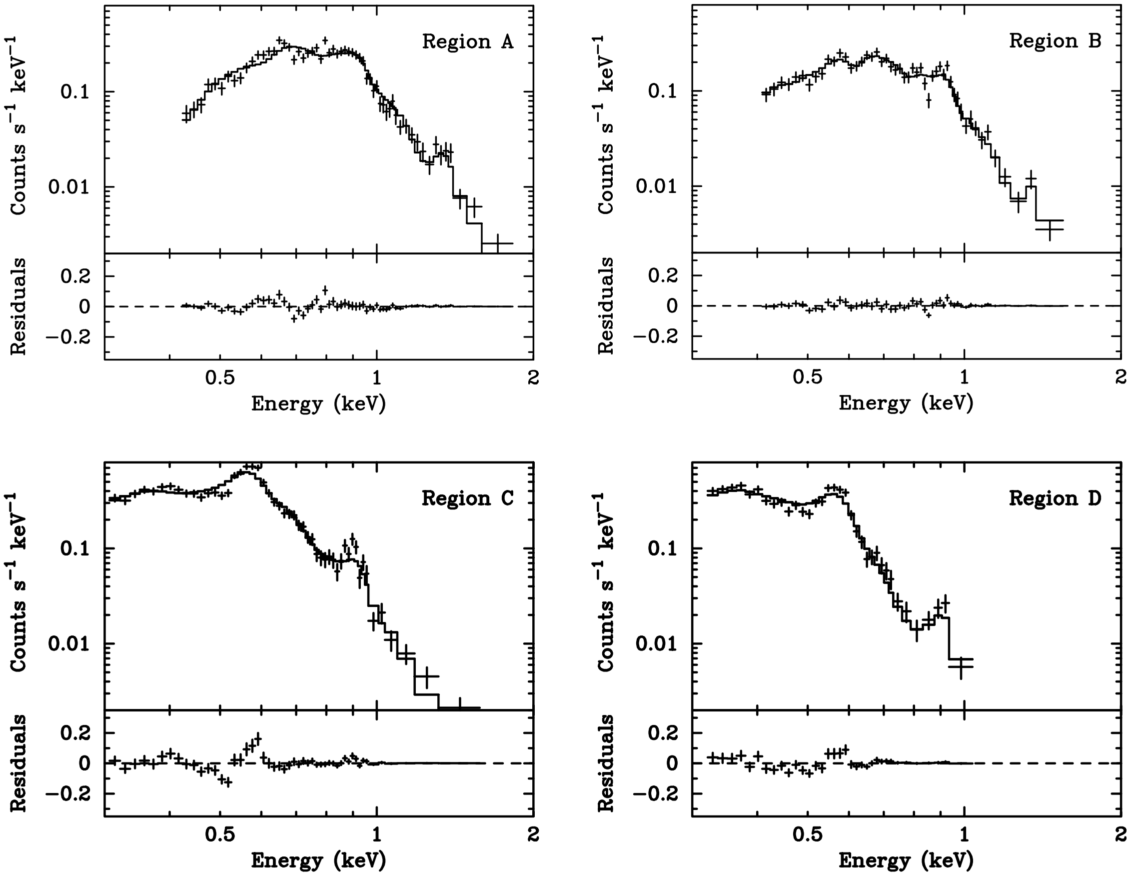

Figure 1.15 Spectra from the four regions depicted in Figure 1.14. Region B is the coolest, best fit with a 0.03 keV equilibrium model.

the NE limb at different energies. This shows a lower temperature component farthest out emitting in the 220 - 320 eV C-band in image (a). Image (f) shows the ratio of O VIII to O VII and clearly shows an increase in ionization towards the inner region as this region has been shocked earlier and had more time to progress to higher ionization states. They extracted spectra from concentric annuli regions in their FOV. These regions were best fit with a non-equilibrium, two temperature model. A followup observation by Chandra was performed and showed a small region on the edge of the NE limb with enhanced abundances than the rest of the limb (Katsuda et al. 2008). This enhanced region is concentrated in a $\sim 200''$ thick region behind the shock front. They suggest that in this region the blast wave has already overrun the cavity wall and is now within the relatively enriched ISM material.

Observations by Tsunemi et al. (2009) show similar results. Using Suzaku on the SE limb, they find higher energy emission interior to colder C-band emission. They find that the outer limb has a higher oxygen abundance ($\sim$ 0.4 solar) compared to the inner regions at $\sim$ 0.2 solar. Both this SE limb and the NE limb show decreased abundances compared to solar. They compare the X-ray emission to Radio emission in these two regions. Based on the lack of emission in Radio in the SE limb, especially when compared to the Radio bright NE limb, they state that the non-thermal emission therefore does not contribute towards the low abundances observed.

Using XMM-Newton, Tsunemi et al. (2007) performed seven observations on the Cygnus Loop. The location of these exposures scanned from the northeast rim to the southwest rim (Figure 1.19). They separated these observations into 313 annular sections, each having at least 60,000 photons. They suggest that they may be detecting the hot temperature component seen by Miyata et al. (2007), but that XMM-Newton's lower sensitivity below 0.5 keV is hiding the low temperature component. They also attempt a two temperature NEI model fit. This second component has metallicities fixed by the northeast rim, which is assumed to be dominated by cavity material due to the lower metallicity than surrounding ISM. They found that the second temperature component was unnecessary at the rim regions, but helped fit the interior of the loop. The results of these fits are shown in Figure 1.20. The rim spectrum was best fit ($\chi^2_\nu \sim 1.3$) with a single temperature NEI

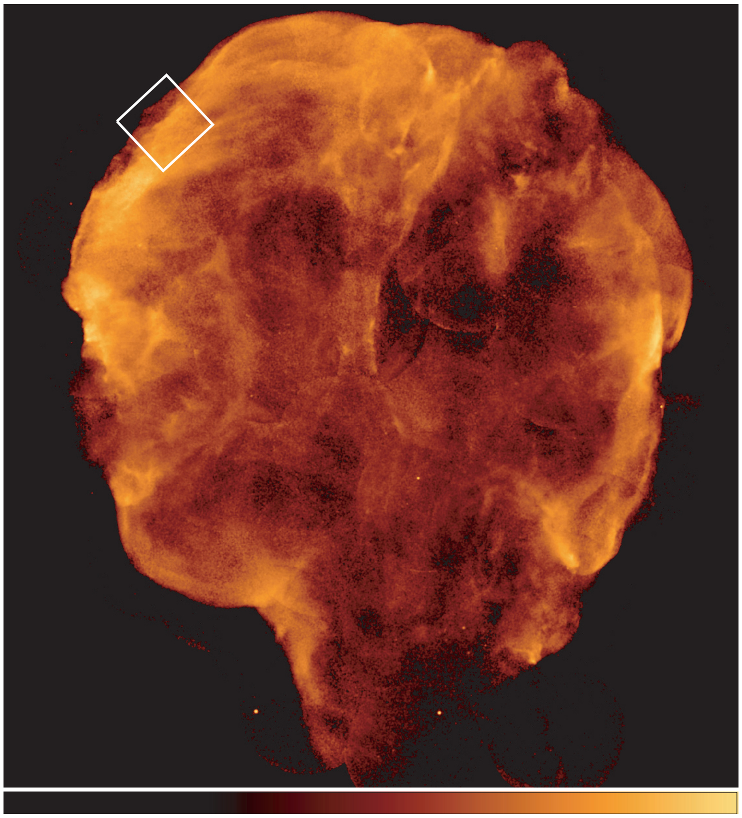

Figure 1.16 Surface brightness map of the Cygnus Loop with a white box detailing the FOV of the XIS instrument on Suzaku.

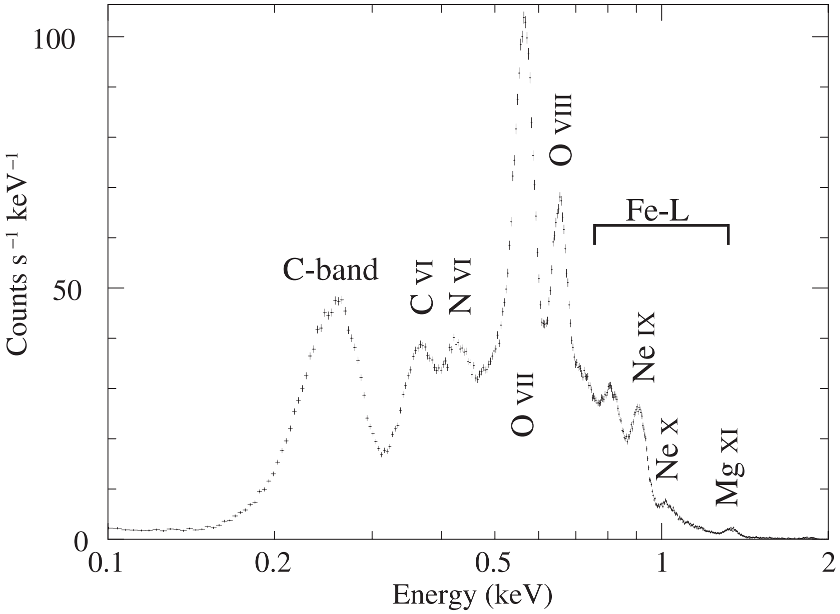

Figure 1.17 Spectrum of the NE region of the Cygnus Loop

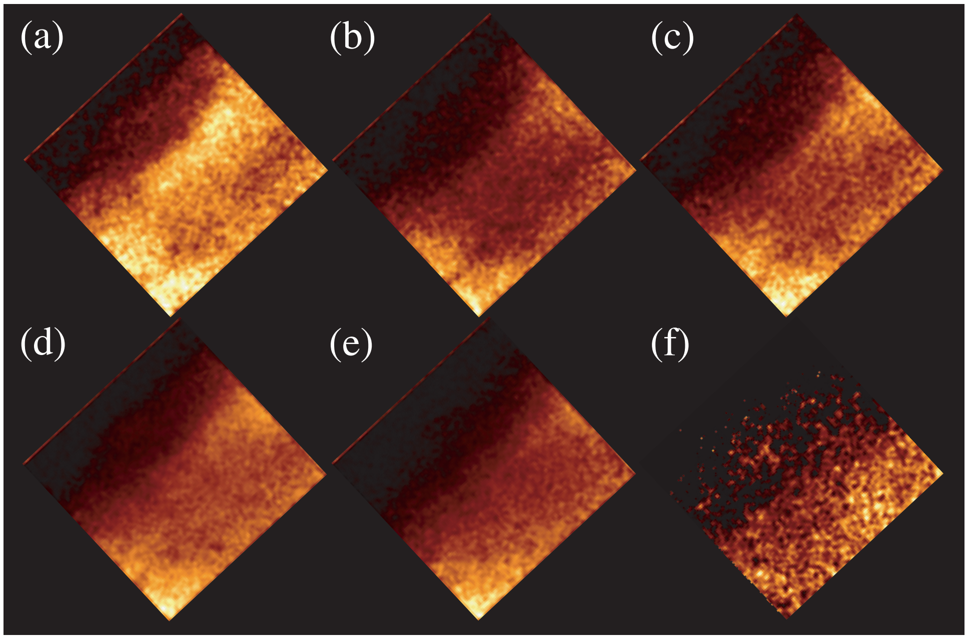

Figure 1.18 Suzaku XIS narrow-band images for (a) C-band, (b) C VI, (c) N VI, (d) O VII, and (e) O VIII. The band-ratio image of O VIII to O VII is shown in (f).

model with a temperature of 0.23 keV, $N_H = 4 \times 10^{20}$ cm^{-2} and reduced metallicity particularly of O, C and N at 0.068 solar. The two component model showed temperatures of 0.2 and 0.48 keV and utilized the same intervening column density. The ionization timescale ($\log(\mathrm{n}_e t)$) ranged from 11.31-11.99. Metal abundances for the high temperature component are generally higher (though O, C and N are lower) leading to the conclusion that this component is likely dominated by fossil ejecta. Based on the metal abundances, they estimate the Cygnus Loop originated from a $15 M_\odot$ star. They also suggest the explosion was asymmetric as two-thirds of the O and Mg are observed in the northern half, while two-thirds of Si and S are observed in the southern half. They also find that the southern half contains the largest ejecta mass. A similar study by Uchida et al. (2009a) used 14 pointings by Suzaku and 7 by XMM-Newton. They find all the spectra are well fit with a two component NEI model. Example spectra of a subregion showed temperatures of 0.19 and 0.42 keV, $\mathrm{N}_H = 3.6 \times 10^{20}$ cm^{-2} and lower abundances in the lower temperature component. They find a "metal center" where Si and Fe distributions peak south of the geometric center towards the blow-out region. An estimate of the progenitor mass from these distributions gives a range of 12-15 $M_\odot$. A follow up study by Uchida et al. (2009b) used 41 observations by Suzaku and XMM-Newton. This survey confirms that there exists a high-kT_e ejecta component surrounded by a low kT_e ISM component. The inner region out to approximately 80% of the shock radius needs this second temperature component (Figure 1.21). The average value of these components is 0.23 keV and 0.52 keV respectfully. The distribution of these components is shown in Figure 1.22, clearly showing the low temperature component peak at the cavity walls, while the high temperature ejecta component becomes necessary within the interior.

An XMM-Newton observation by Zhou et al. (2010) of the XA region along the eastern front of the Cygnus Loop shows a complicated morphology. They find several clumps interacting with the primary blast wave. The joint abundances are found to be lower ($\sim$ 0.2 solar), in agreement with other studies. They also find evidence of ejecta. The two temperature fits used involved a 0.15 keV component and a $>$ 0.24 keV component from region to region within the larger XA region. Another study by McEntaffer & Brantseg (2011) utilized Chandra data in the same region and obtained

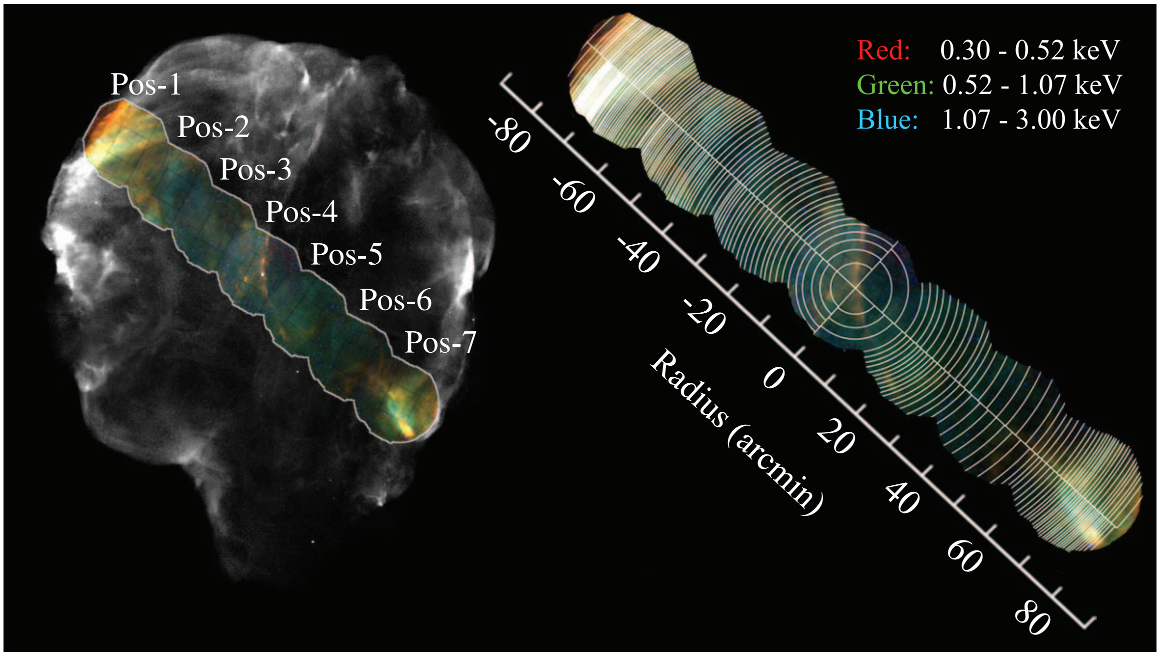

Figure 1.19 **Left** - Regions observed by XMM-Newton (in color) overlaid on top of the ROSAT HRI image of the entire Cygnus Loop in black and white. **Right** - Spectral extraction regions.

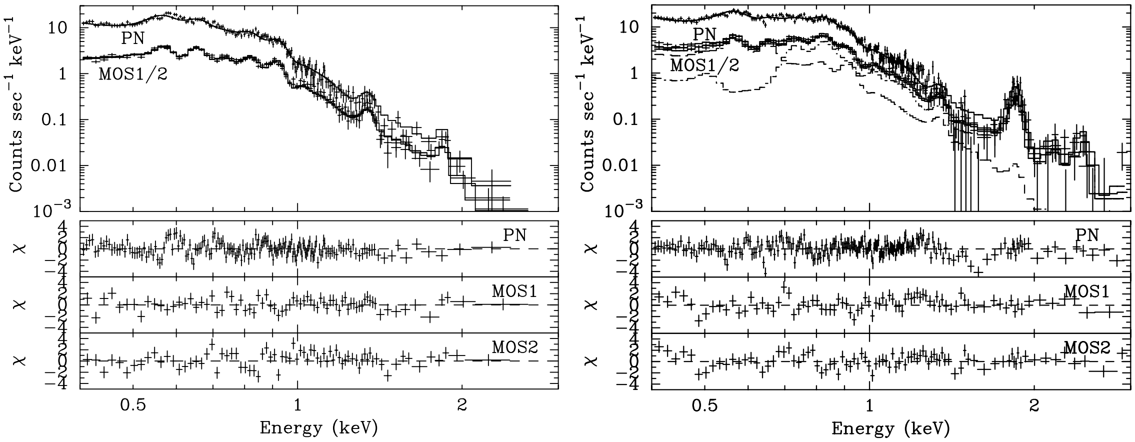

Figure 1.20 **Left** - Sample spectrum near the northeastern rim. **Right** - Spectrum near the center of the remnant utilizing a two component fit. The two components are shown in dashed lines for the MOS1 spectrum.

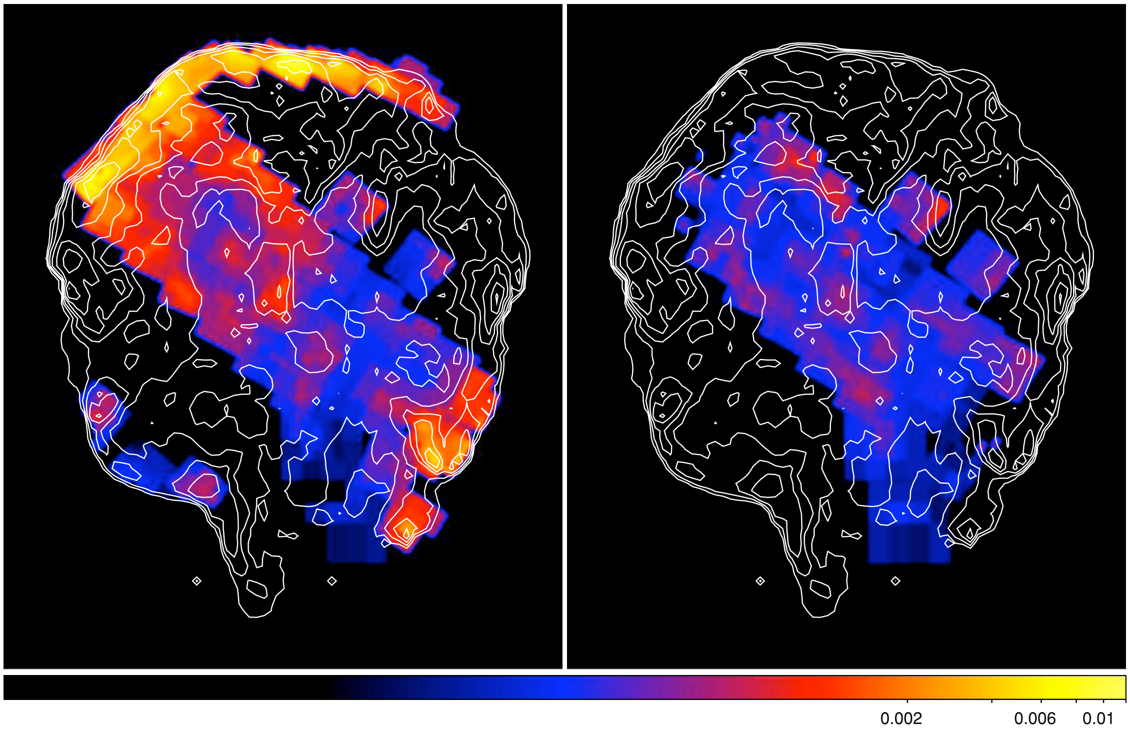

Figure 1.21 **Left** - low kT$_e$ component distribution in units of counts cm^{-2} s^{-1} arcmin^{-2} overlaid with the white contour of the ROSAT HRI image. **Right** - Same, but for the high temperature component.

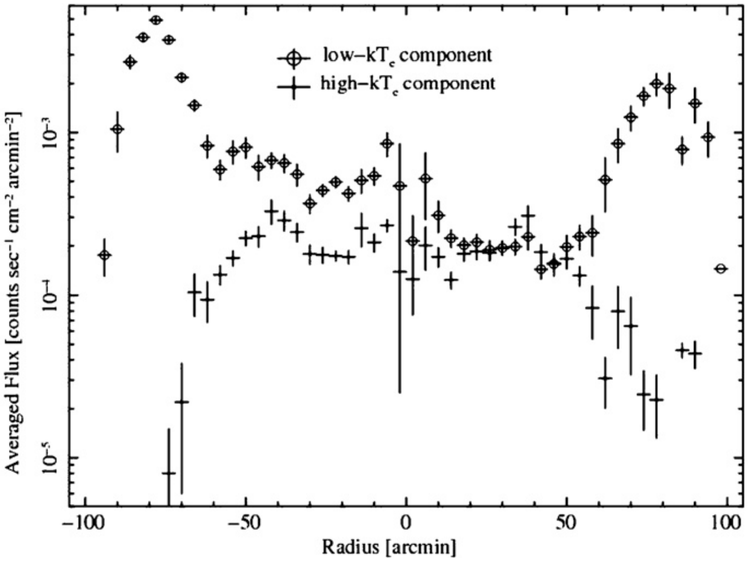

Figure 1.22 Flux profile as a function of radius from remnant center.

similar results. They find blast front temperatures from 0.085-0.123 keV at equilibrium and interior temperatures from 0.166-0.6. Some interior regions required non-equilibrium conditions to obtain adequate fits. Interior regions are still dominated by emission < 0.7 keV, but show significant emission above this, in contrast to the lack of any higher emission in the blast front regions.

This plethora of observations points toward a general understanding of the remnant. The outer limb is typically observed with much softer temperatures ($\lesssim 0.2$ keV), while the inner regions often require a hotter temperature component to adequately model the spectra. This component has been reheated by the reverse shock to temperatures $\gtrsim 0.4$ keV. The chemical abundances vary greatly based on location. The equilibrium state is still unclear, but most models show either equilibrium conditions or non-equilibrium conditions, but with ionization timescales approaching equilibrium levels.

1.4 The Extended X-ray Off-plane Spectrometer

The above studies detail the wide variety of observations performed on the Cygnus Loop primarily using Chandra, XMM-Newton and Suzaku. However these studies are all localized to particular regions. Surveys of several pointings can somewhat represent the entire loop, but accurately combining various data sets from various instruments taken at various times can be difficult to do with great precision and without introducing systematic uncertainties. Therefore an integrated spectrum of the entire Cygnus Loop would complement these region specific spectra. This integrated spectrum could help discern the overall contribution of equilibrium versus non-equilibrium components and the average temperature of the interior ejecta versus the emitting material along the blast wave. Additionally, the overall abundances of the remnant could help narrow down the progenitor mass. Due to the extended emission, the existing observations were unable to use grating spectroscopy. The large angular size of the emission would greatly reduce the resolution as the gratings would see a wide range of incident angles. Therefore these observations utilize only the CCD energy sensitivity for creating the spectra. Comparing theoretical resolution, Chandra achieves a resolution of ~ 6 at 1/4 keV, while EXOS achieves R~ 60. Without this higher resolution data our model fits, and thus our plasma diagnostics, are uncertain. Previous observations of the entire loop (Borken et al. (1972), Gronenschild (1980)) used proportional counters with bandpasses of several hundred eV. Though superior in coverage to the Chandra, XMM-Newton and Suzaku observations, they also lack the spectral resolution necessary for detailed modeling.

Achieving high resolution spectroscopy was the goal of the Cygnus X-ray Emission Spectroscopic Survey (CyXESS) rocket payload (McEntaffer et al. 2006). This payload was launched at 02:00:00 UT, November, 21, 2006 from White Sands Missile Range and recorded data from 345 seconds of flight (McEntaffer & Cash 2008). Unfortunately a high-voltage breakdown event occurred, making one detector inoperable and the other extremely noisy. The observed spectrum is shown in Figure 1.23. This was best fit with an equilibrium plasma with $kT_e = 0.14$ keV and depletion of Si.

EXOS was designed to redo the Cygnus Loop observation with precautionary measures to prevent another high-voltage breakdown event. These improvements are detailed in Section 2. Given the previous flight's count rate and best-fit model of an equilibrium MEKAL model ($\log(T) = 6.2$) a simulated spectrum of the Cygnus Loop was generated. Given perfectly optimal conditions we simulate a total of 5246 counts (both detectors combined) over 6 minutes of flight time.

This flight should prove the true capabilities of the off-plane grating design and GEM detectors in a space environment. With this proven technological flight maturity, the number of modules can be increased to obtain more sensitive observations. This will lead to completion of our final project goal of observing and understanding the solar wind charge exchange process within our solar system.

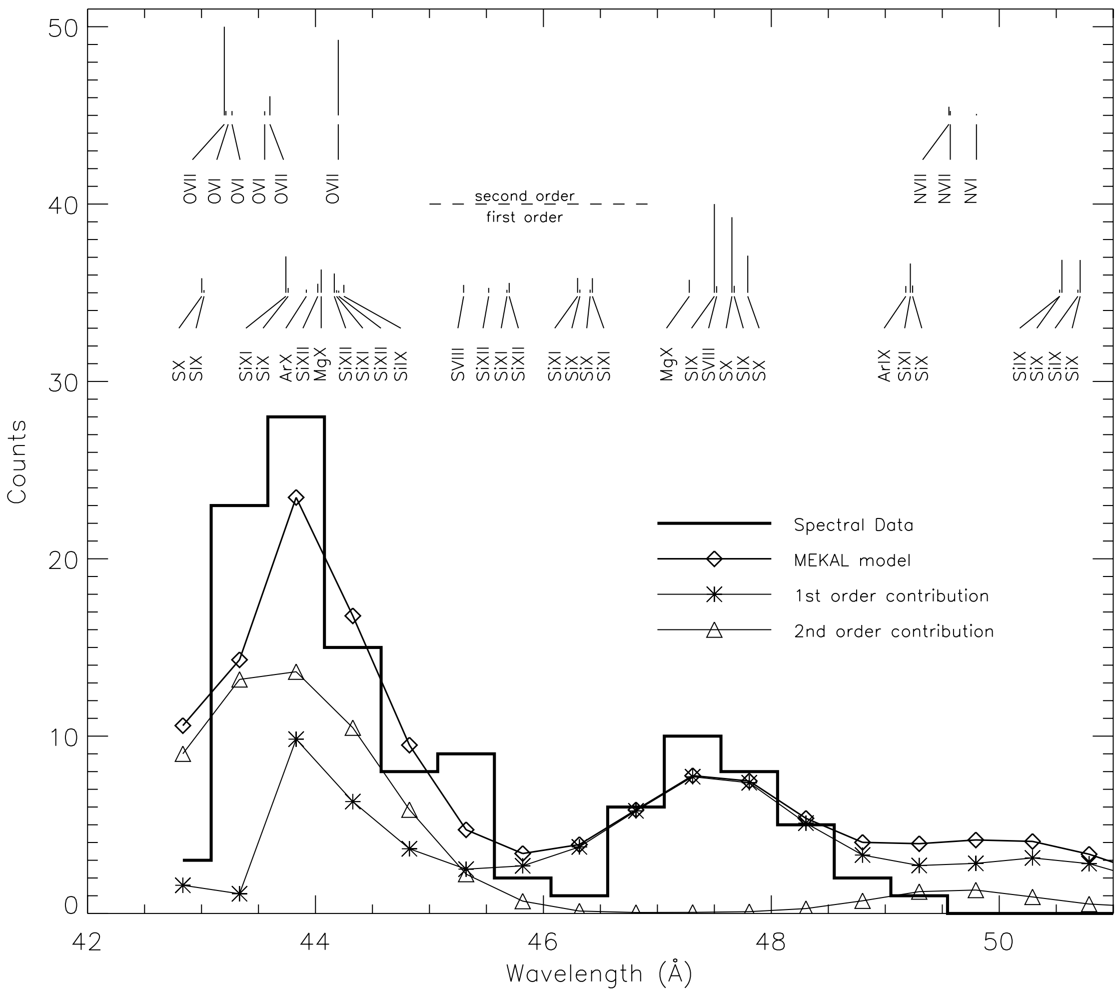

Figure 1.23 Spectrum from the CyXESS rocket-borne payload (McEntaffer & Cash (2008)). The vertical lines are labelled with the relevant element and the height of the line indicates its theoretical relative contribution to the observed emission.

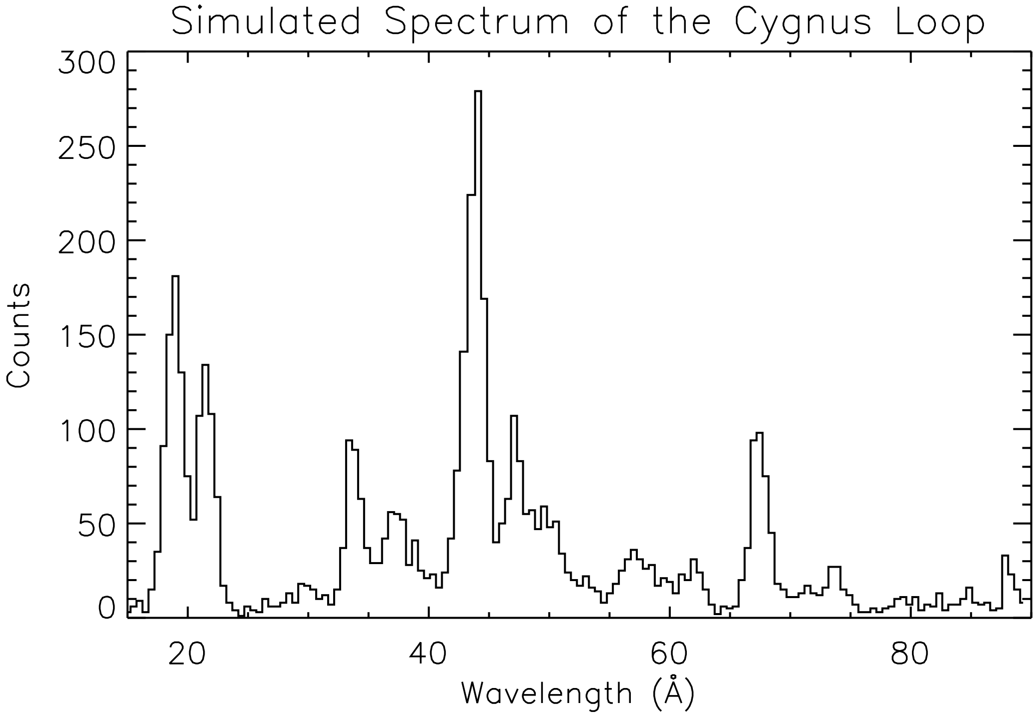

Figure 1.24 Simulated spectrum of the Cygnus Loop with the EXOS instrument by convolving the best fit model from McEntaffer & Cash (2008) with expected EXOS performance. Counts in higher orders are shown where they land on the detector.

Chapter 2

The EXOS Payload

2.1 Design

The Extended X-ray Off-plane Spectrometer (EXOS) payload is a modified version of a previous rocket design called the Cygnus X-ray Spectroscopic Survey (CyXESS). See McEntaffer et al. (2006) and McEntaffer & Cash (2008) for details of the CyXESS design. The payload was designed to contain the entire Cygnus Loop within its FOV. The 3.25° x 3.25° FOV allows approximately $5'$ of pointing error while still obtaining all the soft X-ray flux from the remnant. This FOV is created by a wire grid collimator that passively creates a converging beam with a focus of ~ 3 meters. In order to achieve the desired resolution ($R \sim 50$) we place a grating array approximately a meter from the aperture. To achieve high efficiency we choose an off-plane grating geometry, where the light comes in roughly parallel to the grating grooves. A detector can be placed on the bulkhead face (placed on the collimators plane of convergence) in a location that covers the desired bandpass. Our detectors, known as Gaseous Electron Multiplier (GEM) detectors were the largest format available to us. This maximizes our bandpass as well as effective area. The width of our detectors defines the width of our bandpass, while the height of our detectors helps define the effective area. The arrangement of optical elements in the payload can be seen in the photo-rendered engineering model shown in Figure 2.1.

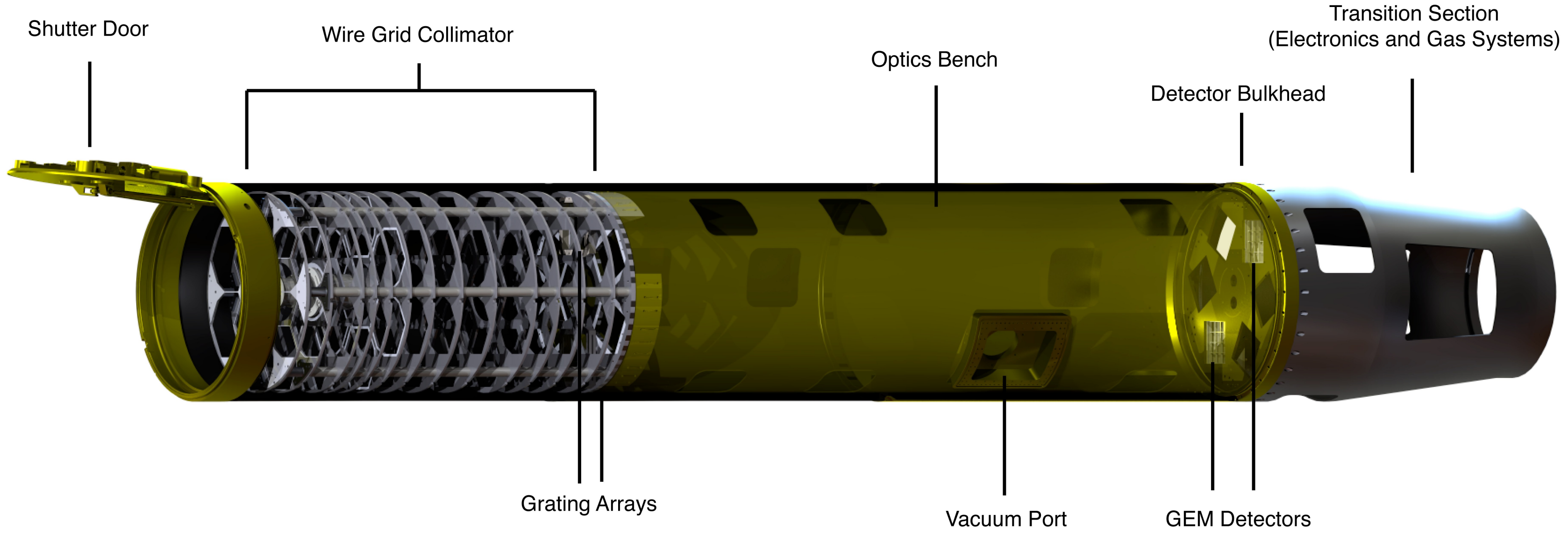

Figure 2.1 SolidWorks rendering of the EXOS payload.

The focal length and FOV define an aperture width of ~ 7 inches. In order to maximize both the aperture size and number of apertures that will fit within the rocket enclosure, an octagonal shape was chosen (Figure 2.2). This allows a maximum of 6 apertures, or modules, to fit within the 22 inch diameter rocket skin. For the CyXESS flight, only two of these modules were filled due to budgetary constraints. This setup was maintained for the first flight of EXOS.

2.2 Wire-grid Collimator

The placement of wire grids in collimators has been widely and effectively used, particularly on rocket payloads (e.g. Gunderson et al. (2000)). We use a similar structure to allow only light traveling towards our focus through the system. Each slit sees a different region on the sky and only allows light traveling towards the same location on the focal plane to pass unimpeded. Thus the term "converging collimator" or "photon discrimanator" or "slit overlayer" is perhaps more accurate. Wire grids are placed along the optical axis with successively smaller slit size between the wires. The location along the optical axis of each wire-grid plate is determined by the raytace of the system. This raytrace places each plate at an optical depth that prevents light from entering a neighboring slit on the next plate. There are 24 total plates per module. Light will travel from the front of the collimator, encountering slits in each plate that vignette any rays not travelling towards the focus. These encounters occur at roughly normal incidence, causing undesired light to be absorbed and removed from the beam. A diagram of this process is shown in Figure 2.3.

The wire grid plates are created by an electroforming nickel process by Thin Metal Parts and mounted on machined aluminum frames for support. Photographs of these wire-grids (referred to also as collimator plates) themselves are shown in Figure 2.4, while the mounting process is photographed in Figure 2.5. The initial slit width is set at 725 microns while the final plate has a slit width of 500 microns. These dimensions were chosen to produce a $1-2$ mm wide line at the focus in order to produce a resolution of ~ 50. The spacer wires have widths descending from 166μm to 114μm. The smallest size of 114μm was originally established due to limitations of acid etching, the manufacturing process used by the CyXESS collimator plates. This value was maintained so

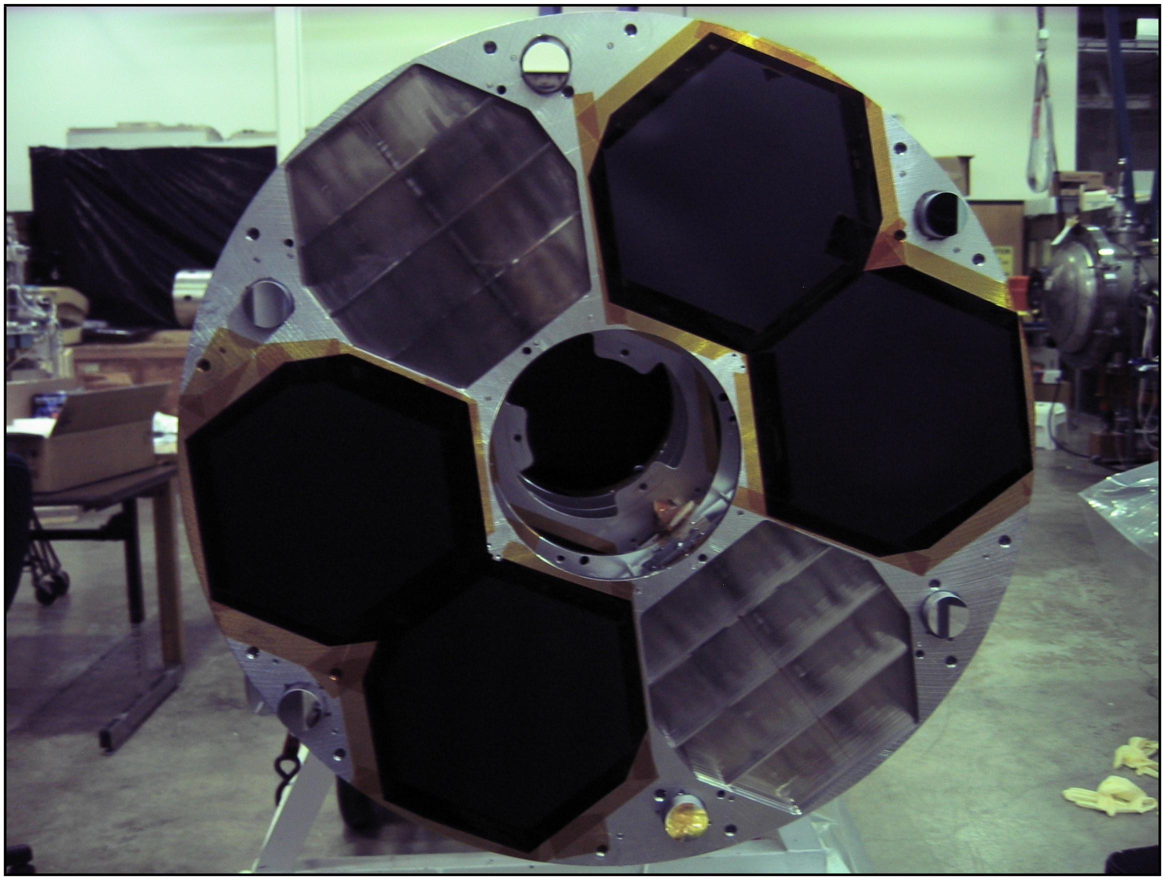

Figure 2.2 A face on view of the EXOS payload. Two of the modules are currently filled, while up to four additional modules can be added for future flights. Currently the four unused modules have been baffled with black kapton MTB series from DuPont to prevent stray light contamination. The center circular aperture is the location of the star tracker (not installed in this photo). The six small mirrors located around the perimeter are for alignment purposes.

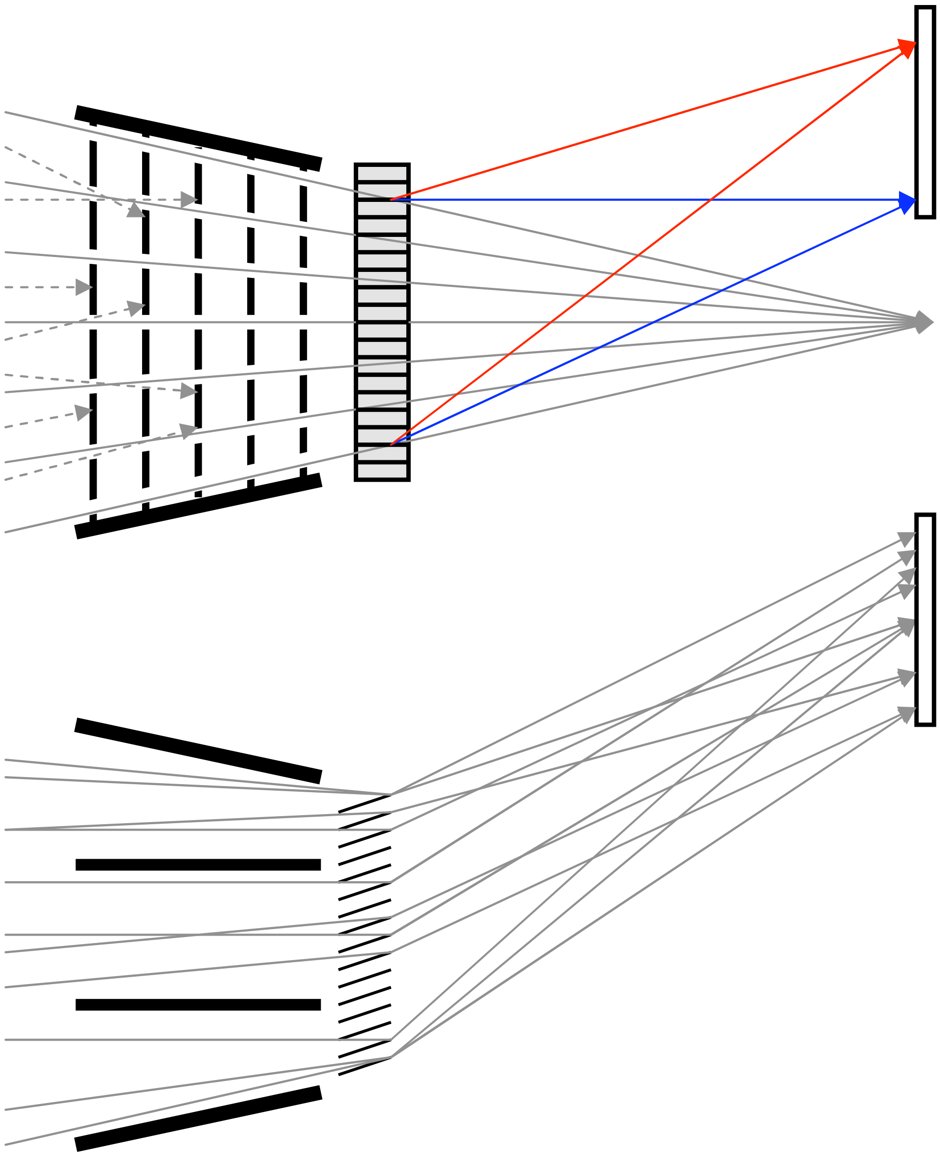

Figure 2.3 Diagram raytrace of the collimator structure, not drawn to scale. **Top** - Here the collimator plates are arranged left to right in descending slit size. The slits are oriented into the page, thus focusing light to a point along this dimension. Vignetted rays are shown with a dotted path and end upon intersecting a spacer wire. The light would travel towards the focal point on the right if not for the gratings which diffract light to a new focus, either above or below the 0 order focus depending upon diffracted order (positive or negative). **Bottom** - Along the orthogonal axis there is no collimating, which creates long thin lines along the focal plane. This limits the information we can derive about changes in spectrum as a function of location on the Cygnus Loop, but that is not one of the goals of this mission.

we could reuse certain CyXESS plates and not worry about conflicting optical designs between the two collimator designs. The aluminum frames / collimator plate assemblies are mounted on a larger aluminum super-structure with 6 openings that form the basis of our collimator super-structure.

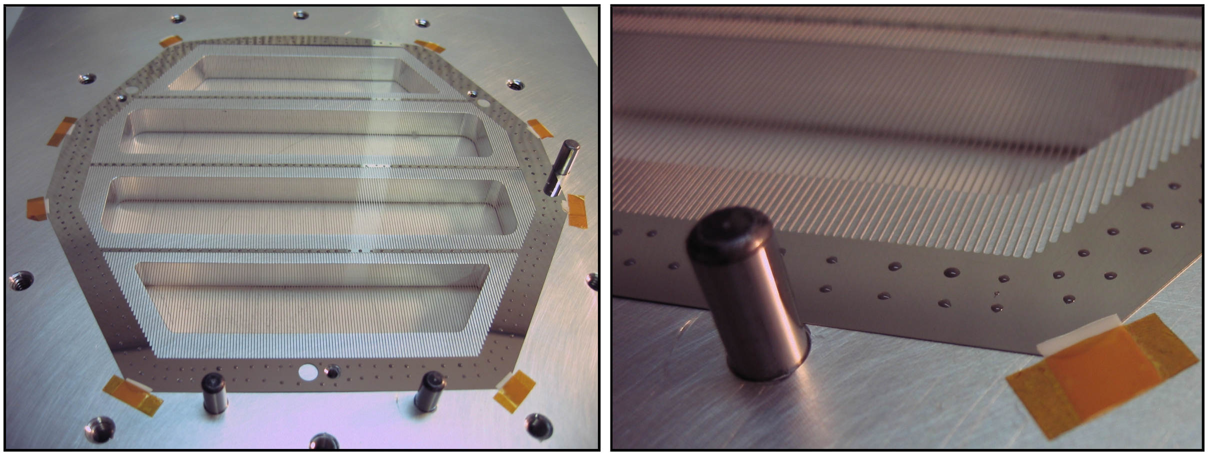

Figure 2.4 **Left** - Electroformed nickel collimator plate placed on the bonding structure. The three pins (two on bottom, one on the right) provide alignment boundaries to properly place the frame at the correct position and orientation. **Right** - Closer view of a portion of the plate. The white teflon tabs hold the plate down via kapton tape. The small gray dots are low-outgassing epoxy used to adhere the plate to its frame.

This technique would perform poorly for a point source, but it is a very practical, lightweight and cheap method for observing extended sources. This structure eliminates the need for expensive and heavy mirrors that would complicate the rocket payload in terms of mounting and aligning. These plates can be manufactured relatively cheaply and quickly, allowing rapid replacement should the need arise.

The original raytrace suggested 46 of these collimator plates be used per module to sculpt a perfect beam without scatter. However several of these plates had to be mounted impractically close together, making assembly impossible. A detailed study determine that many plates could be removed with only minor effect on the beam quality. The result was an assembly of 24 plates which limited scatter to $< 5\%$. This required only 13 structural support plates along the optical axis, as many of the collimator plates could be mounted on top each other without additional support. A photo-rendering of the entire super-structure is shown in Figure 2.6. The collimator is shown in Figure 2.7 mounted to the rest of the payload.

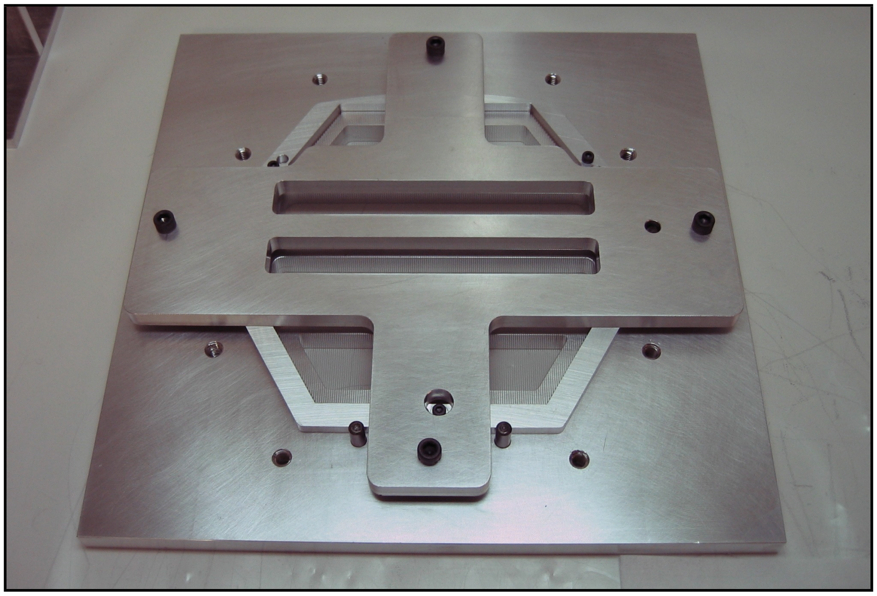

Figure 2.5 The bonding structure fully assembled. On bottom is the bonding plate, a piece of aluminum cut to precision flatness ($\pm 0.001''$). The wire-grid plate is placed on top this plate and its frame lowered onto the epoxy beads. The top cross structure is bolted down with minimal force to provide a clamp to promote a good epoxy bond.

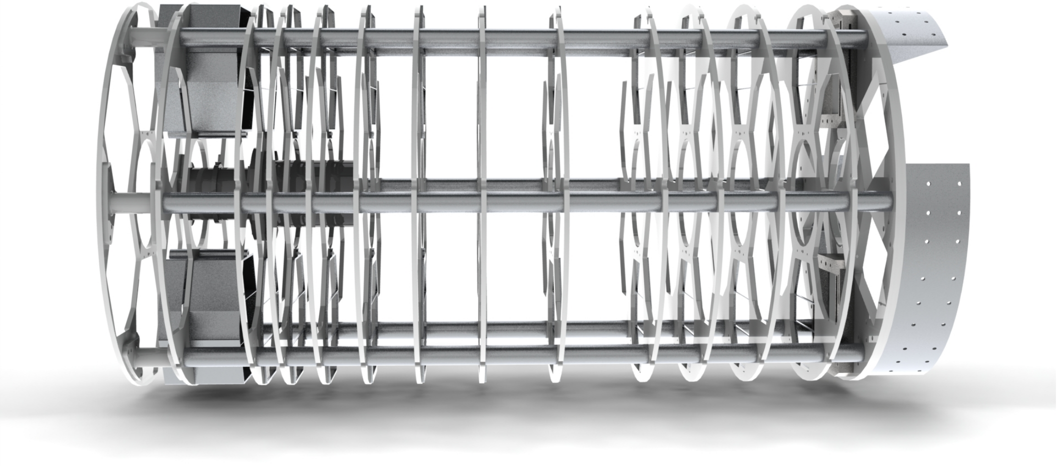

Figure 2.6 SolidWorks assembly of the collimator super-structure. Only the first (leftmost) several collimator grids/frames are shown in this assembly.

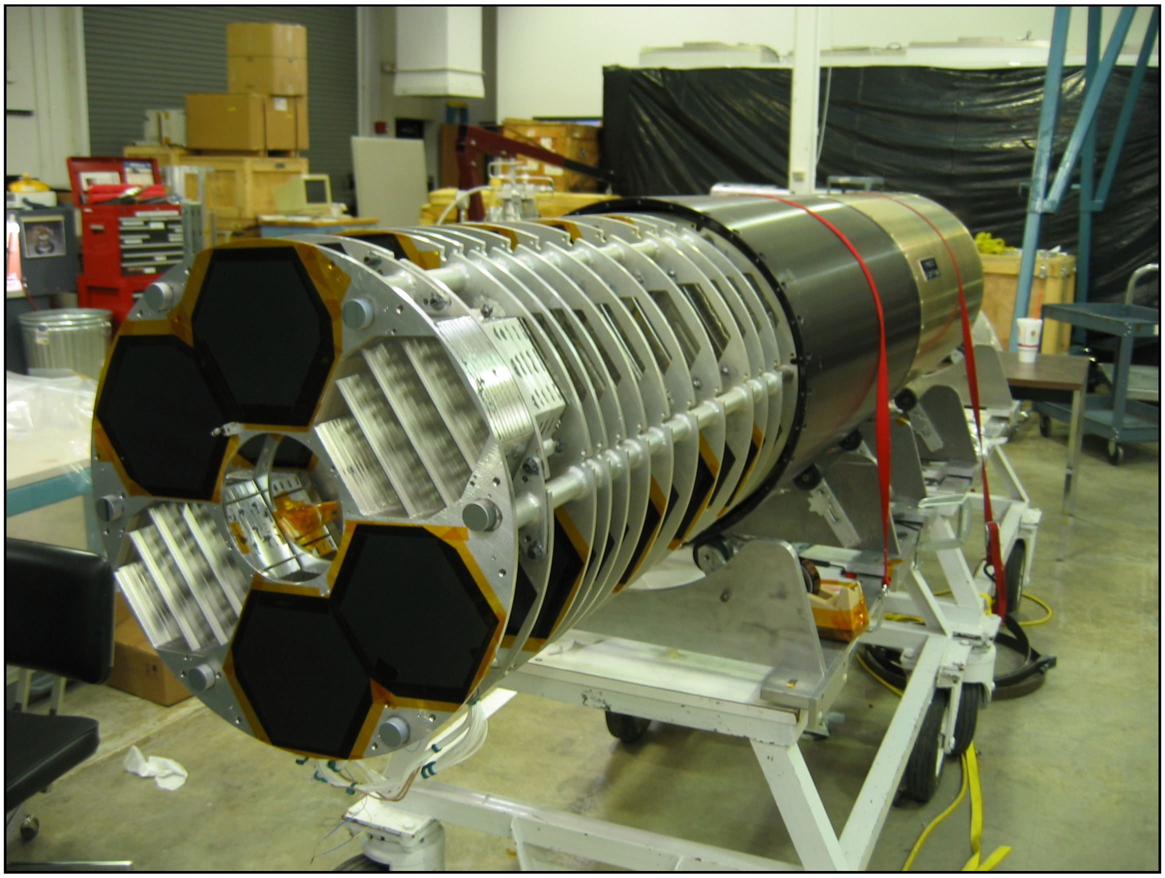

Figure 2.7 Photograph of the collimator structure after attachment to the payload. The collimator is mounted to the end of the optics bench that is encased by the black and gold exterior rocket skins.

This structure was calibrated in the same fashion as the CyXESS payload. Five lasers were mounted on manual goniometers and retro-reflected off of a point 3 meters above them (the focal length of the system). Three of these lasers were placed along the slit of the first collimator plate to define the slit axis. As plates were assembled above the first, these three lasers prevented rotation of the additional plates. The central slit was also marked to ensure against a lateral shift. The other two lasers were positioned approximately two inches to either side of the central slit. These lasers were then angled to converge on the line defined by the first three lasers at the focal plane. These two lasers were used to insure that the structure was indeed allowing converging light to travel unimpeded. A photograph of the laser calibration setup is shown in Figure 2.8

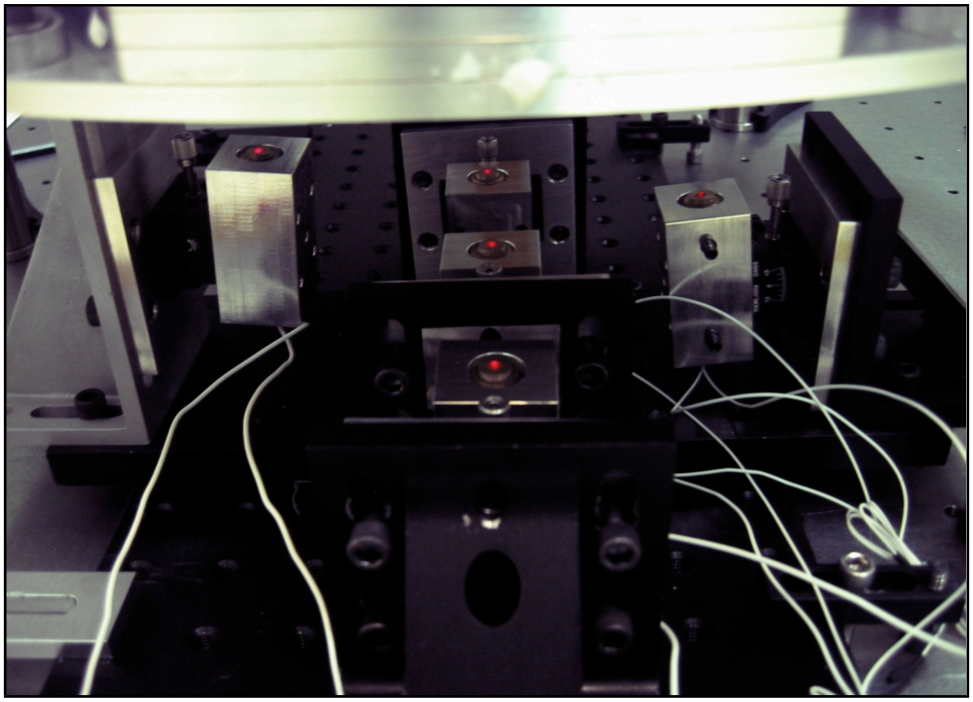

Figure 2.8 Laser calibration of the collimator. The three central lasers were aligned to point directly through the collimator's central slit. The side lasers were angled to converge at the systems focal length of three meters.

The collimator plates are mounted on machined aluminum frames using 3M Scotch Weld 2216 Epoxy mixed with 5% volume of 0.0025″ diameter glass beads. These beads were used to maintain a constant thickness bondline and ensure bond strength. The aluminum frames were designed thicker than those used in CyXESS to avoid warping problems experienced on the previous payload. From here the aluminum frames are bolted down to the larger skeleton plates and epoxied after alignment to prevent vibration defocusing. The skeleton plates were attached via welded rods. Unfortunately this welding process caused some warping of the structure. Additionally over the $\sim$ 4 years of calibrating, launching and use of the payload between launches the structure relaxed and warped an additional amount. Lastly, the skeleton plate nearest the aperture attached with bolts rather than welding. This plate (and every collimator plate / frame) was replaced for EXOS due to flight damage. The new plate was precision machined flat, but when attached to the larger warped structure began to yield to the larger warped shape. All of these effects made alignment of the collimator exceedingly difficult. Due to the warping some lateral shifting of plates was necessary due to space constraints of the frames. This clipped the edge of our FOV by $\sim 3'$. We alloted an error budget of $5'$ of pointing error due to our FOV being slightly larger than necessary, so this should not impact our count rate. However it is a worry that as time passes this new skeleton plate will further warp to match the larger structure it is bolted too. This was mitigated with stainless steel shims placed under some bolts, but constant diligence is necessary to avoid defocusing.

2.3 Off-plane Grating Arrays

The gratings were designed in the off-plane geometry where light approaches the gratings quasi-parallel to the grooves (Figure 2.9). The light is then diffracted through a conical arc. The off-plane grating equation is a slight modification of the traditional grating equation:

$$sin\alpha + sin\beta = \frac{n\lambda}{dsin\gamma} \tag{2.1}$$

with d being the space between grooves, γ the graze angle, α the azimuthal angle of incidence, β the reflected azimuthal angle and n the diffracted order. If γ is small (as is typical for X-ray applications), the radius of the diffracted cone is kept small. The projected area of the gratings is small at these graze angles, thus we require an array of these gratings to achieve high effective areas.

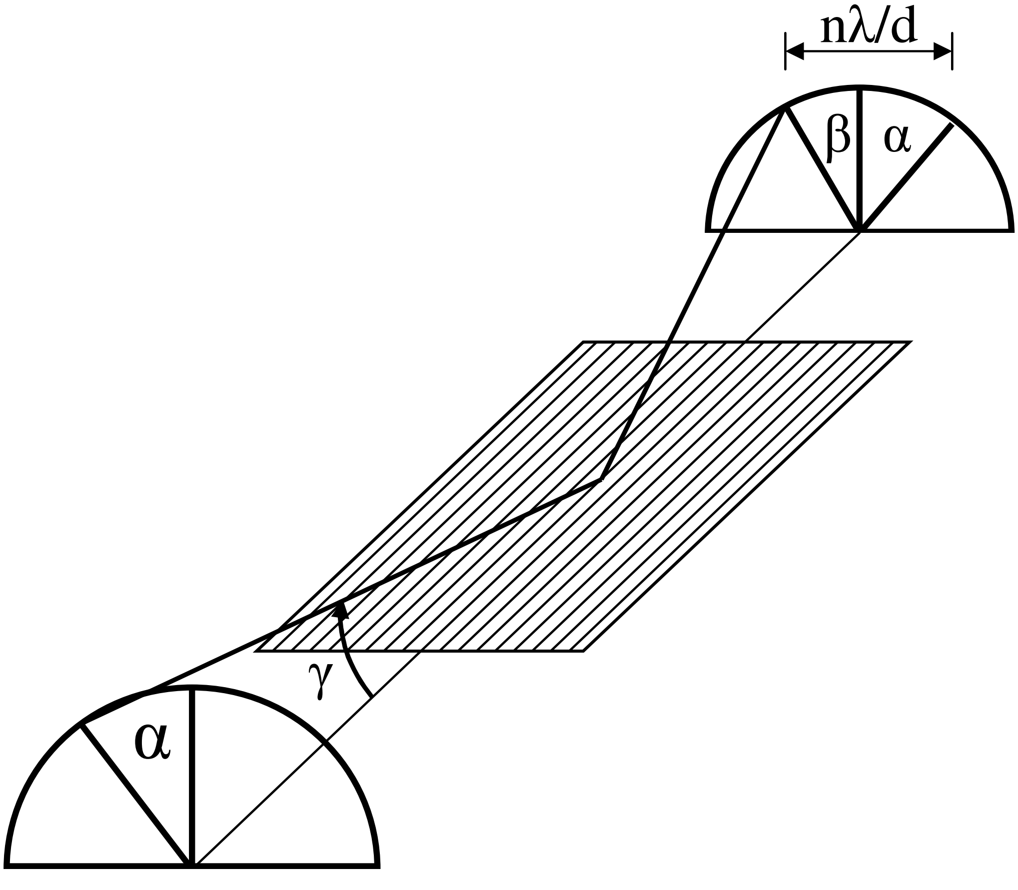

Figure 2.9 Off plane grating geometry.

This off-plane geometry was highly desirable for many reasons. With in-plane geometry one experiences a drop in efficiency due to groove shadowing that is avoided by choosing an off-plane mount which illuminates the entire groove. An in-plane setup could also diffract light into orders that intersect the next grating within the array, thus losing these photons. The off-plane mount disperses light conically at the shallow graze angle (4.4° in our case) allowing collection of all diffracted orders. Additionally, optical errors in fabrication and assembly create blurs that are almost entirely in the in-plane direction. Since the off-plane disperses perpendicular to this direction, there is a significant easing of fabrication tolerances. Finally, the packing geometries can be substantially better. See Cash (1982), Cash (1991), Osterman et al. (2004), McEntaffer et al. (2010), Werner (1977) and Neviere et al. (1978) for more details.

After a meter of travel within the collimator assembly, the beam is still substantially large. This makes it impractical to diffract the beam with a single grating at low graze angles due to the small projected area of an individual grating. Thus we utilize an array of gratings with which we can capture and properly diffract the entire beam with minimal loss. The grating array contains 67 individual gratings per module.

The gratings were replicated off of an existing HORIBA Jobin-Yvon (JY) master. The master has a density of 5670 grooves/mm with parallel grooves and a sinusoidal profile. The gratings were 110mm by 110mm but were laser cut down to 20mm deep to ensure we could obtain the desired resolution of 50 ($\lambda/\Delta\lambda$). To optimize packing geometry we chose a graze angle of 4.4° for the gratings. To minimize the vignetted light due to rays striking the edge of the grating, we chose to use thin electroformed nickel for our substrate. These substrates could be formed to a thinness of $0.005'' \pm 0.0003''$ by Thin Metal Parts and could be obtained rapidly and inexpensively. After replication by JY, the gratings were coated with nickel for high reflectivity over the bandpass (Figure 2.10). We have measured reflectivity in the $20-30\%$ range (for an individual order), and there exists several means of improving this in the future. By lowering our graze angle from 4.4° we can increase reflectivity over the higher energy portion of the bandpass in future flights. Additionally we can blaze our grating and thus direct light into our preferred order. More simply we can place detectors at the appropriate locations to capture the negative spectral orders and double our throughput without adding or modifying any optics. Fortunately these changes do not greatly complicate our physical design. These grating arrays were the same units from the CyXESS flight.

Due to the thinness of these gratings, movement due to the vibrations of launch is particularly worrisome. With this in mind, a mount was designed to prevent loss of optical alignment. This mount was machined out of a single piece of titanium with 67 EDM slots cut at 4.4°. A flexure is cut out of one end, allowing it to be displaced in order to tighten the gratings in their slots. After the gratings were epoxied into their slots the flexure was allowed to pull the gratings with a tension force of 5 lbf. This force maintained flatness on the gratings to within one part in 2000 along their length and prevented gratings from hitting each other during launch vibrations. The gratings and mount structure are shown in Figures 2.11 and 2.12.

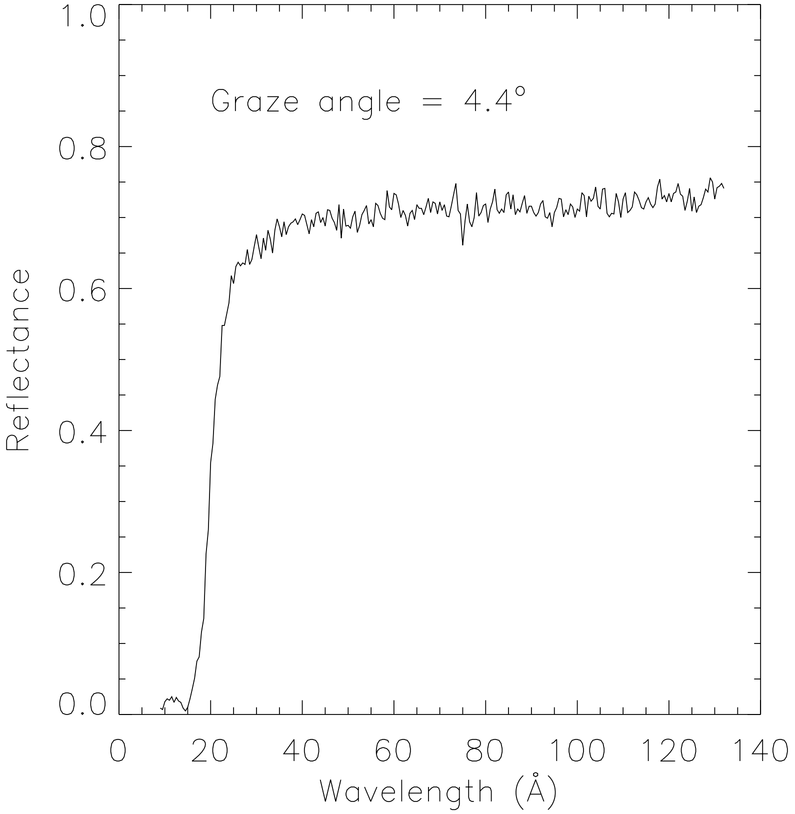

Figure 2.10 Reflectivity of nickel over the soft X-ray bandpass.

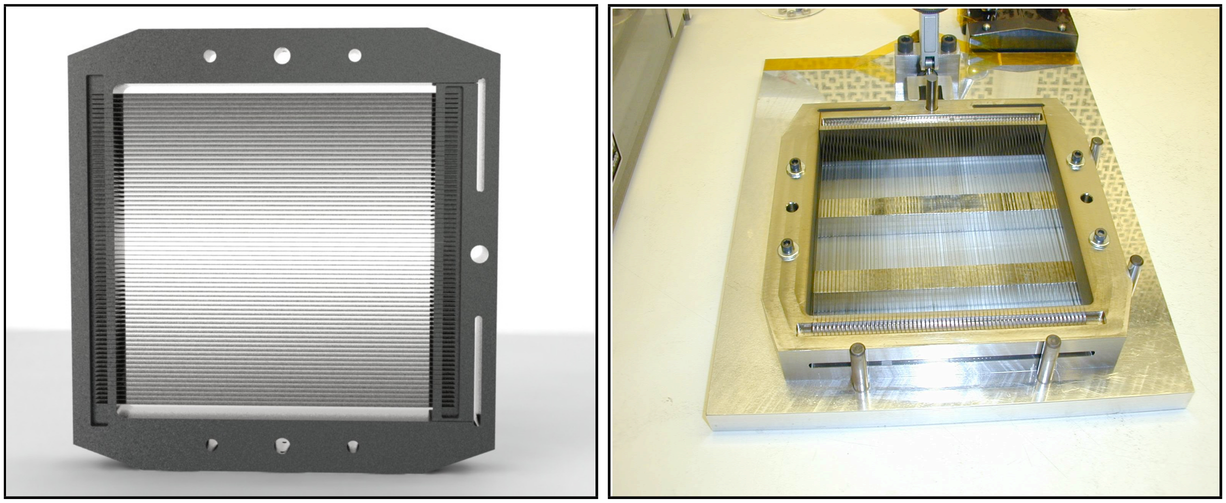

Figure 2.11 **Left** - SolidWorks rendering of the grating array. **Right** - Grating mount after grating installation but before payload assembly.

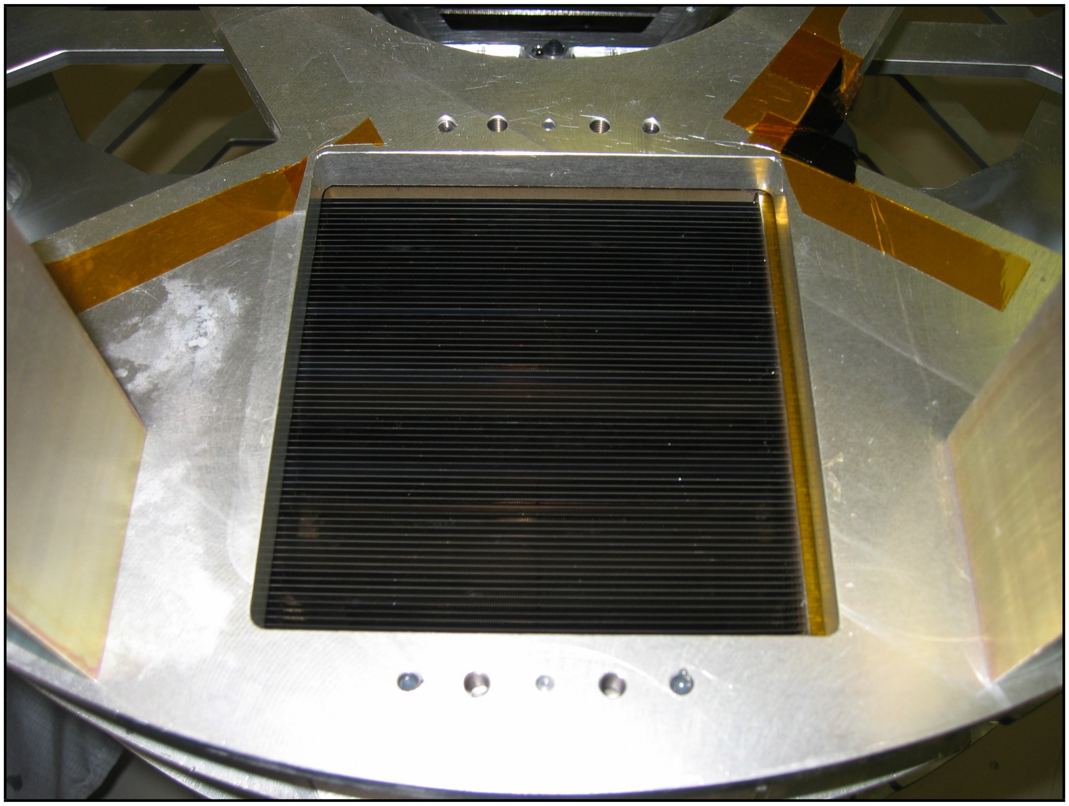

Figure 2.12 Photograph of the grating array as mounted on the end of the collimator structure. The mount is attached via bolts, pins and epoxy on the underside of this final skeleton plate.

2.4 Gaseous Electron Multiplier Detectors

After approximately 2 meters of throw the spectrum is focused as long thin vertical lines along the bulkhead. The positive and negative orders are thrown upon either side of center, and a detector can be located at a horizontal position consistent with the desired bandpass. The horizontal axis is defined here as being orthogonal to the collimator slits. The larger the detector in width along this axis, the larger the recorded bandpass. The larger the detector is in height, the larger the effective area is for each spectral bin. The largest detectors available (without resorting to film or expensive CCD arrays, etc.) were Gaseous Electron Multiplier (GEM) detectors. These detectors are 100 x 100 mm, though GEMs up to 200 x 200 mm are currently possible.

A schematic of the GEM detector is shown in Figure 2.13 and a photograph without it's external housing is shown in Figure 2.14. These detectors have a series of four porous GEM plates held at high voltages encased in a Ar/CO_2 gas (75/25% mixture). The argon provides a reservoir of electrons as the incident soft X-rays ionize the gas. The CO_2 provides a means of replenishing the lost electrons in the argon via charge exchange. Once ionized, the electron is compelled by the electric field downwards in the detector as the aperture window is held at the highest negative voltage. The electrons will be accelerated through each of these 4 GEM plates. The electron will feel the strongest force in the GEM pores, as each side of the GEM is held at successively lower voltages (by $\sim$ 400 volts), and has a thickness of only 116 microns. The collisions within pores will cause a cascade of electrons. After four GEMs worth of gain, the cascade of electrons will reach the anode held at a grounded voltage. The external housing is a type of plastic known as PEEK that provides the necessary strength and is nonconductive.

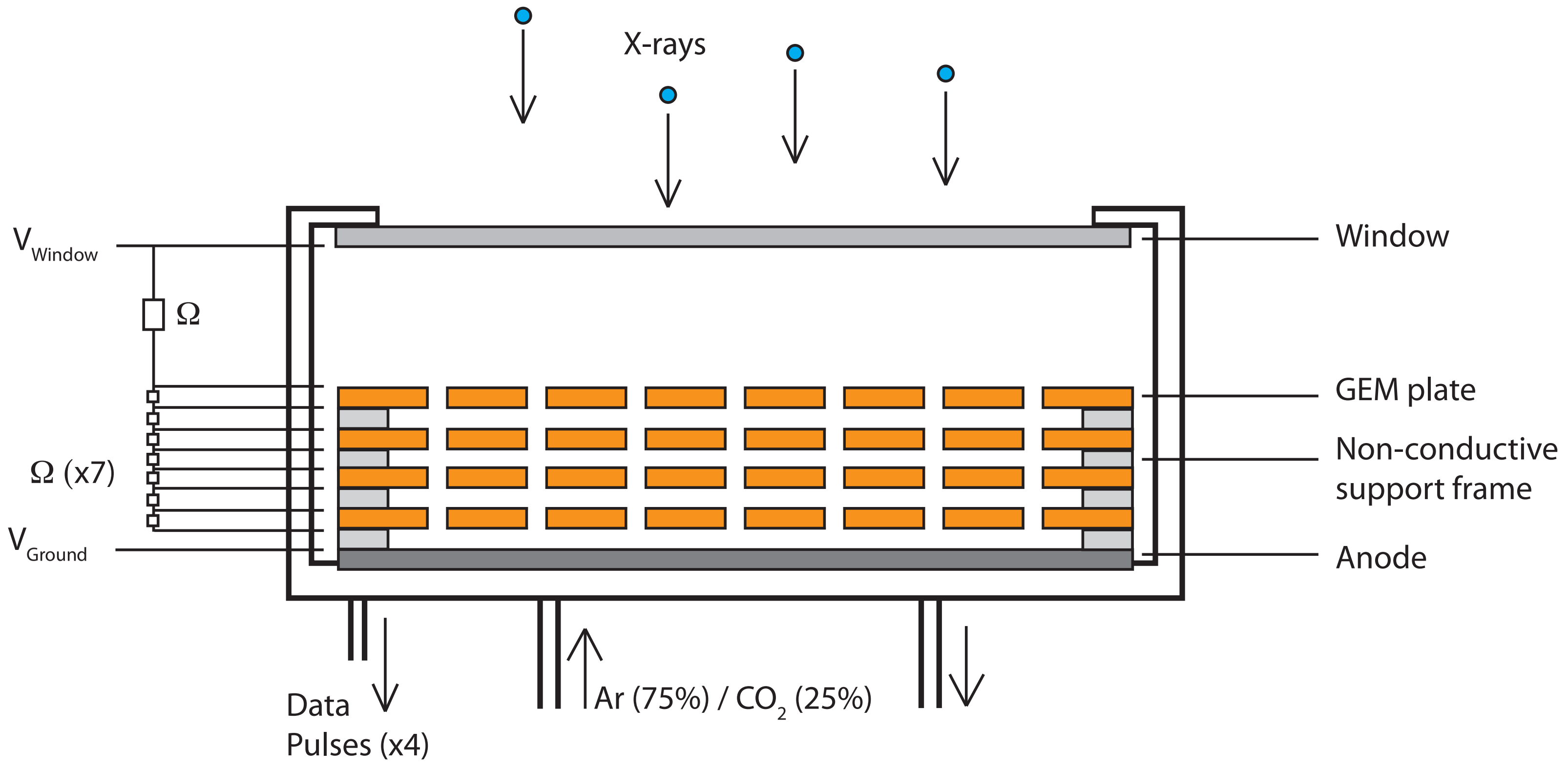

Figure 2.13 Schematic of a GEM detector. Light enters from above through a thin polyimide and carbon window. The X-rays have approximately 5 mm in the drift region before the first GEM foil to ionize the argon gas. The window is held at a high negative voltage, typically 4000 Volts. The voltage drop to the top of the first gem plate is 500-700 volts. Each GEM plate has a potential drop of ~ 400 Volts from top to bottom (there is a 100 micron thick insulator between conductive copper layers). A potential drop of ~ 200 Volts is established in the 1mm gap between plates. The anode at the bottom is held at ground voltage.

The window on the detector needs to accomplish two tasks very different in character. Firstly, it needs to be strong enough to support the pressure differential between the gas needs of the detector and the payload vacuum. This pressure is set at 14.5 PSIA. Given the large area of the detector this would require a window of substantial thickness to provide the necessary strength. However the second requirement of the window is to be thin enough to allow the transmission of soft X-rays. These requirements provide conflict between incredibly important motivations. Too thin a window will likely render it useless due to tears in flight. Too thick a window will likely also render our count rate too low to be scientifically interesting. The CyXESS GEM windows were made by Luxel and were manufactured from polyimide 3600 - 3900 Å thick. To add support this material was mounted on a stainless steel mesh with a thickness of $0.005''$ and 20 lines / inch density. On top of this was a larger course grid of aluminum that creates a 4 x 4 pattern on the detector face. A 300 Å layer of carbon on top of the polyimide is added for conductivity. The geometric transmission of the mesh and frame is 57.8%. The corners of this sandwich are epoxied with a conductive epoxy so that the entire assembly is held at high voltage. This assembly was assessed a strength capable of withstanding 45 PSI differential based upon extrapolations of larger sizes. Unfortunately during the CyXESS flight one of the windows developed a tear, thus rendering that detector useless. To protect against this for the next flight we increased the thickness of the window to 5000 Å . This thickness was chosen based on previously taken Luxel data that showed an increase in burst pressure of nearly 100% between 3600-5000 Å (Figure 2.15). This increase in thickness results in a decrease in transmission, but estimated to be a minor effect (Figure 2.16). A photograph of one of the new windows is shown in Figure 2.17.

The GEM plates themselves were originally a polyimide substrate with chemically etched pores and a layer of copper on both sides for conductivity. The resistor chain (seen potted in a non-conductive epoxy on the underside of the detector in Figure 2.14), controls the voltage drop across each side of a GEM plate and in the gaps between GEM/window, GEM/GEM and GEM/anode. Unfortunately these GEM plates were prone to erratic behavior. Hotspots would develop if the high voltage was ramped up too quickly, causing outbursts of noise that would threaten to hide a weaker

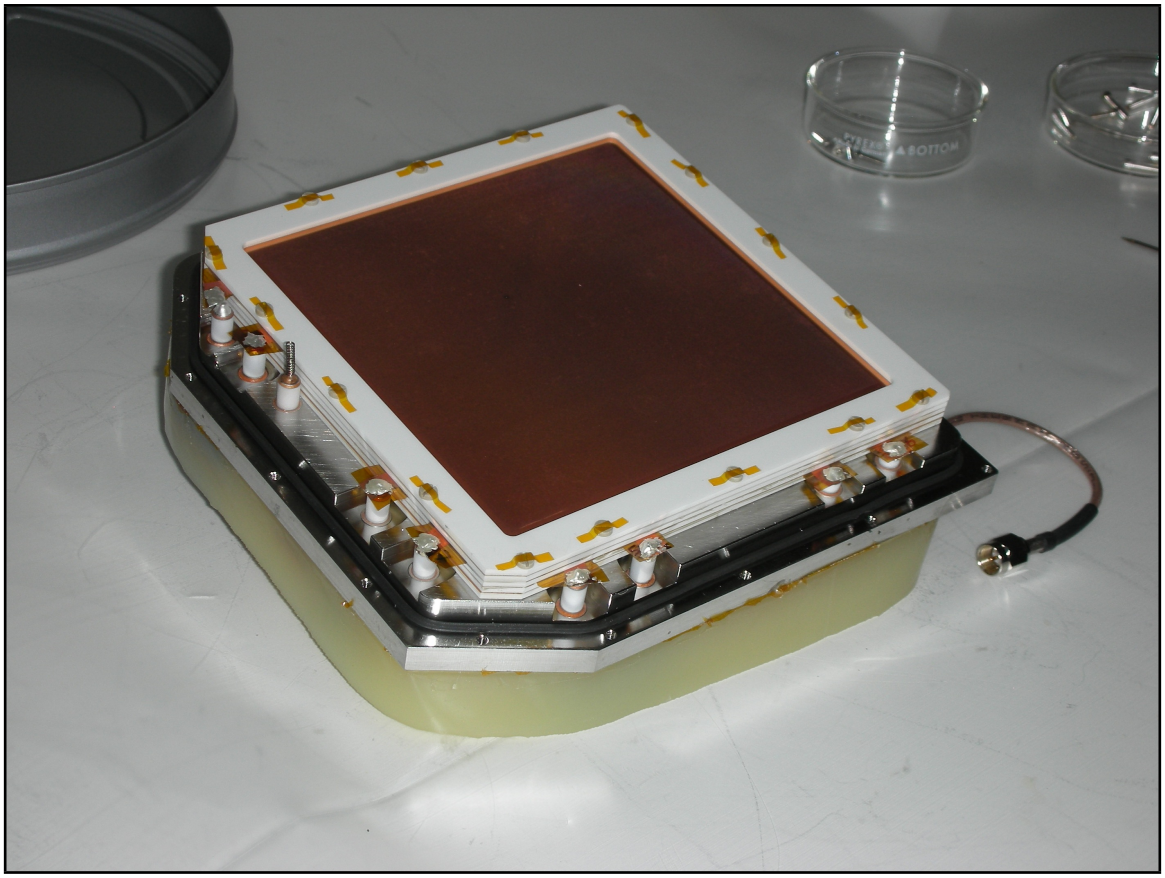

Figure 2.14 A GEM detector without its external housing. The GEM plates are held in place by 16 peek screws. There are 4 pairs of posts around the two frontmost sides of the GEM. These are the high voltage feedthrough that provide the GEM with the appropriate voltage.

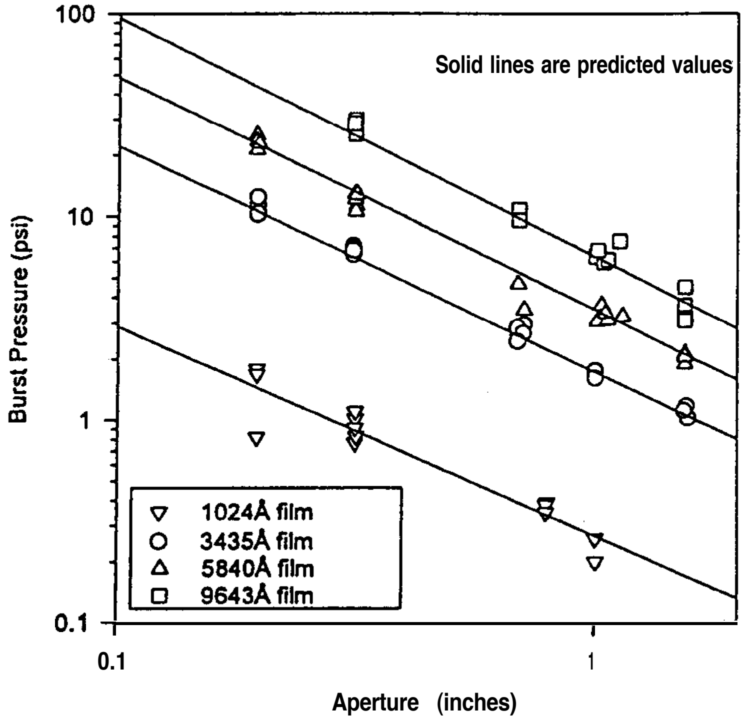

Figure 2.15 Burst pressure of polyimide. Data points indicate experimental results done by Luxel, while solid lines are the predicted values. The CyXESS windows were 3600-3900 Å thick, while the new EXOS windows are 5000 Å thick. The aperture size is 0.05 inches for both payloads.

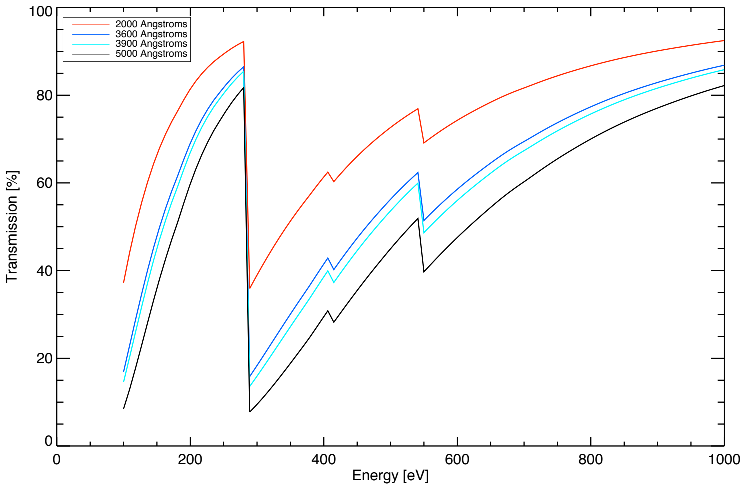

Figure 2.16 Transmission as a function of incident photon energy for various thicknesses of polyimide.

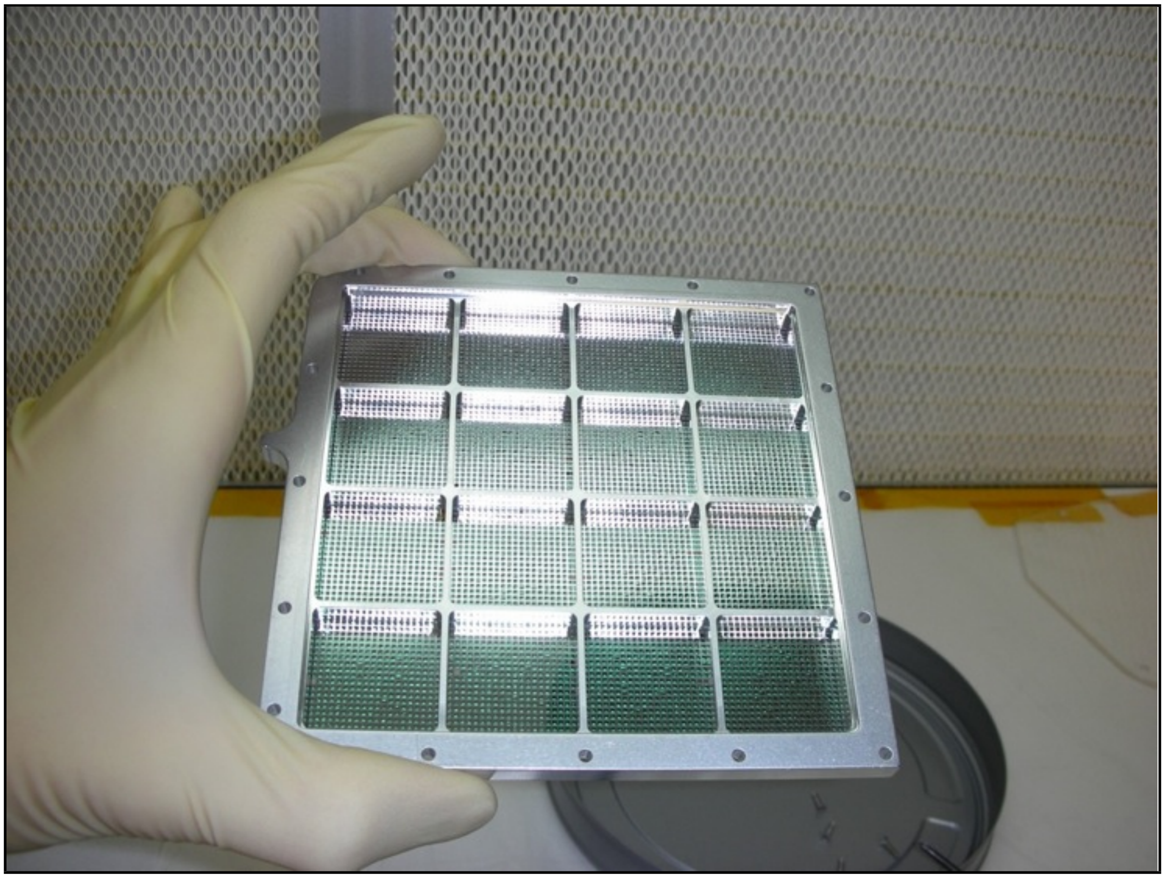

Figure 2.17 One of the GEM flight windows.

scientific signal. These hotspots could be reduced out of the data based upon positional information as well as stronger than usual pulse height distributions, but their unpredictability made calibrations difficult and flight data reduction uncertain. Additionally, chemically etched GEMs suffer from a slow rise in gain after high voltage is turned on, necessitating hours of warmup. Chemically etching the pores creates a double conical shaped hole. This geometry, where more of the insulator is exposed within the pores, leads to charge deposition on the insulator. This causes a modified electric field and to a charging up phase where the gain is sub-optimal. Simon et al. (2007) report a three hour warmup time, where the gain increases by $\sim 30-80\%$. Tamagawa et al. (2009) shows a smaller, but slower gain rise of 10% over 16 hours for chemical etched GEMs. This is highly problematic for a rocket experiment as typically all electronics must be off for the majority of the ~ 2 hours prior to launch, and the ~ 5 minutes of flight time is insufficient for adequate warmup.

These factors led to a new manufacturer of GEM plates. SciEnergy makes GEM plates with a slightly different method. They use a liquid crystal polymer (LCP) substrate and laser etch their pores. The laser etching process creates more cylindrical holes and thus does not require a warmup period (Tamagawa et al. (2008) and Tamagawa et al. (2009)). These plates were also found to be exceptionally quiet with a dark count rate of 1-2 cts/s or ~ 0.01 cts/bin/s. This gives an anticipated background rate of $\sim 3-4$ cts/bin/flight. Given that we expect ~ 100 counts in strong spectral lines, achieving a 3σ detection should not be limited by detector background rates. Geometrically these GEMS have 70 micron diameter holes with a 140 micron pitch. The LCP is 100 microns thick, while the layers of copper (one for each side) are 8 microns thick. A magnified view of a GEM plate is shown in Figure 2.18.

The thinness of the GEM plates presents the same problem as our thin grating substrates. This was solved by heating the GEM plates and bonding them to ceramic frames (white rim seen in Figure 2.14). As the ceramic has a very low coefficient of thermal expansion, the GEM frame maintains its size while the GEM plate expands. Once bonded to the frame, the assembly is allowed to cool, resulting in a taught GEM plate.

After the electrons are accelerated through the series of four GEM plates, the charge cloud

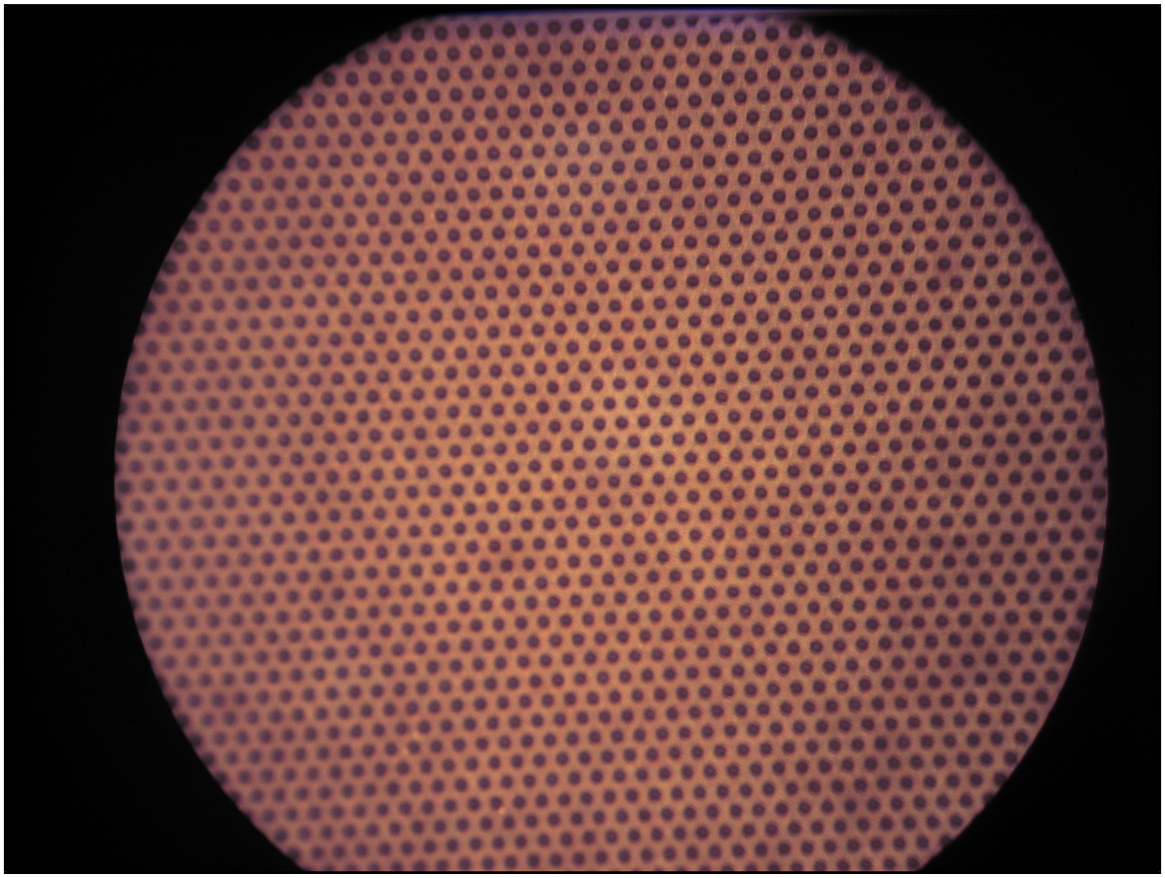

Figure 2.18 A 7x magnified view of a GEM plate showing the pore arrangement.

will strike the detector anode (Figure 2.19). The anode consists of two layers, each a serpentine weave across the face of the anode. The two layers are electronically isolated from each other. As the electron cloud hits, the charge is sent to the corners of the GEM and amplified by separate electronics. From here the arrival times of the pulses are turned in to positional information in X and Y by the Time to Digital Converter (TDC). This information is passed as 12-bit words for X and Y position. The theoretical spatial resolution of the system is $\sim 100 - 200$ microns. Additionally an 8-bit word for pulse height data is passed which is proportional to the total amount of collected charge (and hence the energy of the incident photon). Both detectors are handled by the same TDC unit and passed on to the rocket telemetry. However since the two modules have slightly different wavelength calibrations, it is critical to know from which detector a count originated from. This is accomplished by an electronic adder which takes the signal from both detectors and passes it on to the TDC. The adder sets the least significant beat of the 8-bit word of pulse height depending upon the detector of origin, allowing for easy identification of the responsible module. Unfortunately, this bit was scrambled during the CyXESS flight due to a switching 28 DC to 5 DC volt converter putting noise on ground in the digital telemetry boards. This converter was replaced with a linear regulator, removing the noise on ground and allowing correct identification of each detector.

The detector is supplied with an Ar/CO_2 gas mixture as described above. Unfortunately, the thinness of the windows makes them highly susceptible to small leaks into the payload interior. This intrinsic leak rate necessitates an onboard gas system to ensure the detectors remain at optimal pressure. Even a small (1%) change in pressure significantly impacts the detector gain. A schematic of the gas system is shown in Figure 2.20. The system begins with an umbilical fill port for filling the gas system with the rocket skins on. This port has a check valve to prevent the port from discharging the gas upon the umbilical disconnecting during launch. From here the gas fills a reservoir with a manual purge valve to empty the system when desired. Next in the system is a simple manual valve that allows gas to flow to the detectors. From here the system has a manual regulator (made by Castor Engineering) bookended by a valve and pressure switch, made by Castor Engineering and Precision Sensors respectively. If the regulator were to fail, the pressure

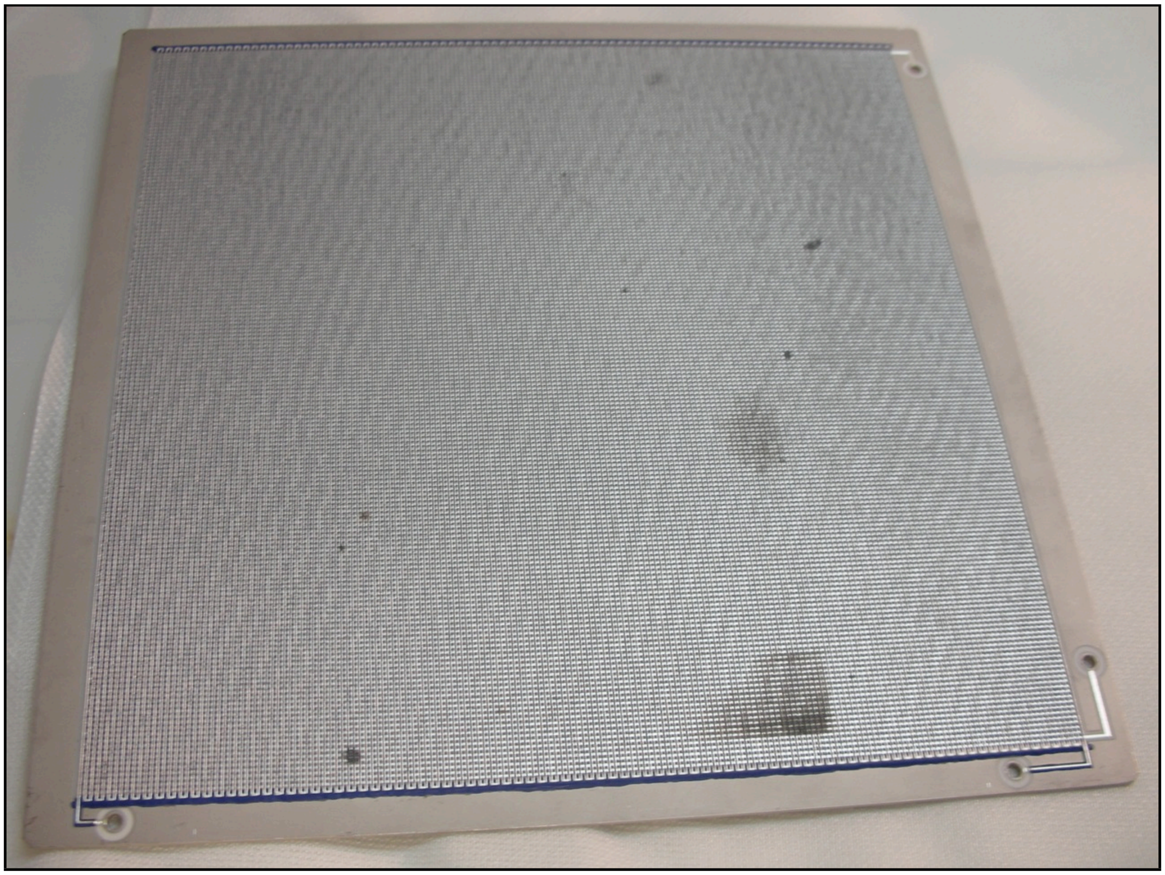

Figure 2.19 The detector anode. The two readouts for each axis are located along the bottom and right sides of the anode in the corners. The dark spots on the anode are damage from discharge events on the GEM plates. These spots don't seem to effect the performance, but to be safe the anode was swapped for a new one.

switch would recognize the spike in pressure and close the latching solenoid valve to protect the detectors from seeing too much pressure. The valve is latching in order to protect the detectors even after the system is powered off for landing. From here the gas system forks towards each detector. A proportional valve (made by Proportion-Air) in the system fine tunes the gas pressure. The manual regulator is very coarse, and alone would produce wild swings (> 10%) of pressure and gain. The proportional valves have an optimal accuracy of 0.1%, resulting in a consistent pressure. Additionally these valves have a pressure transducer which provides a voltage output that is proportional to the current pressure in the valve. This allows monitoring of the detector pressure during flight. From here the gas enters the detector through a VCR feedthrough with a nickel gasket. The detectors have an outlet feedthrough that can be connected to a removable pressure gauge if needed. A photograph of the gas system (mounted within the electronics system) is shown in Figure 2.21. Much of the gas system (valves, manifolds, tubing, etc.) was made by Swagelok and welded by Denver Valve and Fitting.

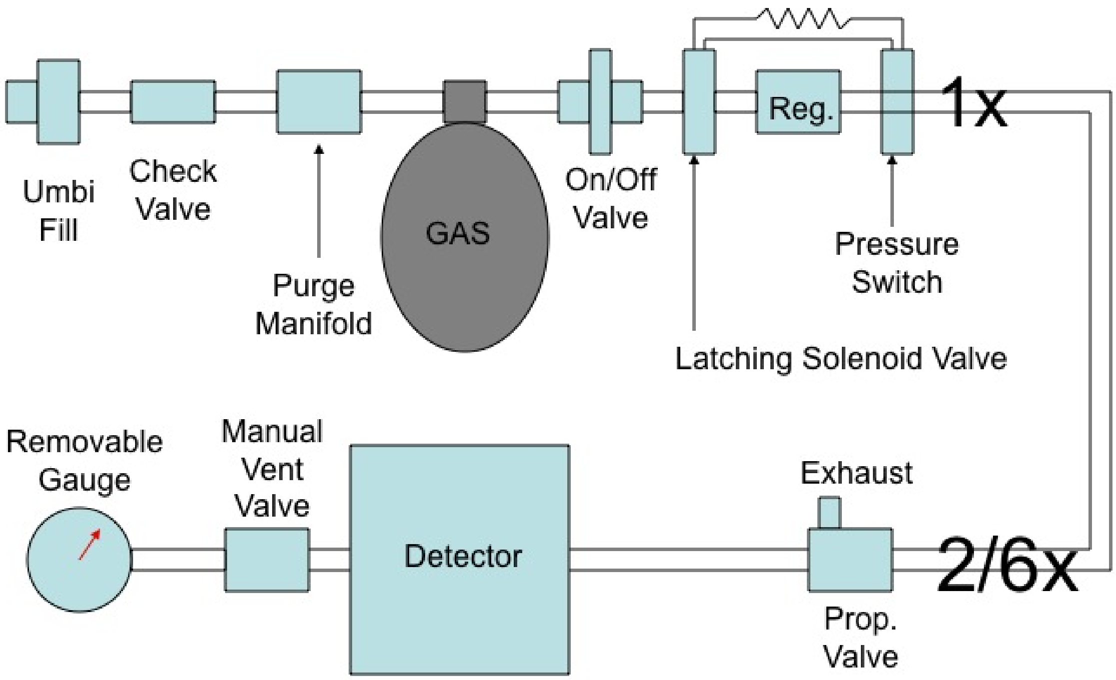

Figure 2.20 Diagram of the detector gas system. The top row applies to both detectors, while the bottom row is forked so that each detector is independent at this stage.

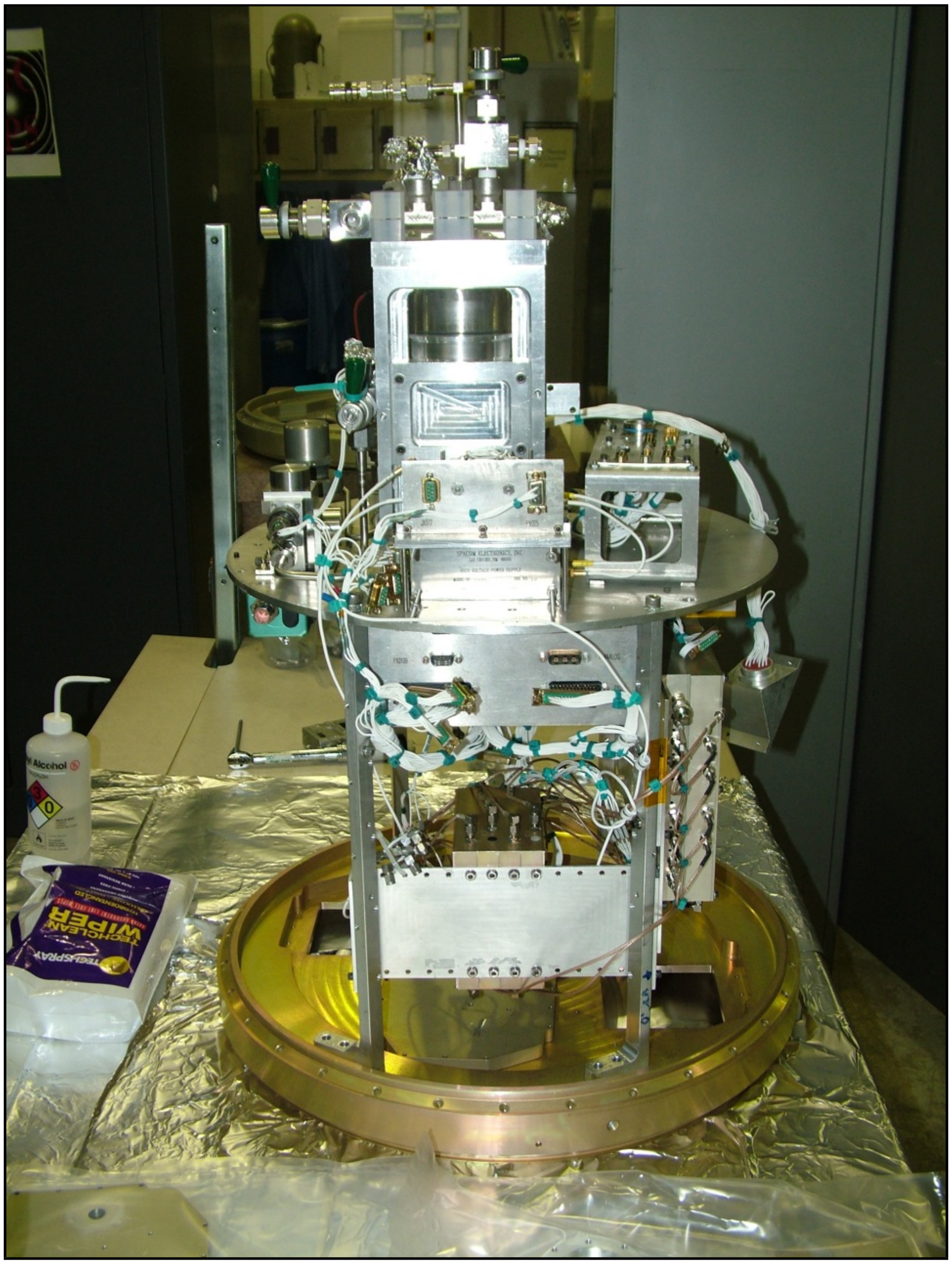

Figure 2.21 Gas and electronic systems shown mounted to the payload bulkhead.

2.5 Performance

The raytrace for the entire system is shown in Figure 2.22. A nonisotropic version is shown in Figure 2.23. The raytrace was performed with the Interactive Ray Trace (IRT) software developed by Parsec Technology Inc. In this raytrace the target object is established as a ring with an outer diameter of 3.25° and an inner diameter of 3° to approximate the Cygnus Loop shape. This causes an increase in density of rays coming from the sides of the collimator, particularly noticeable in the green photons in Figure 2.23.

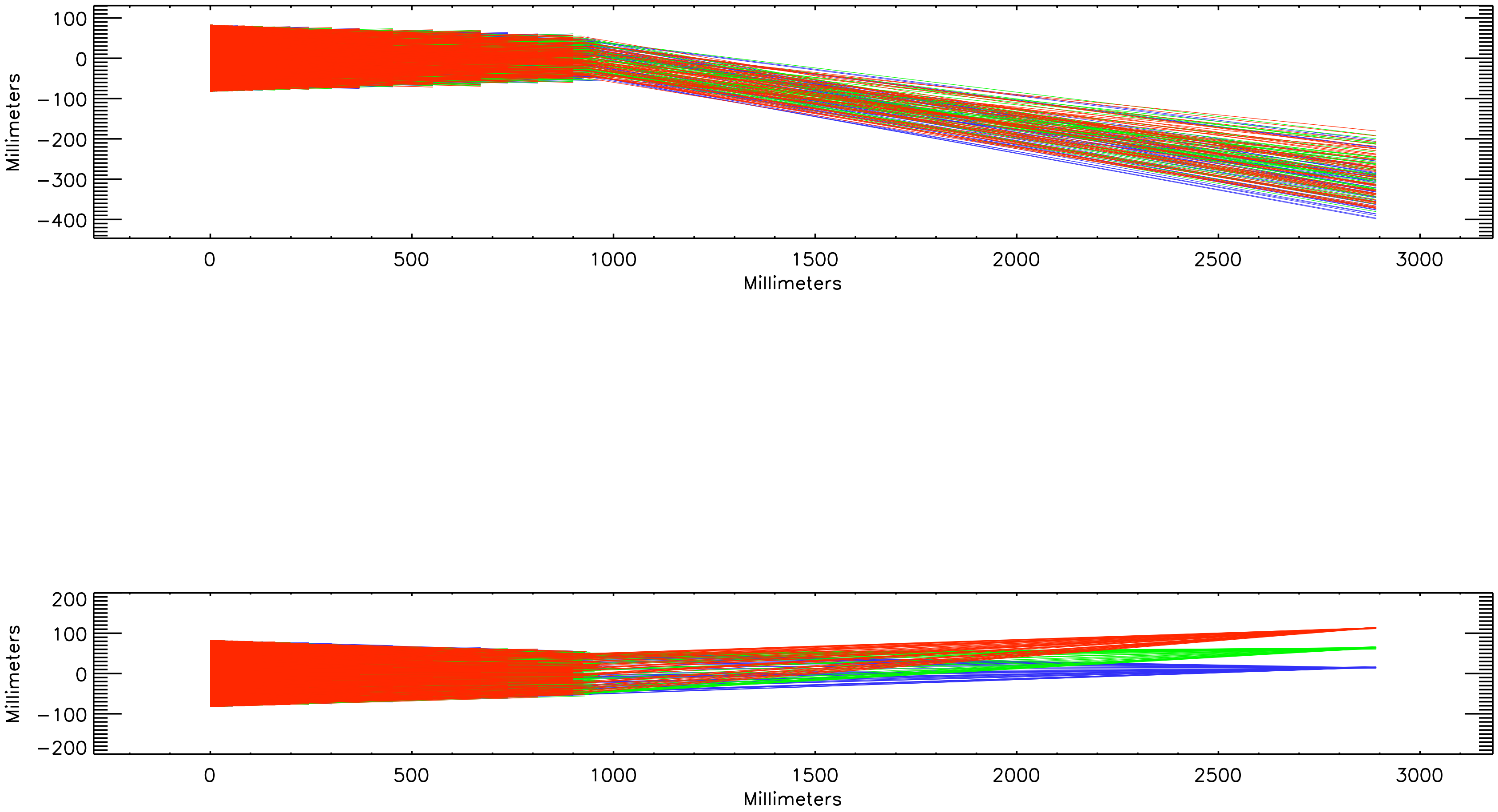

Figure 2.22 Isotropic views of the EXOS raytrace. **Top** - A side view of the payload showing that the photons are not focused along this axis. **Bottom** - A top view showing the focusing and dispersion into 3 spectral lines.

Below we discuss how the actual instrument performs compared to this raytrace in terms of focus, efficiency, stability and bandpass.

2.5.1 Collimator

The resulting histogram of photons at the focal plane for the collimator structure is raytraced in Figure 2.24 (shown as if the rays were allowed to travel unimpeded by gratings to the focal plane at ~ 3 meters). The full width half max (FWHM) of the lines is 1.7 mm. The system also has minimal scatter ($\sim 1\%$). Unfortunately several collimator plates were damaged on the previous flight of CyXESS. These plates were replaced and realigned (Section 2.2). As the new plates were made from electroformed nickel (instead of acid etched stainless steel), these plates were more resistant to warping. On the old plates any unevenness in the aluminum frames caused severe warping over the plate, whereas the new nickel plates distribute stress much more evenly and tolerated external forces much more elegantly. The new plates are somewhat weaker due to the new material, however stress tests showed that an individual wire could still hold ~ 1 pound of weight before permanent damage. Unfortunately, the grating arrays were still attached to the end of the collimator structure, preventing testing of collimator alignment by itself. The grating arrays could have been removed, but breaking the epoxy bond between the grating mount and collimator structure involved substantial risk. Given the massive expense in time and money for these arrays, it was deemed preferable to test the system as a whole rather than risk further disassembly.

2.5.2 Gratings

The gratings are tilted at an angle of 4.4° compared to the optical axis. Because the collimator does not influence light along the slit direction, the gratings actually see a range of photon graze angles (γ in Equation 2.1 and Figure 2.9) from $\sim 2^\circ - 6^\circ$. Depending upon the location and angle of incidence, the photon will reach the bulkhead at given location. As shown in Figure 2.23, the lines are taller than the detector, and are thus not all collected. By creating a histogram of photon graze angles we can determine at what angle most photons are originating from. Figure 2.25 shows

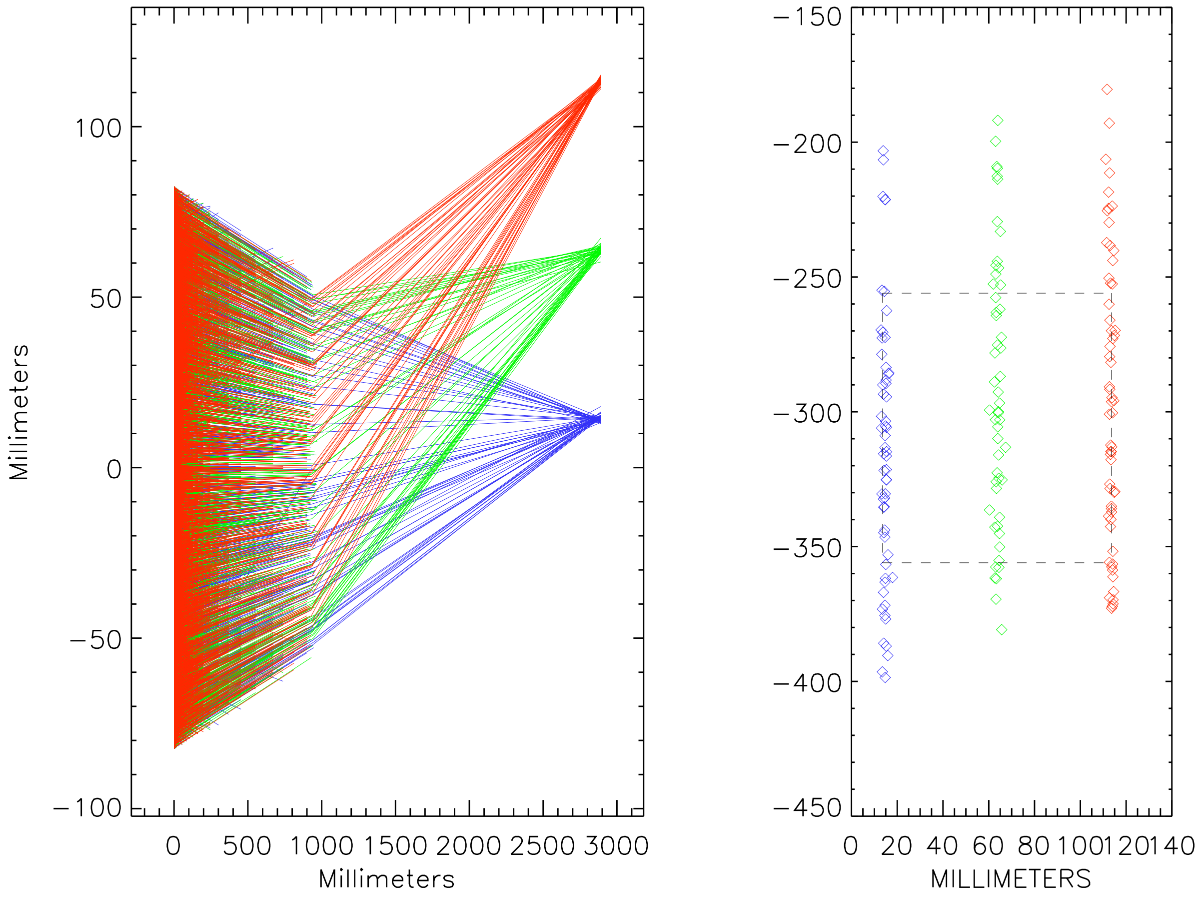

Figure 2.23 Another view of the raytrace. **Left** - This perspective is not isotropic, but it better shows the converging spectral lines. **Right** - Spot diagram on the detector face. Note that the spectral lines are ∼ 200 mm tall, whereas the detector is only 100 mm in height. The detector was placed at the vertical location that maximized the amount of light gathered from the lines and is shown by a black dashed box.

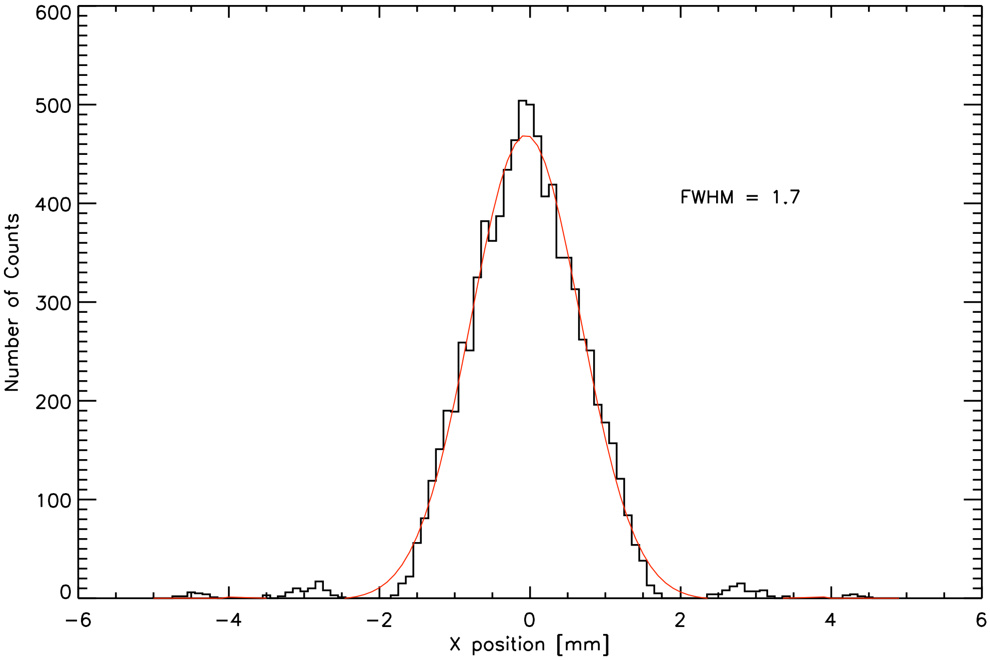

Figure 2.24 Raytraced histogram of the collimator focus.

the distribution of photons that hit both the detector and the bulkhead. This distribution does not take grating efficiency into account as we do not know the incident wavelength of the photons. This plot shows that the majority ($\sim 70\%$) of photons are diffracting at a graze angle of $\geq 4°$. However if the wavelength distribution is dominated by short wavelengths (< 40 Å), then it's possible that the high graze angle photons are absorbed (due to the low reflection efficiency at these higher energies) and the spectrum is dominated by the low graze angle photons.

The efficiency of the grating arrays was tested prior to the CyXESS flight. The setup for this test is shown in Figure 2.26. The procedure involves illuminating the master grating with monochromatic X-rays and comparing the count rate of the dispersed spectrum with the count rate observed with the gratings removed from the beam. This test provides efficiency values in each diffracted order. The results are shown in Figure 2.27. Unfortunately, due to the lack of a high-quality quality X-ray monochrometer, only emission from carbon K-shell at 277 keV (44.76 Å) was useable for calibration. This is due to high carbon contamination on our anodes (typically aluminium or magnesium). These anodes tend to emit in carbon (due to contamination) and oxygen (due to an oxide layer on the surface of the anode). Isolating emission from Al, Mg, Cu or B proved too difficult to achieve. See McEntaffer et al. (2004b) for more information on grating efficiencies in the off-plane mount. Our testing of other gratings has shown good agreement between theoretical and measured efficiencies. Given the excellent match at 44 Å, the atomic force microscopy measurements of the grating surface by JY, and our past experience we feel quite comfortable using this efficiency curve in our effective area calculations.

The light source in our monochrometer is a point source (McEntaffer et al. 2004a) and thus doesn't provide the efficiency averaged over the range of incident angles. This plot shows the efficiency only at 4.4°. A plot comparing the theoretical efficiency of the gratings at various angles is shown in Figure 2.28. This variety of graze angles results in a very difficult calibration as the efficiency varies strongly, particularly at the ends of our bandpass. This illustrates the need for an extended X-ray light source.

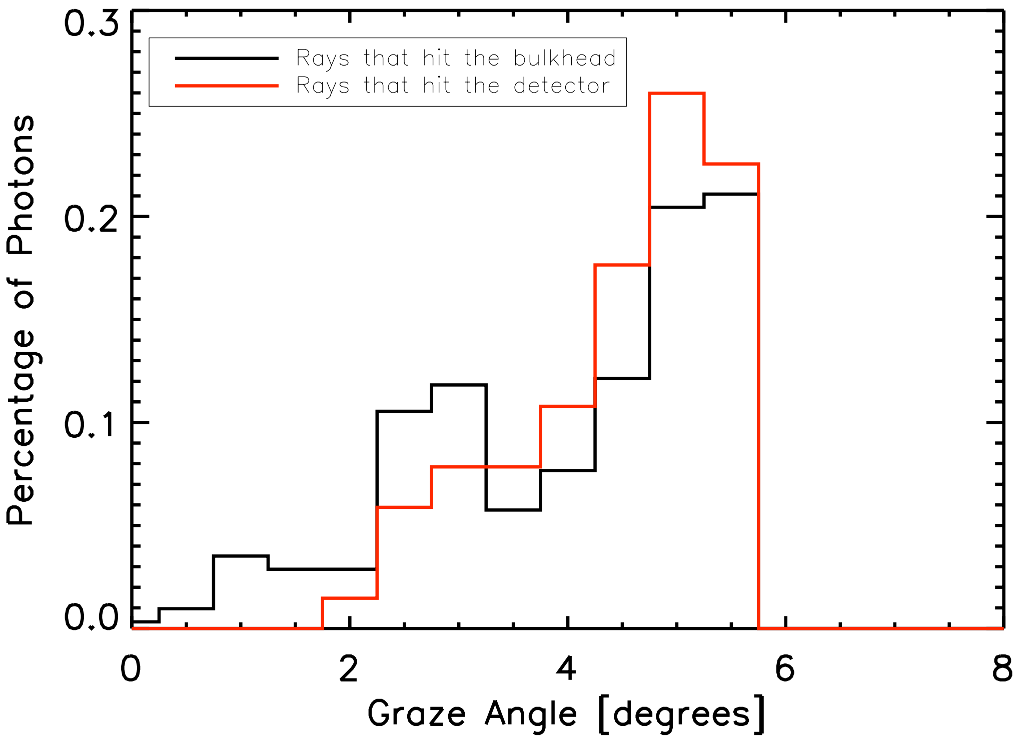

Figure 2.25 Graze angle distribution of photons. This assumes a ring shaped target source such as the Cygnus Loop. More lower graze angle photons could be captured by shifting the detector towards the bulkhead center if the observation is expected to be dominated by higher energy photons (which are absorbed at high graze angles).

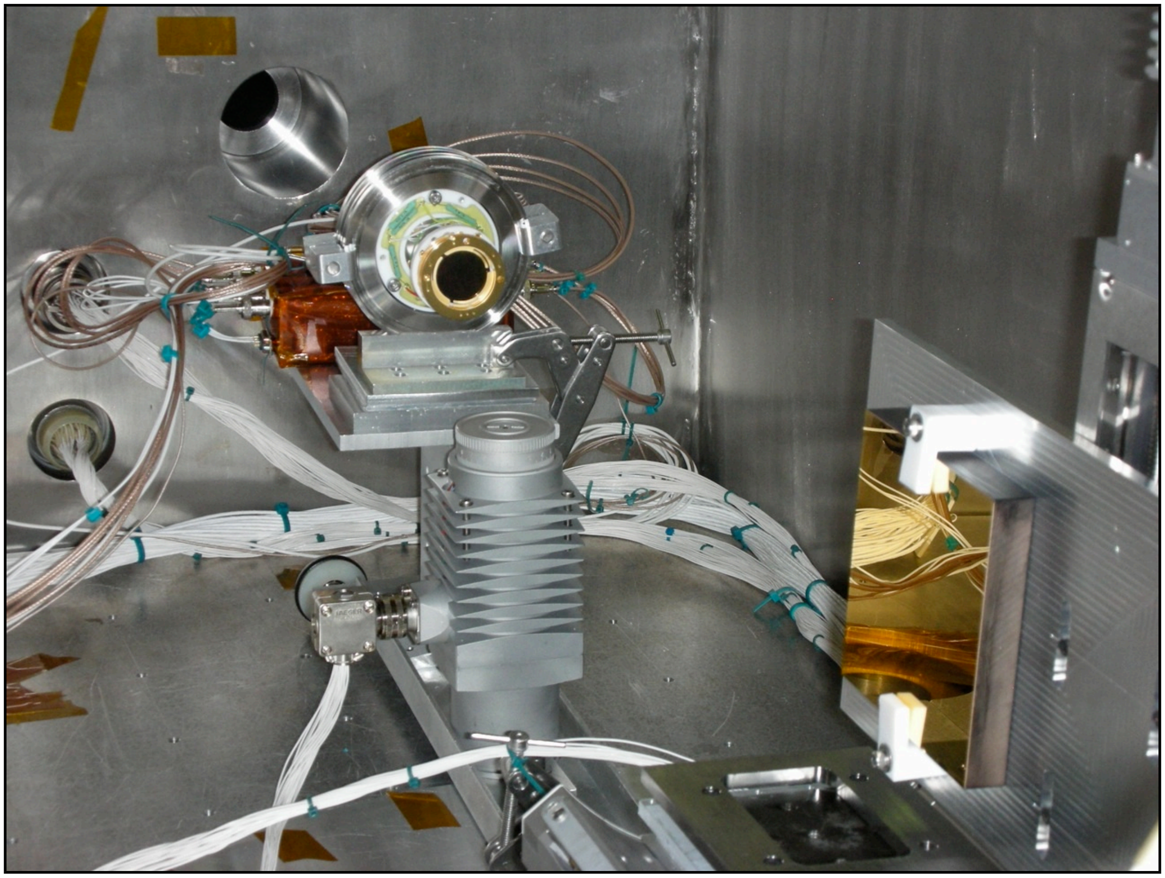

Figure 2.26 Hardware setup for grating efficiency tests. Monochromatic X-rays are sent from the far right (off the image) to the grating shown on the right, and are then dispersed via the geometry shown in Figure 2.9. The detector (a micro-channel plate imager) on the left is moved into the desired spectral line to observe the count rate. This count rate can be compared to the rate without the gratings in the beam to determine the effciency of the gratings.

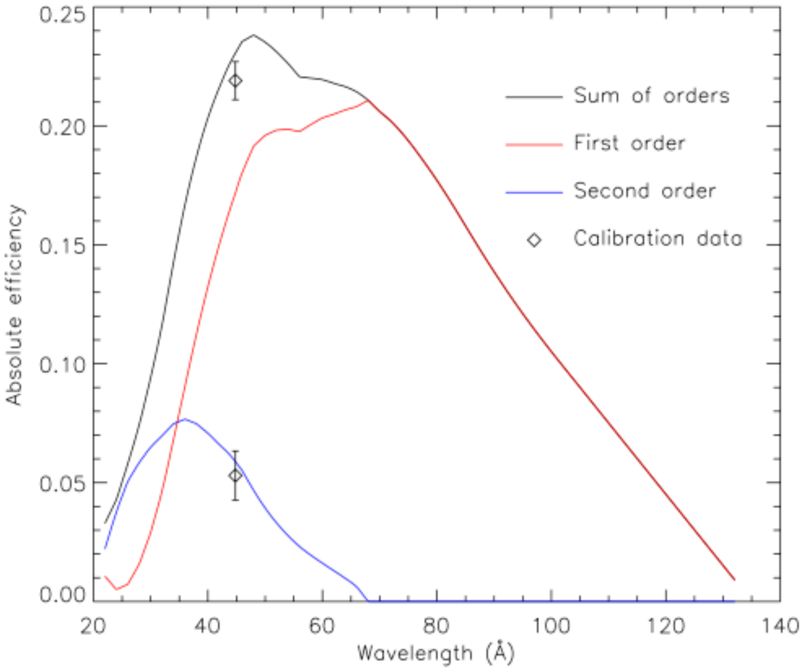

Figure 2.27 Grating efficiency curve at 4.4°.

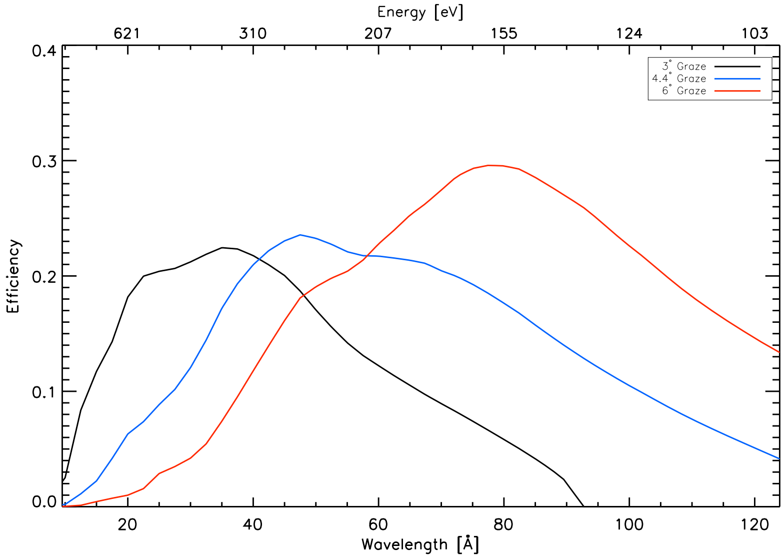

Figure 2.28 Theoretical grating efficiency curves at 3°, 4.4° and 6°. The sum of all positive orders (essentially 1-3) is plotted. Negative order efficiencies are almost identical.

2.5.3 Detectors

As shown in Figure 2.23, the placement of the detector defines the bandpass of our instrument. The bulkhead was machined (Figure 2.29) with openings for the detectors to achieve a bandpass of 17 – 107 Å (for reasons stated in Section 1.4).

The main characteristics of the GEM detectors that we can influence post assembly are: background count rate, efficiency and energy resolution. Background count rates can be easily measured by turning the X-ray source off during an exposure. The absolute efficiency of the detectors is difficult to measure, but a relative measure can be obtained. Additionally the entire detector face can be examined to make sure the gain is sufficient to observe soft X-rays. Lastly the energy resolution can be maximized by monitoring the pulse height of each photon's resulting charge cloud. The energy sensitivity is fairly crude, but may provide a means to resolve order confusion. Energy resolution could also separate soft X-rays from dark counts if the gain is sufficient.

The detectors can be modified both in their gas pressure and voltage. Figures 2.30 - 2.32 shows various relationships between these input parameters and the resultant characteristics. The first plot shows how ramping up the voltage affects dark rate, efficiency and energy sensitivity at a fixed gas pressure. The dark rate is essentially ambivalent to operating voltage up until 4100 Volts. To observe at high efficiencies requires a voltage above 3950. However one detector that was run in the 4050-4150 range experienced sudden and permanent failure in one of the GEM plates. A permanent connection was made between the top and bottom conductive copper layers, and the GEM plate was not creating any gain within the pores. Therefore voltages above 4050 involve considerable risk. Lastly this plot shows that to achieve optimal energy resolution requires a voltage above $\sim$ 4050. Unfortunately this voltage is within the unsafe region of voltages, and thus limits our maximum energy resolution. Our energy resolution is only of marginal usefulness below our cutoff of 4050 Volts and does not provide a definitive resolution to order confusion.

Another parameter we can vary on the detectors is gas pressure. Figure 2.31 shows how count rates decrease as a function of pressure (for a fixed operating voltage). Below $\sim$ 12 PSIA the detector

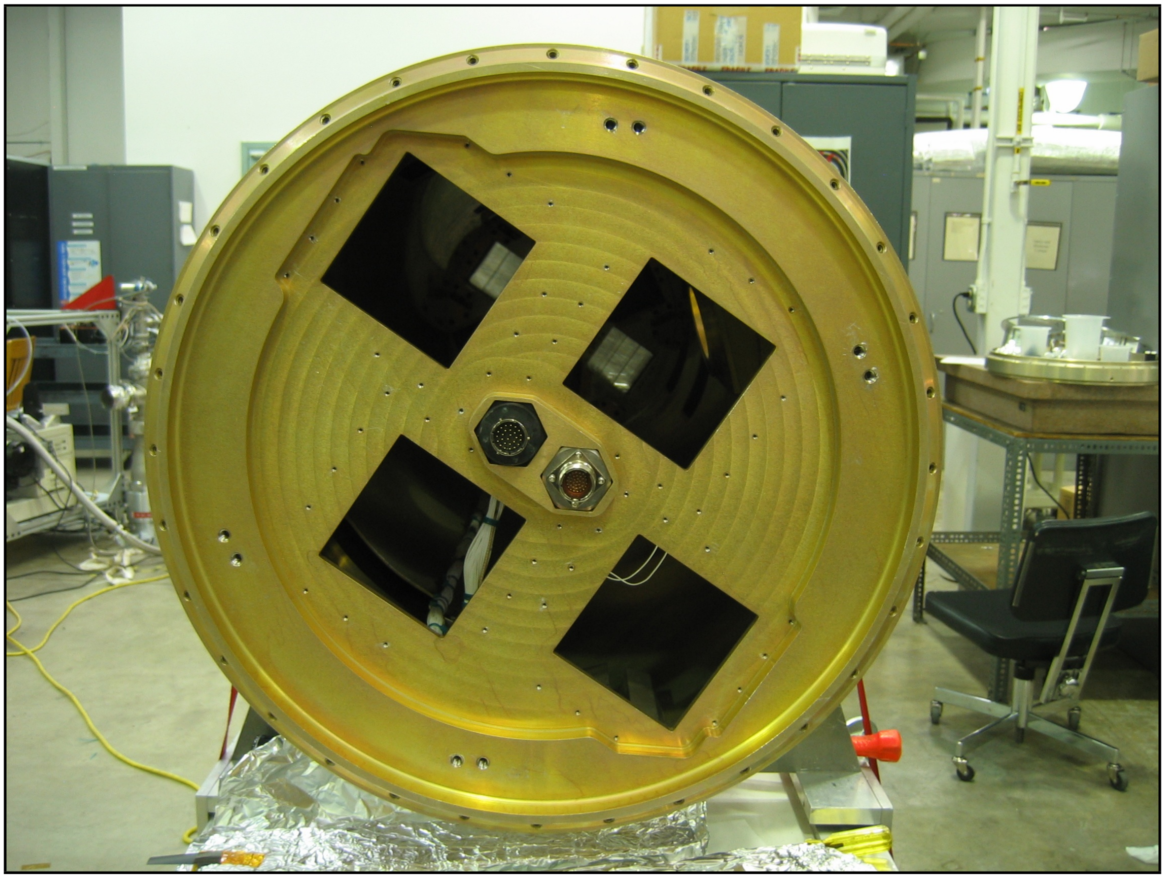

Figure 2.29 The two outermost (top left and bottom right) openings are for mounting the two GEM detectors (note the odd shaped cutouts along the perimeter to accommodate the GEM housing). The other two openings are for interior access, and to mount a vacuum gauge to monitor the payload vacuum level. The two central connectors are feedthroughs to pass signals to the shutter door and star tracker.

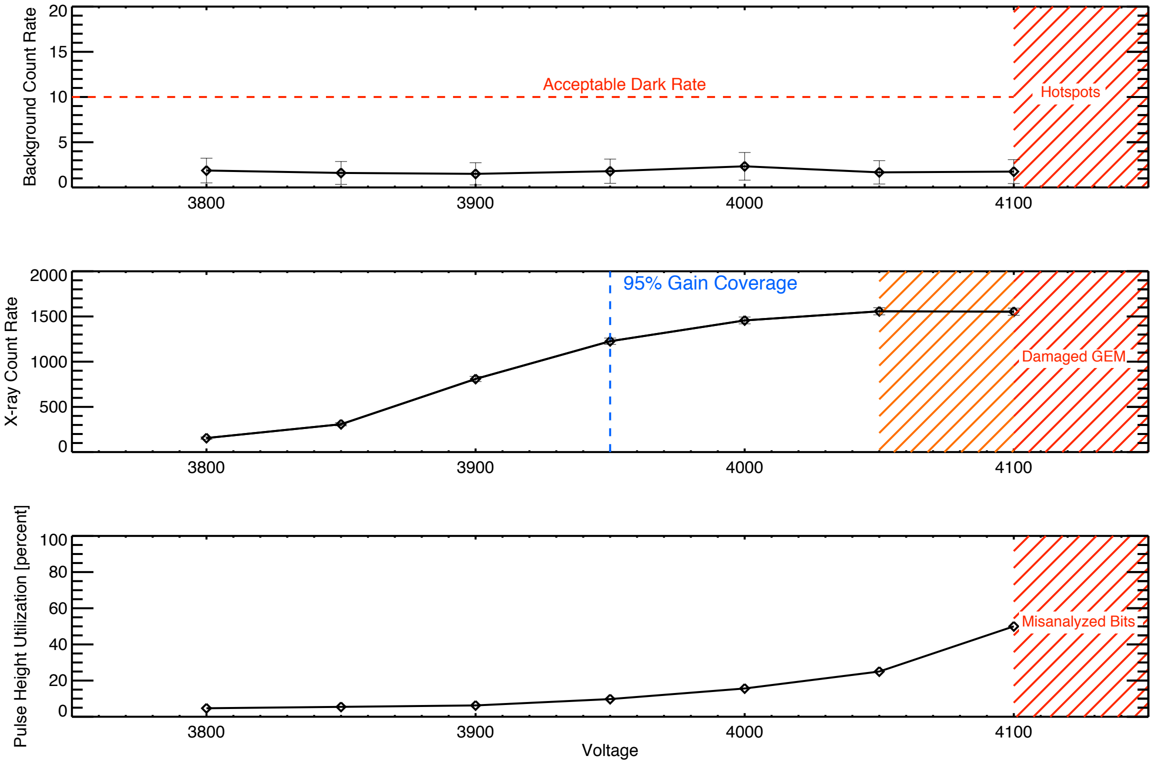

Figure 2.30 **Top** - Dark rate as a function of operating voltage. The desired dark rate was $< 10 counts/s$ (marked in red) which was easily obtained. Above 4100V (marked in orange) the detector became more susceptible to hotspots and this dark rate could spontaneously increase. This defines a fairly soft boundary as hotspots can typically be reduced from the data. **Middle** - Count rate as a function of voltage. The count rates are fairly arbitrary in terms of value as they depend completely upon the source. However it is still useful to examine as one can examine when additional voltage is unlikely to result in additional counts. The entire face ($> 95\%$) of the detector is capable of a high enough gain to register at least $1/2$ keV photons at 3950 Volts, while the maximum efficiency seems to be obtained at 4000-4050 volts. Unfortunately a detector typically run at 4050-4100 (marked in orange) failed during a test when run at 4100-4150 (marked in red). It is unclear whether this failure was due to the higher voltage, or simply the accumulation of operation at the lower voltage. Regardless this entire voltage range was decided to be too risky for flight. **Bottom** - Usage of the charge information on the detector as a function of voltage. At too low gains all soft X-rays (and dark counts) are essentially observed as part of the same population of photons. At higher gains the soft X-rays are distinct from dark counts, and to some extend from each other. This would allow for some amount of resolving order confusion. Unfortunately the voltage at which this pulse height data becomes very useful is also when the detector is prone to failure. Above 4100 volts, a higher percentage of photons become misanalyzed due to their high charge value.

became unstable. Hotspots were more frequent and misanalyzed bits more common. Figure 2.32 shows the optimal voltage as a function of gas pressure. Optimal is defined as a combination of maximized efficiency, stability, energy sensitivity without risking further GEM failure.

2.5.4 System

An example of calibration data for detector 0 is shown in Figure 2.33. This spectrum was achieved by shining X-rays down the payload using a Manson electron impact source. This source is a (approximate) point source so it does not perfectly simulate the extended source our system is designed for. However we mounted the source on moveable linear stages and were able to scan across horizontally and vertically during an exposure to simulate an extended target.

The grid pattern is the result of the course aluminum support structure on the GEM window (Section 2.4). The spot in the bottom left is the detector stim pulse which sends a signal at ~ 10 Hz used to verify that the detector electronics and telemetry are functioning properly. The vertical lines of counts represent various spectral lines. The limits on the detector face are very obvious with the exception of a smattering of counts outside the well defined square. These counts are due to mis-analyzed bits. This happens rarely, except in cases of particularly energetic events (i.e. ions contacting the detector window).

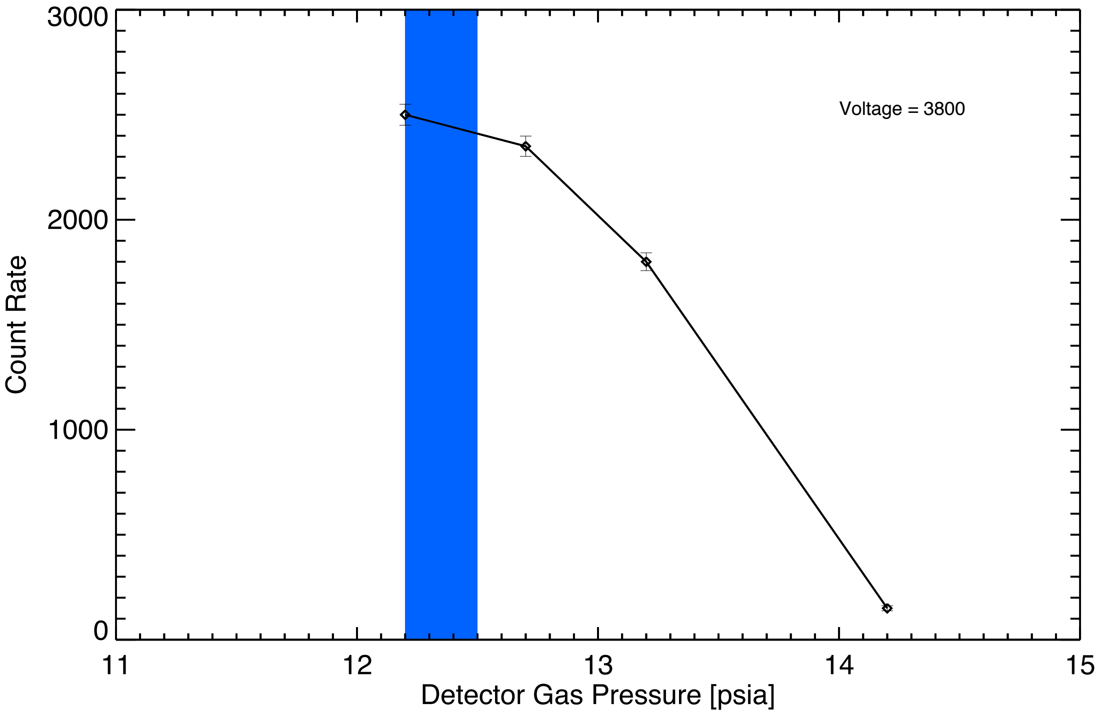

Figure 2.31 Count rate as a function of gas pressure at 3800 volts. Below $\sim$ 12 PSIA the detector was more prone to hotspots and misanalyzed bits, making an accurate assessment of X-ray count rate difficult. The blue bar marks the ambient gas pressure range at Boulder, Colorado and White Sands Missile Range, New Mexico. Operating at, or below, this pressure is possible in the lab, but difficult in the field. Purging the detectors of ambient gas and filling them with only Ar/CO_2 in the field would require substantial modifications to the gas system. Thus operating above this pressure is preferred.

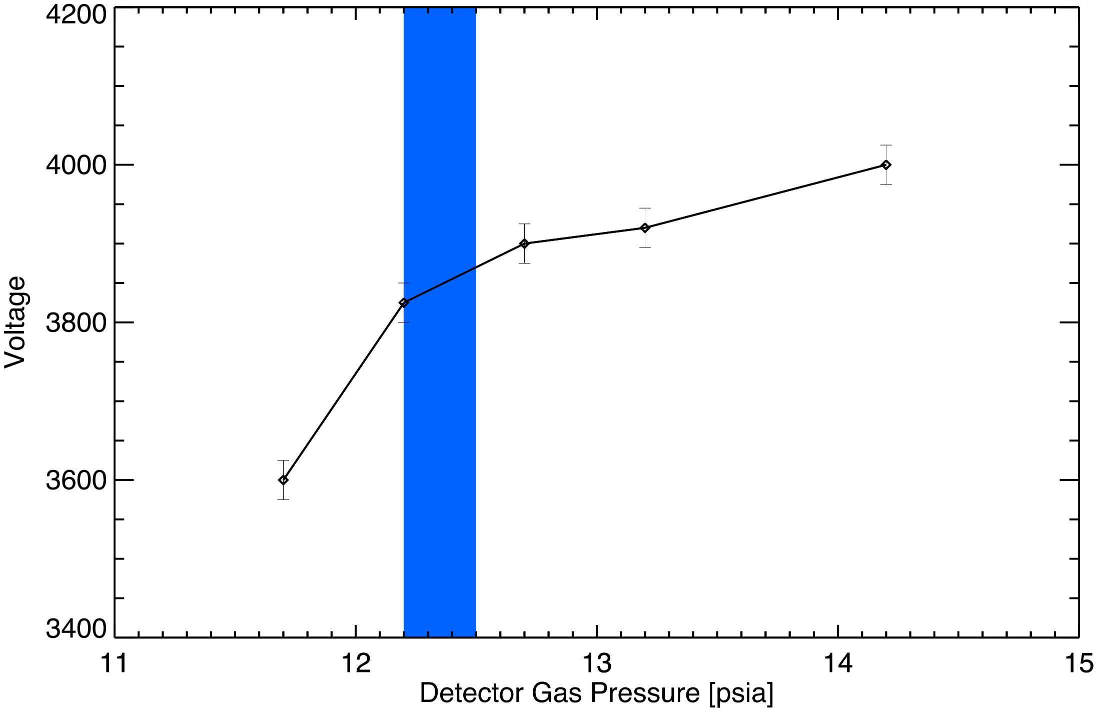

Figure 2.32 Optimal operating voltage as a function of gas pressure. The blue bar marks the ambient gas pressure range at Boulder, Colorado and White Sands Missile Range, New Mexico. Operating at, or below, this pressure is possible in the lab, but difficult in the field. Purging the detectors of ambient gas and filling them with only Ar/CO_2 in the field would require substantial modifications to the gas system. Thus operating above this pressure is preferred. Unfortunately this means operating at both a higher pressure and higher voltage. This somewhat increases our chances of breaking the detector window or damaging another GEM plate. However our lab tests show that these are both still unlikely.

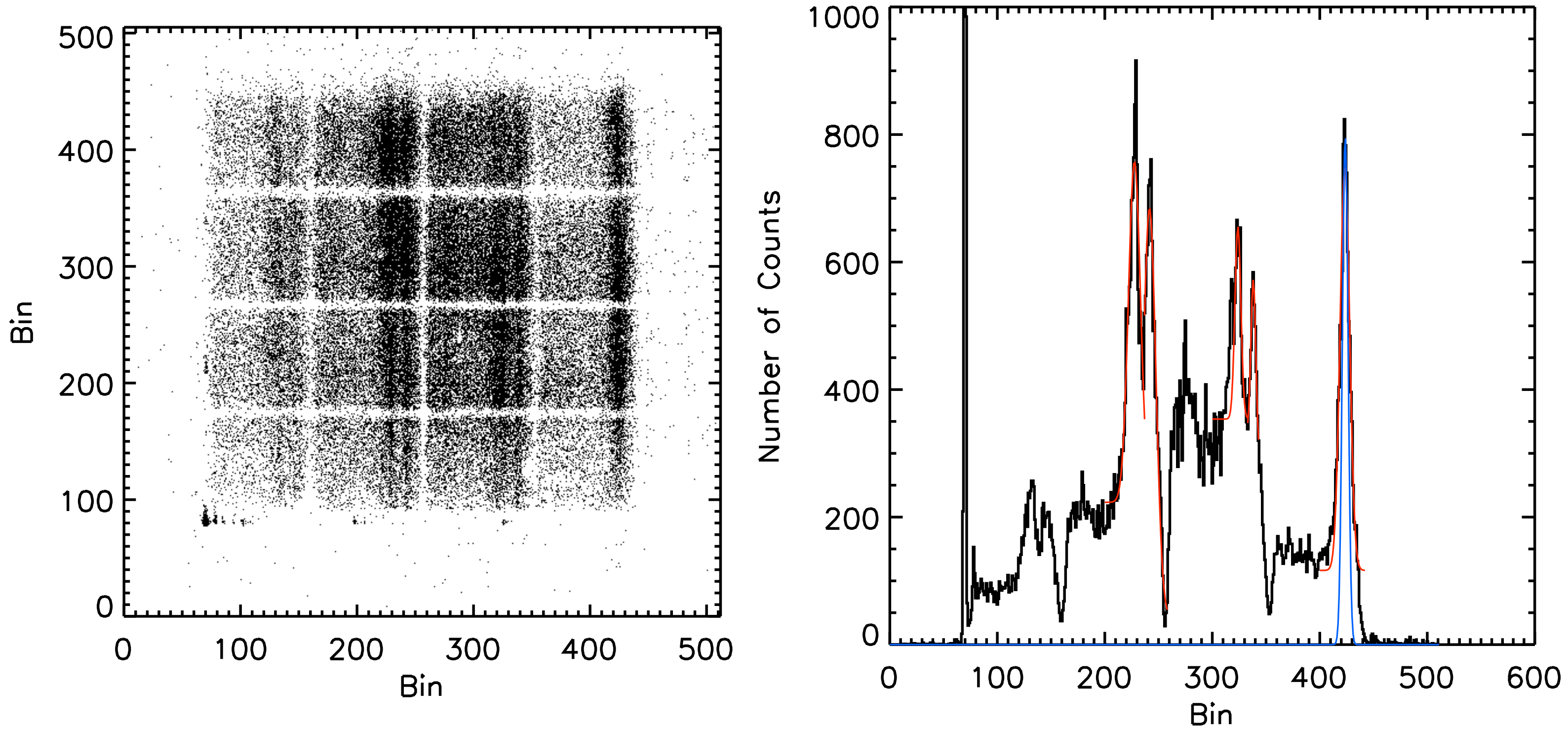

Figure 2.33 Calibration data for Detector 0 using an aluminum anode. **Left** - Raw image of GEM data. The spot in the lower left is the stim pulse from the detector. **Right** - Histogram of counts. Red gaussians mark the best fit gaussian curves. Blue gaussian marks the theoretical gaussian of 1.7 mm FWHM. The rightmost line is oxygen in first order. The leftmost “line” is actually the stim pulse and not a spectral line.

The spectrum shown in Figure 2.33 can reveal several things about the actual instrument performance versus the theoretical raytrace. The FWHM of the lines combined with the dispersion can establish the system resolution. The location of the lines can calibrate the actual observed bandpass. Lastly, the relative strength of the lines can verify our grating efficiency curve (Figure 2.27).

The right most line in Figure 2.33 is oxygen K-shell emission at 23.62 Å. This identification is based upon 3 pieces of information. Firstly, the raytrace predicts that 23 Å should fall at this line's locations. Secondly, oxygen emission typically reflects more efficiently than the magnesium emission at 9.9Å (19.8 Å in 2nd order) therefore we are unlikely to see only magnesium emission. Thirdly, by shining optical light down the system we can locate the zero order reflection and calculate (based on the expected dispersion) the expected wavelength to fall at this location. This was determined to be 25 ± 3 Å, consistent with oxygen emission.

The line to the left is likely carbon K-shell emission at 44.7 Å in first order. Carbon emission off the Manson source is typically very broad, but is possibly trimmed here due to the window bar shadow at a bin of ~ 350. To it's left is oxygen in second order. There's a smaller peak almost merged with this line on its left side. This is likely a 5th order magnesium line. The small peak at bin ~ 270 is likely magnesium in 6th order. The next two lines are magnesium in 7th order and oxygen in 3rd order. Carbon in 2nd order and magnesium in 8th order are likely blocked via the leftmost window bar (bin ~ 260). The last line on the left is oxygen in 4th order.

The majority of flux here is between bins $\sim 230 - 340$. This corresponds to a blaze of $\sim 10 - 20^\circ$. These gratings have a sinusoidal profile, which typically acts as a pseudo blaze. The profile is usually fairly shallow, so a pseudo blaze of $\sim 10 - 20^\circ$ is entirely reasonable.

Taking Equation 2.1 we can calculate the angular dispersion of the system by taking the derivative with respect to wavelength.

$$\frac{\delta}{\delta\lambda}(sin\alpha + sin\beta) = \frac{\delta}{\delta\lambda}(\frac{n\lambda}{dsin\gamma}) \tag{2.2}$$

$$cos\beta\,\frac{\delta\beta}{\delta\lambda} = \frac{n}{d\ sin\gamma} \tag{2.3}$$

$$\frac{\delta\beta}{\delta\lambda} = \frac{n}{d\ sin\gamma \cdot cos\beta} \tag{2.4}$$

Here d is the distance between grooves. However gratings are typically described by their groove density rather than this distance. So we can convert the above formula to:

$$\frac{\delta\beta}{\delta\lambda} = \frac{l \cdot n}{10^7 \cdot sin\gamma \cdot cos\beta} \tag{2.5}$$

where l is the groove density, measured in grooves per mm. To convert to linear dispersion dispersion of the system we multiply by the radius of the arc:

$$R = L \cdot sin(\gamma) \tag{2.6}$$

where L is the throw of the system and is equal to 1954.84 ± 10 assuming a starting position halfway along the gratings 20 mm depth. We also take the average graze angle of $\gamma = 4.4°$. Linear dispersion is typically measured in Å/ mm so we also invert the derivation. This makes the linear distance between two wavelengths:

$$\frac{\delta\lambda}{\delta D} = \frac{10^7 \cdot cos\beta}{n \cdot l \cdot L}\left[\frac{\text{Å}}{\text{mm}}\right] \tag{2.7}$$

We are primarily interested in the distance along the x-axis. This distance is:

$$x = R \cdot sin\beta \tag{2.8}$$

$$x = L \cdot sin\gamma \cdot sin\beta \tag{2.9}$$

The dispersion in first order ($n = 1$) along the x-axis works out to:

$$\frac{\delta\lambda}{\delta x} = \frac{1}{L \cdot sin\gamma \cdot cos\beta} \cdot \frac{\delta\lambda}{\delta\beta} \tag{2.10}$$

$$\frac{\delta\lambda}{\delta x} = \frac{1}{L \cdot sin\gamma \cdot cos\beta} \cdot \frac{10^7 \cdot sin\gamma \cdot cos\beta}{l \cdot n} \tag{2.11}$$

$$\frac{\delta\lambda}{\delta x} = \frac{10^7}{n \cdot l \cdot L} = \frac{10^7}{5670 \cdot 1954.84} = 0.90 \text{ Å/ mm} \tag{2.12}$$

Measuring the distance between lines in bin space (or more usefully in physical space) versus wavelength space gives the actual dispersion of the system. This was measured to be 0.90 Å/ mm. This is in perfect agreement with theory and is also very similar to the measured CyXESS value of 0.89 Å / mm.

The blue gaussian plotted in Figure 2.33 represents the raytraced result for oxygen emission in first order. The two lines agree very well, though the actual data has a slightly wider FWHM than predicted. Our optimal FWHM for our spectral lines is 1.69 Å, 1.74 Å and 2.06 Å for $\lambda = 17$ Å, 62 Å and 107 Å respectively. These are the minimum, center and maximum wavelengths of our bandpass. They increase in width at higher wavelengths is due to the geometry of the spectrum in relation to the gratings. At small wavelengths, the spectral line is located roughly equidistant from either end of the gratings. However, at high wavelengths the spectral line is significantly closer to one side of the grating, thus light from the opposite side travels a significantly longer distance, causing this aberration. These values produces the theoretical resolution shown in Figure 2.34. The average FWHM of the system is measured at 2.07 Å. This is on the wide end of the expected range, probably due to some of the difficulties in aligning the collimator discussed in Section 2.5.1. However, given that there are 4440 slits in the collimator and 67 gratings in the array (per module), we are well within an acceptable performance regime.

The last item we are interested in is the grasp of the system, measured in cm^2 sr. This calculation has several components: the reflection efficiency of the gratings, the transmission efficiency through the detector windows, the FOV of the collimator, the collecting area of the detectors and the number of modules. The grating efficiency is shown in Figures 2.27 and 2.28. The transmission efficiency of the GEM window is shown in Figure 2.35. This efficiency does not consider the support

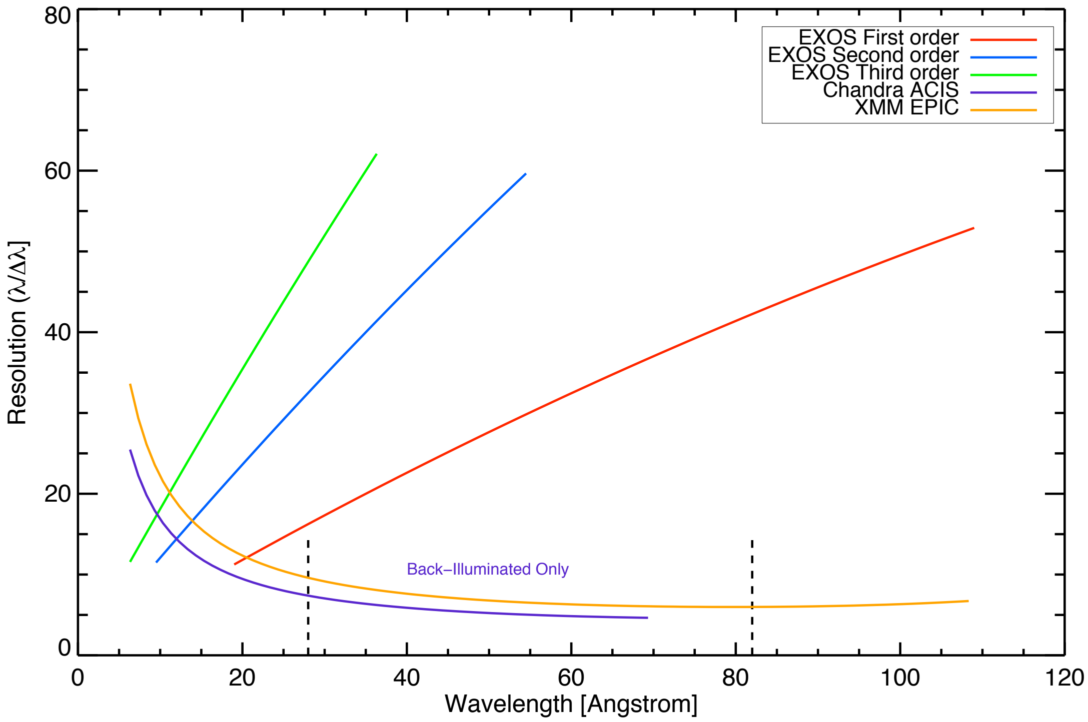

Figure 2.34 EXOS resolution. Plotted for reference are the resolutions for Chandra and XMM when utilizing CCD energy sensitivity. Only the back illuminated chips onboard Chandra are capable of observing the softest of X-rays. This soft range is designated by the vertical dashed lines.

mesh on the window which has a transmission of 57.8%.

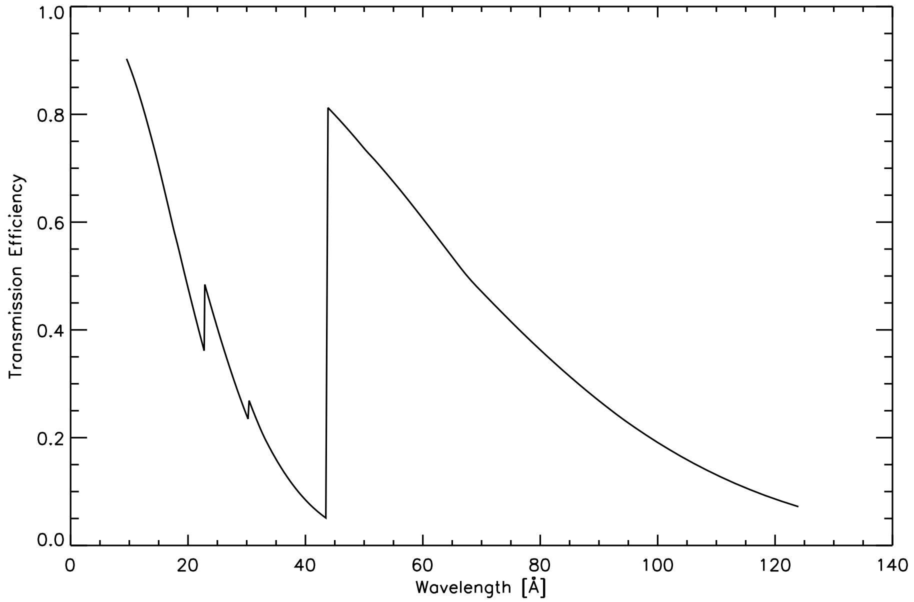

Figure 2.35 Transmission efficiency of GEM detector windows. The sharp drop at ∼ 44Å is the carbon edge. This curve is due to the window material only, and does not consider the stainless steel support mesh.

Combining the various efficiencies results in the system efficiency shown in Figure 2.36 (top). This curve is assuming an incident angle of $\gamma = 4.4^\circ$ off the grating. Figure 2.36 (bottom) also shows how drastic this angle is in determining the overall system efficiency.

Unfortunately we observe a variety of these angles, and thus determining an overall system efficiency is remarkably difficult. By taking the raytrace shown in Figures 2.22 and 2.23 we can determine the γ for each individual photon and assign it a specific efficiency curve. This process assumes the Cygnus Loop is an annulus of emission. This is equivalent to convolving Figure 2.25 with Figure 2.36 (right). This is the most accurate efficiency we can calculate and the one we will utilize from here on.

The field of view of the system is 8.93 deg^2 or 0.0027 sr. The collecting area is the size of the zero order image: a 1.7mm x 100mm line gievs 1.7 cm^2. Lastly we have 2 utilized modules in the payload. The combination of all efficiencies, collecting area and FOV is shown in Figure 2.37. With this blend of graze angles, the efficiency at lower wavelength (∼ 20 Å) is roughly equal

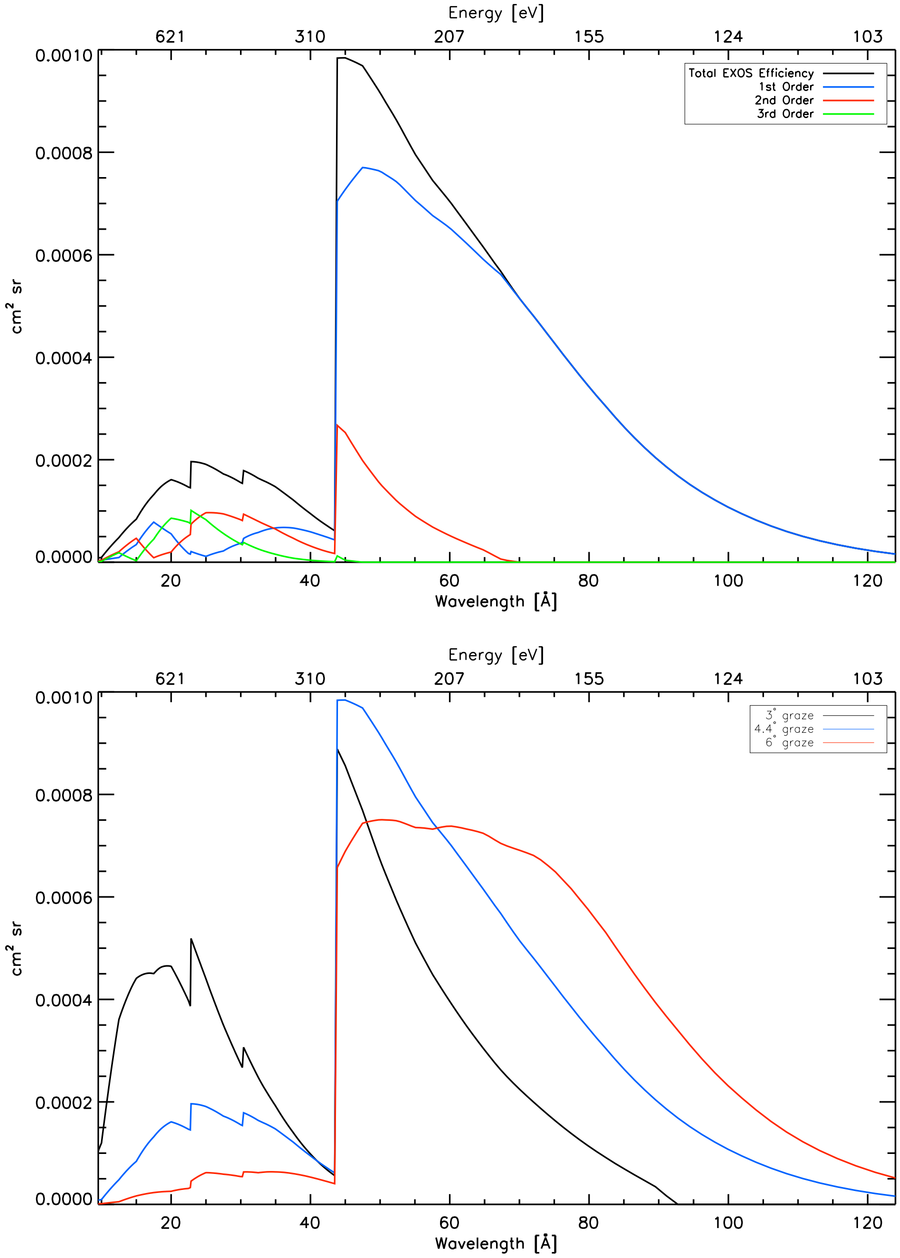

Figure 2.36 **Top** - Efficiency of EXOS assuming a graze angle of 4.4°. **Bottom** - Comparison of EXOS efficiency at various angles of incidence. Values here are the sum of all positive orders. Graze angle is particularly important at wavelengths < 40 Å .

between the orders. This matches what we see in Figure 2.33, where the oxygen line has roughly equal strengths over the first three orders.

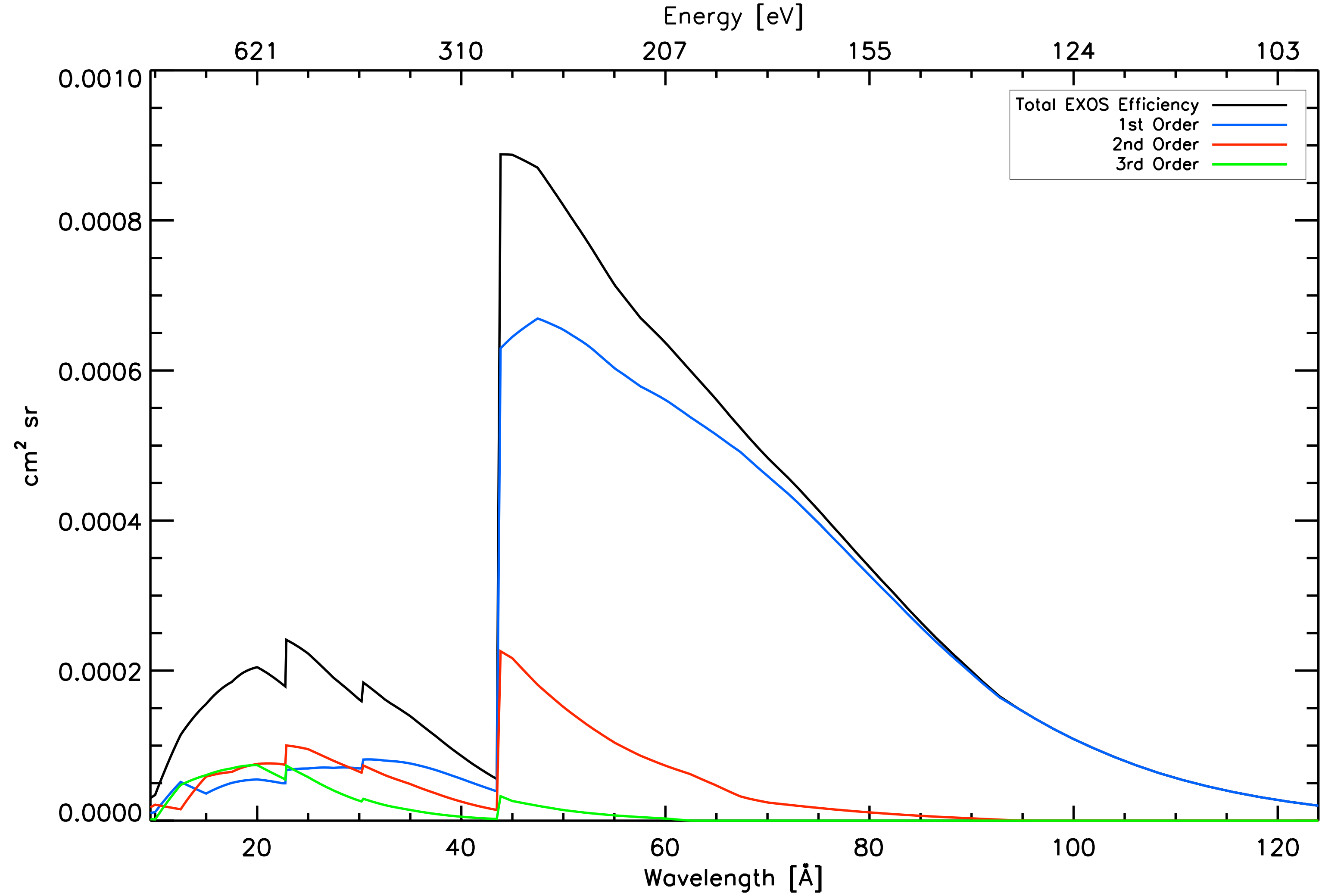

Figure 2.37 Overall EXOS instrument efficiency blended via the distribution of incident angles (Figure 2.25) for a target with a ring-like morphology.

Chapter 3

Flight Data

The EXOS payload (flight 36.252) was launched out of White Sands Missile Range, New Mexico aboard a Black Brant Terrier (Figure 3.1) at Friday, November 13th at 7:30 pm local time (02:30:00 UT, November 14, 2009). During flight, the detectors were powered and collected photons for 363.834 seconds. The detectors were turned on at time 411.4 seconds. This time was 30 seconds after the shutter door to the payload was opened. This delay could have been decreased by powering the detectors sooner after the shutter door was opened. This delay was only 14 seconds on the CyXESS flight. Unfortunately on that flight the buildup of gas in the payload during pre-launch testing from the leaky windows (Section 2.4) created too high a pressure in the payload (specifically in front of the windows). Upon HV turn on the windows (held at $\sim$ 4000 Volts) discharged into the gas and created a storm of counts (> 5 kHz). Due to this event, we elected to delay HV for the EXOS flight, and allow the gas additional time to pump into space. Figure 3.2 shows the timing of various tasks in flight. The commands issued during flight include an LED turn on to verify star tracker functionality, a telemetry reset to insure proper transmission of data, a vacuum gauge test to determine vacuum levels in the payload and high voltage turn on.

Figure 3.1 EXOS launch on Friday, November 13th at 7:30 pm local time (02:30:00 UT, November 14, 2009) from White Sands Missile Range, New Mexico.

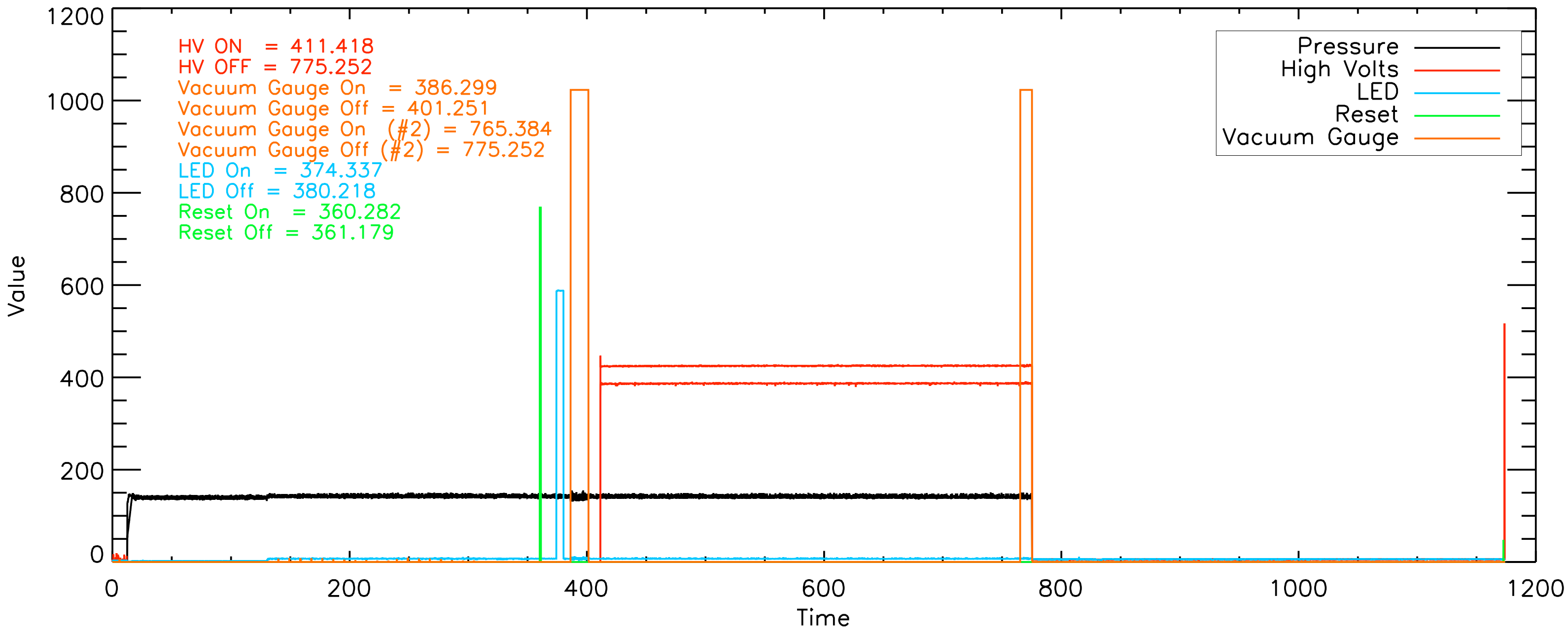

Figure 3.2 Timing of events during flight. The rocket was launch at t=309 seconds. The green reset command is to reset telemetry in case of any issues caused by launch acceleration. The LED is used to verify star tracker functionality and is turned on between 374-380 seconds. The vacuum gauge was installed in order to provide real time data on the vacuum level inside the payload. This allows for a real-time decision to be made for when to turn on high voltage. This gauge is turned on between 386-401 seconds, chosen to allow space to pump on the payload before taking a reading, and a buffer time prior to turning on HV. However the readout voltage of the gauge pegged the maximum that could be telemetered down. The gauge is not designed to return voltages this high, indicating that the gauge malfunctioned in some fashion. The two high voltage power supplies turned on at 411 seconds. Each detector is set to a slightly different voltage for optimal performance. The black pressure line indicates the pressure inside the GEMs and reads a consistent value at 14.5 PSIA (the pressure is approximately a tenth of the digital value). At the end of flight the vacuum gauge was again turned on. This was intentionally turned on at the same time as our detectors in order to cause the ions created in the gauge to strike the GEM window. This would create an in-flight flat field on the detector and provide an indication of detector performance. Again the value pegged higher than could be telemetered down. As our detectors were functioning well (i.e. the vacuum level was adequate), the gauge was obviously malfunctioning.

During flight the pressure in the GEMs was optimal (14.5 PSI), indicating no tears or excessive leaks in the GEM windows caused by launch. This is particularly important because our flight experienced far worse vibrations than typical. Due to a modification of the Black Brant booster we experienced a “vibration anomaly” as shown in Figure 3.3. The power, especially at low frequencies that do the most damage, exceed specifications by a factor as high as ~ 600. The windows surviving this brutal of a launch validated our decision to increase their thickness at the cost of some throughput.

The experimental section turned off at the appropriate time, coincident with the shutter door closing. The parachute deployed as intended at 4.9 km altitude (Figure 3.4). Unfortunately due to high wind velocity, the payload impacted the ground with more force than is typical. This caused severe damage to several components of the payload. The primary damage was to the aft end of the payload. The crash bumper was completely compressed and torn from the payload. The shutter door was severely damaged, as was the front of the collimator structure. Several skins were significantly dented. The gas tubing to our detectors was also damaged in some locations. This damage drastically altered the optical path and quality of the instrument, rendering post-flight calibrations impossible.

3.1 Data Reduction

The entire data set is shown in Figure 3.5. We can deduce several thing from this image. In the lower left corner the two stim pulses (small dots ~ 50 pixels in diameter) are visible, indicating that both sets of detector electronics and the rocket telemetry system were functioning with optimal resolution. The 4×4 window grid caused by shadows from the window support structure is also visible, giving further proof that both telemetry and data extraction and analysis software are functioning properly. Several hotspots in the top right quadrant account for approximately a third of the total counts. These are fairly easy to remove from the observation as they are highly localized in physical space. One can also remove these from time space and try to restore some functionality from these pixels. Even a simple cut of these of pixels out of the data still does not strongly reduce

Figure #2

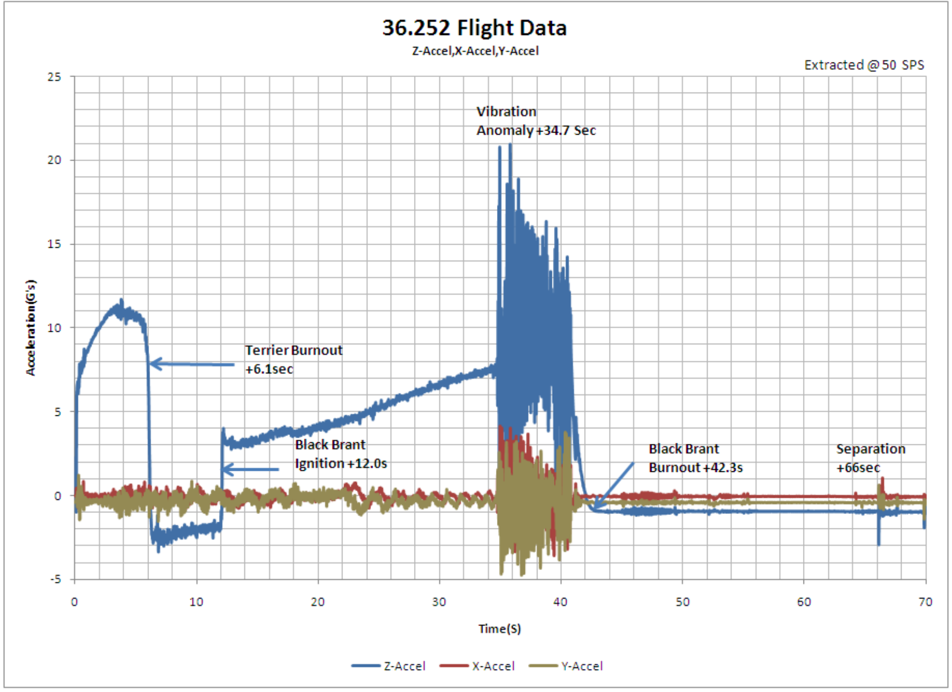

19

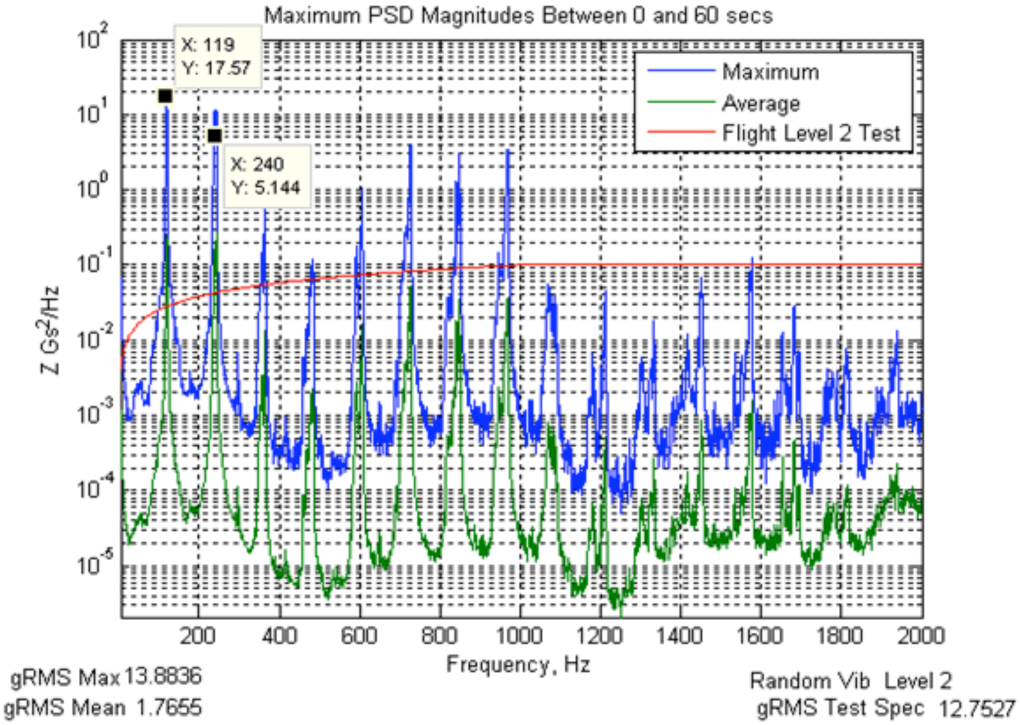

Figure 3.3 **Top** - Launch vibration anomaly with acceleration as a function of time. The anomaly lasted $\sim$ 6 seconds and produced G-forces in excessive of 20. **Bottom** - Power spectrum of the vibrations. The red line indicates the expected power. Note how far the actual launch exceeded this value, particularly at low frequencies. The power seems focused at about every $\sim$ 100 Hz.

Figure 3.4 Landing site. Photo taken aboard a helicopter during recovery.

our effective area. There is also a smattering of counts outside the tightly defined square face of the GEMs. These represent misanalyzed bits (see Section 2.5.3).

Overall there are 253,841 counts recorded, including stim counts, hotspots, misanalyzed bits, etc. Figure 3.6 shows how the detector count evolved over time and payload altitude. The sharp spike at 411 seconds is the detector high voltage being turned on. Prior to that the count rate is due to the stim pulse that the detector electronics (powered by low voltage) puts out. The few spikes prior to HV turn on are due to various rocket events (separation, etc.) that cause momentary noise in the electronics. Immediately after turn on the count rate spikes to $\sim 10^4$ counts/s. This flight suffered from a more minor version of what happened to the CyXESS flight. Residual gas in the payload (most likely leaking from the detector windows) caused a discharge event. Fortunately this gas quickly evacuated the payload and the count rate settled down. The count rate spikes throughout flight are due to the hotspots shown in Figure 3.5. Figure 3.7 shows the count rate plot after data reduction. This shows only counts assumed to be external X-rays. The steady count rate of X-rays is 87.3 ± 12.8 counts/s total. This is a factor of ~ 10 more than our pre-flight count estimates. This plot shows a slow rise in detector 0 from $\sim 12 - 57$ counts/s and a relative constant rate in detector 1 of 53.1 ± 8.0 counts/s. The payload altitude appears to have no effect upon the count rate. Additionally, the soft X-ray flux should only vary $\sim 5\%$ over the varying atmospheric thickness from 80-170 miles. This would only result in a rise and fall of 4.4 counts/s on data with a $\sigma = 12.8$ counts/s. If the count rate had a strong altitude dependence then we would have to consider the contribution of the Ly-α airglow. Thus, besides the easily reduced initial spike and localized hotspots, our instrument appears to be operating optimally, though the higher than expected count rate is worrisome. Since the slow rise in detector 0's count rate does not seem to correlate with altitude, it is probably due to an increase in gain as the detector warms up. As mentioned in Section 2.4 this rise in gain used to be very common on the old GEM plates as detailed in Section 2.4. The new GEM plates are much more stable, but a quick rise over a few hundred seconds is still fairly reasonable, especially considering the unexpectedly rough ascent.

From here it becomes useful to separate the data by detector. This is accomplished by

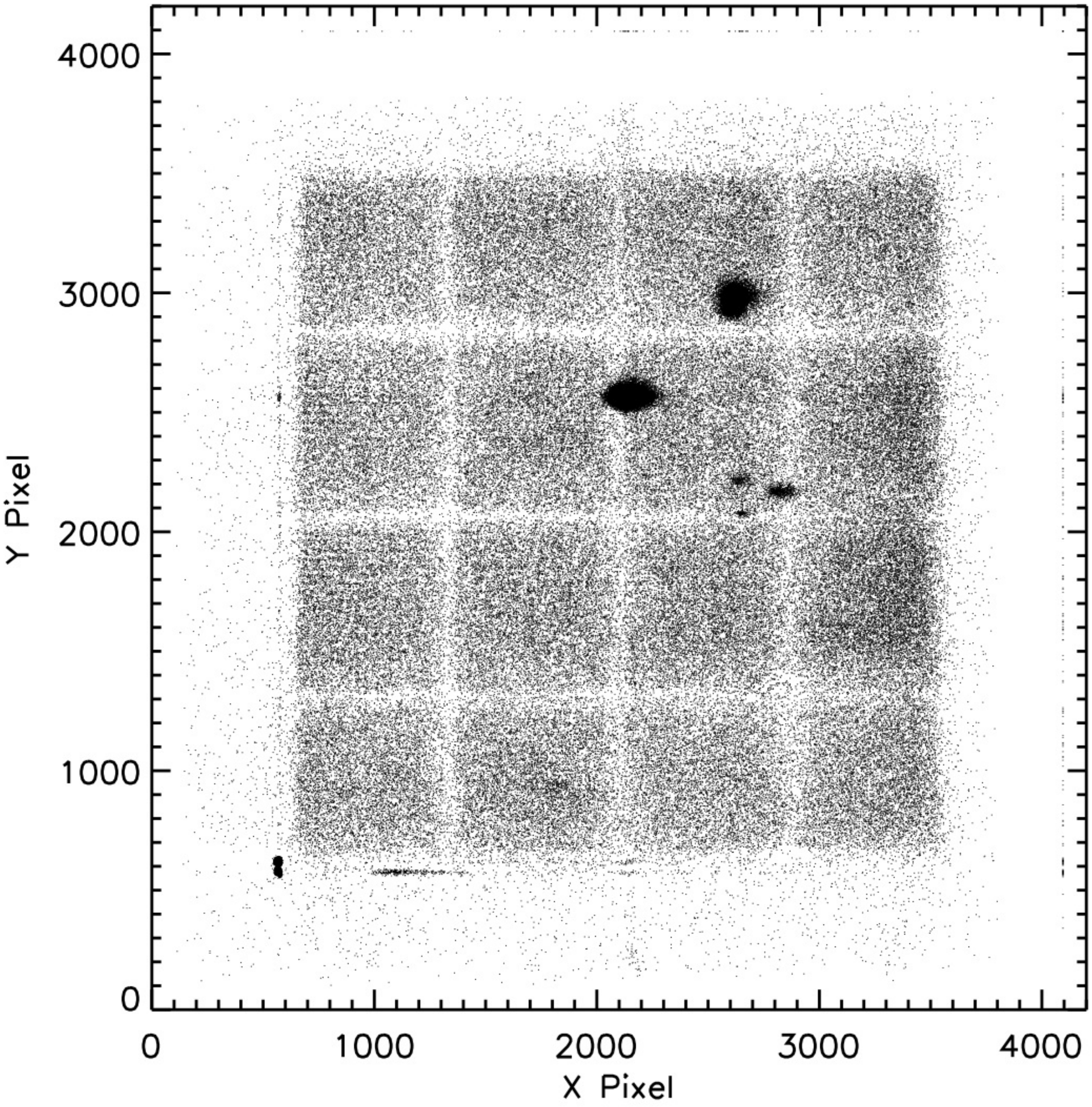

Figure 3.5 All 364 seconds of flight data from both detectors.

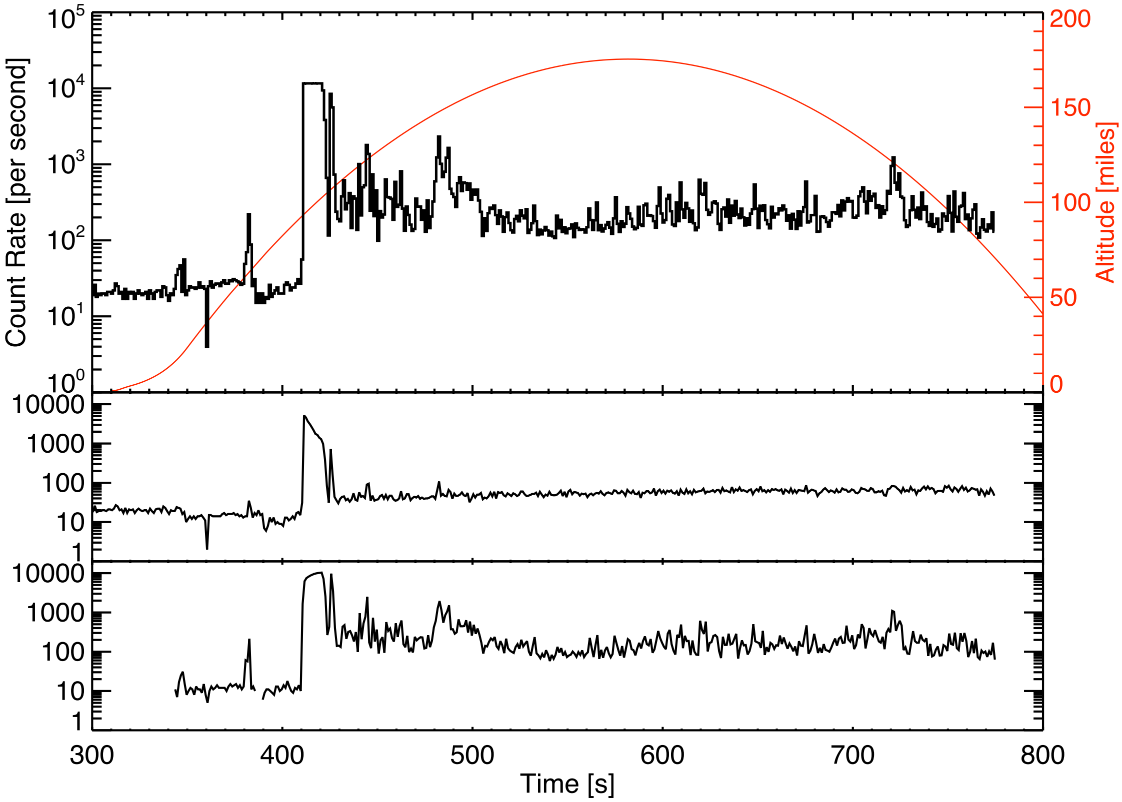

Figure 3.6 Count rate versus time and altitude. The rocket was launched at 309 seconds. The top plot shows the count rate logarithmic for both detectors combined. The red line signifies the altitude of payload. The next plots show the count rate for detector 0 and 1 respectively.

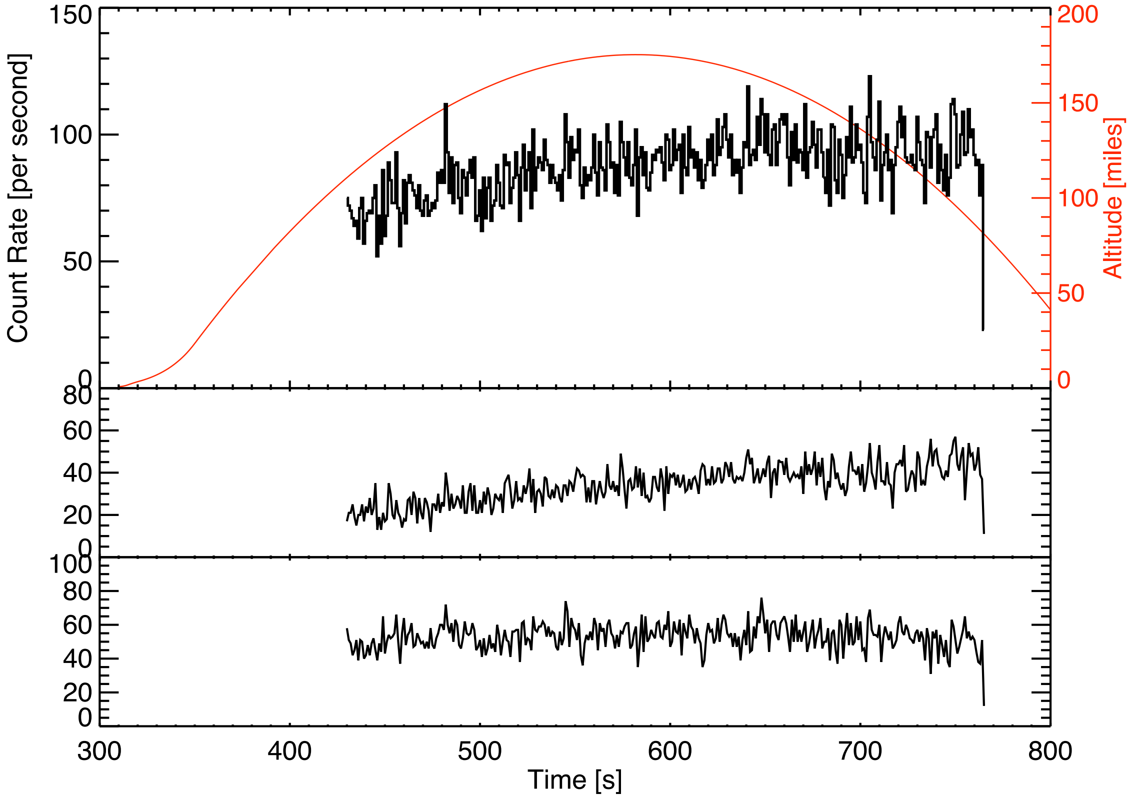

Figure 3.7 Count rate of assumed X-rays only versus time and altitude. The top plot shows the count rate (in linear scale this time) for both detectors combined. The red line signifies the altitude of payload. The next plots show the count rate for detector 0 and 1 respectively.

examining the least significant bit (LSB) of the pulse height data. This bit is set by the TDC depending upon the responsible detector. This separation is performed in Figure 3.8. There is some correlation between the two detectors, particularly in the hotspots and stim pulses. Counts being put on the wrong detector, called cross-talk, was a serious issue with the CyXESS electronics that was fixed for EXOS (see Section 2.4). Unfortunately, the stim pulse and highly energetic events (such as hotspots) are still susceptible to cross-talk. Another item of interest is that detector 0 has a significant increase in counts near the right edge. This could be due to spectral shape (more higher energy photons), some discharge localization on that side of the detector, or to a gain variation across the detector face.

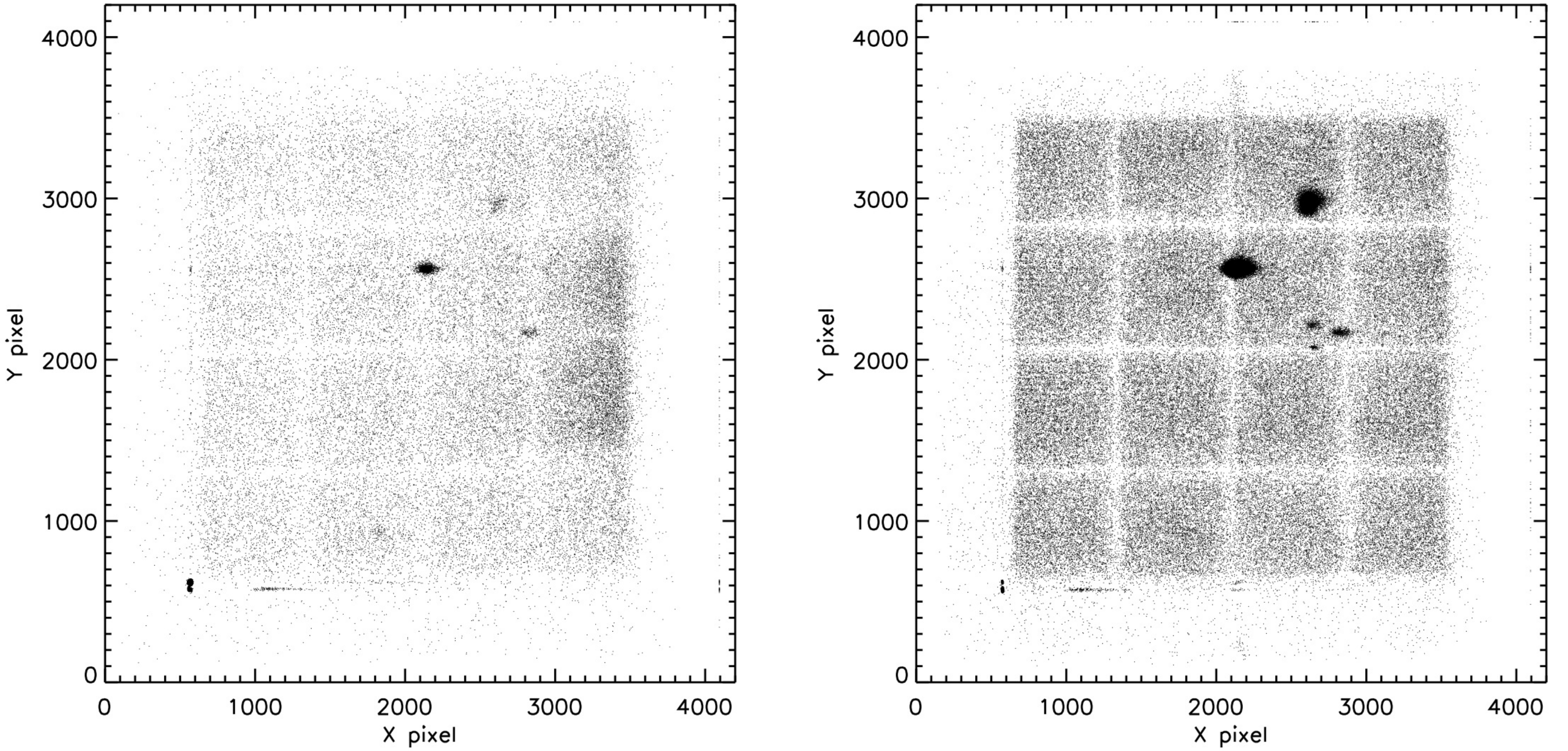

Figure 3.8 All data separated by detector. Detector 0 is on the left while detector 1 is shown on the right. Higher pulse height channels correspond to higher energy photons, though the energy resolution is poor at the chosen flight voltages.

The first issue to address is the initial discharge event lasting 14 seconds on detector 0 and 18 seconds on detector 1. Comparing this event with the rest of the observing time shows a few items of interest. Figure 3.9 shows the detectors during and after this event. Detector 0 still shows a higher concentration of counts on it's right side (higher energy photons), indicating that this shape is not due to the discharge. The post-discharge image does not show the familiar shape of the 4x4 window grid. This issue will be discussed further in Section 3.3.2. Figure 3.10 shows the difference in pulse height distributions between the discharge events and all events after this. Detector 1 shows the expected distribution. The discharge event has a higher percentage of more energetic events than post-discharge events, as expected when energetic ions are accelerated into the window (which is held at a high negative voltage). However detector 0 shows the opposite, with more discharge events showing up in low energy channels than post-discharge events. This provides further evidence that the early stages of observation had a less than optimal gain. As the observation continued, the detector gain increased, moving the expected pulse height channel for a photon of given energy up. This low initial gain may have been an unexpected advantage for this detector. The low gain reduced this detector's response to the discharge event and may have helped protect it from damage. The discharge count rate dwarfs the x-ray count rate by a factor of ~ 100. The first 20 seconds of data are dominated by the discharge and the low signal to noise makes extracting useful signal impossible. Thus this small timespan of data is removed before analysis, costing $< 5\%$ of our observation time.

During the last 10 seconds of flight the on-board vacuum gauge was remotely activated. This was done to intentionally flood the detector with counts from the ions created by the gauge. This would provide a pseduo flat field from which a gain map might be generated. The energy of the incident event is too high to directly compare to soft X-rays, but the test may have provided a rough gain map, illustrating any regions with significantly fewer counts. These data, combined with the initial discharge event, would have bookended the science data nicely. With this information at both ends of the observation a better calibrated gain map could be utilized during data analysis. This event produced the images shown in Figure 3.11. To differentiate from the initial discharge

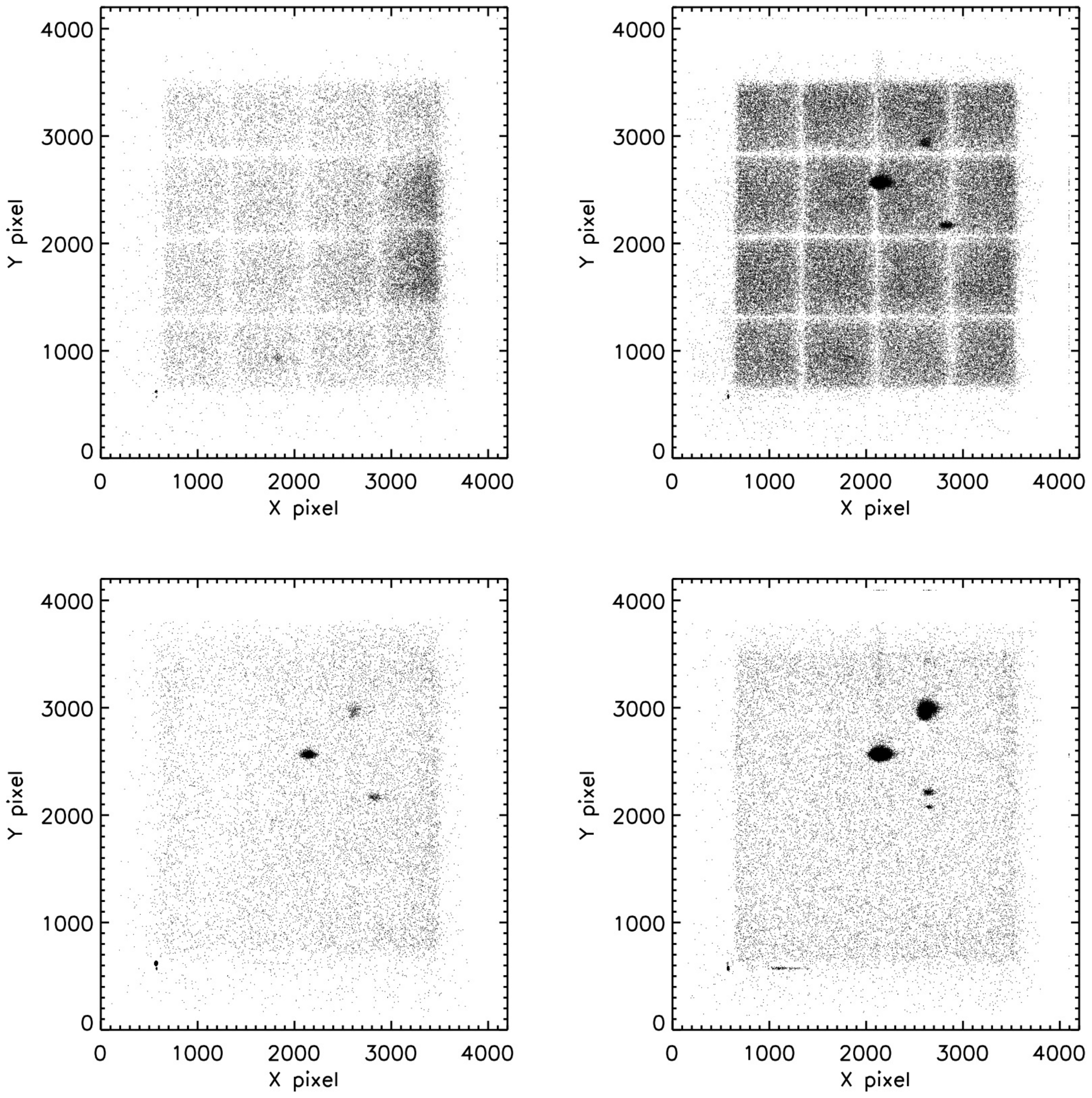

Figure 3.9 Comparison of detector data during the discharge event (first ∼ 20 seconds) on top versus the rest of flight on bottom. Detector 0 is on the left, detector 1 on the right.

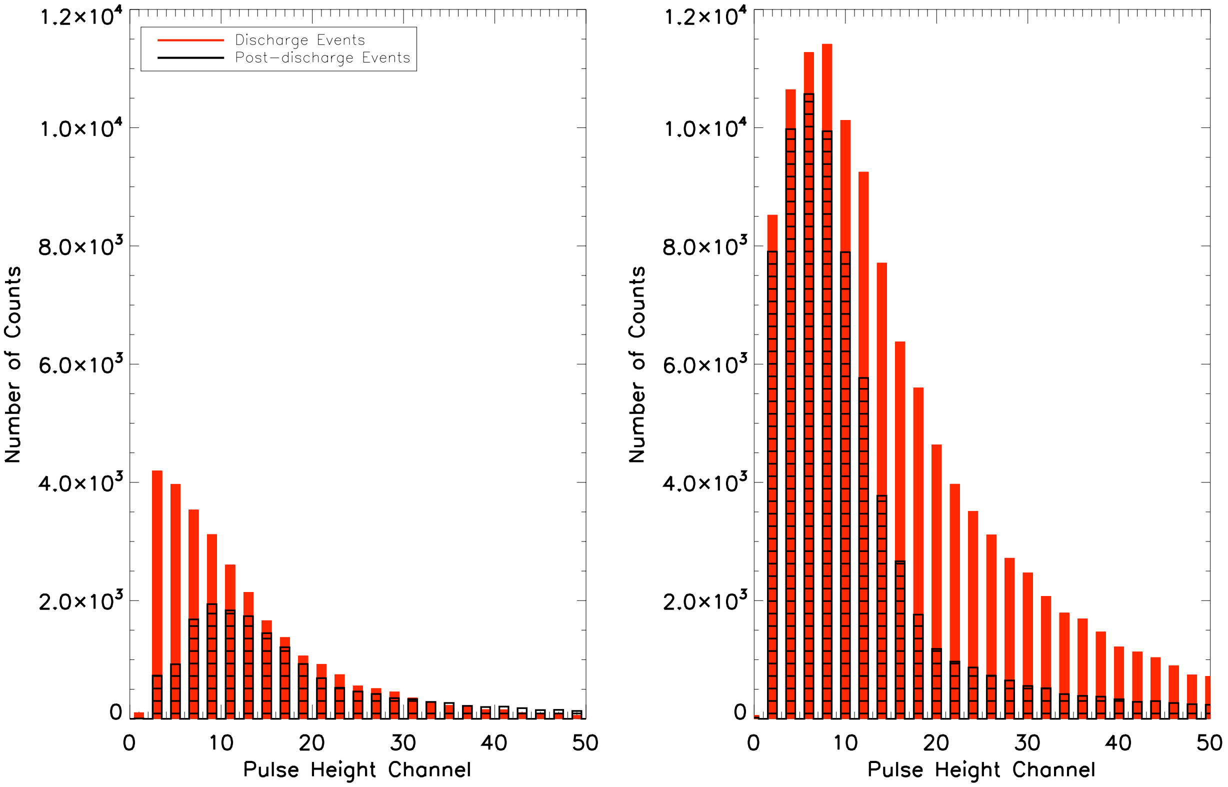

Figure 3.10 Pulse height distribution of photons during and after discharge event. Left side is Detector 0, right side detector 1. The red bars represent discharge events immediately after the detectors were turned on. The black boxed bars represent counts assumed to be X-rays.

event, this event will be referred to as the vacuum gauge event. This image does not resemble the events seen during laboratory tests with the vacuum gauge. The lab events resembled the discharge events seen in Figure 3.9. The vacuum gauge event appears to have cooperated with the brightest recurring hotspot (at a bin location of $\sim$ [2100, 2600]) in some fashion. This in combination with the invalid vacuum reading indicate that the gauge was malfunctioning during flight. These gauges have not been flown on previous suborbital flights and may not be reliable enough for use. These gauges can sometimes take time to return valid pressure readings after being turned on, and may simply require more than the 10 seconds allotted here, especially after experiencing higher than expected launch vibrations (Figure 3.3).

This vacuum gauge time period is obviously not useable without significant reduction. On first glance it appears quite possible to reduce out the cross structure and restore at least some portion of the counts. Given that we have no information about what quantity or distribution of ions the gauge is creating in its malfunctioning state we may be introducing a systematic error by including any of these counts. Because of this uncertainty, this 10 second time period is simply removed from the data set, causing a loss of only 2.7% of our observation time.

From here the next step is to remove the unwanted counts including: stim counts, mis-analyzed bits, and hotspots. Stim counts are easily removed because they appear in the bottom left corner as two small spots. At times they smear across the x or y axis, but always in a familiar pattern, and always well outside the active area of the detector.

Removing mis-analyzed bits is a complicated process. By examining times when the detector was swamped with counts, either from a discharge event (like in flight) or when the ion gauge is turned on in the lab, we can examine where the edges of the detector drop off. Figure 3.12 shows an image and two histograms (one in x and one in y) of a pseudo flat field in the lab. The drop-off is not instantaneous at the edge. At the edge of the detector several possible effects can alter the efficiency. The bulkhead cutout for the detectors is 109 mm square, while the inner window frame width is 105 mm square. The actual GEM plates have an active area of 100 mm square and the anode is 105 mm square. From light coming in at an angle, this lip caused by the bulkhead cutout

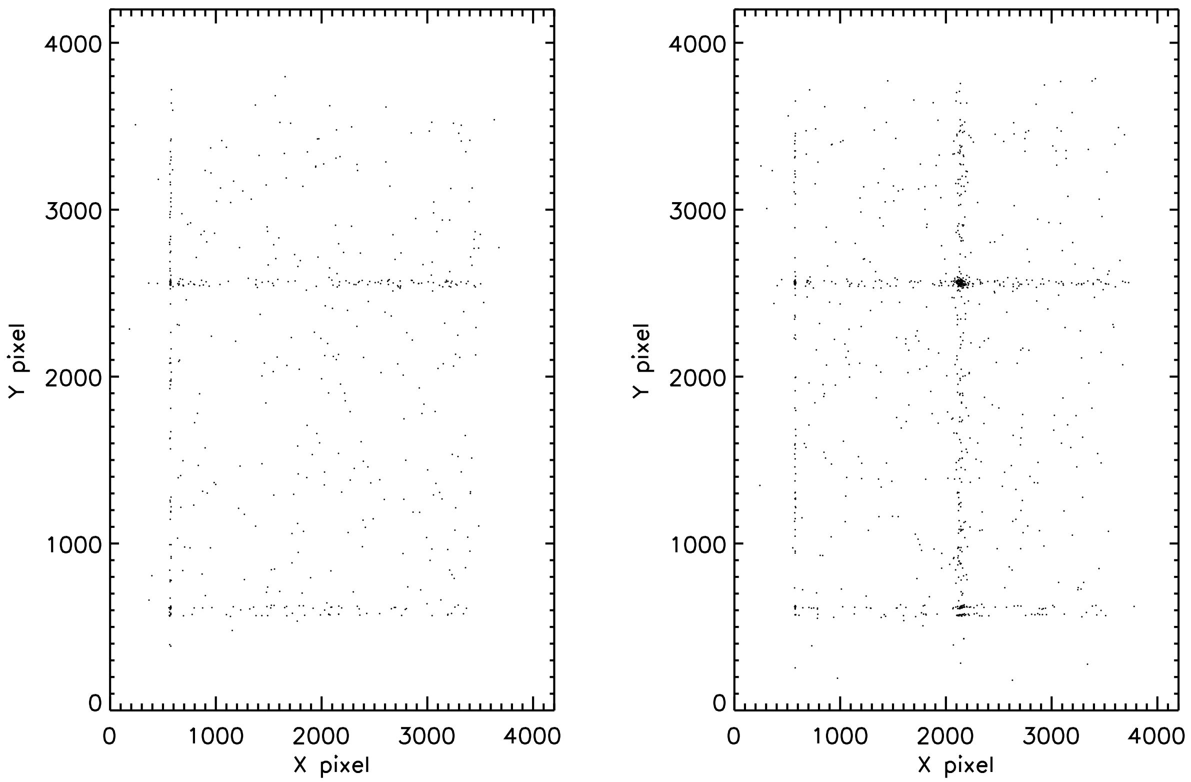

Figure 3.11 Data during the vacuum gauge event. Detector 0 on the left and detector 1 on the right. Hot spots have been observed to bloom counts vertically and horizontally before, but the vacuum gauge has never caused anything besides a large amount of randomly distributed counts.

and window could cause a shadowing effect on the detector edge. However based on the GEM size and the height of this obstruction, this shadowing only occurs for light coming in at an angles $\geq 16.6°$. The steepest angle along the x-axis coming from the gratings and hitting the very edge of the detector is only 1.7°. Thus edge shadowing is not an effect we should have to worry about.

Even without edge shadowing, there could still be edge issues. The anode is 5 mm larger than the active area of the GEM plates. The relationship between digital bins the electronics output to physical size on the anode is 28.8 bins / mm. Fitting the edge of the spectrum along the x-axis to a half-gaussian gives a HWHM of 45.2 ± 0.46 bins, corresponding to 1.6 mm. This is of similar size to the resolution of the telescope. However, one would expect the spectrum to drop off over a width similar to the resolution of the detector. In theory this could be as high as $\sim 100 - 200\mu$m (corresponding to $\sim 2.9 - 5.9$ bins). In practice this resolution is more likely ~ 0.5mm (corresponding to 14.4 bins).

However this curve will depend upon the source, as the ion gauge has a different distribution of incoming ions than the photons coming from our science target. The morphology of the target is important because the shadow cast by the cutout could depend upon which side of the gratings is dominating the illumination. Additionally any change in geometry due to the vibrations of launch (regular and anomaly) could alter the edge geometry slightly. However given the staking of detector components this is unlikely. Defining the edge along the y-axis is fairly straightforward as any deviation above or below the optimal edge will either uniformly decrease the effective area across all spectral bins or uniformly add a small amount of noise counts to every spectral bin. Defining the edge along the x-axis is more difficult as moving this edge adds or removes entire spectral bins. Removing bins will simply be a straight loss of data and may affect our fits. Adding bins will potentially permit more data and allow better fits, however the effective area of these bins is uncertain. The edge bins are set to $679 < x < 3513$ and $673 < y < 3479$.

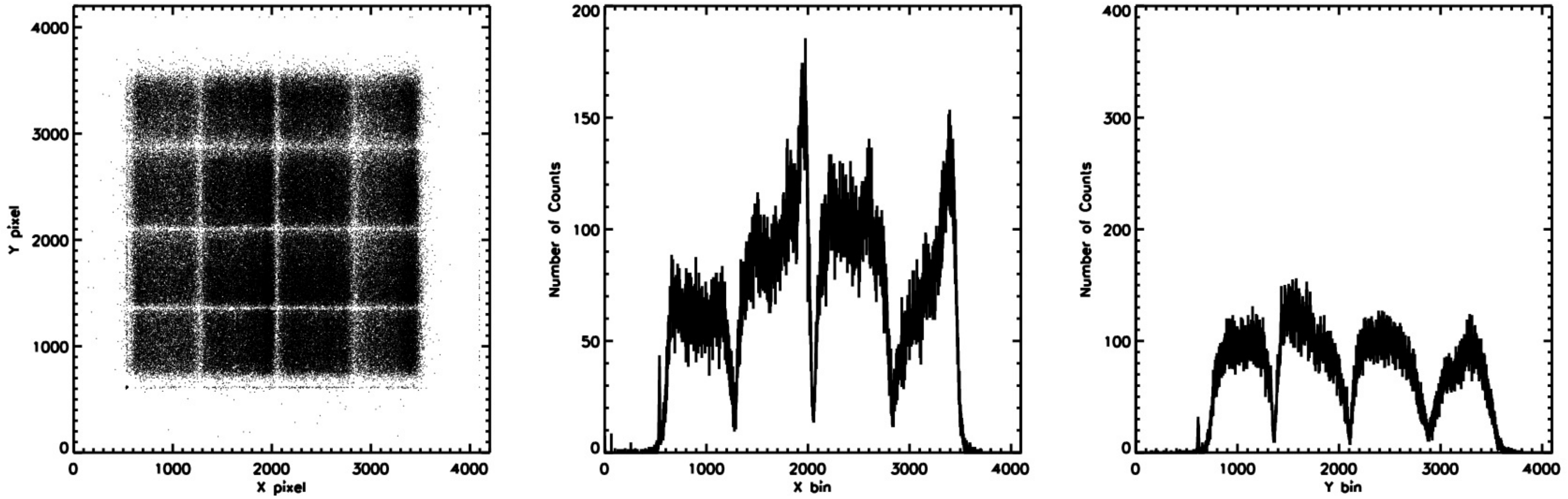

Figure 3.12 Flat field taken in the lab with the ion-gauge turned on.

Hotspots in general can be removed rather easily. The first cut at reducing these was done by removing counts clustered at these locations in several second increments. This had the benefit of preserving the utility of these pixels during non hotspot activity and maximizing our available detector area. However, the hotspots typically appeared and reappeared constantly throughout flight, making it quite difficult to discern when counts were real X-ray events, or just a leadup to the hotspot fully reappearing. Additionally, because hotspots are susceptible to cross-talk, leaving in potential counts for these pixels may risk including false counts from the opposite detector. Due to these dangers it is safer to simply remove these pixels from all of space-time and sacrifice some minor effective area. The total loss is rather minimal, affecting only a few spectral bins by a few percent each. Unfortunately, when a hotspot is strong enough, it can register counts along a straight line, typically along the cardinal directions, but rarely at 45° angles. An example of this is shown in Figure 3.13. The most abusive of this "blooming" effect occurs in the first few seconds after high voltage turn on. These few seconds are simply reduced out of the data. However for the next 80 seconds the main hotspot erratically blooms only in the direction above it. These counts can be removed either on an individual basis, or by defining this bloom region and removing any count within it during this 80 seconds. Due to the erratic nature and relatively low count rate of this bloom, it would be difficult to remove properly without introducing bias into the reduction process. Therefore we again go with the more conservative approach and simply remove this bloom region and adjust the effective area curve appropriately. The final reduction is shown in Figures 3.14 .

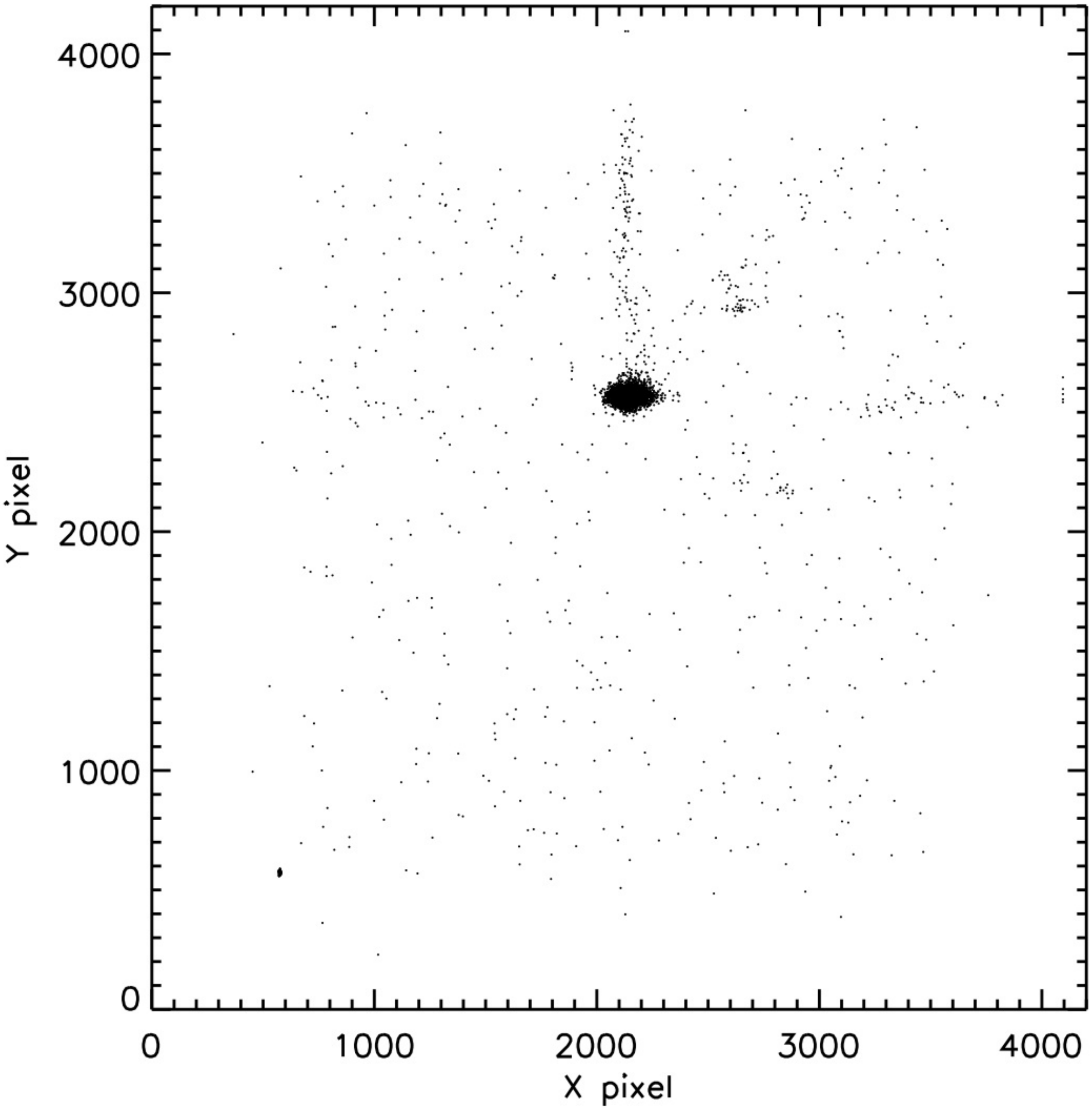

Figure 3.13 An example of hotspot blooming. The blooming straight up and down is the most common, followed by straight left and right. The blooming rarely occurs at 45° angles as it does in this image.

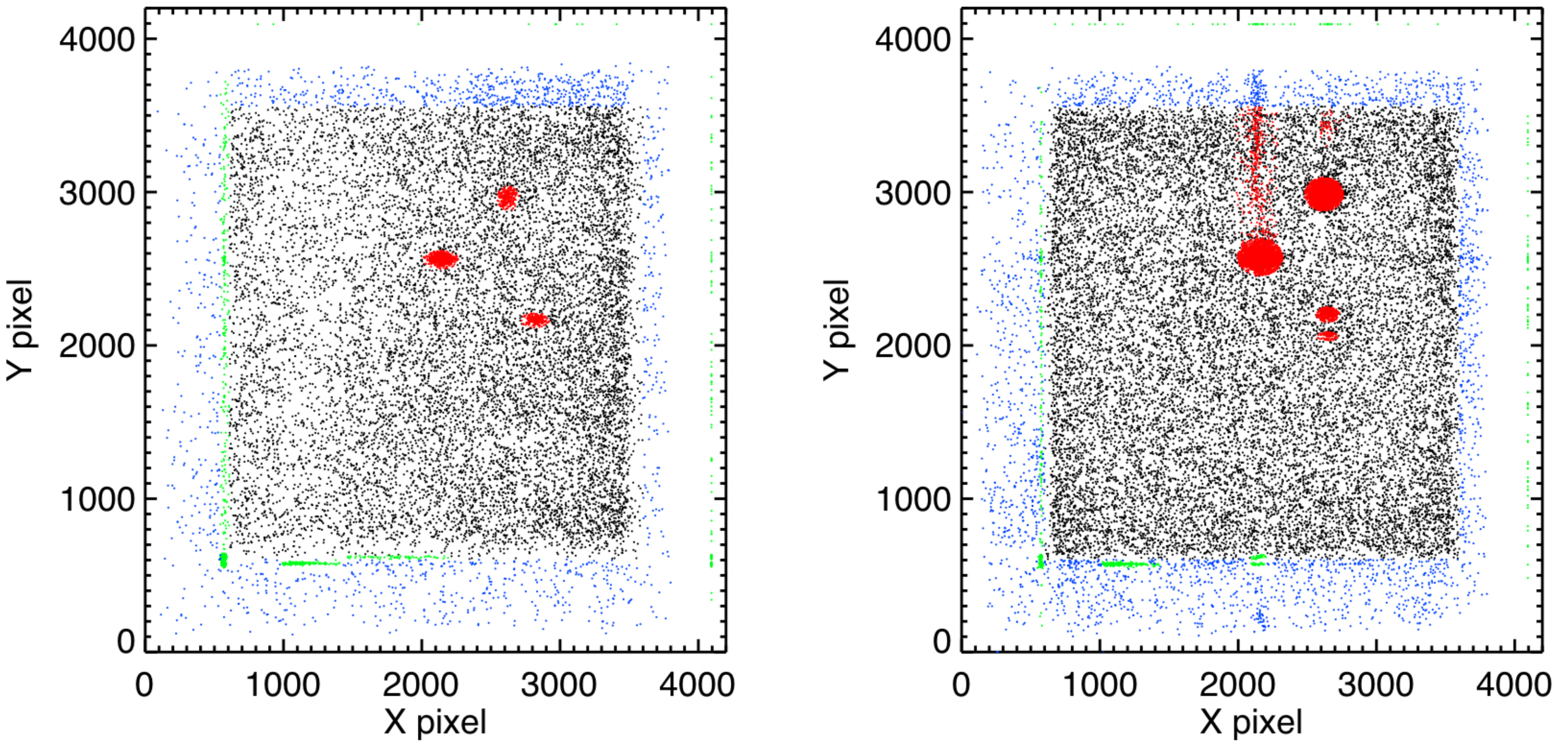

Figure 3.14 Data with stim pulse, hotspots and mis-analyzed bits categorized. The green counts correspond to stim counts, the red counts to hotspots (and their blooms) and the blue to mis-analyzed bits. Some of the blue counts are actually stim counts that have spread along the x/y-axis or hotspot related counts, but are far enough away from the active area that differentiating is unnecessary.

Another aspect of the data to consider is the pulse height distribution. In an optimally operating detector actual X-ray counts should have a more energetic charge cloud and be registered as higher pulse height events than stim counts, dark counts, etc. Additionally counts at the higher end of the spectrum are ~ 5 times more energetic, and should obtain higher pulse height bins due to the larger electron cascade caused by more free electrons created in the drift region of the detector. However due to a detector failure during pre-flight calibrations, the operating voltage of the detectors was decreased by ~ 100 volts. If the detectors are run at too high a voltage for too long it is possible to permanently damage them (Section 2.5.3). Too much damage results in a connectivity between the top and bottom of a GEM plate. When this happens, no gain occurs within the pores of this plate, and the detector gain drops below what is necessary to observe soft X-rays. By lowering the operating voltage, we decreased the odds of this occurring in flight. Our lower flight voltage was still capable of registering soft X-rays, but it did collapse the range of typical pulse heights of an incident X-ray. Thus the pulse height of any particular count becomes significantly less meaningful. The distribution of pulse heights as a function of bin is shown in Figure 3.15. Detector 1 shows a relatively even distribution across the detector face. High pulse height events are just as likely at low wavelengths as high wavelengths. Detector 0 however shows more interesting behavior. Here the low wavelength end of the spectrum has a much higher percentage of high pulse height counts, as one would expect. It is likely that this detector had a high enough voltage (and therefore gain) to distinguish between 1/2 keV and 1/4 keV photons, whereas detector 1 does not. However this seems to contradict the fact that detector 1 has more counts, and detector 0 experiences a gain variation during flight (Section 3.3.1). Interestingly, this uneven distribution of high pulse height events is somewhat persistent in time. By examining only the later portion of flight (after the gain variation has equilibrated with what we see in detector 1) the low energy events are roughly evenly distributed while the high energy events are more frequently found at the low wavelength end of the spectrum (Figure 3.16). However, this unevenness is diminished and it is not perfectly clear whether the gain has completely peaked.

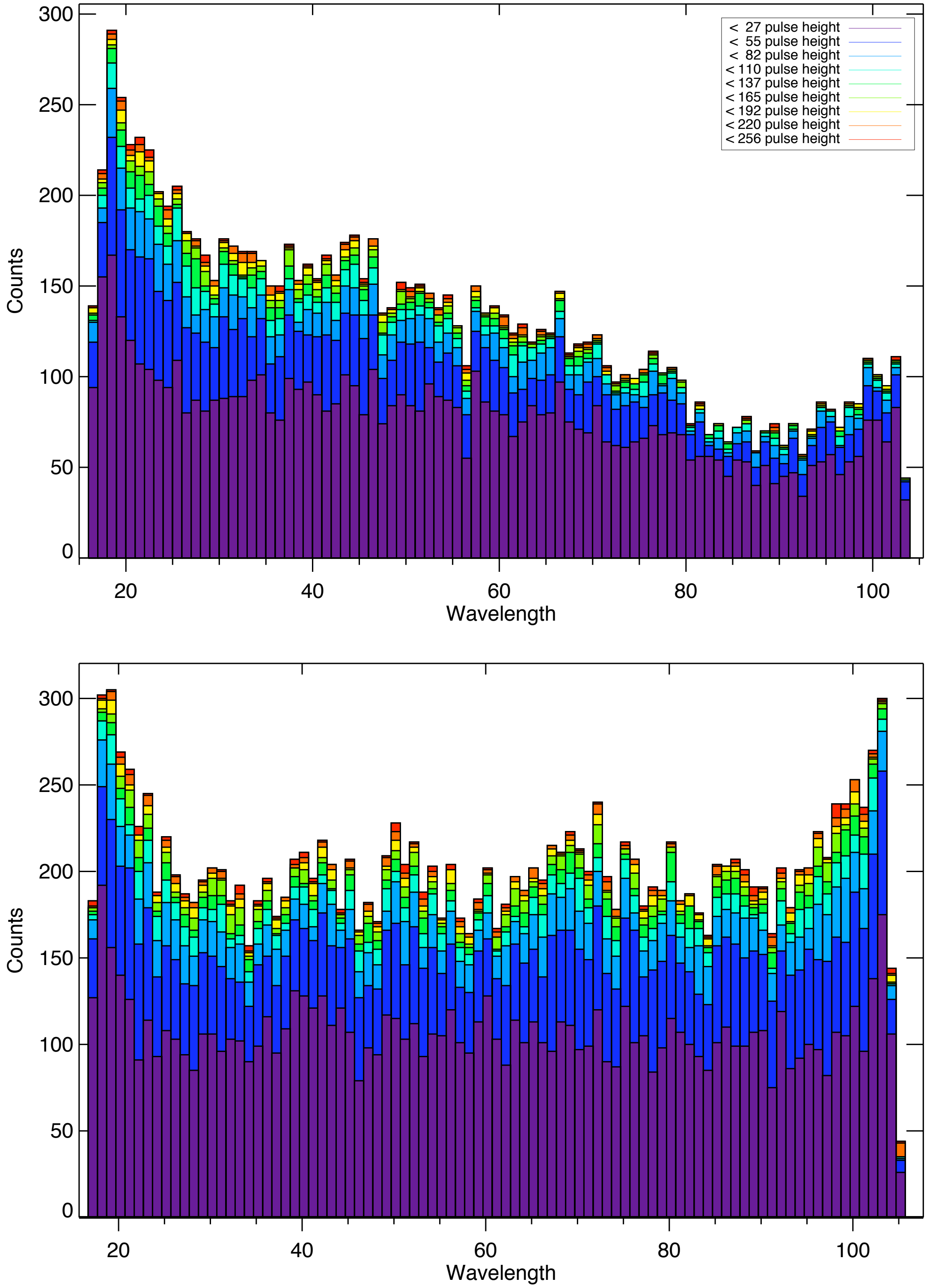

Figure 3.15 Flight spectra with energy distribution. Each bin is color coded to show the fraction of counts in a given energy range. Each color corresponds to 10% of the pulse heigh channels (of which there are 256). Purple represents the lowest channels and red the highest. Detector 0 is on top, detector 1 on bottom.

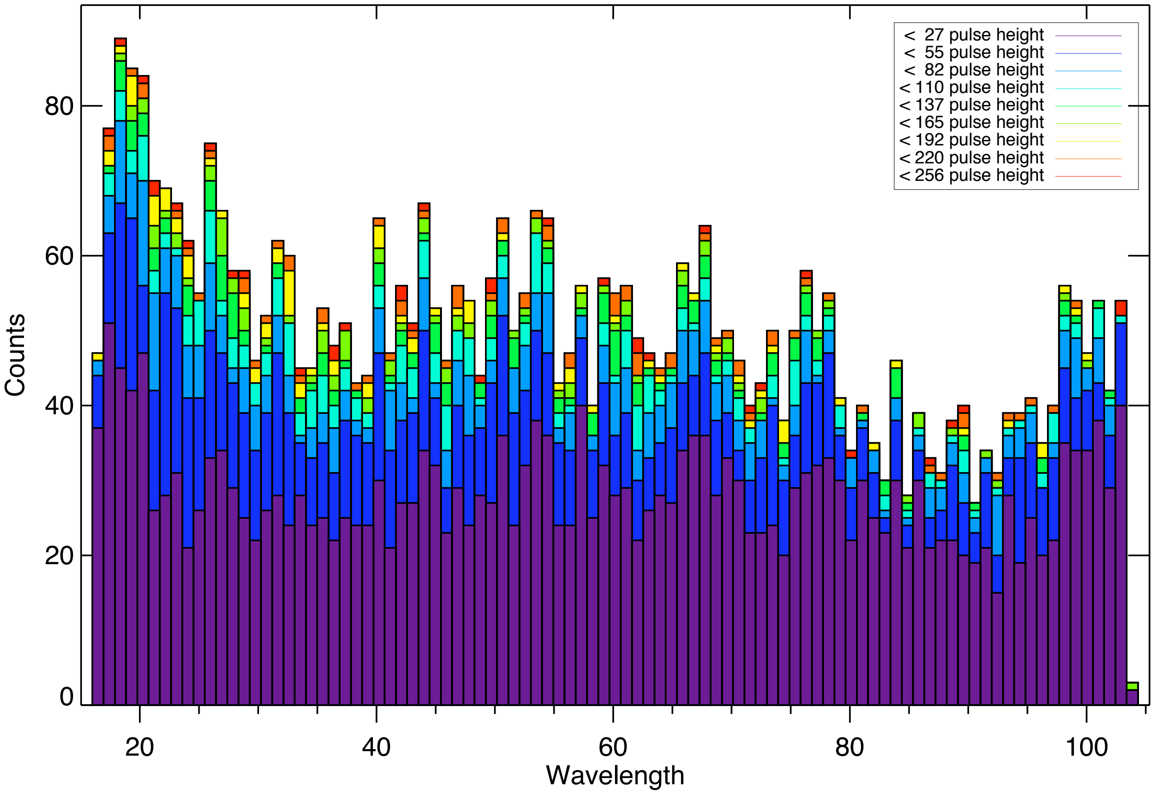

Figure 3.16 Flight spectrum from detector 0 from the last third of the flight with energy distribution. Same color coding as the previous figure. The differentiation seen in the previous figure (for detector 0) is noticeable to a lesser degree. It is unclear whether an additional few minutes of warm up time would even the distribution, or whether this unevenness is due to the energy sensitivity of the detector.

3.2 Wavelength Calibration

The next step is to implement our wavelength calibration. Unfortunately, the pre-flight calibration (Section 2.5.4) is likely no longer accurate for two reasons. Firstly, the collimator structure is bumpered to the interior of the rocket skin with eight pieces of delrin. In the field at WSMR (after the calibration data were taken at Colorado), the bumpers were adjusted, likely moving the collimator and the resulting spectrum by a minute amount. Secondly, the vibration anomaly discussed above would have almost certainly modified the collimator position. For future flights we hope to have an onboard calibration source, but that was not available for this flight. Unfortunately, due to high winds on launch night, the EXOS landing was not a gentle one. The impact was so hard that during landing the collimator was damaged and two bumpers ripped off of the top of the collimator. This effectively destroyed any information that post-flight calibrations would provide. Due to the hard landing we have to rely solely on pre-flight and flight data for our calibration. Fortunately we do have one means of using flight data as a calibrator. If the collimator shifts in one direction then the bandpass shift for one detector is equaled by the inverse shift in bandpass for the other detector (assuming that structural warping is small compared to translational shifts). Since the linear dispersion of the system is well measured (and agrees well with the theory and raytrace outlined in Section 2.5.4) we can compare the position of spectral lines in the two spectra to each other. If the two lines are identical in bin-space then our raytrace defines the bandpass exactly. Otherwise we can use the observed shift, the known dispersion and pre-flight calibration data to define the bandpass shift.

Figures 3.17-3.18 shows the two spectra. The most obvious spectral lines to correlate are the two lines at high energies in both spectra. Running a cross correlation function using only the high end of the spectra (bins > 3000) will reveal how much one spectrum should be shifted in order to maximize the correlation of these lines. The highest correlation is obtained by shifting detector 1 by forty bins. This corresponds to 1.6 Å towards longer wavelengths. Comparing this shift to the original detector offset shows that the bumper adjustment and flight forces caused a 2.24 Å shift of the spectrum or 154 arcsec change in pointing when compared to pre-flight calibration data. This is significantly larger than the 41″ change noted in post-flight calibrations of CyXESS. However that shift was due solely to bumper adjustment as the flight did not experience a vibration anomaly. This wavelength calibration is applied to the top y-axis in Figures 3.17 and 3.18.

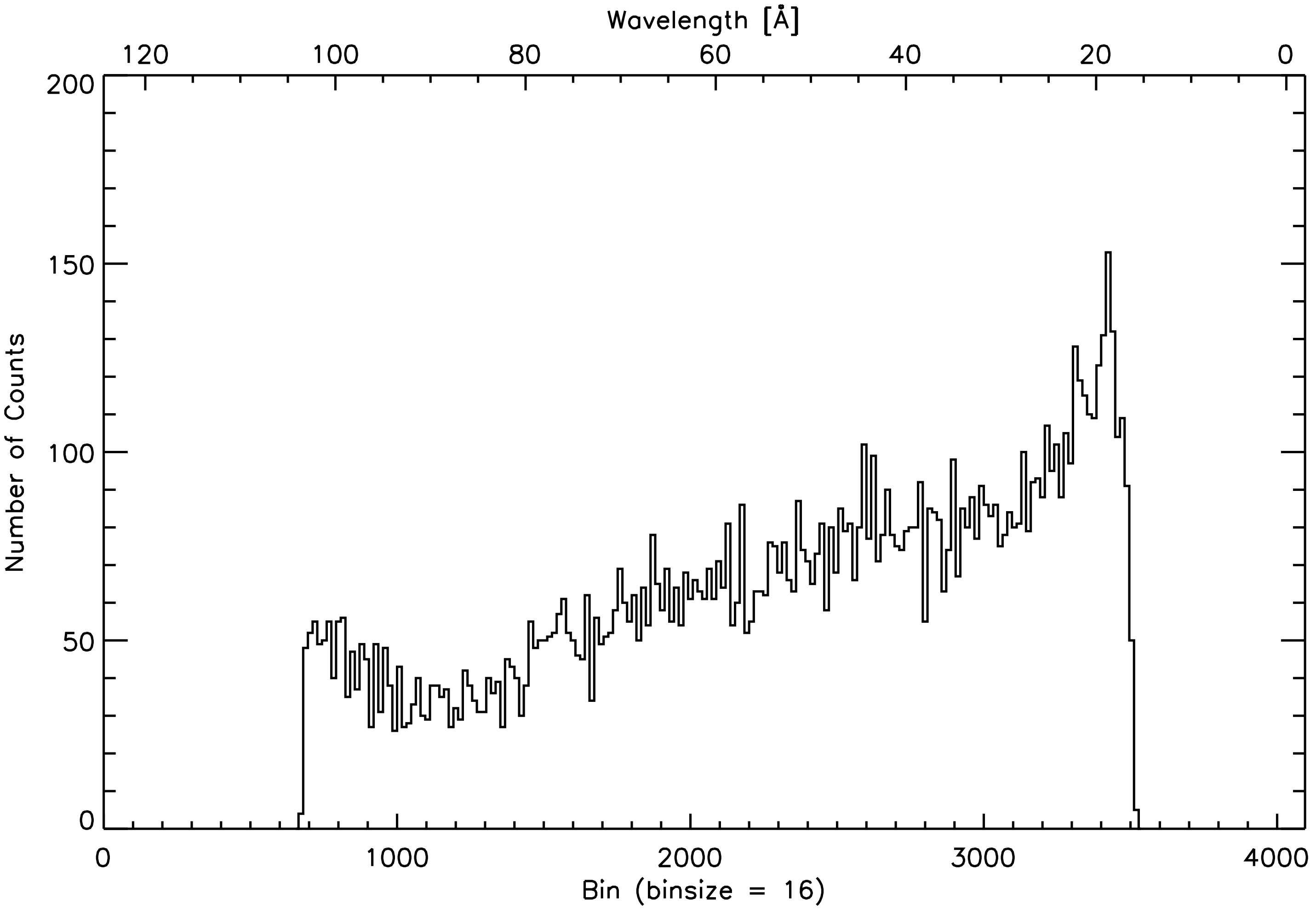

Figure 3.17 Detector 0 data with wavelength calibration.

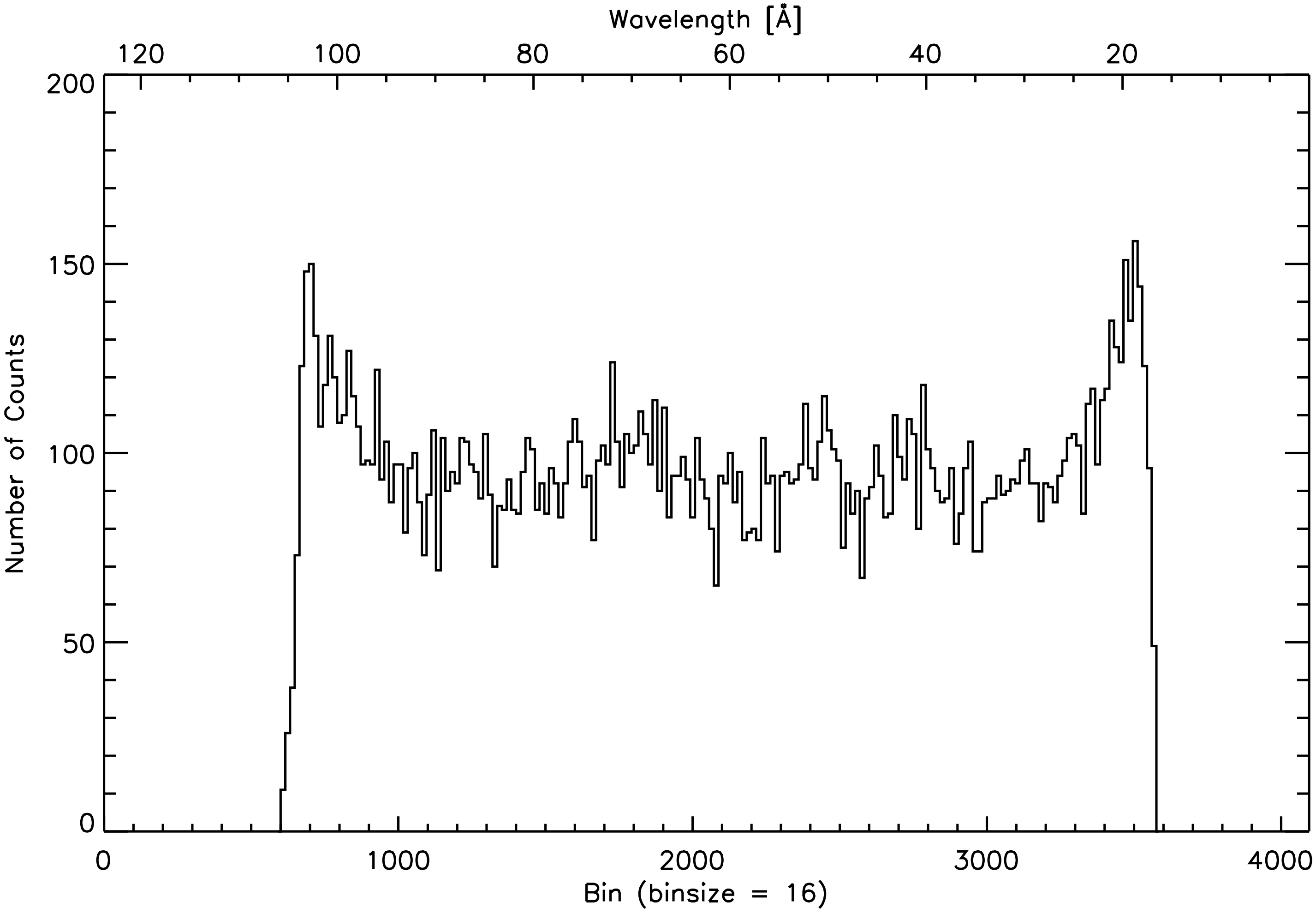

Figure 3.18 Detector 1 data with wavelength calibration.

Checking the post-flight collimator effectiveness revealed that one module still focuses optical light reasonable well, while the other appears to have lost some effectiveness. This likely occurred during landing, as the crash bumper was torn from the shutter door and completely flattened in addition to a dent in the rocket skin. This event likely knocked the bumpers off the collimator and damaged the structure, causing loss of collimation. However there is no way to prove that some of this damage wasn't due to the vibration anomaly. The large shift in wavelength calibration may have been caused by the bumper movement during launch. This seems less likely, but does nicely explain why the shift was greater than seen on the CyXESS flight. Regardless we will assume a large systematic uncertainty in our wavelength calibration.

3.3 Effective Area Calibration

The initial pre-flight effective area calculation was described in Section 2.5.4. In this section further modifications are performed based upon flight results. The primary modifications are to compensate for detector 0's gain variation, for the diminished collecting area at the detector edges and for hotspots.

3.3.1 Gain Variation

Both the spatial (Figure 3.8) and pulse height (Figure 3.10) data provide strong evidence that detector 0 experienced an uneven gain distribution during flight. Further evidence can be found by more closely examining the spectra. Figure 3.19 shows the spectral evolution as a function of time. The spectrum is broken down into five equal time blocks of 68 seconds each. All of the blocks are after the initial discharge event, prior to the vacuum gauge event and have hotspots, stim and mis-analyzed bits removed. The initial time block shows a fairly steep spectrum with almost no counts in the lower bins. The lower bins equate to lower energy photons assuming the first diffracted order. By the final time block, the spectrum is approximately flat. Interestingly, the high numbered bins (corresponding to high energy photons) are not affected. Two possibilities can explain this: the gain was depressed over the whole detector, but the high energy photons were sufficiently energetic to create enough electrons to register a count, or that side of the detector was already at full gain. The second possibility is observed frequently in the lab as different sections of the detector ramp up to full gain at different voltages. Additionally this steep spectral slope is evident during the initial discharge event. As these ions are typically of very high energies and likely uniformly distributed over the detector, this implies a spatial distribution of gain rather than a flat but rising gain.

The best fit linear model for detector 1 has a slope of 0.0033 ± 0.004. The best fit linear model for detector 0 during the last time block has a slope of 0.0070 ± 0.008. These two fits are equivalent within their respective uncertainties. The final slope of detector 0 will therefore be used as a baseline efficiency. By interpolating the linear fit as a function of time, the efficiency of the detector as compared to the baseline efficiency can be calculated. Integrating this efficiency over the full flight time gives a modification term for each bin:

$$\epsilon_{gain}(x) = \frac{1}{n_t} \sum_{t=0}^{t_o} \frac{x(t)}{x(t_o)} \tag{3.1}$$

where x is the value of the linear fit at a given time t, t_o is the final time block (i.e. the baseline efficiency) and n_t is the number of time blocks. As our detector accepts multiple orders of diffraction, the efficiency curve will be the sum of the effect on each order. This assumes the efficiency is independent to the photon energy which seems plausible based upon the initial discharge event (of high energy ions) having a similar gain curve. Thus the efficiency modification term is:

$$\epsilon_{gain}(\lambda) = \frac{1}{n_t} \sum_{t=0}^{t_o} \sum_{n=1}^{3} \frac{x(\lambda, n, t)}{x(\lambda, n, t_o)} \tag{3.2}$$

This term will be multiplied by the existing efficiency curve (based upon gratings and window efficiencies).

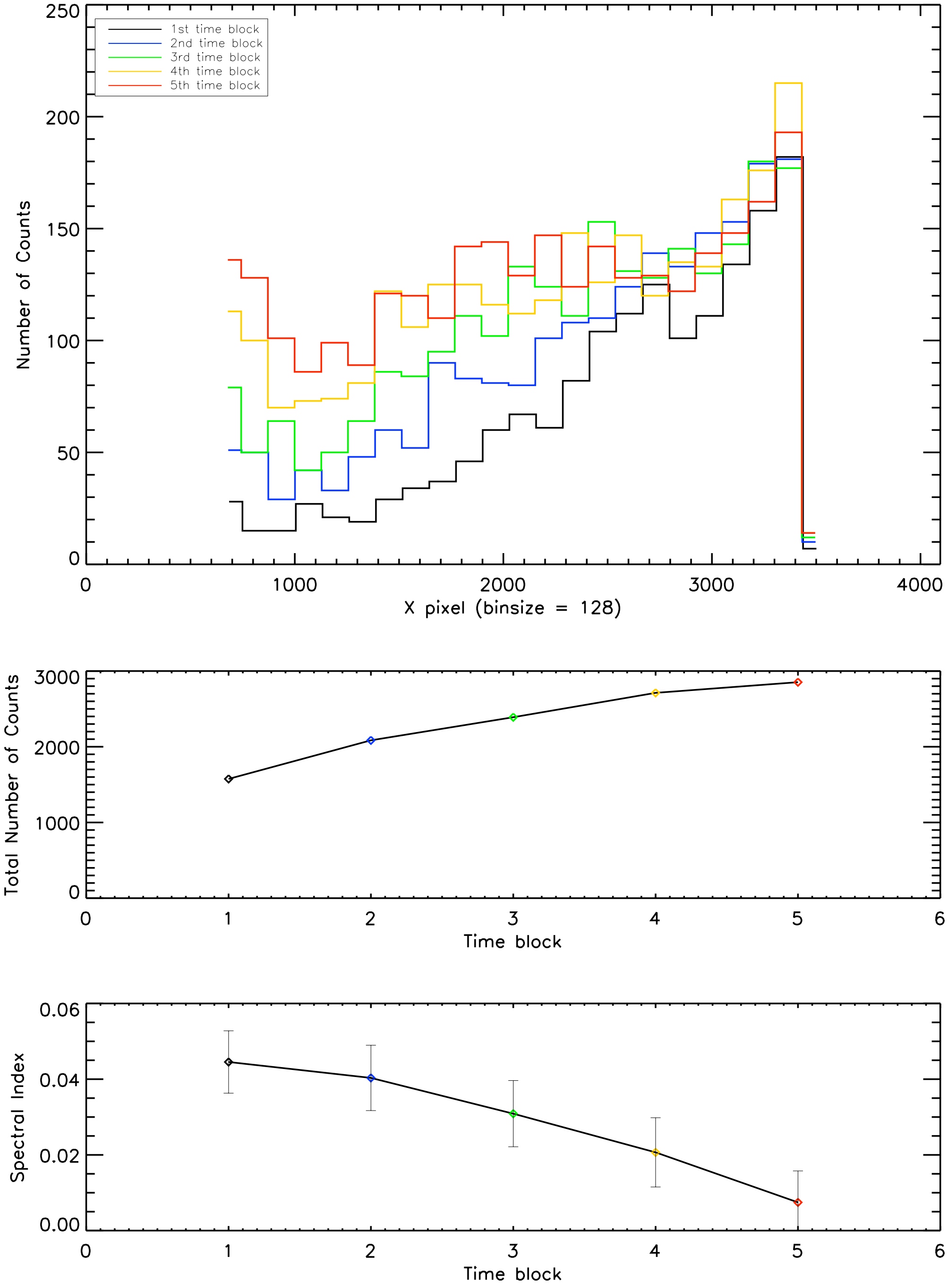

Figure 3.19 Gain variations over detector 0. **Top** - Spectrum from detector 0 spliced into 5 equal time blocks of 68 seconds. The low bin numbers slowly increase in count rate until they are approximately equal the high energy bins by the end of flight. **Middle** - Counts per time block as the flight progresses. **Bottom** - Spectral index (assuming a linear fit of the entire spectrum) as a function of time block.

3.3.2 Window Bar Anomaly

As described in Section 2.4, the GEM windows have an aluminum 4x4 support grid on the payload facing side. As expected this grid casts a shadow on observations (see Figures 2.33 and 3.5 for examples). This shadow is visible in all lab calibration data regardless of whether the source was the X-ray electron impact source, an ion discharge event or a radioactive source. This shadow is also visible during the discharge event of flight (Figure 3.9). Thus it is puzzling that the window grid is not visible after the discharge event in flight. There are several possible explanations for this:

(1) Our count rates in flight (post-discharge) are substantially lower than in the lab (by a factor of ≥ 10). Given that background counts, misanalyzed bits and hotspots can appear in the shadow it's possible that the shadow will be difficult to observe statistically given our reduced count rates.

(2) If our detector electronics or payload telemetry lost resolution during flight then the neighboring counts could be spread into the shadow. Electronic noise can also lead to flipping digital bits, thus changing either the positional information or pulse height information of counts.

(3) If the lab calibrated background rate is not sufficient to hide the shadows, then a flight induced higher background rate might fill in the shadow with counts.

(4) If the expected shadowed bins are significantly different between detectors, it is possible that cross-talk between the detectors has occurred and eliminated the shadows.

(5) The geometry of the incoming beam is different between flight, calibration tests and discharge events. Calibration tests involve a point source that has some allowed movement, but is still not a true extended source. A discharge event typically happens directly in front of the window and is likely pointed directly toward the window with minimal angling.

An extended source likely sends X-rays with a wider range of incident angles, and could possibly spread the grid shadow out to where it is less noticeable.

The detector background level in the lab followed a Poisson distribution with a mean between 0.5 - 2 counts/s/detector that varied slightly between each turn on (likely caused by slight modifications to the high voltage and gas pressure settings). The window bars are 1.5 mm in width, corresponding to 48 bins (note that this corresponds to 6 bins on Figure 2.33). This corresponds to 1.4 Å which is of similar scale to the theoretical resolution of the optics. By examining the histogram of counts with a binsize of 16 (0.5 Å) we should see some reduction in counts over the shadowed bins. Figures 3.20 and 3.21 show where these bars should be located. Also plotted is the same histogram with a binsize of order the best theoretical detector resolution ($\sim 100 - 200\mu\text{m}$) possible, as well as a histogram without binning (binsize of one). None of these plots, nor the image itself shows evidence of shadows more significant than the typical variations shown throughout the spectra.

The background levels measured in the lab (0.5 - 2.0 counts/s average) are less than the $\sqrt{N}$ Poisson noise of a typical bin (~ 10) and are not capable of hiding a window bar. Thus the first possible explanation in our list of the missing window bars is not valid. In order to investigate this issue we produce a binary map of the detector face (Figure 3.22) showing the transmission along one axis. Also shown is the histogram from the flight discharge event showing the window shadow centroid and FWHM. This figure is what we expect in the high count regime (i.e. in the lab). Given a detector with no background counts and perfect resolution, this binary map would be the representative flat field with a scaled count rate and Poisson noise in each bin. Given perfect electronics, the detector resolution would be defined by the spacing between pores on the GEM plates (140μm). Sensor Science reported obtaining resolutions between 0.5 - 1.0 mm at their facility. During system calibration the CyXESS payload was found to have typical FWHM of spectral lines typically ~ 2 mm. This is consistent to the values found with the EXOS payload. The degradation from the raytrace predicted 1.7 mm FWHM was assumed to be to imperfect co-alignment of 24

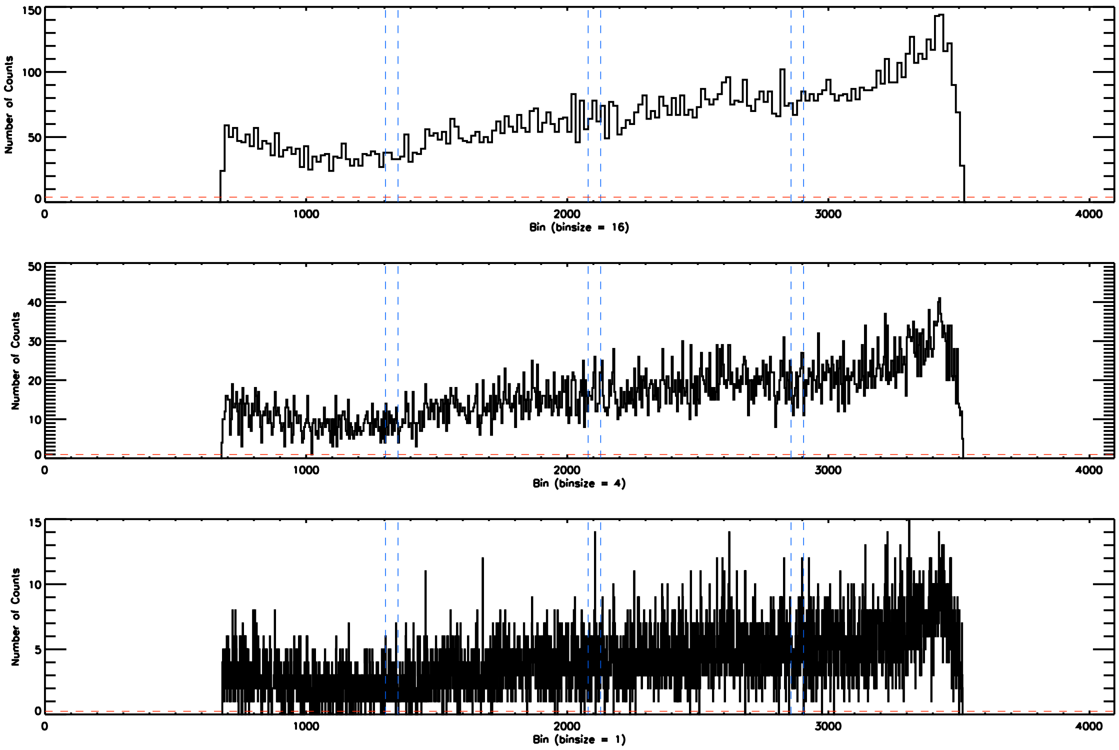

Figure 3.20 Detector 0 histogram along the x axis with blue lines showing the location of the window grid and red lines showing the expected background rate based on laboratory tests.

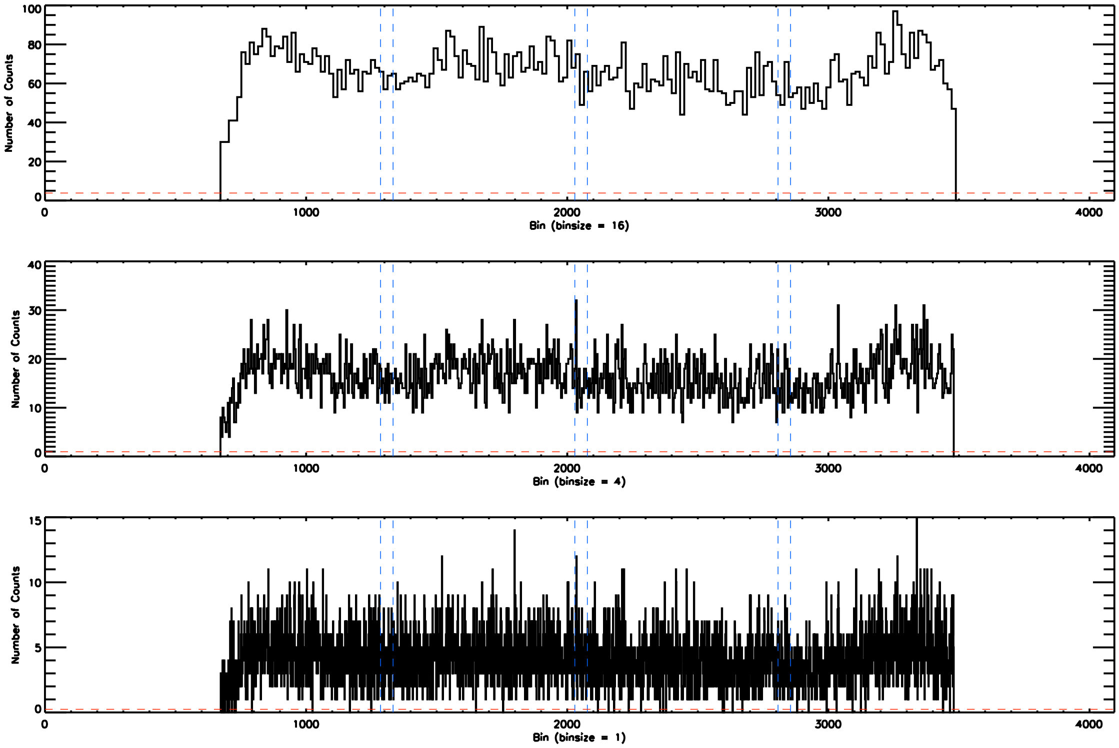

Figure 3.21 Detector 0 histogram along the y axis with blue lines showing the location of the window grid and red lines showing the expected background rate rate based on laboratory tests.

collimator plates or 67 gratings per module. However, it is possible that the detector electronics lost precision in the conversion between time delays and digital positions. A subset of the GEM amplifiers have been shown to introduce waviness in the detector images due to cross-talk between the two channels on each amp. The amps are also prone to noise on the positional channels if any physical change (including loosening of the amplifier box lid or even a $.005''$ thin conformal coating on the boards) is made near the actual amplifier chips. This danger was mitigated by staking and shielding the chips, but it is possible that the vibration anomaly (Figure 3.3) shifted the shielding and led to noise that was seen in the lab before the shielding was added. Loss of precision due to electronic timing issues is thus a likely culprit. The counter argument is that the stim locations are identical to lab measurements, and the window bars are observable during the discharge event. These two observations imply a properly functioning electronics system.

Before examining the low count rate regime of our flight data, we first attempt to utilize the better statistics of data from the high count rate regime to determine the best-fit parameters. We run a χ^2 minimization routine between the convolution of this binary map and a gaussian representing the detector resolution and the flight data. This routine has the following parameters: count rate between window bars, detector resolution, dark count rate, misanalyzed bits count rate, left and right edge locations. Misanalyzed bits are allowed to extend outside the active area of the GEM detectors while dark counts are restricted to this 100mm x 100mm region. The spatial distribution of misanalyzed bits is difficult to determine as they are typically negligible ($\sim 1-2\%$ of total counts) and thus their presence is only noticeable outside the effective area of the GEMs. By examining this edge region we can calculate the rate of misanalyzed counts and determine the magnitude of their effect on the data. Dark counts manifest themselves by artificially raising the level of each bin. Once the dark rate is comparable to the X-ray count rate, this could have the effect of hiding the window bars.

The best fit result is shown in Figure 3.23 and the parameters shown in Table 3.1. The dark rate here is highly uncertain as its contribution over < 20 seconds is minimal. The overall $\chi^2_\nu = 1.48$ and 2.10. This is not a particularly great fit for a few reasons. Some of the bins are very low in

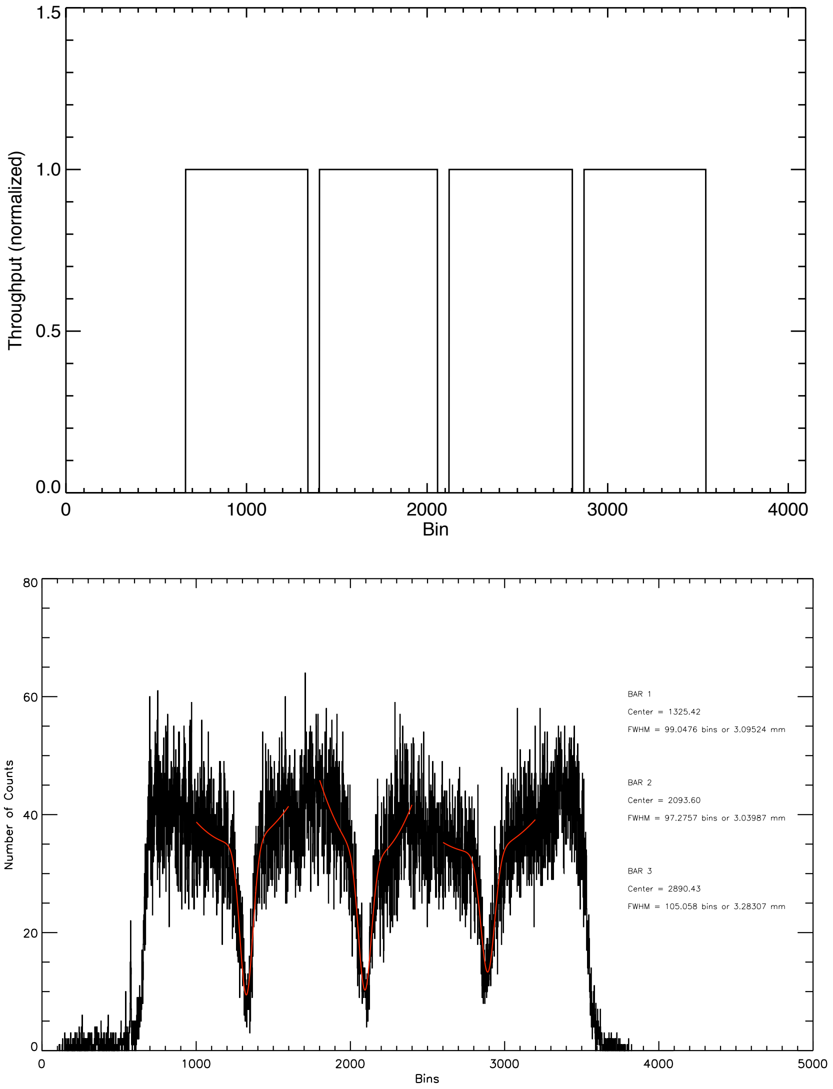

Figure 3.22 **Top** - Transmission due to the machined aluminum frame that supports the window. The transmission outside the window bars has been normalized to 1, while the aluminum supports are justifiably assumed to be perfectly opaque. **Bottom** - Gaussian fits to the discharge event during flight.

counts and thus the gaussian statistics used in the χ^2 calculation are not strictly correct for these bins. Additionally this fit completely ignores any gain variations seen across the detector face.

The next step is to test this model in the low count regime (i.e. the actual flight data of interest). We examine detector 1 flight data as it shows more promising hints of window bars than detector 0 data. Unfortunately these hints of a shadow are no greater than the typical variations seen in other parts of the spectrum. The count rate is too low to use gaussian statistics here without binning. By using a binsize of 4 however, we achieve similar counts in a bin as in Figure 3.23. As four bins is significantly smaller than the detector resolution this should not effect the shape of the result in any fashion. To fit these data we freeze the edge boundaries, FWHM and dark rate at the best-fit values determined above, while allowing the continuum level and misanalyzed bit rate to vary. The result is shown in Figure 3.24 for both axis. This fit is significantly worse and is no longer of acceptable quality. This fit only achieves reduced chi squared values of 2.18 and 2.63 along the x and y axis respectively. Some of the poor fit is due to the edges and misanalyzed bits, but the window locations are obviously not appropriately fit, particularly along the y-axis.

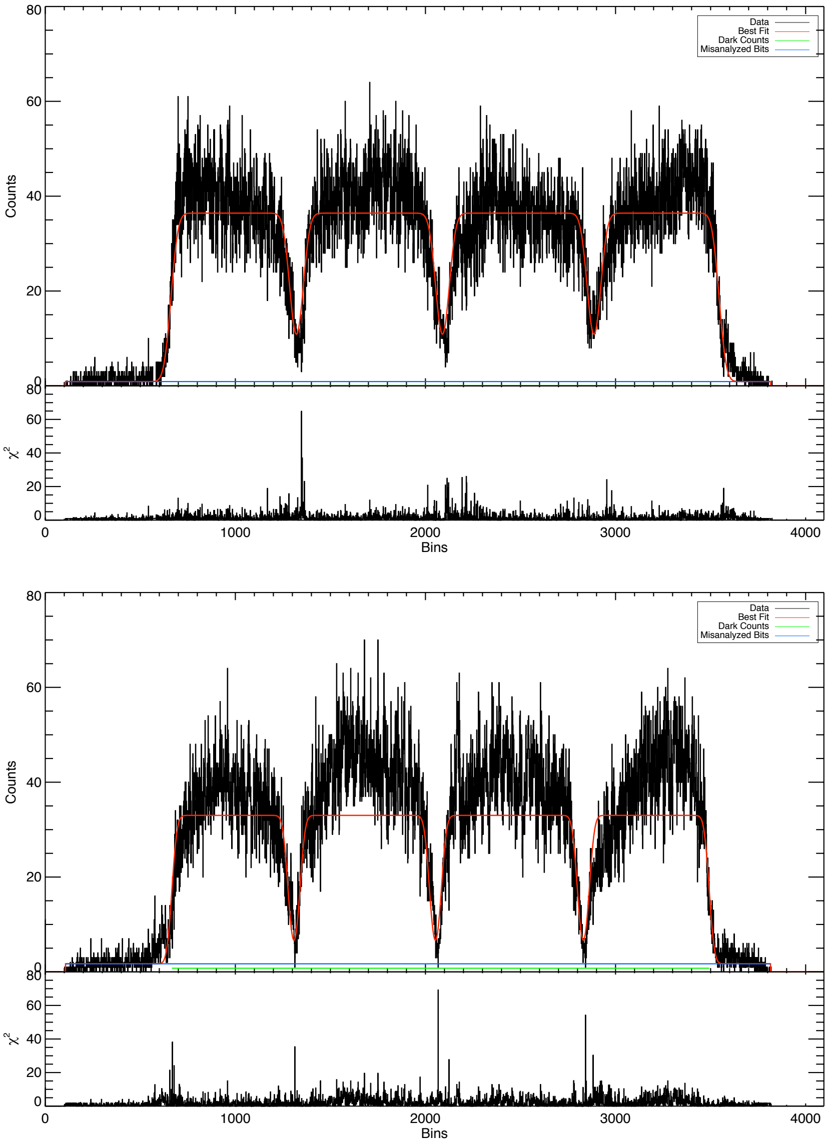

Figure 3.23 Best fit model for the discharge event. The dark count rate is negligible, as expected during any 20 second integration. The misanalyzed bit rate is a bit high, likely due to the energetic nature of a typical discharge event. Top plot is a histogram along the x-axis, while the bottom plot is along the y-axis.

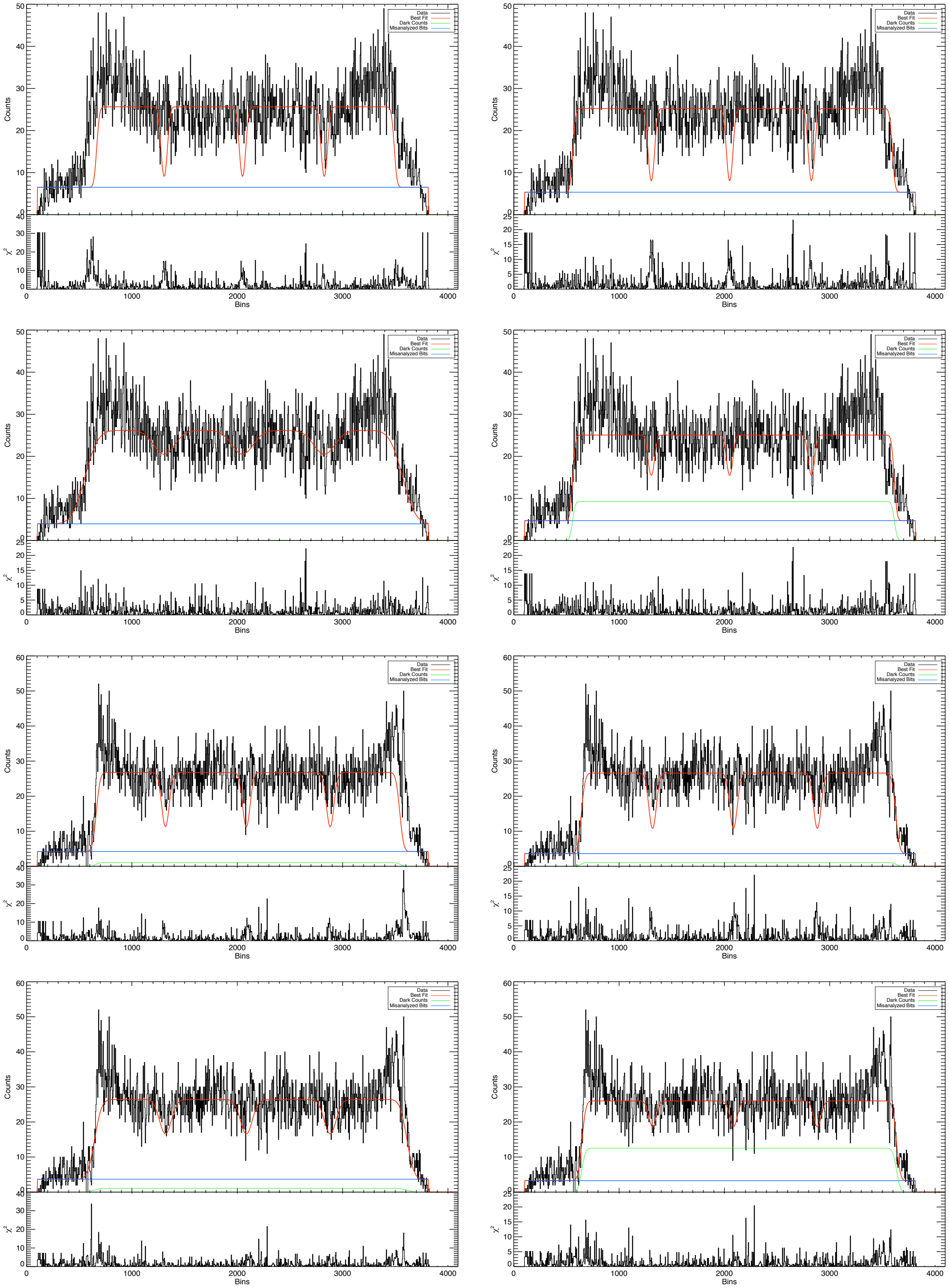

Figure 3.24 Various fits to the data as described in the text. The top four plots are along the y-axis, while the bottom for are along x. The fits correspond to Table 3.1 in order left to right then top to bottom.

Table 3.1 Parameters for fitting. Discharge fits represent fits to the short discharge event during flight. Science fits refer to fits of the data between the discharge event and the vacuum gauge event shown in Figure 3.24. Parameters left unchanged between fits (marked with ”) were frozen while other parameters allowed to vary.

Data	FWHM [mm]	Continuum [Counts/bin]	Left Edge [bin]	Right Edge [bin]	Dark Rate [counts/s/bin]	Misanalyzed Rate [counts/s/bin]	χ^2_ν
Y-discharge	1.20	30.0	666	3493	0.0375	0.0779	2.10
Y-science	”	18.4	”	”	”	0.0044	2.63
Y-science	”	19.0	560	3596	”	0.0037	2.11
Y-science	5.74	22.3	580	3584	”	0.0028	1.62
Y-science	1.2	10.4	560	3588	0.0081	0.0027	1.88
X-discharge	1.65	35.4	661	3545	2.2×10^{-6}	0.0454	1.48
X-science	”	22.5	”	”	”	2.8×10^{-5}	2.18
X-science	”	21.6	652	3632	”	0.0027	1.84
X-science	3.5	23.0	644	3644	”	0.0023	1.69
X-science	1.65	10.2	644	3644	0.0086	0.0023	1.51

Obtaining a perfect fit is unlikely at this stage without detailed modeling of the input science spectrum, but obtaining an acceptable fit in the window bar regions is highly important. Without a background calibration in flight, this fit represents the only method we have of determining the dark count rate and detector resolution in flight. To attempt better fits, we first unfreeze every parameter except the dark count rate, and run our same χ^2 minimization routine. Then we repeat this with an unfrozen dark count rate and a frozen detector resolution. The results are shown in Figure 3.24. These fits improved in quality. The increased dark rate was 0.0086 counts/s/bin, compared to the lab rate of 0.0004 counts/s/bin. While this is a marked increase, it is still below the dark rate of the previous generation of GEM detectors. However this increase in background has never been seen in the lab despite several months of use. Localized hotspots are common, but a general high dispersed background hasn't been observed.

Before progressing towards fitting scientific models, we must first examine items 4 & 5 of our original list of explanations on page 120. Examining the two detectors images and centroiding the window bars during the discharge event shows that the bar centers are identical to within 1 bin. Thus in the event of cross talk between detectors, the shadow would still be cast over the same digital bins. The calibration light source was a point source that was moved vertically and horizontally to simulate an extended source. However, due to experimental logistics, it did not have the full range of motion to fully capture all the necessary angles involved. Therefore it is worth considering the impact of light hitting near the window bars originating from both extreme edges of the gratings. For example, the middle bar on the window sees a cone of light coming off the grating array. This cone has a range of angles between $0.4° - 3.3°$ along the axis of dispersion. Assuming these photons penetrate all the way to the top GEM plate inside the detector before ionizing the Argon gas this amounts to a translation of $350\mu\text{m}$. As this is significantly smaller than both the window bar width and observed detector resolution, this geometry has no impact upon the shadow shape.

The need to include a noise component in the data to explain the missing window bars provides a strong argument in favor of an internal noise source within the detectors. Another means of testing the likelihood of a significant increase in detector noise is to compare the observed count rates with those of other missions. Figure 3.25 shows data from rocket payloads (Gorenstein et al. (1971a)) as well satellites (Gronenschild (1980) and Aschenbach & Leahy (1999)). These observations encompass all of the Loop and thus our observations should yield similar count rates. The error bars are substantial due to two main factors: the different effective area curves between instruments and the uncertainty in diffracted order of EXOS photons. By using these past observations we calculate an expected count rate on the order of 10^3 counts per detector. The actual observed count totals were 11626 and 17941 counts in detector 0 and 1 respectively. Thus our observed count rate is an order of magnitude higher than expected based upon previous X-ray observations. The actual ratio of observed to expected count rate lies between 17^{+30}_{-6} and 39^{+68}_{-13} depending upon the wavelength and diffracted order chosen for comparison. Thus the extreme bounds of this ratio are 11 - 107, indicating that our true count rate from the Cygnus Loop is between $\sim 1\% - 10\%$ of the observed count rate. Some of this discrepancy is likely due to the uncertainty in our effective area calibration (see Section 2.5.2 for details). However it is unlikely that our effective area differs by an amount this large, indicating that the origin of a large fraction of our counts is internal noise.

Given the importance that noise reduction will likely play in our scientific interpretation, it is of paramount importance to accurately model the distribution of noise over the detector. Figure 3.26 shows this distribution over several minutes of background observation taken during lab calibration. The red line represents the best fit with a slope of $.025 \pm .021$ (1σ uncertainty). This line is consistent with a flat line at the 2σ level. The noise level does seem to ramp up slightly at the long wavelength end of the detector. The nature of this factor of ~ 20 increase in noise is unknown. Some possibilities include: instabilities induced by the vibration anomaly (Figure 3.3) as seen on other rocket flights (Schindhelm et al. (2010)), electronic noise produced by either Wallops or EXOS systems (seen on the CyXESS flight (McEntaffer & Cash 2008)), or field emission at the high voltage connectors inside the GEM detectors. Noise reduction will be examined in further detail in Sections 4.1.3 and 4.2 during model fitting.

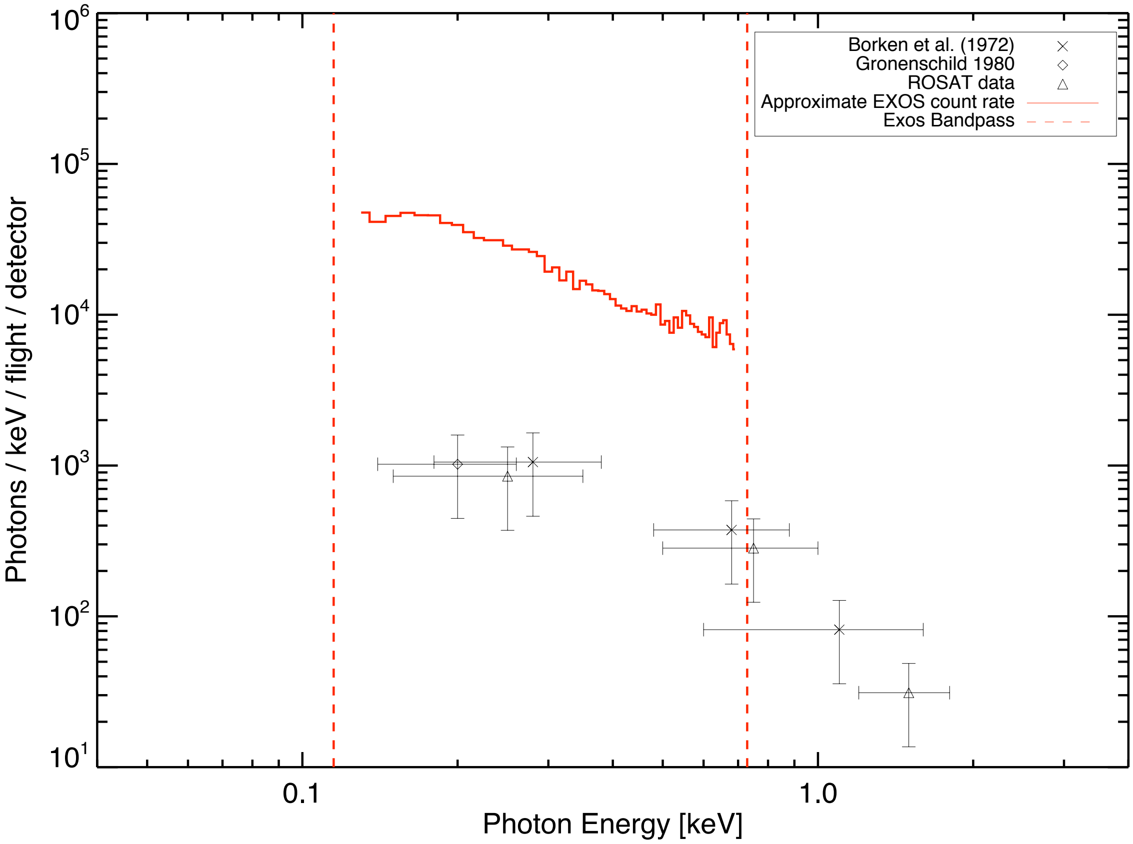

Figure 3.25 Count rate comparison to past observations. This plot has large uncertainties due to the variety of instrumental characteristics (bandpass, effective area, etc). The counts from EXOS are assumed to be from first order diffraction. Even with generous uncertainties, the observed count rate by EXOS is obviously too great by a factor of > 10.

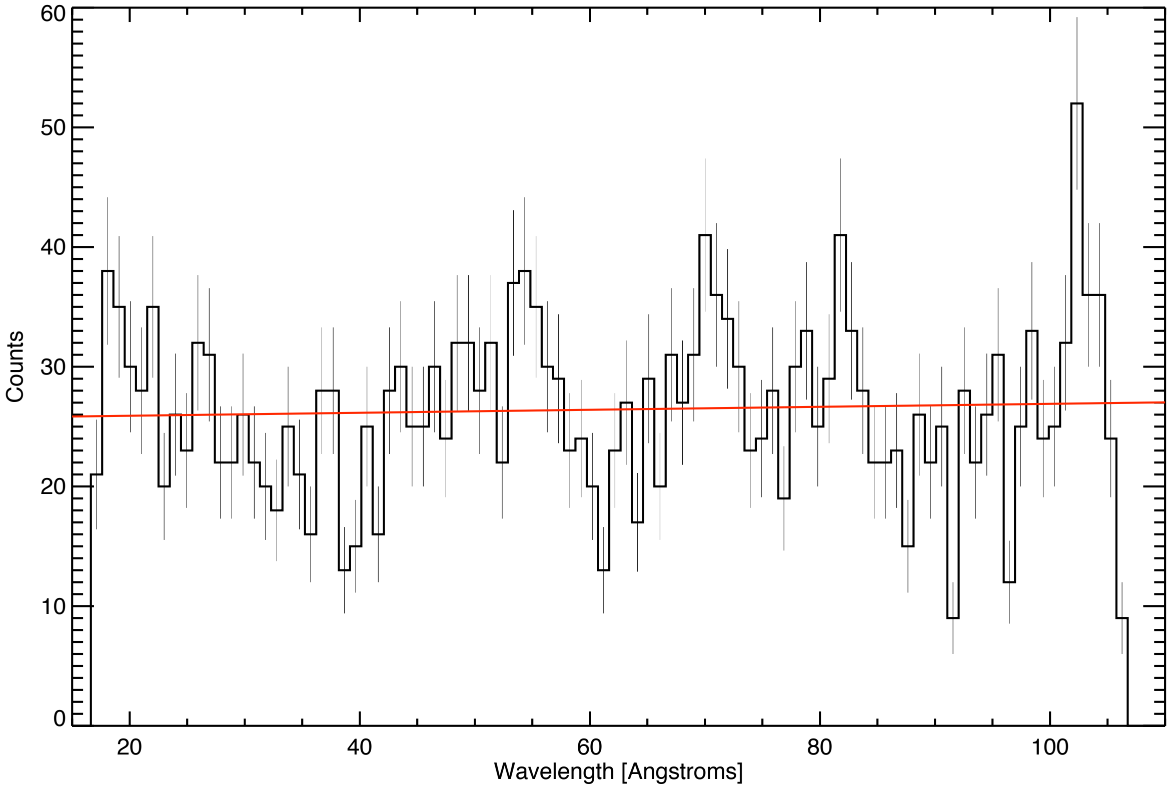

Figure 3.26 Noise distribution over the detector during lab tests.

3.3.3 Complete Effective Area Curves

In order to calculate the exact effective area curves for each module Figure 2.37 is taken as the baseline and modified in several ways. Locations of hotspots are modified based upon the percentage of time these pixels were unuseable in each diffracted order. The response near the window bars and detector edges is modified as per the description in Section 3.3.2. Detector 0 is modified via the gain variability described in Section 3.3.1. Thus the final efficiency calculation is:

$$E = (E_o - \epsilon_{hotspots}) \cdot \epsilon_{gain} \cdot \epsilon_{window} \tag{3.3}$$

$$E(\lambda, n) = \left(E_o(\lambda, n) - \sum_{i=1}^{hotspots} \epsilon_h(i, \lambda, n) \, \frac{t(i)}{t_f} \right) \cdot \left(\frac{1}{n_t} \sum_{t=0}^{t_o} \frac{x(\lambda, n, t)}{x(\lambda, n, t_o)} \right) \cdot (\delta_{window}(\lambda, n) * f(x)) \tag{3.4}$$

Here E_o is the efficiency calculated from theoretical grating efficiency and window transmissivity as outlined in Sections 2.5.2 - 2.5.4. The function ϵ_h details what percentage of a spectral bin is contaminated by a hotspot, while $t(i)$ is the duration of contamination and is scaled by the total flight time (t_f). The last term represents the convolution of the detector resolution with the binary window transmissivity (Section 3.3.2). These functions are all unique to each module, as is the $\lambda(x)$ described in Section 2.5.4. The result of this calculation for each module is shown in Figure 3.27.

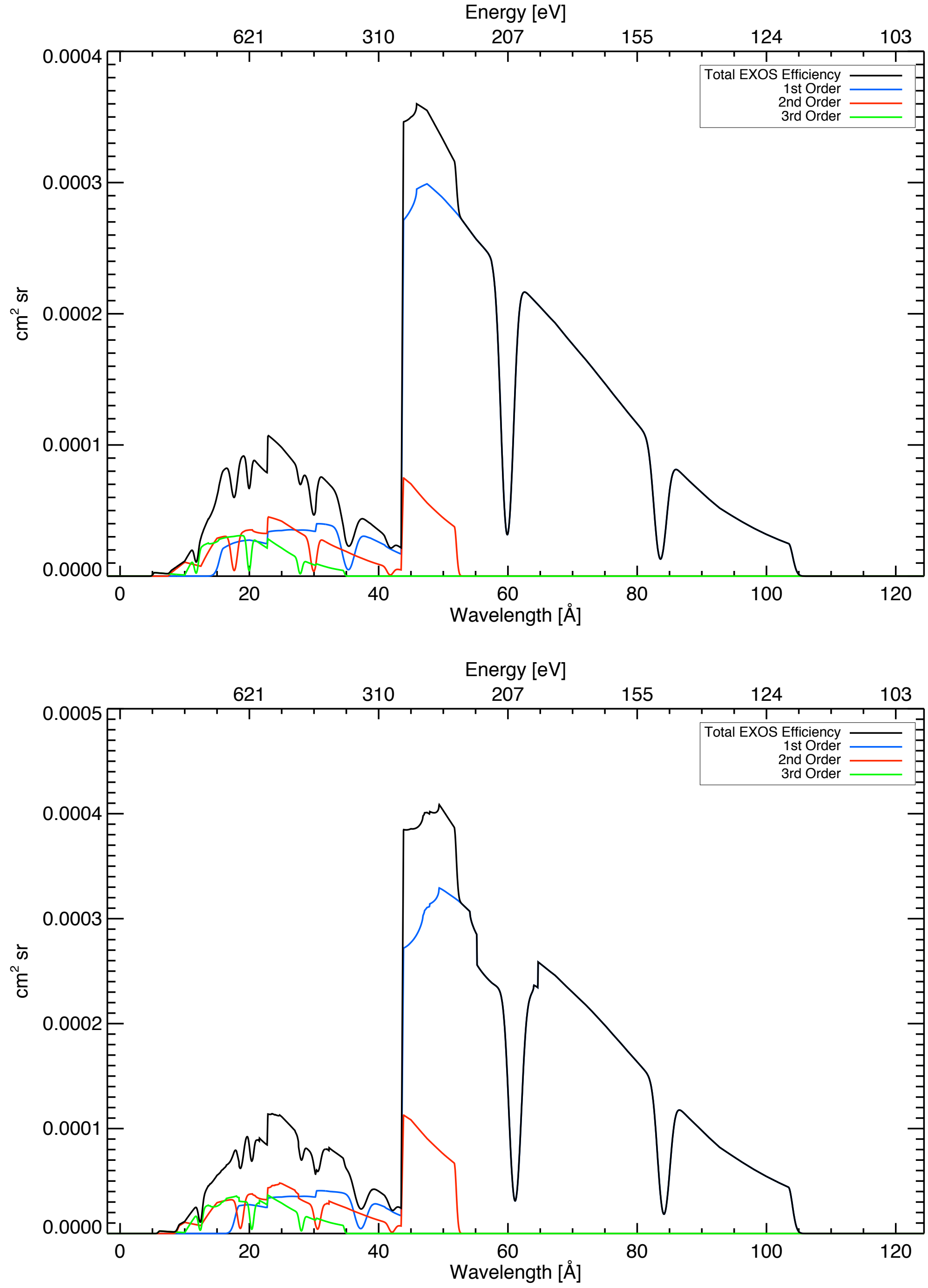

Figure 3.27 Flight calibrated effective area curves for detector 0 (top) and detector 1 (bottom) during flight.

Chapter 4

Discussion

Many models have been utilized to fit the observed X-ray emission from the Cygnus Loop. Most of these past observations involve only small portions of the remnant and the few that analyze the entire loop are at low resolution. This lack of higher resolution spectra over the entire remnant is the prime motivation for the EXOS payload. Most of these past data were fitted by various optically thin thermal plasma models. Some of these observations require two components (i.e. two temperatures) to obtain an acceptable fit, whereas other authors find no need for an additional component. Some authors require that the remnant be in a non-equilibrium state, whereas many authors find equilibrium models provide an acceptable fit. See Section 1.3 for details on these past fits. We will attempt model fits using the variety of thermal plasma models that have been previously successful.

Thermal models in the $\sim 10^5 - 10^6$ Kelvin temperature range are typically dominated by a few transitions of certain elements and ionization states with a low level of continuum and weaker lines between the dominant features. However our data is fundamentally different in appearance. The majority of the spectra show a flat flux level with respect to position with a few bright lines toward the low wavelength end of the detector. Detector 0 saw a sloped spectrum, but this slope was driven by gain variability and not necessarily by a sloped incident spectrum. Figure 3.19 shows how the spectrum becomes flat as the gain reaches optimal levels during the latter half of the flight. This flat appearance is an odd occurrence as the window transmissivity varies with respect to wavelength. Convolving an incident spectrum with the complicated effective area curves of Figure 3.27 to obtain a flat (to first order) resultant spectrum will likely be a difficult challenge. As detailed in Section 3.3.2 the addition of a noise component is likely necessary to explain the too-high count rate, lack of window bars, and flatness of the spectrum. However, we will initially assume the optimistic approach, that our count rate is higher than expected due to uncertainties in calibration rather than internal noise. If we are unable to fit the data without a noise component, this provides further evidence that our data are noise dominated.

The flat appearance implies a model that is dominated by continuum emission rather than emission lines. Thermal models with plasma temperatures $\gtrsim 10^7$ Kelvin are typically dominated by continuum. Temperatures this high typically show strong photon emission above 1 keV. This emission is not observed from the Cygnus Loop (Section 1.3.4), casting doubt on the possibility of such high temperatures. Another mechanism to produce continuum dominated emission is non-thermal synchrotron radiation. This mechanism results in strong continuum emission (typically fit with a powerlaw model) and has been observed in other supernova remnants (Koyama et al. (1995), Hwang et al. (2002) and Reynolds et al. (2007)). Figure 4.1 shows images of many of the historical supernova remnants. From these images the synchrotron dominated regions are easily discernible from the thermal regions. The synchrotron regions have a thin filamentary structure while the thermal regions are more clumpy in appearance. Additionally the thermal regions are typically observed towards the center of the remnant with the synchrotron emitting from the exterior.

From a purely morphological standpoint, the Cygnus Loop resembles the outer synchrotron filaments more closely than the clumpy thermal regions in the interior of the younger remnants. The Cygnus Loop appears to follow an evolution similar to SN 185's, where the central regions are dimmer, while the outer limbs have spread apart and are still emitting synchrotron radiation. Additionally the X-ray emission and Radio synchrotron emission are in very close proximity. Aschenbach & Leahy (1999) found the Radio and X-ray edges to be within an average of $7''$ as shown in Figure 1.12. As the radio emission is driven by synchrotron emission, the proximity of X-ray brightness implies a possible link between emission mechanisms.

Unfortunately there are many arguments against the Cygnus Loop having a synchrotron

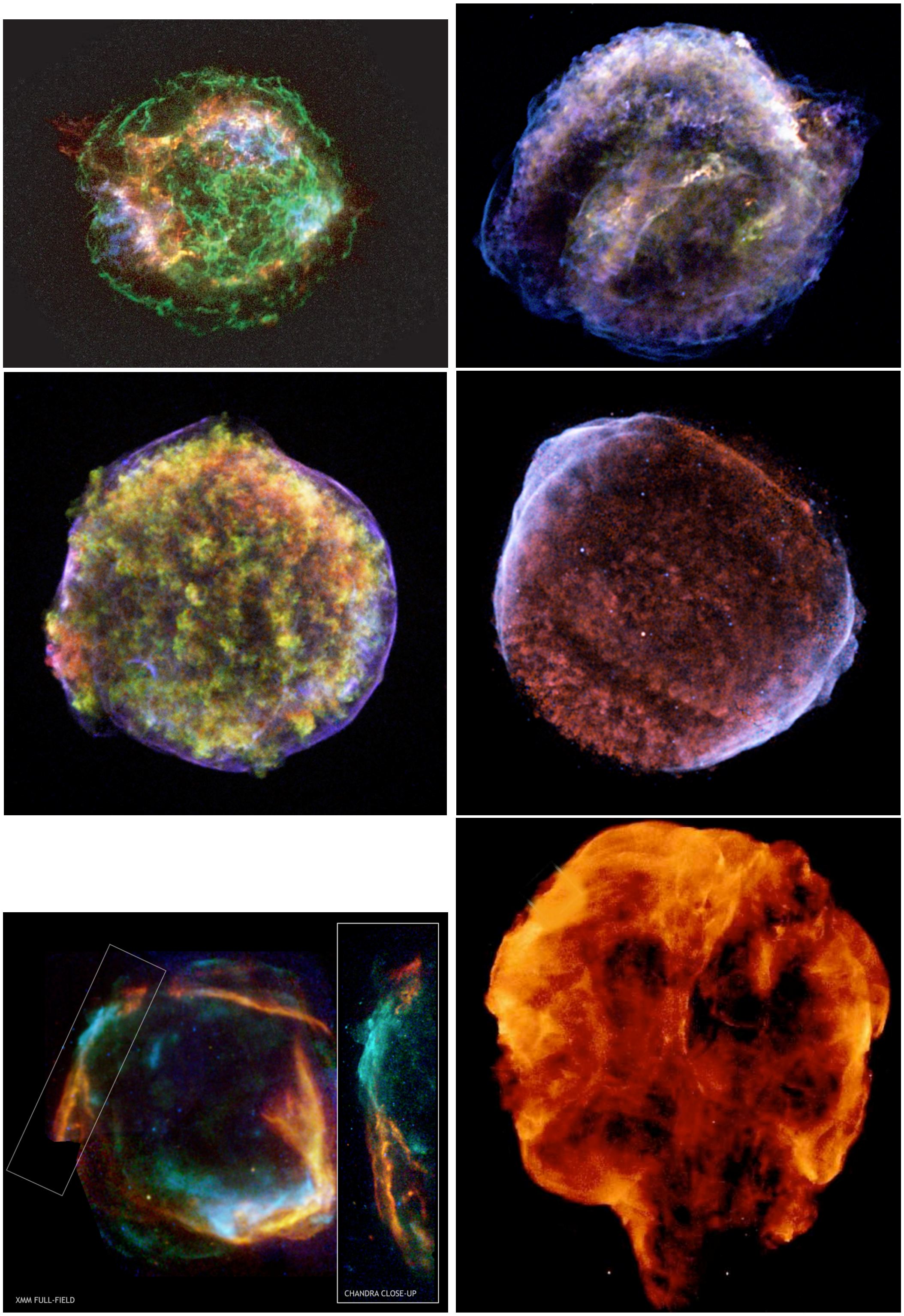

Figure 4.1 Historical supernova remnant images. Moving left to right and top to bottom: Cassiopeia A (Hwang et al. 2004), Kepler (Reynolds et al. 2007), Tycho (Warren et al. 2005), SN1006 Cassam-Chenai et al. (2008), SN185 (Vink et al. 2006) and the Cygnus Loop (Levenson et al. 1998). This order is from most recent to oldest. The filamentary structures (green in Cas A, blue in Kepler, purple in Tycho and SN 1006 and green in SN 185) represent the synchrotron continuum regions. The clumpier emissions regions towards the center (particularly noticeable in Tycho and SN 1006 are the thermally emitting regions.

component. Firstly, the remnants listed in Figure 4.1 are all significantly younger than the Cygnus Loop is thought to be. The shock velocities of Cygnus are typically an order of magnitude slower than these younger remnants, supporting this older age assumption. All older remnants have traditionally been fit with thermal bremmstrahlung models. Although the proximity of Radio and X-ray emission may provide a possible link to emission mechanisms, the proximity of X-ray emission to optical and UV emission indicates the exact opposite. The Optical and UV emission are thermal in nature and thus provide equally compelling evidence that the X-ray emission should be thermal.

Due to the conflicting evidence between thermal (line-dominated) and synchrotron (continuum dominated) models we will examine a variety of model fits to the data besides the typical thermal models fit by other studies. Fitting these various models will be accomplished using the Xspec X-Ray Spectral Fitting Package (Arnaud (1996)) version 12.5.1. Within this package are numerous scientific models developed separately to address a range of astrophysical situations. The models used in this document are listed in Table 4.1 with their relevant citations. The various thermal equilibrium plasma models (raymond, mekal, equil) are similar, but differ in their line lists and emission calculations. These differences are substantial enough to justify the effort of fitting each model. Abundances for all models are set to cosmic levels unless otherwise stated. Custom response matrices were created for use in Xspec to match the effective area curves shown in Figure 3.27. The FWHM of the response function was set to 2.07 mm, the average value determined from calibration data. These response matrices are used for all model fits unless otherwise stated.

Fitting two sets of data simultaneously can be challenging, especially with the various uncertainties we have in calibration and noise levels. We will therefore examine in detail each detector separately. Afterwards we will attempt to reconcile the two sets of analysis. Tables 4.2 and 4.3 will serve as a reference for all the model fits. These table lists the various parameters, response functions and notes of interest for every fit applied to each detector. Many more models were attempted beyond those listed here. For brevity's sake, not every failed fitting attempt was included in the discussion below. The list (and text) below provides an interesting and representative sample of the fits that were attempted.

Table 4.1. Scientific models used in Xspec and their citations

Model Name	Citations
srcut	Reynolds & Keohane (1999), Reynolds (1998)
raymond	Raymond & Smith (1977)
mekal	Mewe et al. (1985), Mewe et al. (1986), Liedahl et al. (1995)
equil	Borkowski et al. (2001), Hamilton et al. (1983), Borkowski et al. (1994), Liedahl et al. (1995)
nei	Borkowski et al. (2001), Hamilton et al. (1983), Borkowski et al. (1994), Liedahl et al. (1995)
pshock	Borkowski et al. (2001), Hamilton et al. (1983), Borkowski et al. (1994), Liedahl et al. (1995)

Note. — Additional references for these models can be found within the Xspec manual. The models powerlaw and gaussian were also used, unmodified from their standard mathematical formulae. The interstellar absorption function "phabs" was also used. This function utilizes standard photoelectric cross sections to compute absorption using the formula: $M(E) = \exp[-n_H \sigma(E)]$

Table 4.2. Models used in spectral fitting of detector 0

Model	Noise	Response Functions	Notes	Figure	Page	χ^2_ν
srcut	None	Full	Best extrapolation from Radio data	4.3	147	poor
phabs * srcut	None	Full	Best extrapolation from Radio data	4.3	147	poor
phabs * (srcut + 2 gaussians)	None	Full	Best extrapolation from Radio data normalized to EXOS flux	4.4	149	poor
phabs * (powerlaw + 2 gaussians)	None	Full, no bars	No restrictions to fit parameters	4.5	150	poor
phabs * equil	None	Full	Best fit with realistic absorption and temperature	4.6	152	poor
phabs * mekal	None	Full	Same parameters as above with a different model	4.6	152	poor
phabs * (equil + equil)	None	Full	Two temperature components	4.7	153	poor
phabs * nei	None	Full	Best fit with a non-equilibrium model	4.8	155	poor
phabs * equil	Linear Fit	Full	Thermal equilibrium model	4.12	161	148/99
phabs * nei	Linear Fit	Full	Thermal non-equilibrium model	4.13	163	147/98
phabs * (srcut + 2 gaussians)	Linear Fit	Full	Synchrotron and two gaussians	4.14	165	140/95
phabs * vequil	Linear Fit	Modified	Thermal non-equilibrium model	4.15	168	91/95
phabs * vnei	Linear Fit	Modified	Thermal non-equilibrium model	4.17	171	88/94
phabs * vpshock	Linear Fit	Modified	NEI with a range of τ	4.19	173	88/93

Table 4.3. Models used in spectral fitting of detector 1

Model	Noise	Response Functions	Notes	Figure	Page	χ^2_ν
phabs*(srcut + 2gaussians)	Linear Fit	Full	Best fit with two gaussians	4.21	175	poor
phabs*equil	Linear Fit	Full	Best fit with thermal equilibrium	4.21	175	poor
phabs*nei	Linear Fit	Full	Best fit with thermal non-equilibrium	4.21	175	poor
phabs*(equil+equil)	Linear Fit	Full	Best fit with two thermal equilibrium components	4.21	175	poor
phabs*srcut	Reduced Linear Fit	Full	Best fit with synchrotron emission	4.21	175	poor
phabs*(srcut+equil)	Reduced Linear Fit	Full	Best fit with synchrotron and thermal equilibrium components	4.21	175	poor
phabs*equil	Linear Fit	Modified	Best fit with thermal equilibrium	4.22	177	147/97
phabs*equil	Reduced Linear Fit	Modified	Best fit with thermal equilibrium	4.23	178	147/96
phabs*(srcut + 2gaussians)	Linear Fit	Modified	Best fit with synchrotron and two gaussians	4.24	179	146/95
phabs*(srcut + 2gaussians)	Reduced Linear Fit	Modified	Best fit with synchrotron and two gaussians	4.25	181	110/60

4.1 Detector 0

This section is devoted to analysis of detector 0. We will start with analyzing synchrotron models and then proceed to thermal plasma models. From here we examine these same fits with a noise contribution and various modifications to the response matrices.

4.1.1 Synchrotron Emission

If the X-ray emission of the Cygnus Loop does have a synchrotron component, it is essential to compare this to the intensity of the known synchrotron emission at radio frequencies. By taking the integrated radio flux values reported in Uyaniker et al. (2004) we plot a best fit powerlaw up to the EXOS X-ray bandpass with a spectral index of 0.50 ± 0.06 (3σ uncertainty). The X-ray flux values were taken from the three detector energy channels aboard the Borken et al. (1972) suborbital rocket payload, observations with the ANS satellite (Gronenschild 1980) and ROSAT data (Aschenbach & Leahy (1999) and Levenson et al. (1999)). These observations are highly useful to this study as they observe the entire remnant unlike the more recent Chandra, XMM-Newton and Suzaku observations which view $< 10\%$ of the remnant per exposure. As spatial variations may play a strong role in the spectra we begin by using only observations of the entire Cygnus Loop. Figure 4.2 shows the various observations of the entire Cygnus Loop from Radio to X-ray.

The observed X-ray values in the 0.1-2 keV bandpass are not consistent with an extrapolated powerlaw from radio observations. The Cygnus Loop is also much dimmer than predicted by our extrapolated model at higher (> 2 keV) energies as Gorenstein et al. (1971b) reports $< 2 \times 10^{-10}$ erg/cm^2/s over the 2-10 keV bandpass. Observations by HEAO-1 (Leahy et al. 1990) record $\lesssim 10^{-10}$ erg/s/cm^2/keV at > 2 keV. At 4.1 keV our extrapolated radio emission still predicts $\sim 1 \times 10^{-8}$ erg/cm^2/s/keV, too bright by 2 orders of magnitude. Thus a powerlaw index must steepen substantially at $\lesssim 1$ keV to account for the observed fluxes. The blue model illustrates this steepening powerlaw, based upon the XSpec model srcut developed by Reynolds & Keohane (1999). They took 14 of the brighter galactic SNR and extrapolated the radio flux (using the Green

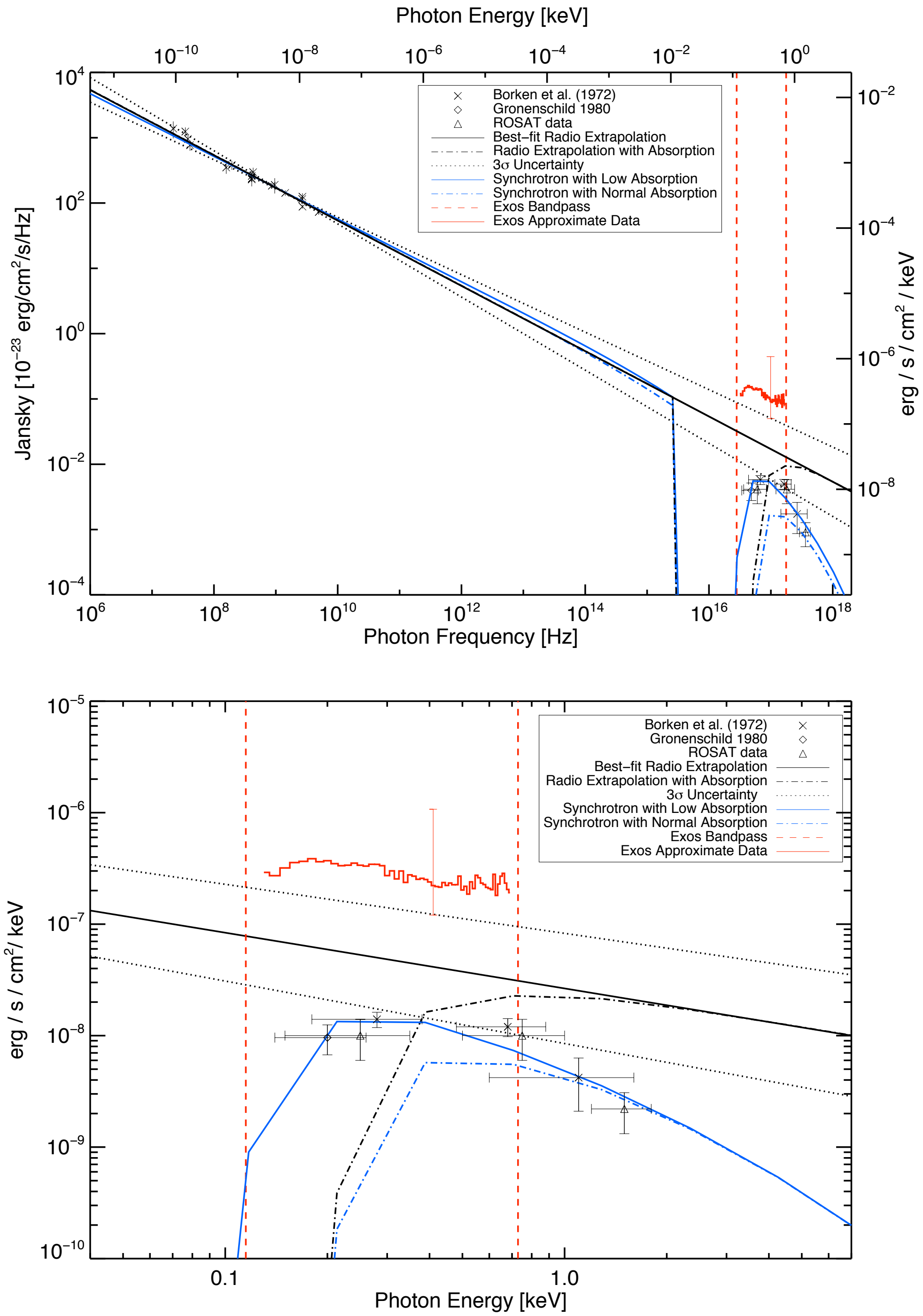

Figure 4.2 Extrapolation of radio synchrotron emission down to X-ray energies. The EXOS flux values are not properly deconvolved with the EXOS effective area as we are not certain of which counts correspond to which diffraction order (and thus their effective area). The error bars are indicative of the possible range of flux given the EXOS effective area curves (Figure 3.27). These data are plotted for order of magnitude reference only. The solid black line represents the extrapolation of radio emission, while the dotted lines are the 3σ uncertainties on that spectral index. The blue lines are synchrotron models detailed in the text. The steep drop in flux for some models at $\sim 3 \times 10^{15}$ Hz and reemergence at $\sim 3 \times 10^{16}$ is due to interstellar absorption. The energy uncertainty of past data are based upon the width of the respective energy channel in the relevant proportional counter. **Top** - Full range from Radio to X-ray. **Bottom** - Same plot but cropped to relevant soft X-ray bandpass.

(2009) and Seward (1990) catalogues) up to X-ray energies. They then compared this expected flux to the count rate observed by the Monitor Proportional Counter (MPC) detector aboard the Einstein observatory. They found that the X-ray emission was dimmer than expected from their extrapolation (much like we see for the Cygnus Loop in Figure 4.2) and concluded that the spectrum of the electrons responsible for the radio emission must steepen or cut off before reaching X-ray emitting energies to account for this drop in flux at higher photon energies. However the MPC is sensitive over a wide bandpass (1-20 keV) and the authors do not detail the strength of the discrepancy between extrapolated and observed fluxes. It is also unclear whether the authors consider the uncertainty in the spectral indices when extrapolating from radio to X-ray energies. They then attempted to determine at what maximum energy the electron spectrum must begin to steepen in order to account for the observed X-ray fluxes. They calculate X-ray fluxes by assuming an electron spectrum of the form:

$$N_e(E) = KE^{-s}e^{-E/E_{max}} \tag{4.1}$$

and folding this distribution through the single particle synchrotron emissivity. They fit X-ray spectra and determined a rolloff frequency, $\nu_{rolloff}$. This frequency is related to the cutoff electron energy via the relation:

$$\nu_{\text{rolloff}} = 0.5 \times 10^{16} \left(\frac{B}{10\ \mu G}\right) \left(\frac{E_{max}}{10\ TeV}\right)^2 \tag{4.2}$$

Several of the remnants had rolloff frequencies corresponding to soft X-rays in the 0.1 - 1.0 keV bandpass. This correlates to electrons in the 20 - 80 TeV range. We perform a similar analysis on the Cygnus loop, using Xspec to numerically calculate the best-fit rolloff frequency necessary to diminish the flux to observed levels. We find a necessary ν_{rolloff} of 5×10^{16} Hz ($\sim$ 100 TeV) using interstellar absorption at $N_H = 7 \times 10^{20}$ cm^{-2}. This model is shown in blue (dash-dot) in Figure 4.2. Using reduced absorption at $N_H = 1 \times 10^{20}$ cm^{-2} produces a better fit at softer energies (shown in solid blue). These electron energies are in agreement with values determined by Reynolds & Keohane (1999) on other younger, historical supernova remnants. The maximum electron energies determined for the young historical remnants and now for the Cygnus Loop casts doubt that young SNR are capable of accelerating electrons up to the "knee" of their distribution at 1000 TeV.

This solid blue model fits past data reasonably well, indicating that synchrotron emission could play a role in the observed X-ray emission by these instruments. This model uses a spectral index of $\alpha = 0.48$ which is within 3σ of the best-fit index. This model also utilizes the Xspec absorption model "phabs" with an absorption of $\mathrm{N}_H = 1 \times 10^{20}$ cm^{-2}. The most commonly quoted value is $7 \pm 3 \times 10^{20}$ cm^{-2} from Levenson et al. (1999), but this observed value varies in the literature depending on target location and FOV of the instrument. Thus any value in the 10^{20} cm^{-2} order of magnitude is justifiable. This model fits the observed values well, but the flux remains too high at higher photon energies. Though the resolution and extent of these past observations is inadequate, this fit is an indication that a synchrotron model should be considered when fitting at higher resolutions, despite the Cygnus Loop's older age.

As mentioned in Section 3.3.2, the count rate predicted by the model is insufficient to account for the EXOS flux even when ignoring interstellar extinction (set by default at 7×10^{20} cm^{-2}). This discrepancy is quite obvious in Figure 4.2. Here the EXOS flux is not deconvolved with the EXOS effective area as we are not certain of which counts correspond to which diffraction order (and thus their effective area). The error bars are indicative of the possible range of flux given the EXOS effective area curves (Figure 3.27). Figure 4.3 shows the result of taking the extrapolated radio spectrum and convolving it with the EXOS effective area curve. The result is a poor fit. Even if the model count rate was normalized to the observed flux, the actual shape of the model is a poor fit. The drastic increase in our instrument's effective area at > 44 Å makes obtaining a flat result nearly impossible.

In order to account for the observed EXOS count rate, the normalization would have to drastically increase. Figure 4.4 shows the convolution of spectral index and rolloff frequency that best fit the existing radio and X-ray data and a normalization that best fits the EXOS data with

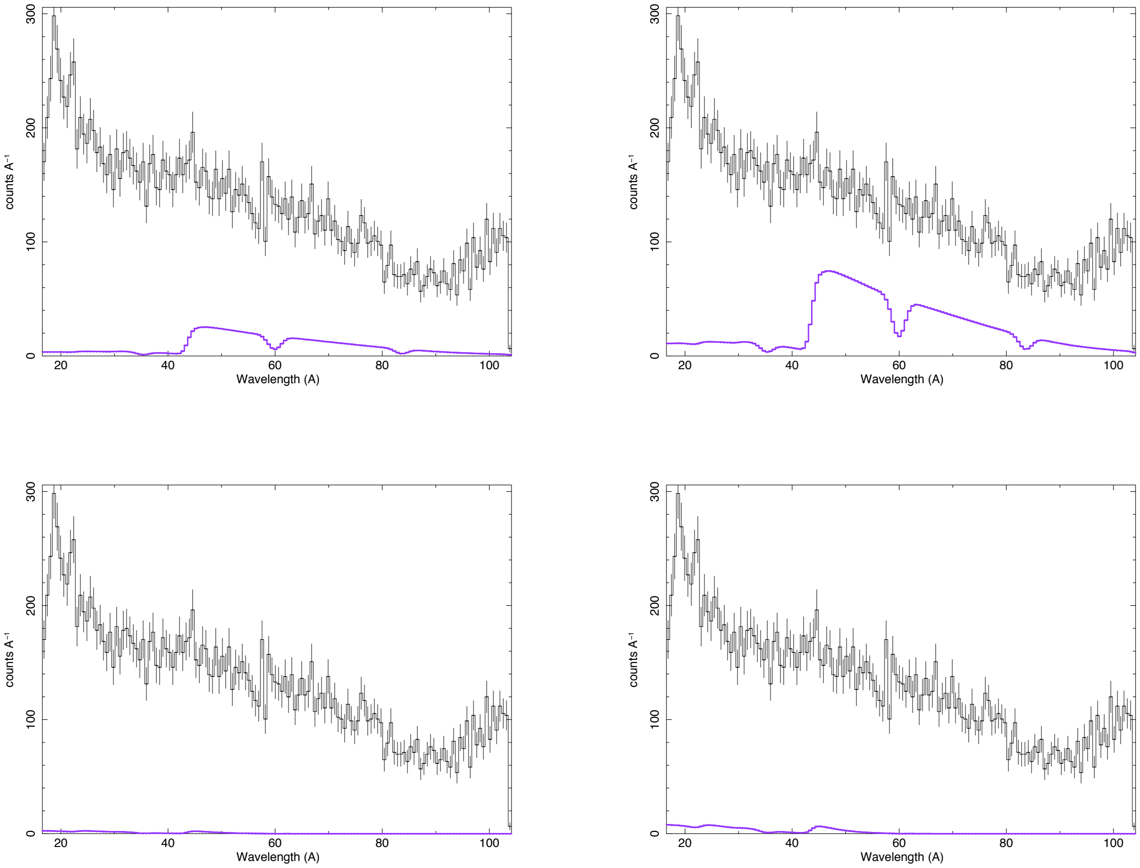

Figure 4.3 Radio power law extrapolation convolved with the EXOS response function for detector 0. The three dips are the window bar shadows. Even the non-extinction cases (top row) still have a large deficiency in model counts when compared to the data. **Top Left** - Best fit spectral index ($\alpha = 0.5$) with no interstellar extinction. **Top Right** - Spectral index at 3σ flatter ($\alpha = 0.44$) than best fit with no interstellar extinction. **Bottom** - Same as top plots with interstellar extinction set at 7×10^{20} cm^{-2}.

the EXOS effective area curve. This model is obviously a poor fit, even with the artificially boosted count rate. We also compare the data to an absorbed power-law spectra where the parameters are not constrained by radio observations or past extinction measurements. Additionally we utilize a response function that ignores the predicted window bar shadows. The result is also shown in Figure 4.5. This model has a powerlaw of photon index of $\Gamma = -2.2$, an absorption of 1.9×10^{21} cm^{-2}, and two emission lines at 19.3 Å and 21.8 Å. At this high level of extinction the spectrum is dominated by flux $<$ 44 Å (the carbon throughput cutoff on our windows) and the model counts shown longward of this mark are 2nd and 3rd order flux off of the diffraction gratings. Any attempt to increase the count rate appearing at the long wavelength end of the detector thus necessitates an undesireable rise in counts shortward of 44 Å. Alternatively a reduction in absorption would greatly increase the lower energy photon count rate without increasing the high energy photon count rate. Unfortunately the drastically different efficiencies above and below the carbon cutoff make obtaining a flat (to first order) convolved spectrum exceedingly difficult.

The comparison of EXOS data to previously observed X-ray and Radio count rates, the lack of window bars and the inconsistent spectral shape with previous results (Section 1.3.4) all give compelling evidence that the observed spectra have a significant noise component rather than a continuum dominated spectrum. Additionally no continuum model is capable of producing an approximate fit to the data. The lack of emission lines in higher orders argues that most of the flux we see is in first order. However the lack of a feature near the carbon edge in the data argues that we are seeing a combination of diffracted orders. No model is capable of achieving a fit good enough to provide any convincing evidence for a continuum dominated Cygnus Loop.

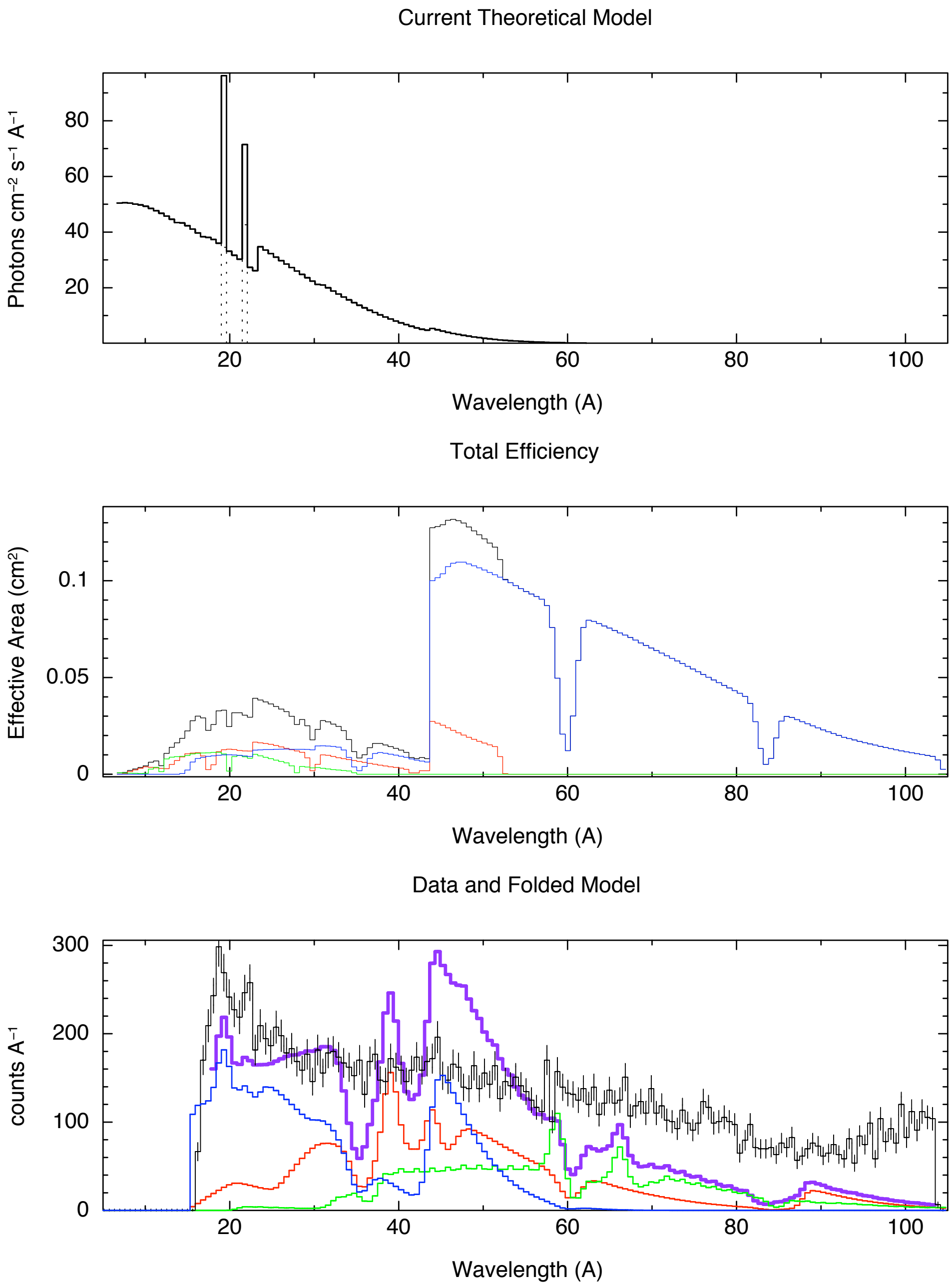

Figure 4.4 Best fit power law spectra that is consistent in slope (but not normalization) to Radio data. **Top** - Incident model: a synchrotron model with $\alpha = 0.48$, an interstellar absorption at $N_H = 7.0 \times 10^{20}$ cm^{-2} (Levenson et al. 1999) and two gaussians at 19.3 Å and 21.8 Å binned at the same width as the data. **Middle** - EXOS effective area curves for all orders. Black is the sum of the first (blue), second (red) and third (green) orders. **Bottom** - Convolution of incident model with effective area curves. Same color scheme with purple as the sum of the convolved orders.

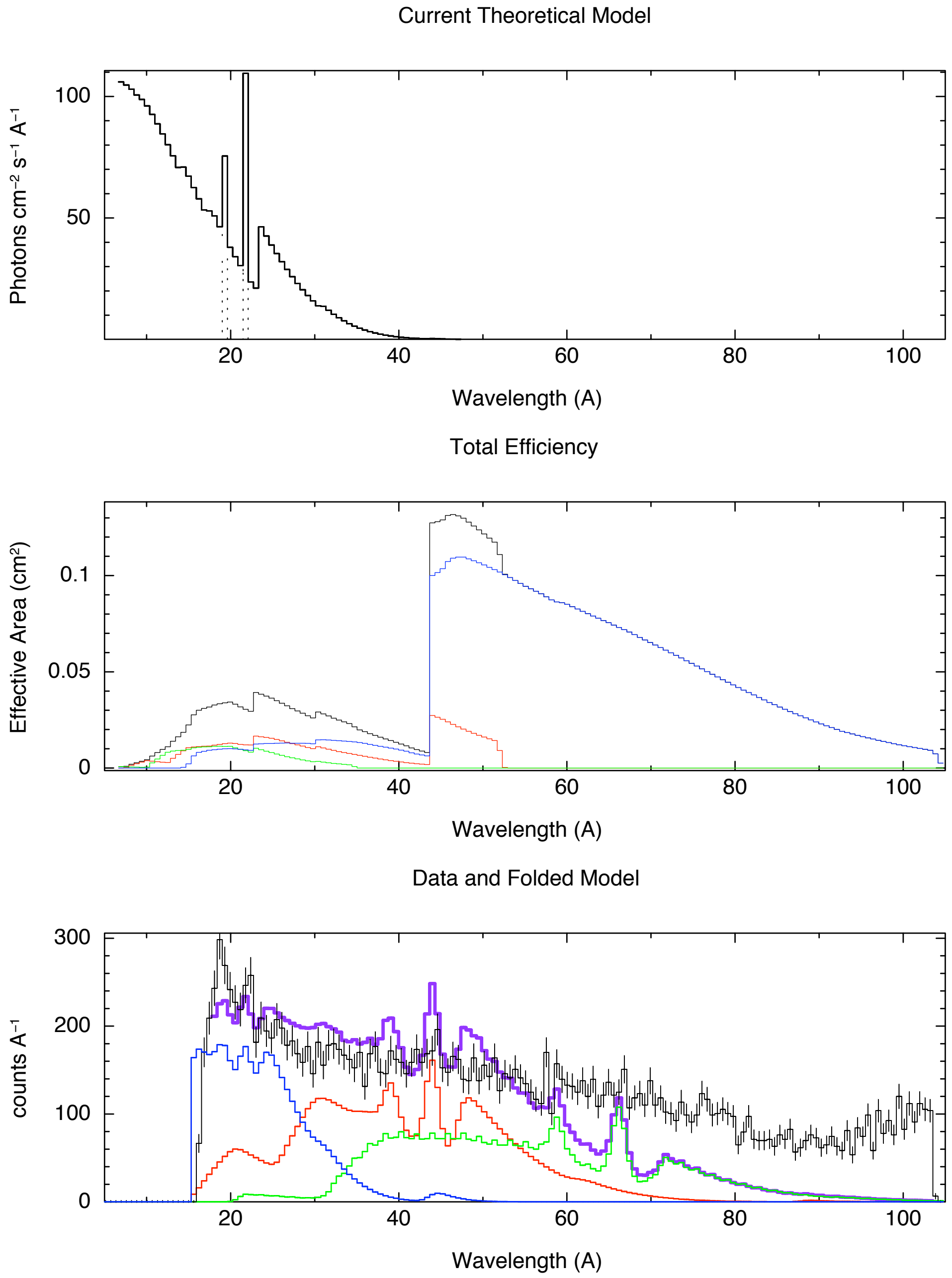

Figure 4.5 Best fit power law spectra that has no constraints based upon Radio observations. **Top** - Incident model: a powerlaw with photon index $\Gamma = -2.2$, an absorbing column density of 1.9×10^{21} cm^{-2} and two gaussian emission lines at 19.3 and 21.8 Å binned at the same width as the data. **Middle** - EXOS effective area curves for all orders. Black is the sum of the first (blue), second (red) and third (green) orders. **Bottom** - Convolution of incident model with effective area curves. Same color scheme with purple as the sum of the convolved orders.

4.1.2 Thermal Emission

The Cygnus Loop has traditionally been fit by means of an optically thin thermal plasma model. At the typically quoted temperatures ($\sim 10^6$ K), these models are dominated by a few major species, often O VII, O VIII, C VI and N VII. The oxygen lines (located at 17-22 Å) are of particular interest, as the ratio of their ionization states provides strong constraints on the remnant's temperature. The EXOS data show two strong features in this range that could be from O VII and O VIII. The FWHM of these lines (2.59 ± 0.40 Å and 1.52 ± 0.36 Å) is similar to the FWHM of 2.07 Å determined in calibration data. This is a strong piece of evidence that these features are caused by X-rays emitted from thermal regions in the Cygnus Loop diffracting through the EXOS optical system.

The EXOS data were compared to several thermal models in the Xspec library. These models main input is the electron temperature. The range of this temperature is restricted to the .08-0.7 keV range. The lower bound is the minimum temperature these models are calculated for, while the upper range is set to limit the amount of higher energy ($\gtrsim$1 keV) photons. Models of plasmas (in collisional ionization equilibrium) with temperatures above ~ 0.7 keV begin to show significant flux at these higher energies, in conflict with past observations (Section 1.3 and 4.1.1) that show little flux at these energies. Plasma in a non-equilibrium state could potentially be at higher temperatures without showing as many high energy photons due to their underpopulation of highly ionized atoms. These models are allowed to fit to higher temperatures. The absorbing column density was restricted to $1 \times 10^{20} - 1.3 \times 10^{21}$. This range was chosen as an approximate 3σ level from previous observations (See Borken et al. (1972), Gronenschild (1980), Levenson et al. (1999), and others referenced in Section 1.3).

Two initial attempts are shown in Figure 4.6. These models were best fit to a $T_e = 0.28$ keV and an absorbing column density of $N_H = 5 \times 10^{20}$ cm^{-2} and completely fail to obtain an adequate fit. The strongest lines observed are O VII, O VIII, Si XII and Fe XVI. These models have the capability of individually modifying the abundance of any element, which would allow individual lines to be observed at different flux levels. However these models obviously require more than just slight modifications to the elemental abundances to achieve a quality fit.

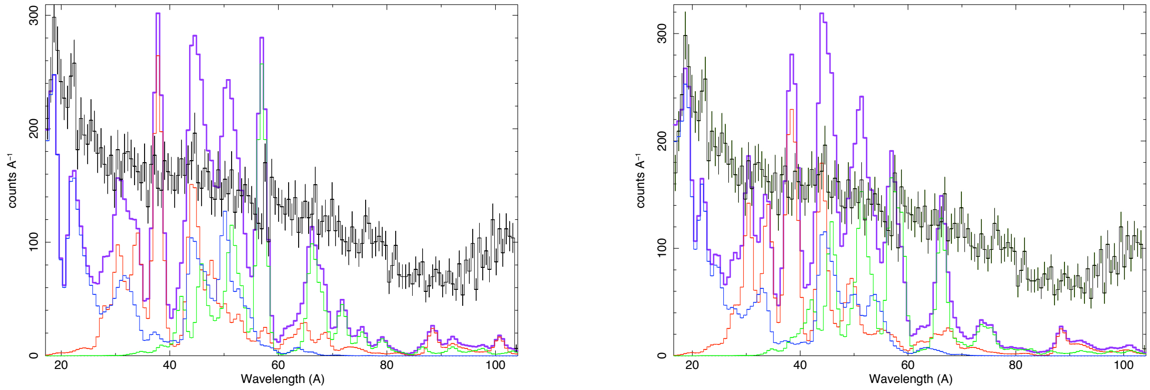

Figure 4.6 Failed thermal equilibrium fits. The colors here are arranged to match the effective area curves in Figue 3.27: the blue, red, and green lines represent the convolution of the model with the EXOS effective area in orders one, two, and three respectively. **Left** - Fit based on the Xspec model “equil” (Borkowski et al. 2001) with a $T_e = 0.28$ keV and an absorbing column density of $N_H = 5 \times 10^{20}$ cm^{-2}. **Right** - Same parameter values with the Xspec model “mekal” (Mewe et al. 1985)

Many of the previous spectra from the Loop have utilized a two component thermal model to obtain higher quality fits. This strategy makes intuitive sense as the reverse shock will reheat material causing a higher temperature interior to the softer limb. This exact geometry is seen by Levenson et al. (1999). Using ROSAT observations they detect a soft, thin ($5'$) shell around the entire remnant, providing ample observational motivation for these two temperature fits. A two component equilibrium model was fit to the data in Figure 4.7. This fit had a harder ($T_e = 0.32$ keV) component in addition to the softer ($T_e = 0.18$ keV) component and an absorbing column density of 7×10^{20} cm^{-2}. This fit also failed to obtain an acceptable fit to the data.

All of the these models assume that the remnant is in a state of collisional ionization equilibrium. As described in Section 1.3, several authors have shown that this may be inaccurate. We therefore attempt a non-equilibrium model fit (Figure 4.8). The best-fit parameters converged on a temperature of $T_e = 0.5$ keV, an absorbing column density of $N_H = 1 \times 10^{20}$ cm^{-2} and an ionization

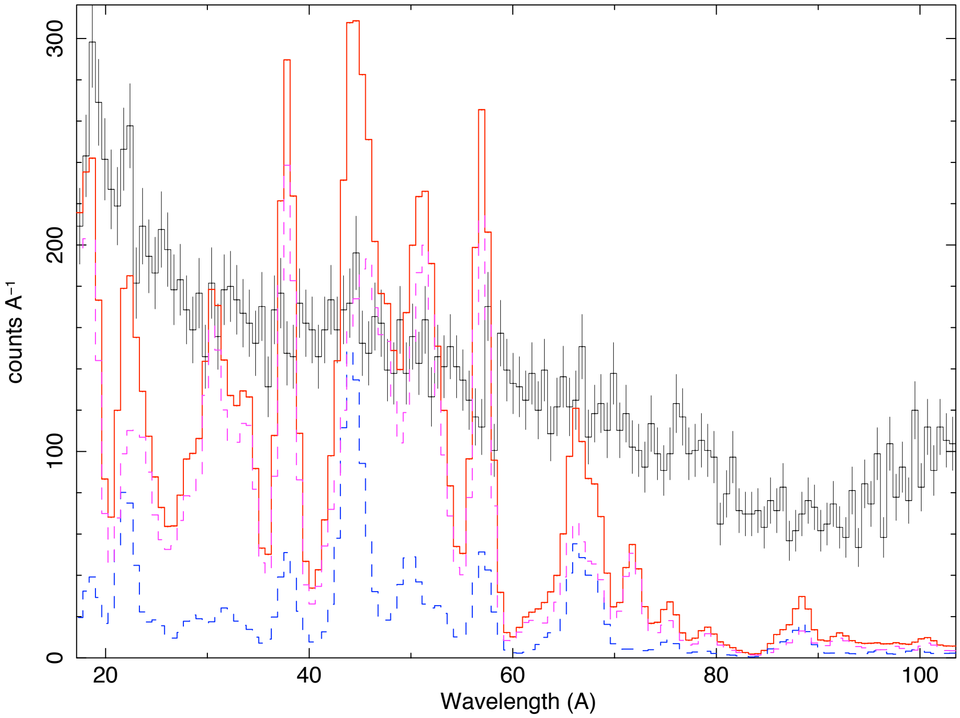

Figure 4.7 Failed two component thermal equilibrium fit. This fit utilized temperatures of T_e = 0.18 (in blue) and 0.32 (purple) keV with an absorbing column density of $N_H = 7 \times 10^{20}$ cm^{-2}. The summed model is shown in red.

timescale of $\tau = 1.5 \times 10^{10}$ s/cm^3. This model also fails in obtaining a fit to the data.

Several other attempts to fit the data were made including: a variety of multiple equilibrium and non-equilibrium components, an evolving temperature, different electron and ion temperatures, a range of ionization timescales, and the addition of a synchrotron component to thermal models. None of these fits made significant progress in providing a proper fit to the data. Given our expectation of a strong noise component, the lack of adequate fits is not surprising. A thermal component is still a possibility if it lies on top of a significant amount of noise counts. We now fully abandon the optimistic count rate regime and begin fitting with the expected noise component.

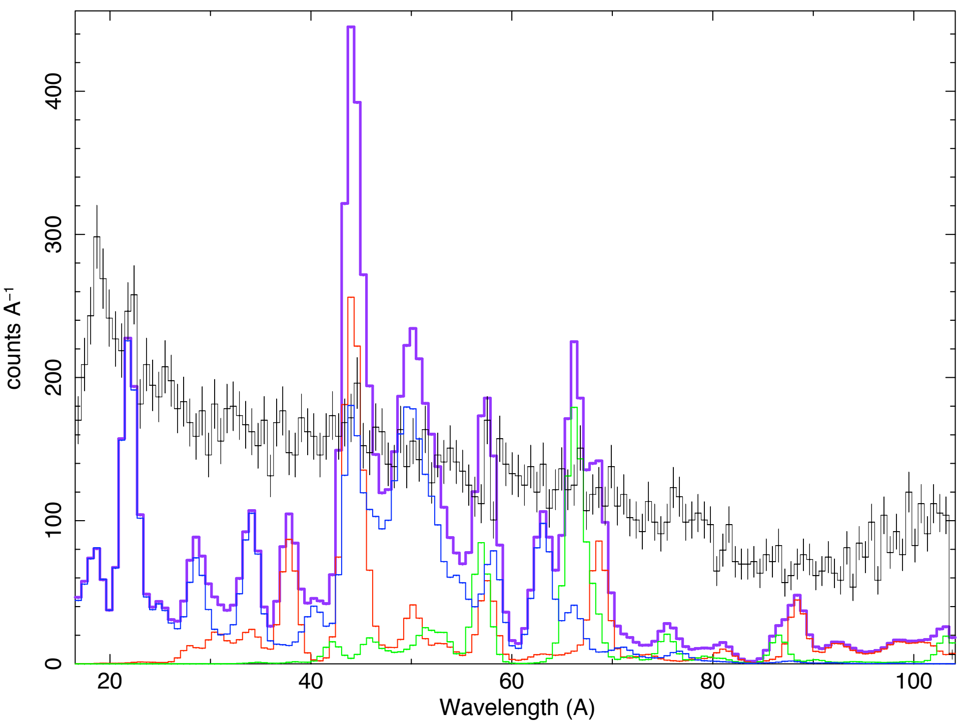

Figure 4.8 Failed thermal non-equilibrium fit based on the Xspec model “nei”. This fit utilized a temperature of $T_e = 0.5$ keV, an absorbing column density of $N_H = 1 \times 10^{20}$ cm^{-2} and an ionization timescale of $\tau = 1.5 \times 10^{10}$ s/cm^3. The colors here are arranged to match the effective area curves in Figue 3.27: the blue, red, and green lines represent the convolution of the model with the EXOS effective area in orders one, two, and three respectively. The purple line is the sum of all model components.

4.1.3 Noise Contribution

We now introduce a noise component to our data. As discussed in Section 3.3.2, the unexpectedly high count rate indicates a strong noise contribution on the order of $90\% - 99\%$ of the total counts (post discharge event). The noise distribution seen in the lab was best fit with a nearly flat distribution (Figure 3.26). The data from detector 0 are more complicated due to the gain instability observed in flight (Section 3.3.1). The bulk of the spectrum can be well fit with a linear model, however both ends are ignored in this fit for separate reasons. At bin locations $\gtrsim 3200$ there are what appear to be legitimate spectral lines. The FWHM and location of these lines coincide to what we expect from O VII and O VIII emission. This emission is both predicted in many of the thermal models referenced above and seen in previous observations (Miyata et al. 2007). Due to the high likelihood of significant true X-ray counts in this region we exclude it from our noise fit. Additionally the region of bins $\lesssim 1400$ presents a difficulty as it appears to deviate from the expected linear slope seen in the $1400 \lesssim$ bins $\lesssim 3000$ range. This effect has been seen in the lab before. Certain regions on the detector are the last to achieve the necessary gain to detect soft X-rays (which typically produce only a few initial electrons more than background noise events). In the CyXESS detectors, the gain would typically rise quickest in the center and slowly spread to the edges. With the new GEM foils this is no longer accurate. Instead these regions correspond to seemingly random (though consistent) locations. These regions are easily visible in Figure 4.9. The lower bin region corresponds to the deviation from the linear slope of the data. Thus we ignore this region from our fit as its shape is dominated by its unique gain profile rather than the overall gain profile of the detector (which we showed to be flat in Figure 3.26). The same argument could be made to ignore the region $2640 \lesssim$ bins $\lesssim 3120$. However, in lab calibrations this region typically achieves full gain much quicker (i.e. at lower voltages) than the region $960 \lesssim x \lesssim 1460$. Additionally, a count rate analysis of this detector (Figure 3.19) shows that the region with bins ~ 3000 to be much more stable than the bins $\lesssim 1460$ region during flight. Lastly the very long wavelength end of the detector is seen to have a higher expected noise count rate (Figure 3.26).

This corresponds to the upturn at bins $\lesssim 1000$. Thus we include the region $2640 \lesssim$ bins $\lesssim 3200$ for the noise component fit, but not the region < 1400. The noise fit is shown in Figure 4.10.

Since we have a large uncertainty on noise count rate, the normalization of this parameter will be allowed to float without restriction to determine the best fit models. However Figure 4.11 illustrates the extremes of background subtract as detailed in Section 3.3.2. The bottom plot shows the lowest X-ray count rate, while the top plot shows the highest expected X-ray count rate. A best-fit noise normalization within this range would support our count rate calculations. With the expected count rate the resulting spectrum now shows the expected Bremsstrahlung-like appearance.

The background subtracted data now appear to be dominated by a few strong emission lines and qualitatively resemble what we would expect for a thermal bremsstrahlung model (in the $\sim 10^5 - 10^6$ K range). Our first attempt (Figure 4.12) is therefore the thermal plasma model "equil". The best fit spectrum was produced with a $T_e = 0.17$ keV and absorbing column density of 1.3×10^{21} cm^{-2}. However this fit only produced a $\chi^2_\nu = 148/99$. This fit primarily fails due to the inability to adequately account for the amount of flux in the first spectral line at ~ 19 Å. At this temperature the strongest line at this location is expected to be O VIII. An increase in the line strength here results in an unwanted increase at higher orders (located at ~ 38 Å and ~ 57 Å on the detector). One possible explanation is that a fraction of the counts in this line are in fact due to noise. The noise calibration data shows in upwards peak at the long wavelength end of the detector, and it is possible that the short wavelength end mirrors this behavior. However the data itself don't support this (Figure 3.26), and noise would have to account for this entire line due to the complete lack of a second order emission line at ~ 38 Å.

An attempt at a non-equilibrium fit is shown in Figure 4.13. This fit performs no better than the equilibrium fit, utilizing a temperature of 0.18 keV and $\tau = 4.2 \times 10^{11}$ s/cm^3 and achieves only a $\chi^2_\nu = 147/98$. This ionization timescale is large enough that it is essentially identical to the equilibrium model. The fundamental problem of fitting the first spectral line without creating too many second and third order counts remains.

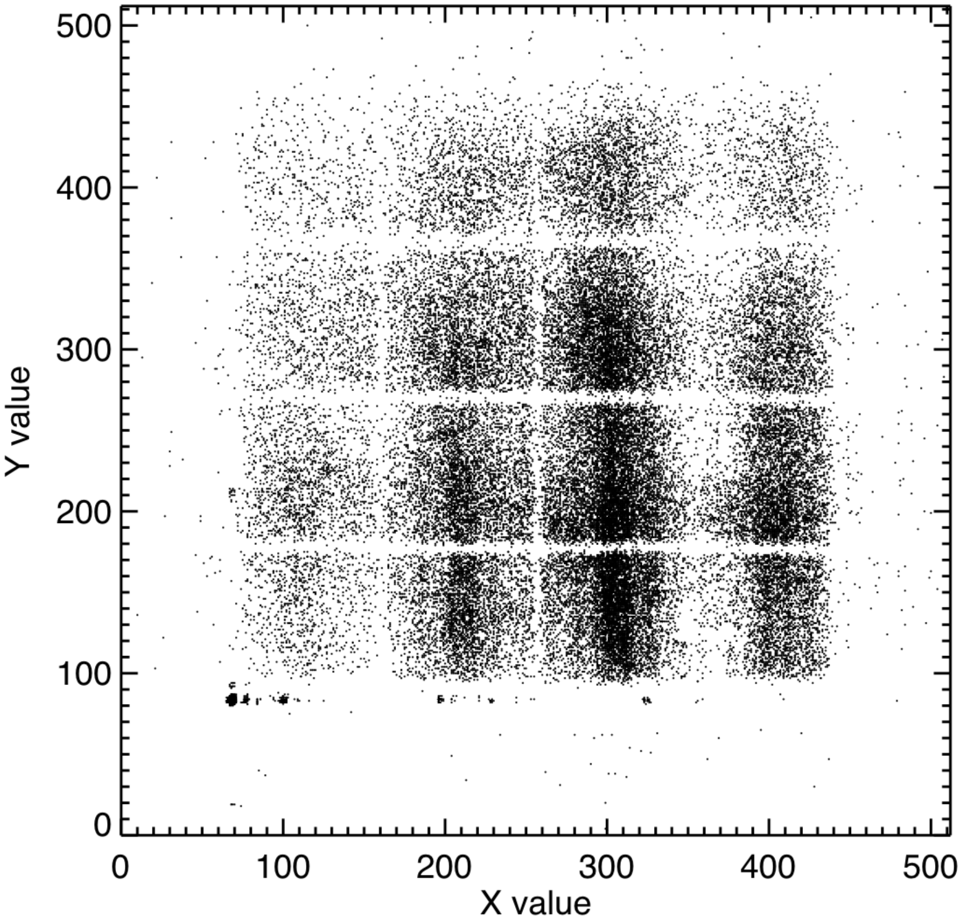

Figure 4.9 Hole in gain distribution. This image was taken at a slightly lower than optimal operating voltage. Specific regions show far fewer counts than expected, particularly in the $120 \lesssim x \lesssim 180$ and the $330 \lesssim x \lesssim 390$ region. This corresponds to regions: $960 \lesssim x \lesssim 1460$ and the $2640 \lesssim x \lesssim 3120$ in the data taken via telemetry. Differences in flux density are caused by both gain instabilities at lower operating voltages and the light sources emitting more strongly at certain wavelengths. The count rate deficiency in these regions increases with voltage, and thus gain instability is initially dominating the lack of emission over this part of the detector.

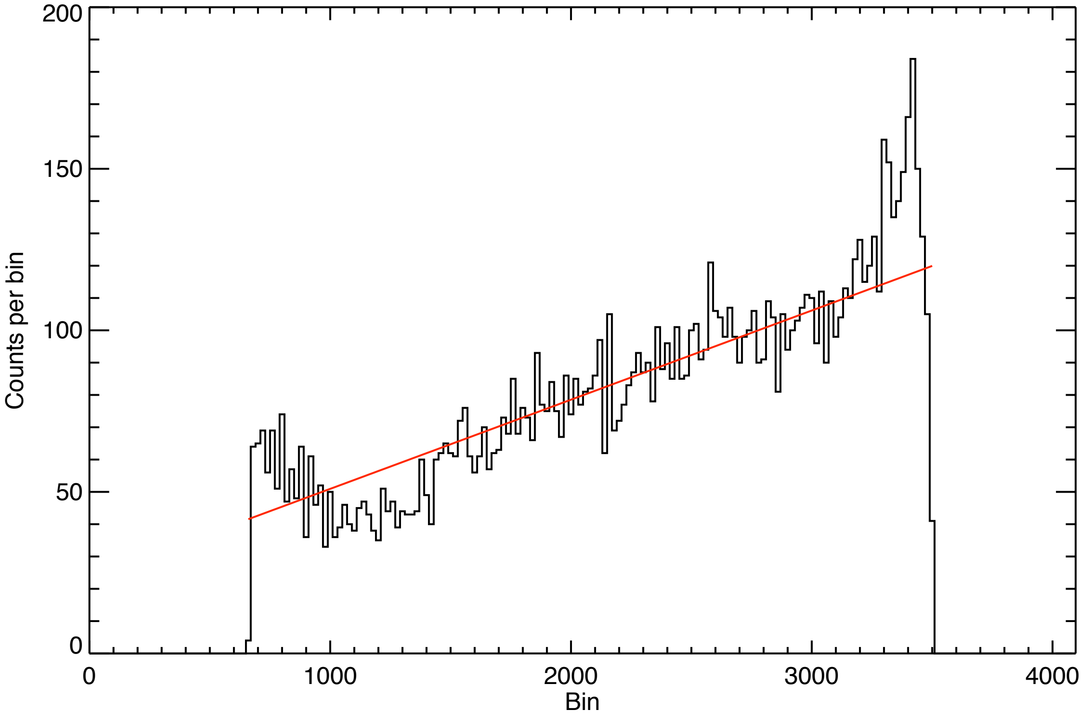

Figure 4.10 Detector 0 noise profile. The red line is fit between bins 1400 and 3200.

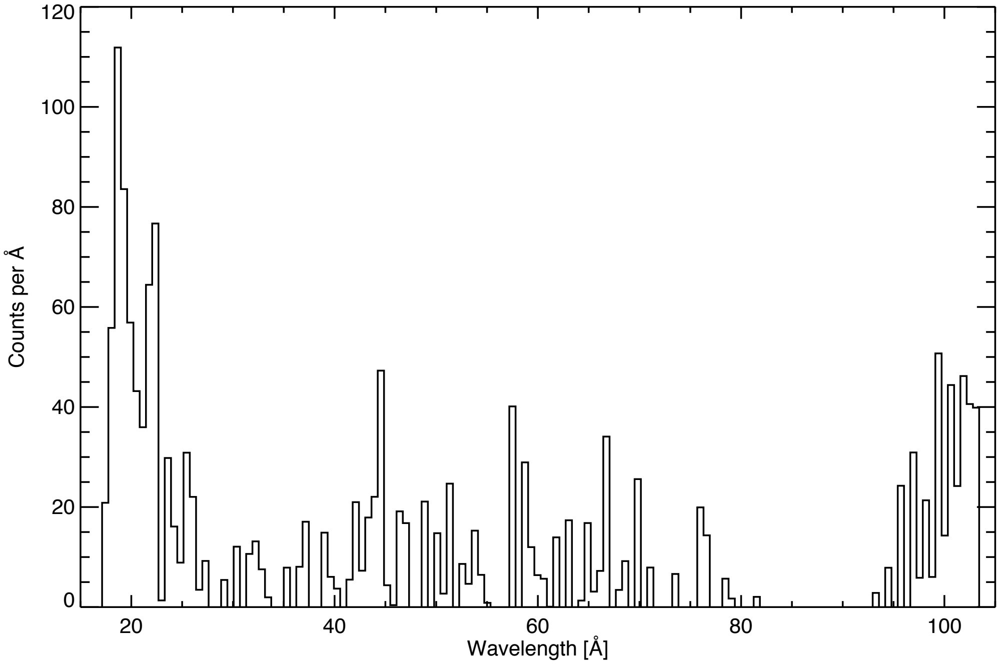

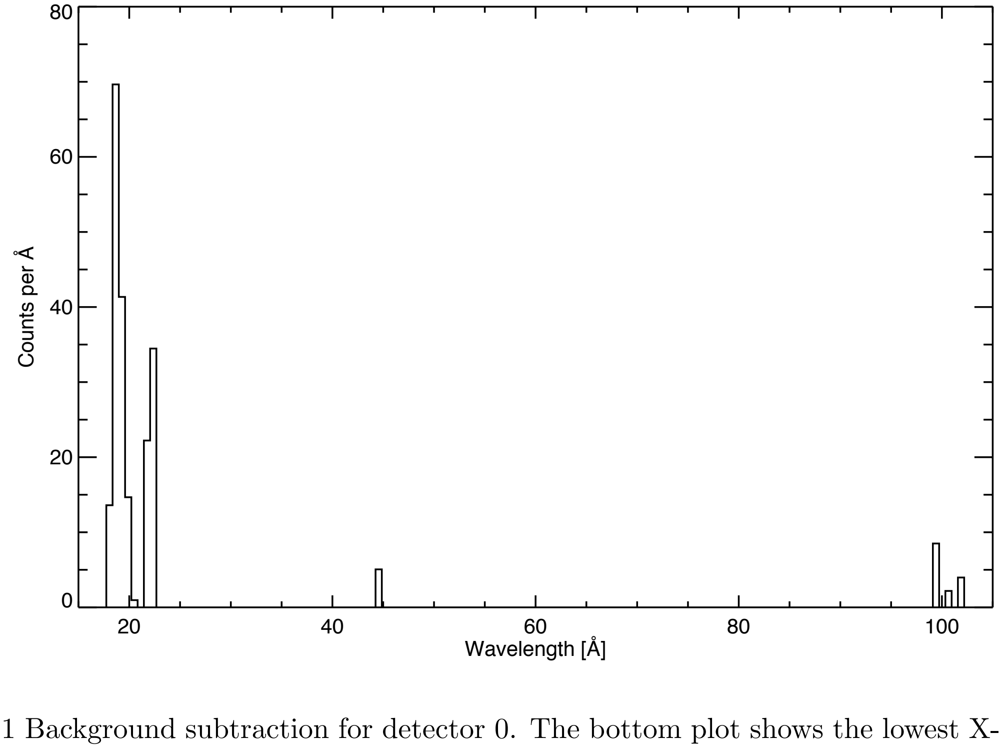

Figure 4.11 Background subtraction for detector 0. The bottom plot shows the lowest X-ray count rate, while the top plot shows the highest expected X-ray count rate. The upturn at ∼ 100 Å is likely due to the higher noise count rate seen in Figure 3.26 rather than a complex of emission lines.

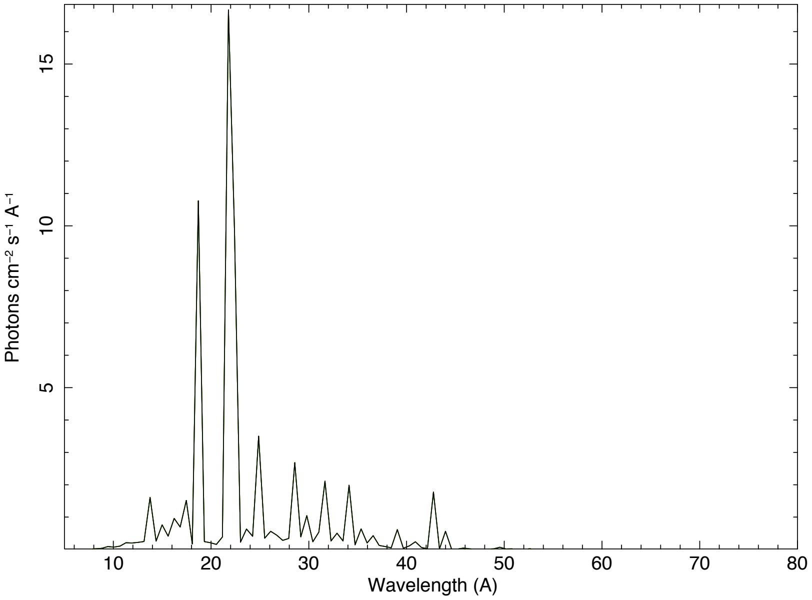

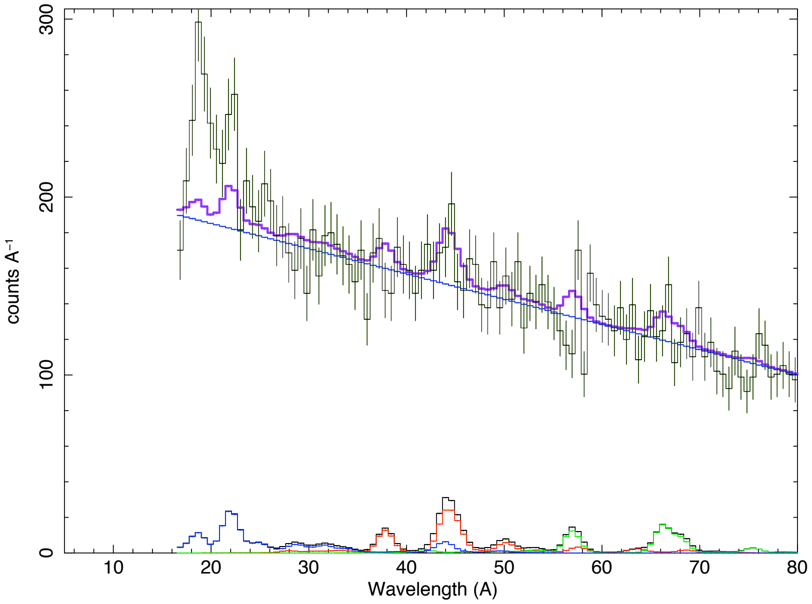

Figure 4.12 Thermal equilibrium model plus a noise contribution and fit. **Top** - Incident model. Here the black line represents the equilibrium plasma model. **Bottom** - Convolution of the model with the EXOS effective area curve. The colors here are arranged to match the effective area curves in Figue 3.27: the blue, red, and green lines represent the convolution of the model with the EXOS effective area in orders one, two, and three respectively. The blue line is the noise response (which doesn't have multiple order responses as it is generated inside the detector). The purple line is the sum of all model components. This model is a thermal equilibrium model with a $T_e = 0.17$ keV and absorbing column density of 1.3×10^{21} cm^{-2}.

Several other attempts were conducted including models with: two temperature components, temperature-evolving plasmas, a range of ionization timescales, etc. These models all suffer from this same issue of the second and third order fluxes being insufficient to account for higher order diffraction from the strong first order lines. Due to our limited calibration data on the gratings (Figure 2.27) it is possible that the amount of flux being distributed to higher orders is less than predicted by theory. However calibration data taken with the whole system show strong flux in many orders (Figure 2.33). However these data were not taken with an extended source, so it is not a perfect analysis of order distribution. Most of the calibration data were taken such that the incident conical angle (α in Figure 2.9) is $\sim 0°$. Much of the flux from the Cygnus Loop will enter the system from the most exterior slits of the collimator plates (Figure 2.4) and encounter the gratings at alpha angles as high as $\pm 20°$. This, in addition to the variety of graze angles that strike the grating (Figure 2.25), could drastically change the distribution of flux in diffracted orders. Gratings with a sinusoidal profile (such as those onboard EXOS) typically have efficiency curves that behave as if they were pseudo-blazed on the order of $\sim 10°$. First order light at ~ 20 Å is expected to diffract with $\beta = 9°$. This could explain why the majority of counts collected during flight appear to be concentrated into first order diffraction. The raytrace of the full system (Figure 2.22) does not predict a large discrepancy in order distribution. However the complexity of the system with 24 collimator plates and 67 gratings per module results in a high level of uncertainty. Detailed testing with an extended source is necessary prior to the next flight.

Though the continuum has been removed from our data, we still wish to quantify the possible presence of any synchrotron emission. We thus employ a synchrotron model with two gaussian emission lines. We limit our synchrotron spectral index to $0.36 < \alpha < 0.56$, as these are the extreme limits found in Uyaniker et al. (2004) for their two fitting attempts. The breaking energy (and hence rolloff frequency) is unrestricted in value, while the normalization (at 1GHz) is set to 170 ± 30 Jy. The uncertainty on this normalization is to simulate a large uncertainty in overall system throughput. The column density is again limited to $1 \times 10^{20} < \mathrm{N}_H < 1.3 \times 10^{21}$ cm^{-2}. The best fit (Figure 4.14) maximized the amount of synchrotron flux with a spectral index of 0.36, a

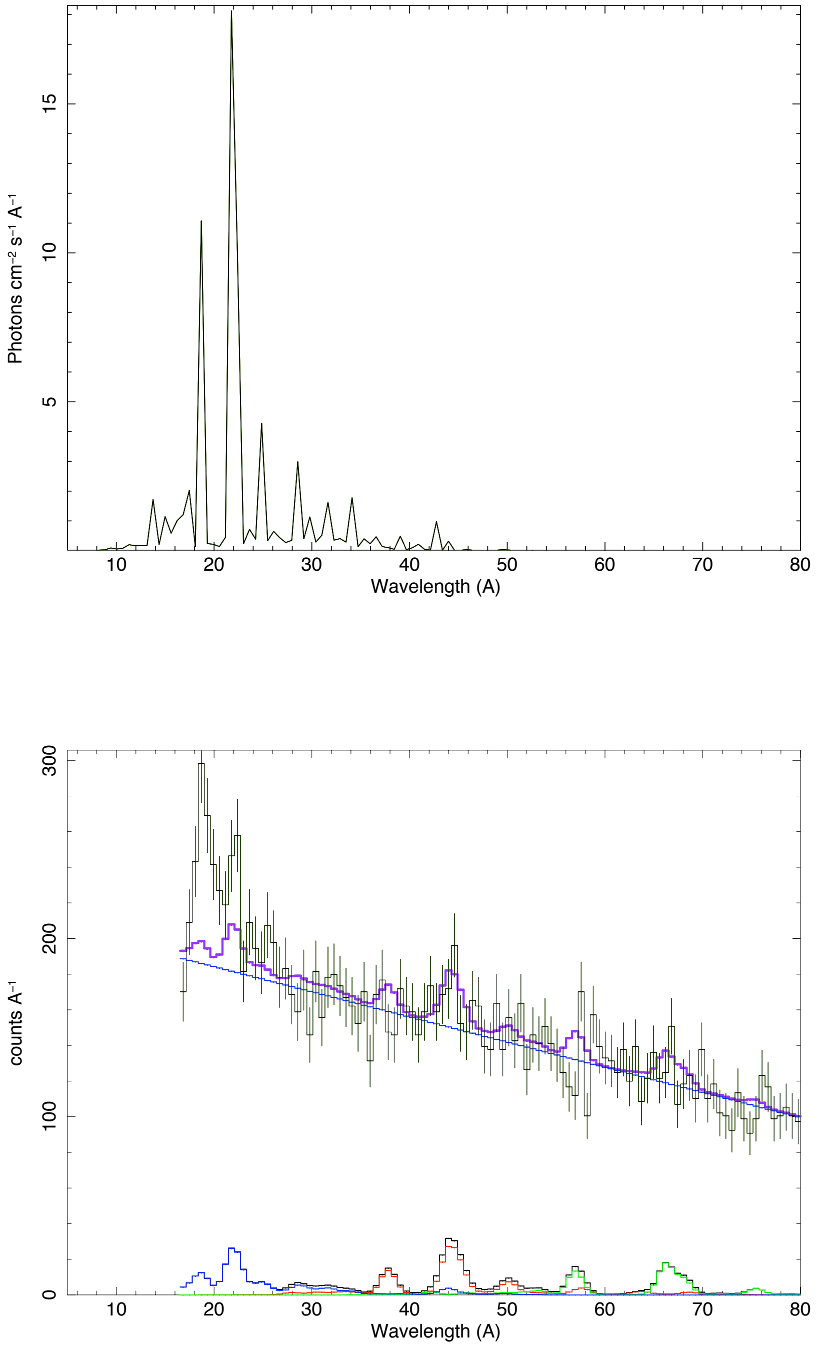

Figure 4.13 Thermal non-equilibrium with noise model and fit. **Top** - Incident model. Here the black line represents the non-equilibrium model. **Bottom** - Convolution of the model with the EXOS effective area curve. The colors here are arranged to match the effective area curves in Figue 3.27: the blue, red, and green lines represent the convolution of the model with the EXOS effective area in orders one, two, and three respectively. The blue line is the noise response (which doesn't have multiple order responses as it is generated inside the detector). The purple line is the sum of all model components. This model is a thermal non-equilibrium model with a $T_e = 0.19$ keV, an absorbing column density of 1.3×10^{21} cm^{-2} and a ionization timescale of 4.2×10^{11} s/cm^3.

normalization of 200, and a rolloff frequency of 2.4×10^{17} Hz. The two gaussians were centered at 19.5 ± 0.26 and 21.9 ± 0.19 Å respectively. These lines could be generated by thermalized gas or could possibly be generated by fluorescence from synchrotron emission. The two spectral lines are insufficient in flux to account for the observed counts in first order. However any increase in their strength will also increase the strength of their respective second and third order lines beyond what is supported by the data. Even with flattest synchrotron spectral index and maximum normalization, the total flux generated by synchrotron emission is substantially less than the flux in spectral lines. The spectral lines make up 66% of the flux, while continuum emission generates only 34%. Thus even with a noise component we are unable to find any compelling evidence in favor of a synchrotron emission model.

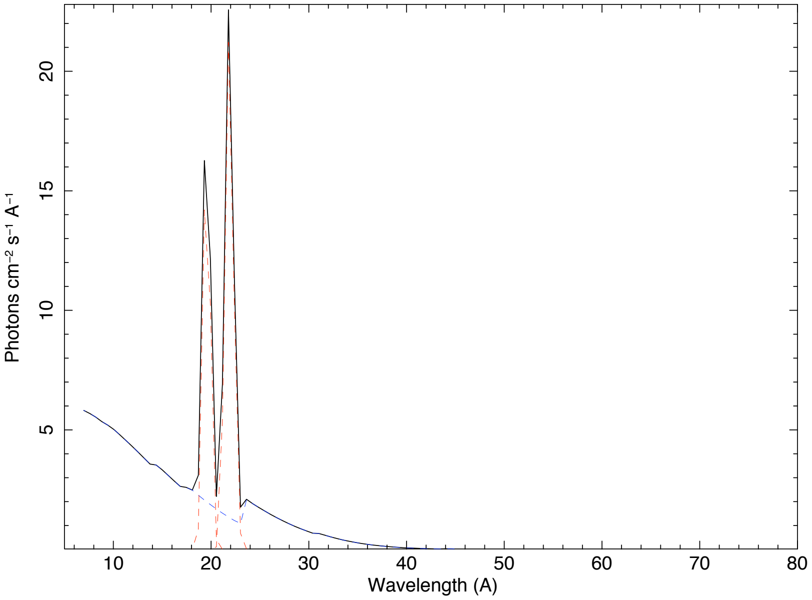

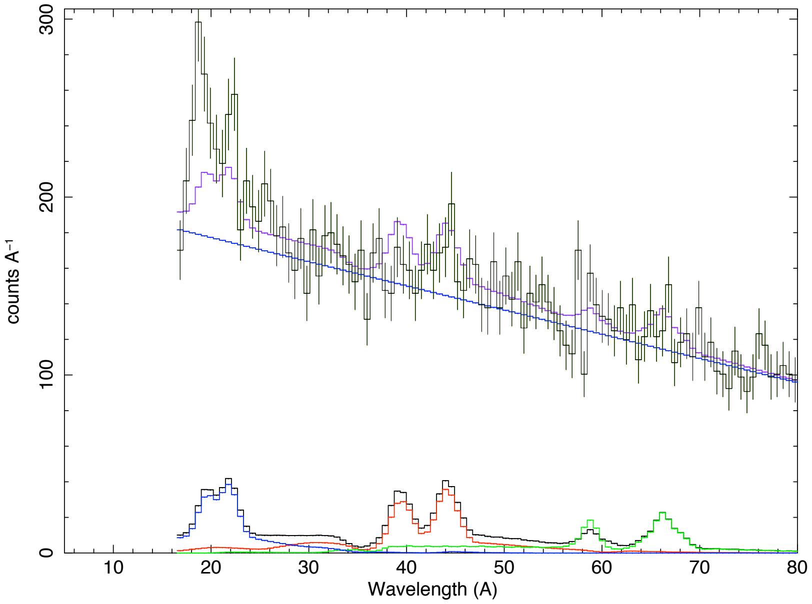

Figure 4.14 Synchrotron model with two gaussians and a noise component and fit. **Top** - Incident model. Here the black line represents the sum of the synchrotron component (blue dashed line) and two gaussians (red dashed line). **Bottom** - Convolution of the model with the EXOS effective area curve. The colors here are arranged to match the effective area curves in Figure 3.27: the blue, red, and green lines represent the convolution of the model with the EXOS effective area in orders one, two, and three respectively. The blue line is the noise response (which doesn't have multiple order responses as it is generated inside the detector). The purple line is the sum of all model components.

4.1.4 Modified Order Distribution

This section describes our fitting attempts utilizing variables to characterize the efficiency of higher order diffraction. The relationship between wavelength and efficiency shown in Figure 3.27 is preserved, but the absolute value of the efficiency is allowed to float for each order. The best fit parameters for these efficiencies (ϵ_2 and ϵ_3) will be described as a percentage of the efficiency in first order.

Our first attempt with variable efficiencies is the equil thermal equilibrium model (Figure 4.15 and Table 4.4). This model achieves far better fits with a $\chi^2_\nu = 91/95$. The parameters of interest are: an absorbing column density of $\mathrm{N}_H = 9.5^{+1.5}_{-1.0} \times 10^{20}$ cm^{-2} and a temperature of $\mathrm{kT}_e = 0.23 \pm .02$ keV. The joint confidence intervals are shown in Figure 4.16 for n_H and kT_e. The distribution of diffracted orders was dominated by first order. The normalization compared to first order was: $0^{+6.4}_{-0}$ % for second order and $3.0^{+13.7}_{-3.0}$ % for third order.

The main lines of interest are produced by C, N, O and Si. It is important to set the overall abundance of these four elements properly. Most observations of the Cygnus Loop have determined low abundances for metals. Unfortunately these abundances vary rather dramatically. For example Miyata et al. (2007) found abundances for O as low as 0.08, while Levenson et al. (2002) determined an abundance of 0.53. This is mostly due to observing in different regions of the loop, as well as utilizing different thermal models. Abundances of Si are even more varied depending upon location, ranging from 0.19 (Miyata et al. 2007) to 1.9 (Miyata et al. 1998). This makes it difficult to set initial values for these abundances. We initially set carbon, nitrogen and oxygen abundances equal to each other which is a crude, but common technique for fits of this nature (Miyata et al. (1998), Miyata & Tsunemi (2001), etc.). The most relevant metallicity measurement for our spectrum is that from the CyXESS spectrum (McEntaffer & Cash 2008). They determined an abundance of 0.44 for Nitrogen, however did not deplete C or O despite previous findings. For the EXOS spectrum we use a 0.44 abundance for these three elements. This also agrees with the 0.44 value for O found by Levenson et al. (2002) (who did not vary N or C). This abundance is also within the

Table 4.4. Best fit parameters for various thermal fits on the EXOS detector 0 spectrum

Parameter	vequil model	vnei model	vpshock model
N_H (cm^{-2})	$9.5^{+1.5}_{-1.0} \times 10^{20}$	$7.4^{+1.4}_{-1.0} \times 10^{20}$	$7.1 \pm 0.1 \times 10^{20}$
kT_e (keV)	$0.23 \pm .02$	$0.28 \pm .03$	$0.28 \pm .02$
τ_u (cm^3 s)	-	$3.0^{+1.3}_{-0.7} \times 10^{11}$	$2.8^{+1.4}_{-0.9} \times 10^{11}$
τ_l (s/cm^3)	-	-	$2.7^{+1.3}_{-0.8} \times 10^{11}$
ϵ_2 (%)	$0^{+6.4}_{-0}$	$0^{+7.4}_{-0}$	$0^{+3.5}_{-0}$
ϵ_3 (%)	$3.0^{+13.7}_{-3.0}$	$1.7^{+12.7}_{-1.7}$	$0^{+8.4}_{-0}$
C = N = O	$0.44\ Z_\odot$	$0.44\ Z_\odot$	$0.44\ Z_\odot$
χ^2_ν	91/95	88/94	88/93

Note. — Variables ϵ_2 and ϵ_3 are the normalization of second and third order diffraction strength with respect to first order.

uncertainty of the best fit for C, N and O found by Miyata & Tsunemi (2001) for several regions. Due to the drastic variability of Si we leave this abundance set at cosmic levels. Attempts to vary these levels did not produce significantly better fits.

A non-equilibrium model also fits well ($\chi^2_\nu = 88/94$) with a temperature of $kT_e = 0.28 \pm .03$ keV, an ionization timescale of $\tau = 3.0^{+1.3}_{-0.7} \times 10^{11} cm^3 s$ and an absorbing column density of $N_H = 7.4^{+1.4}_{-1.0} \times 10^{20}$ cm^{-2}. The higher order efficiencies were: $\epsilon_2 = 0^{+7.4}_{-0}$ % and $\epsilon_3 = 1.7^{+12.7}_{-1.7}$ %. The abundances of C, N and O were again frozen at 0.44 cosmic. The fit values are listed in Table 4.4 and the fit is shown in Figure 4.17. This ionization timescale is large enough ($\gtrsim 3 \times 10^{11}$) that this model is functionally in a state of equilibrium. This model describes the same basic physical situation as the previous equilibrium model as the temperatures and equilibrium status are consistent. The parameters of most interest are the temperature and ionization timescale. The joint confidence intervals for these are shown in Figure 4.18. The χ^2 value becomes large quickly as τ decreases to $\sim 1 \times 10^{11} cm^3$ s. This implies that any amount of non-equilibrium conditions quickly deteriorates the fit quality.

This ionization timescale in combination with the electron density can provide an estimate of the remnants age ($\tau =\ n_e\ t_{\rm age}$). The best-fit model normalization to our model contains the emission measure of the remnant. Assuming a distance of 440^{+130}_{-100} pc (Blair et al. 1999), and

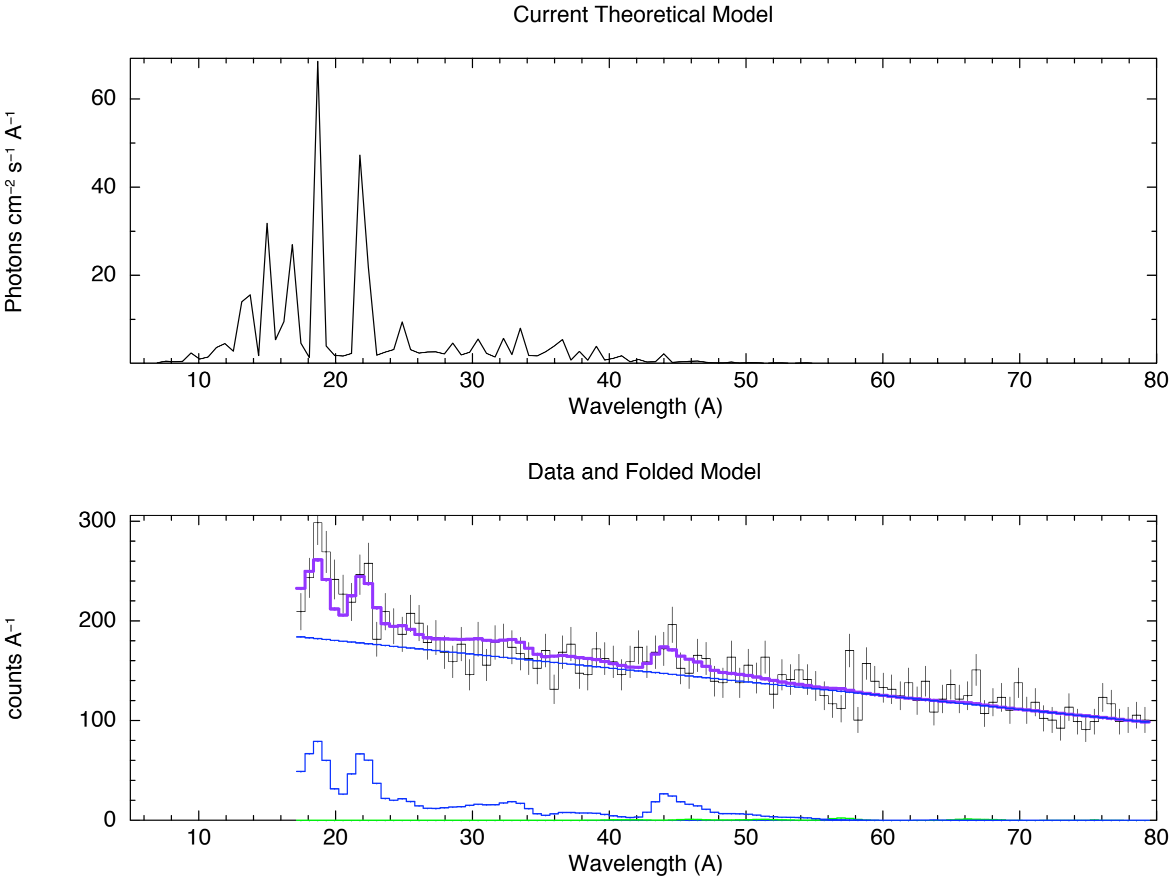

Figure 4.15 Thermal equilibrium with noise model and fit convolved with modified order distributions. **Top** - Incident model. Here the black line represents the thermal equilibrium model. **Bottom** - Convolution of the model with the EXOS effective area curve. The blue curve represents the incident model convolved with the effective area curve in first order. The green curve is the incident model convolved with the third order response. The second order best-fit efficiency is negligible and is therefore not shown. The best-fit parameters had no second order response. The blue line is the noise response. The purple line is the sum of all model and noise components. This model is a thermal equilibrium model with a $T_e = 0.23$ keV, an absorbing column density of 9.5×10^{20} cm^{-2}.

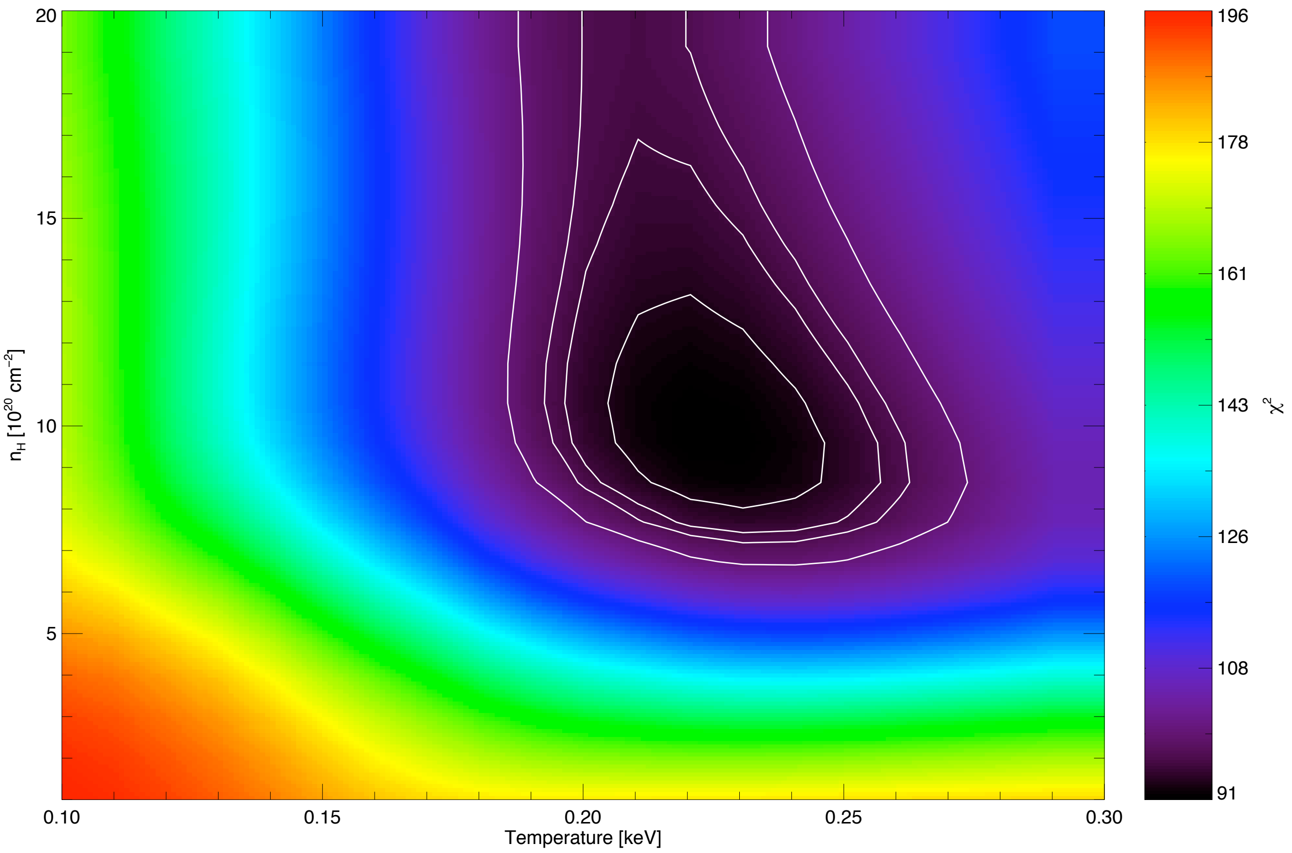

Figure 4.16 Joint confidence interval for temperature and ionization timescale. The contours represent, 68%, 90% and 95% confidence intervals.

estimating an emitting volume of 15 ± 10 % from the high resolution ROSAT image of the Cygnus Loop (Levenson et al. 1997) provides the necessary information to set up a Monte Carlo simulation to determine the electron number density and it's associated 90% confidence interval. The result is a number density of $n_e = 1.24^{+0.65}_{-0.32}$ cm^{-3}. Simulating this density distribution with the ionization timescale (including uncertainties) listed above produces a remnant age of 7595^{+3135}_{-3075} years. As the shock speeds observed in the Cygnus Loop are significantly lower than the young historical remnants (Figure 4.1), this older age is very reasonable and agrees with past findings. The observed shock speeds are 170 - 380 km/s (Blair et al. (1999) and Shull & Hippelein (1991)), compared to the 2700 km/s observed in SN 185 (Vink et al. 2006). Using this age in equation 1.13 gives an expected velocity of 463^{+169}_{-87} km/s. Our model derived age predicts a shock velocity consistent with the observed velocity.

This model is not completely realistic as it only incorporates a single ionization timescale. A more realistic model would consider a range of ionization timescales to account for the variety of densities and ages since the shock interaction began. This model is available in the Xspec package as vpshock. A fit with this model was attempted in Figure 4.19 with the parameters shown in Table 4.4. The best-fit parameters converged on $N_H = 7.1 \pm 0.1 \times 10^{20}$ cm^{-2}, $kT_e = 0.28 \pm 0.02$ keV, and a range of ionization timescales between $2.7^{+1.3}_{-0.8} \times 10^{11}$ and $2.8^{+1.4}_{-0.9} \times 10^{11}$ s/cm^3. This model achieved a $\chi^2_\nu = 88/93$ with order efficiencies of $\epsilon_2 = 0^{+3.5}_{-0}$ % and $\epsilon_3 = 0^{+8.4}_{-0}$ %. Due to the narrow range of ionization timescales, this model results in a nearly identical physical model as the singular ionization timescale model. This fit reveals, both physically and statistically, that a range of ionization timescales does not significantly improve the fit.

The non-equilibrium models do not obtain significantly better fits and have the same physical identically. Thus we do not find it necessary to incorporate non-equilibrium conditions in order to properly fit the spectrum from detector 0.

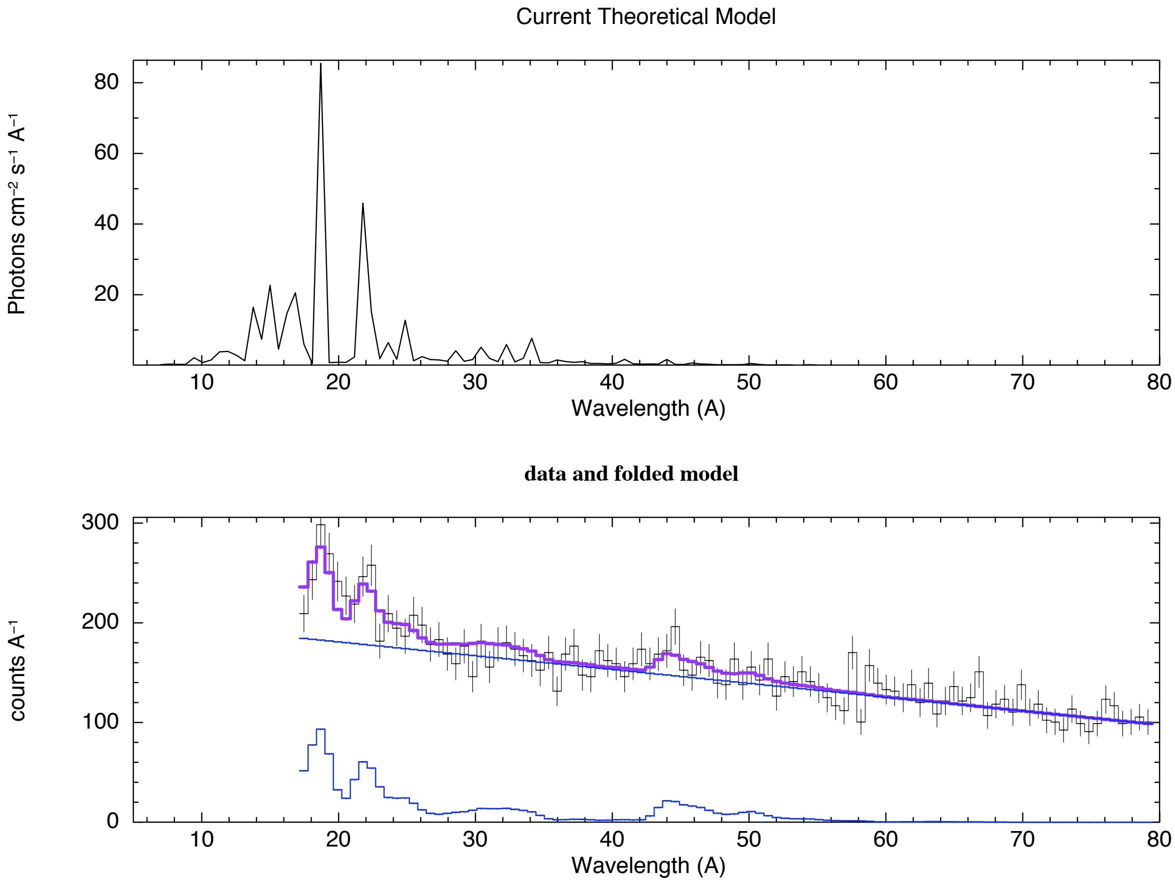

Figure 4.17 Thermal non-equilibrium with noise model and fit convolved with a modified order distribution. **Top** - Incident model. Here the black line represents the non-equilibrium model. **Bottom** - Convolution of the model with the EXOS effective area curve. The blue curve represents the incident model convolved with the effective area curve in first order. Higher order efficiencies were negligible and are therefore not visible in this plot. The blue line is the noise response. The purple line is the sum of all model and noise components. This model is a thermal non-equilibrium model with a $T_e = 0.28$ keV, and ionization timescale of $\tau = 3.0 \times 10^{11}$ and an absorbing column density of 7.4×10^{20} cm^{-2}.

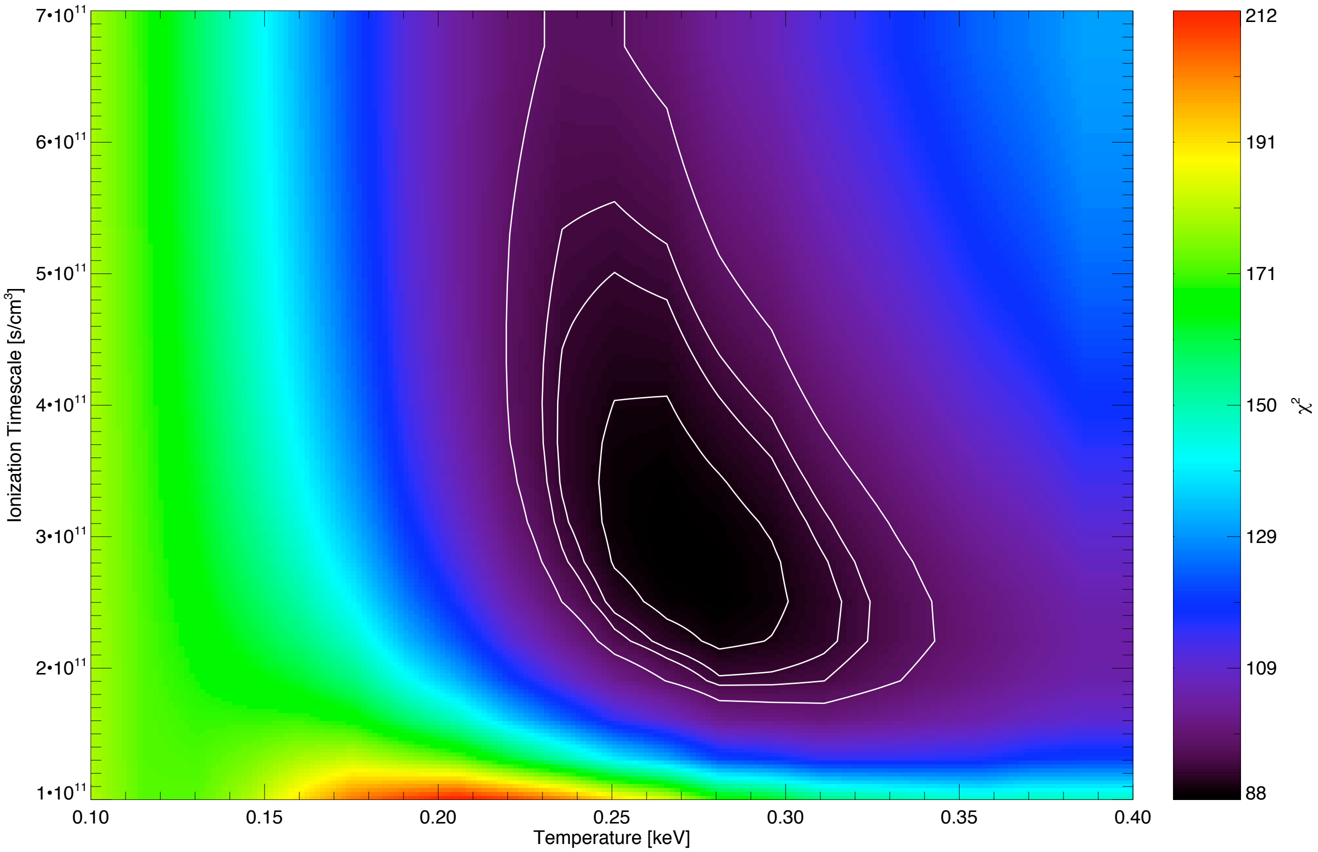

Figure 4.18 Joint confidence interval for temperature and ionization timescale. The contours represent, 68%, 90%, 95% and 99% confidence intervals.

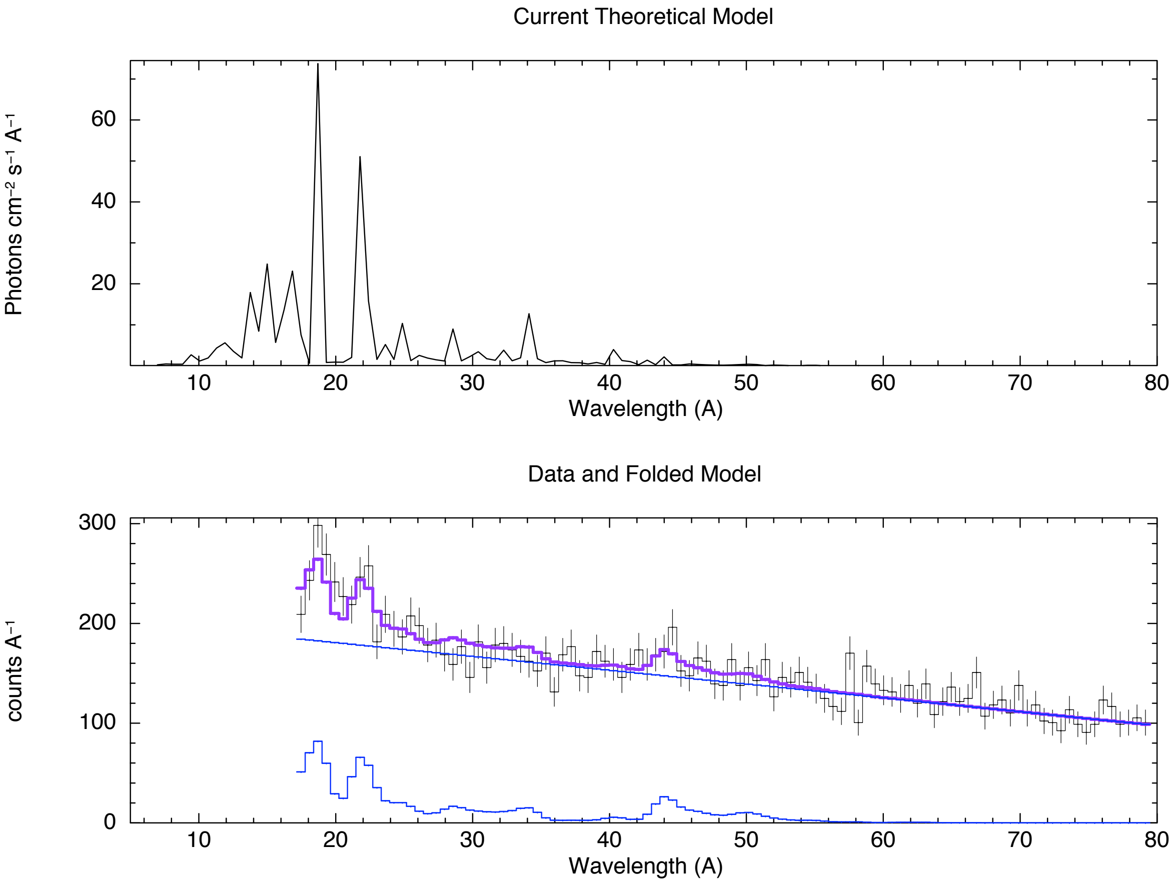

Figure 4.19 Thermal non-equilibrium with a range of ionization timescales and a noise model and fit convolved with only the first order response. **Top** - Incident model. Here the black line represents the non-equilibrium model. **Bottom** - Convolution of the model with the EXOS effective area curve. The blue curve represents the incident model convolved with the effective area curve in first order. The blue line is the noise response. The purple line is the sum of all model components. This model is a thermal non-equilibrium model with a $\mathrm{T}_e = 0.5$ keV, and ionization timescale of: $9.0 \times 10^8 < \tau < 2.1 \times 10^{11}$ s/cm^{-3} and an absorbing column density of 4.6×10^{20} cm^{-2}.

4.2 Detector 1

This section is devoted to analysis of detector 1. Based upon the analysis of detector 0, it is obvious that no global model will account for the observed flux, particularly at longer wavelengths, without a noise component. Consequently we proceed directly to fitting with a noise contribution (shown in Figure 4.20). The fits in Figure 4.21 represent a sample of the attempted global models. These fits include thermal plasma models (both equilibrium and non-equilibrium), synchrotron models as well as various combinations. These models are all poor fits, primarily due to the difficulty of fitting the lack of higher order emission lines. This leads to the same conclusion as detector 0, that our understanding of the efficiency of higher order diffraction is poor.

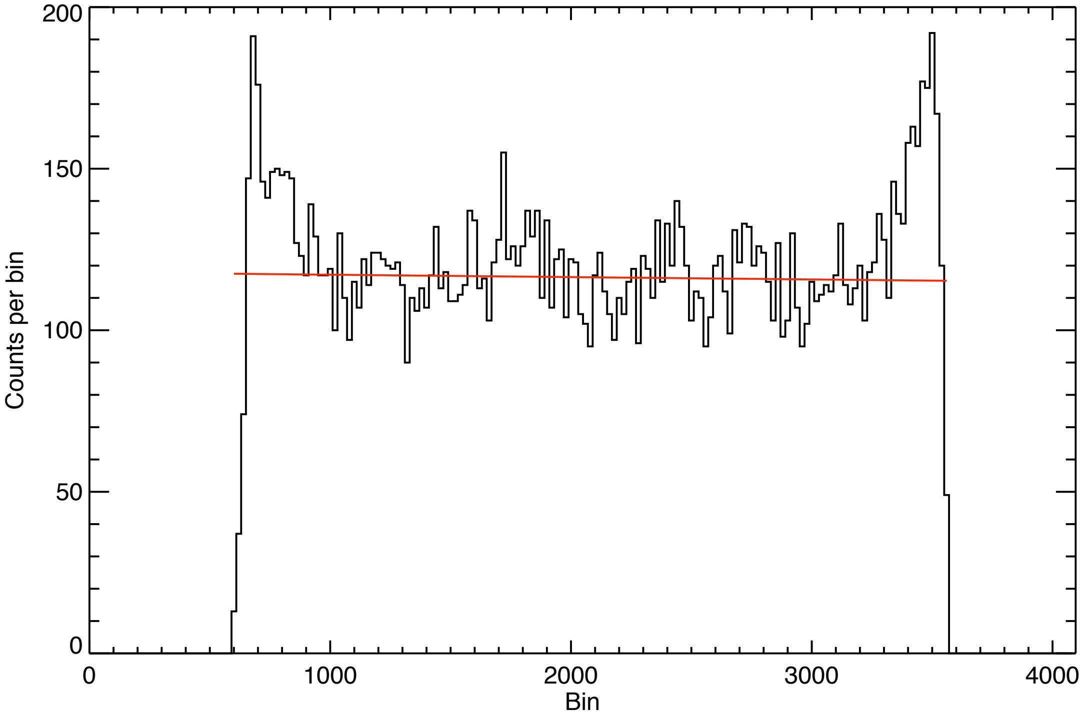

Figure 4.20 Detector 1 noise profile. The red line is the best fit line.

As before we will also attempt fits allowing the higher order efficiencies to vary. These fits are shown in Figures 4.22 - 4.24. We will also cut off the long wavelength end due to the high likelihood that the rise in flux at bins $\lesssim 1000$ is due to the upturn in noise shown in Figure 3.26.

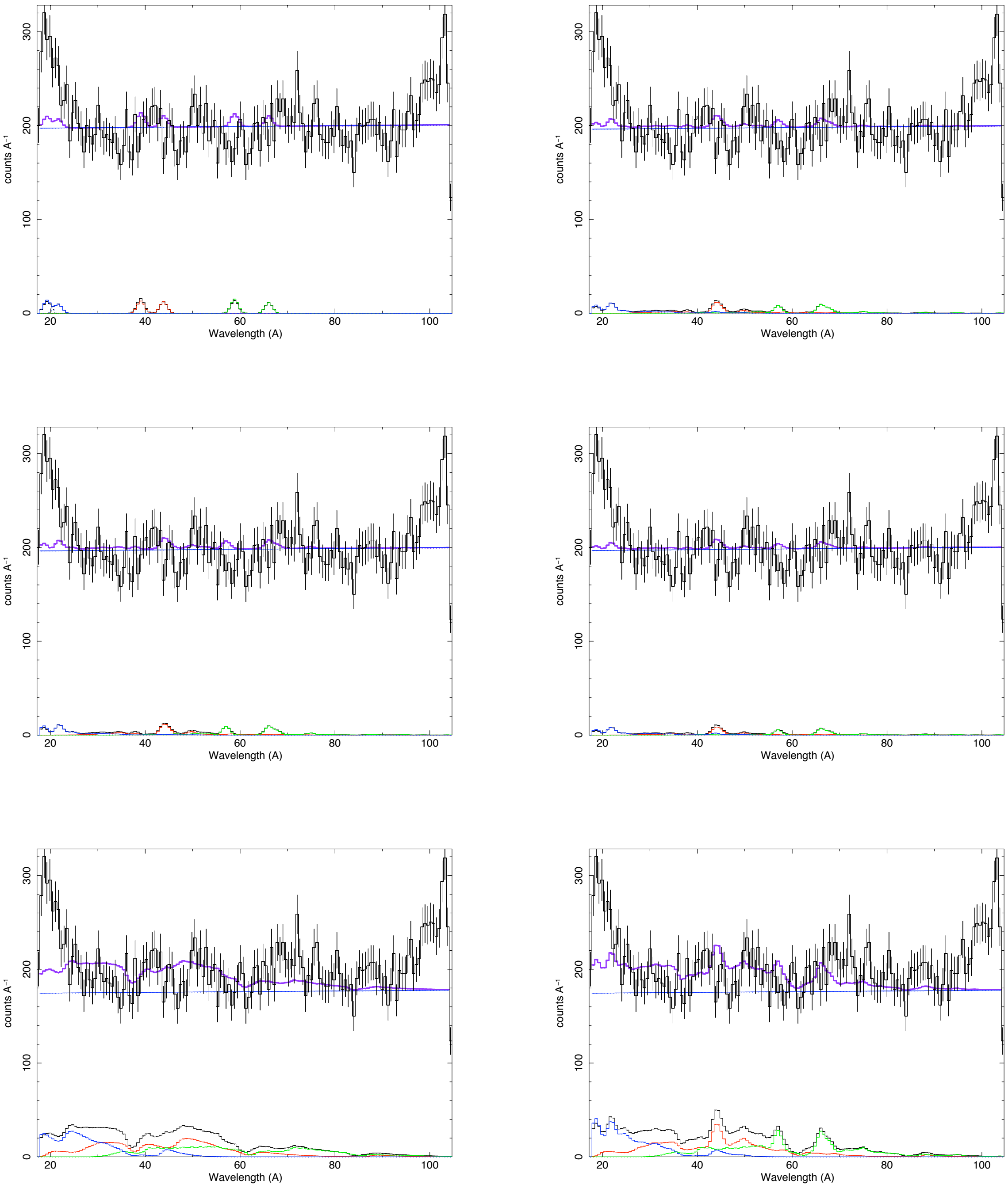

Figure 4.21 Various failed models for detector 1. The colors here are arranged to match the effective area curves in Figue 3.27: the blue, red, and green lines represent the convolution of the model with the EXOS effective area in orders one, two, and three respectively. The black line represents their sum. The blue line is the noise response (which doesn't have multiple order responses as it is generated inside the detector). The purple line is the sum of all model and noise components. **Top Left** - Synchrotron model with two gaussians. **Top Right** - Thermal equilibrium model. Middle Left - Thermal non-equilibrium model. **Middle Right** - Two component equilibrium model. **Bottom Left** - Synchrotron model with reduced noise. **Bottom Right** - Synchrotron and thermal equilibrium models with a reduced noise level.

Table 4.5. Best fit parameters for various thermal fits on the EXOS detector 1 spectrum

Parameter		vequil model	vnei model	vpshock model
N_H (cm^{-2})	....	$1.3^{+0}_{-0.1} \times 10^{21}$	$1.3^{+0}_{-0.1} \times 10^{21}$	$1.3^{+0}_{-0.1} \times 10^{21}$
kT_e (keV)	....	$0.25 \pm .03$	$0.25 \pm .03$	$0.69^{+0.19}_{-0.15}$
τ_u (s/cm^3)	....	-	$1.3^{+48.7}_{-0.5} \times 10^{12}$	$5.5^{+1.5}_{-1.0} \times 10^{11}$
τ_l (s/cm^3)	....	-	-	$0.0^{+1.6}_{-0} \times 10^{10}$
ϵ_2 (%)	....	$0^{+3.1}_{-0}$	$0^{+3.3}_{-0}$	$0^{+1.4}_{-0}$
ϵ_3 (%)	....	$5.2^{+11.4}_{-5.2}$	$3.6^{+10.3}_{-3.6}$	$4.3^{+6.3}_{-4.3}$
C = N = O	....	0.44 $Z_\odot$	0.44 $Z_\odot$	0.44 $Z_\odot$
χ^2_ν	....	147/97	147/96	146/95

Note. — Variables ϵ_2 and ϵ_3 are the normalization of second and third order diffraction strength with respect to first order.

These fits are able to account for the observed emission lines at ∼ 20 Å, but fail to account for the longer wavelength flux. This could be an indication that the noise level on this detector (which was greater than detector 0 during the discharge event) has contaminated the data beyond use. This detector was also less reliable during laboratory testing.

Table 4.5 shows the best fit values for these models. The equilibrium model (Figure 4.22) provides the best statistical fit with a $\chi^2_\nu = 147/97$. The column density for this fit pegs the upper limit of our allowed fit values at 1.3×10^{21}. Values greater than this would conflict with all other previous observations of the Cygnus Loop. The single ionization timescale non-equilibrium model (Figure 4.23) determines an identical temperature (0.25 ± 0.03 keV) and column density. The ionization timescale is also large enough ($1.3^{+48.7}_{-0.5} \times 10^{12}$ s cm^{-3}) that is identical to thermal gas in an equilibrium state. The non-equilibrium model with a range of ionization timescales (Figure 4.24) has a full range from $0 - 5.5 \times 10^{11}$ s cm^{-3} and a higher temperature ($0.69^{+0.19}_{-0.15}$ keV). This fit is not statistically better ($\chi^2_\nu = 146/95$) than a pure equilibrium model. Given that the data from detector 0 shows no need for a non-equilibrium model (and produces much better fits), we find that the equilibrium model produces the most likely scenario.

We conclude our analysis with detector 1 by creating a model with gaussians at optimal locations. The model was fit using lines defined by their first order locations. The higher orders

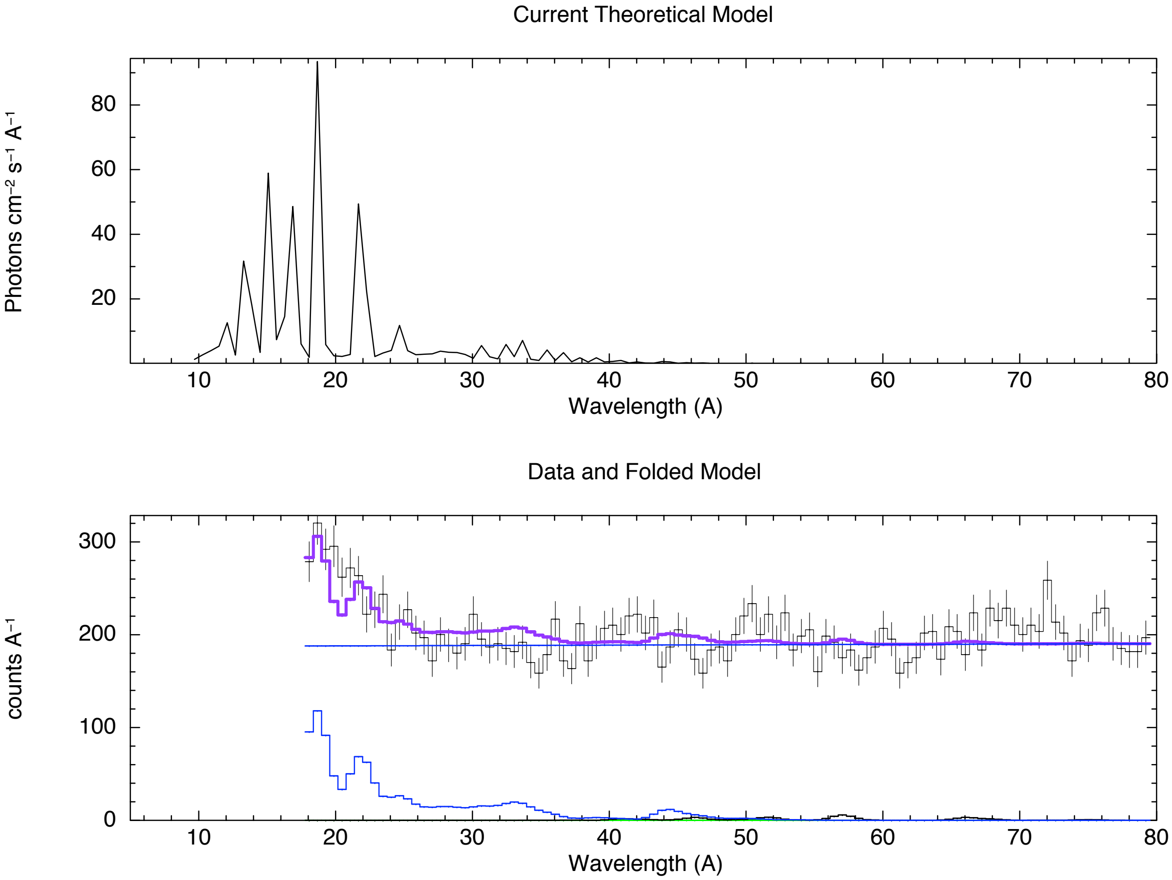

Figure 4.22 Thermal vequil model for detector 1 using modified order distributions. **Top** - Incident model. **Bottom** - Data and folded counts. The blue curve represents the first order response to the incident model, while the green curve represents the third order response. The second order component is negligible and is thus not shown here. The blue line is the noise level. The purple line is the sum of all model and noise components.

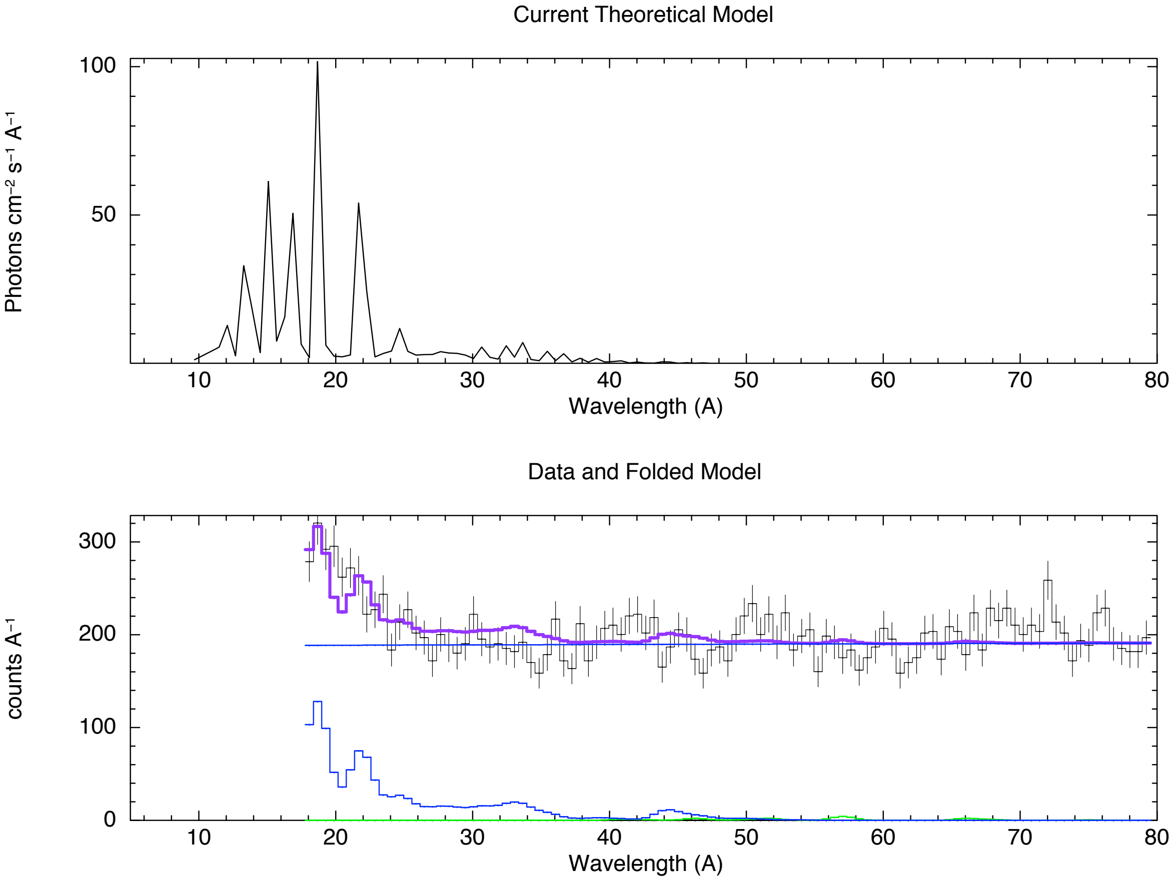

Figure 4.23 Thermal vnei model for detector 1 using modified order distributions. **Top** - Incident model. **Bottom** - Data and folded counts. The blue curve represents the first order response to the incident model, while the green curve represents the third order response. The second order component is negligible and is thus not shown here. The blue line is the noise level. The purple line is the sum of all model and noise components.

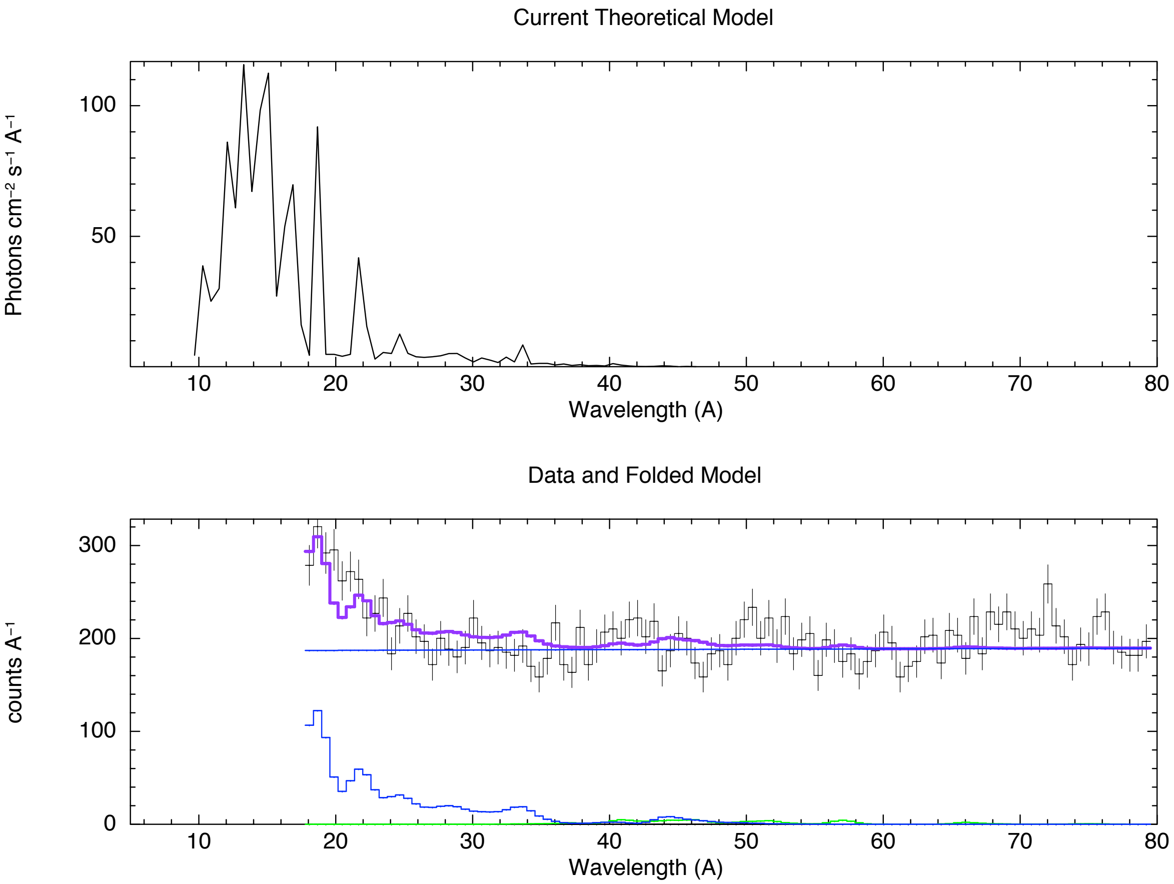

Figure 4.24 Thermal vpshock model for detector 1 using modified order distributions. **Top** - Incident model. **Bottom** - Data and folded counts. The blue curve represents the first order response to the incident model, while the green curve represents the third order response. The second order component is negligible and is thus not shown here. The blue line is the noise level. The purple line is the sum of all model and noise components.

Table 4.6. Possible line identifications for a Gaussian model

λ (Å)	ϵ_2(%)	ϵ_3(%)	Possible Transition
18.6	0	0	O VIII
20.6	4.3	2.6	O VII
23.3	0	36.6	N VI
24.8	143.3	70	N VI
29.9	5.3	17.2	C VI, N VI, Ca XI, Si XII
41.2	0	5.1	C V, Si XI

Note. — Variables ϵ_2 and ϵ_3 are the normalization of second and third order diffraction strength with respect to first order.

were then allowed to vary in strength to best fit the data. The result is shown in Figure 4.25. The locations of the lines are detailed in Table 4.6. The end result is fairly similar to the global thermal models and achieves a $\chi^2_\nu = 110/60$. It is difficult to determine whether some of the lines seen in higher order show evidence of stronger than expected higher order diffraction (based upon the detector 0 analysis), or whether the noise was simply worse for this detector. The possible transitions listed in Table 4.6 are based on the results of thermal models (equil) and possible fluorescent transitions (Cash 2011, private communication).

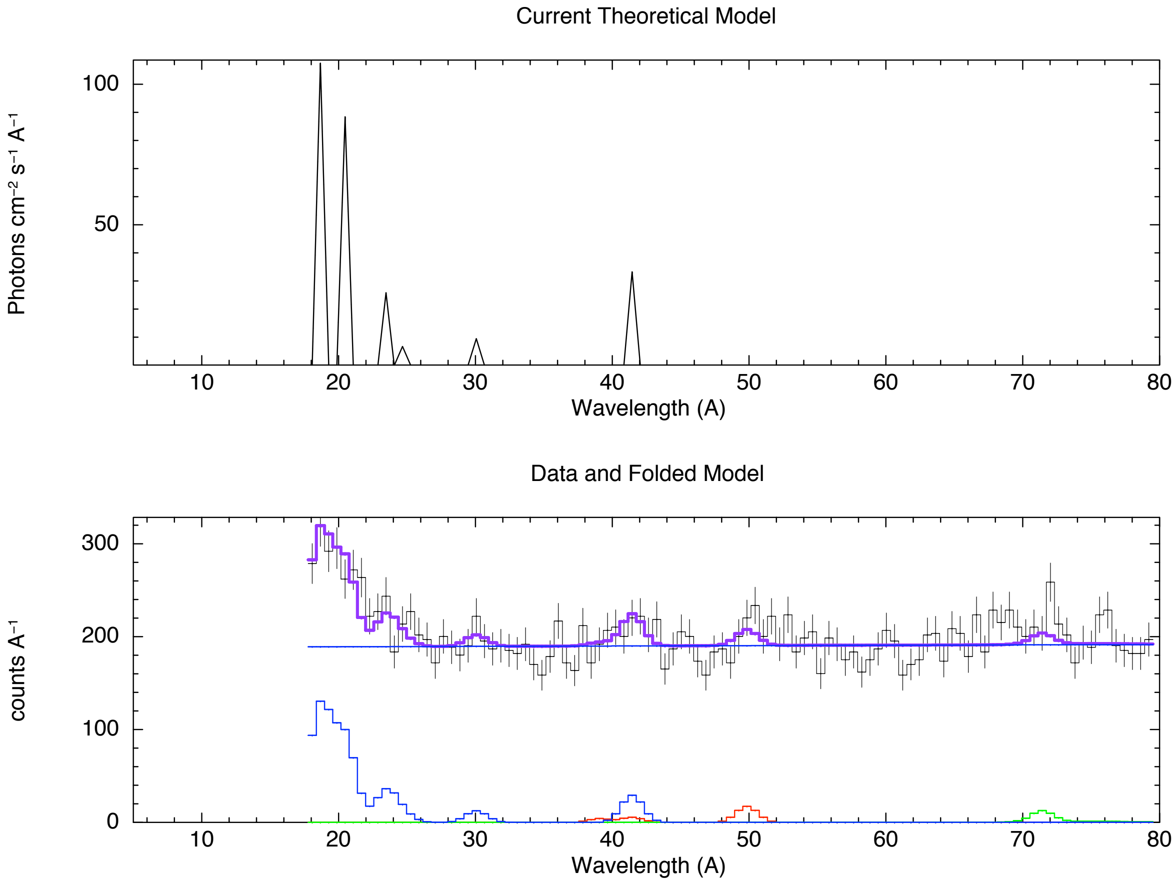

Figure 4.25 Gaussian model using modified order distributions. **Top** - Incident model. **Bottom** - Data and folded counts. The blue curve represents the first order response to the incident model, while the red and green curve represents the second and third order responses. The blue line is the noise level. The purple line is the sum of all model and noise components.

4.3 Results

The model fitting results from detector 0 were successful, achieving a $\chi^2_\nu = 87/94$. The best model was a thermal equilibrium model (vequil) with a temperature of 0.23 ± 0.02 keV and an absorbing column density of $9.5^{+1.5}_{-1.0} \times 10^{20}$ cm^{-2}. This model utilized efficiencies of $\epsilon_2 = 0^{+6.4}_{-0}\%$ and $\epsilon_3 = 3.0^{+13.7}_{-3.0}\%$ and an abundances of 0.44 for carbon, nitrogen and oxygen. Further abundance modifications did not produce significantly better results. Figure 4.26 shows the spectrum and fit with the noise level subtracted. This fit determines a total of 772 photons, which is 8.2% of the total counts recorded by EXOS. This is within the expected count rate range ($1\% - 10\%$) determined in Section 3.3.2. Above the spectrum are the line identifications that are expected given the model parameters. The height of the line indicates its relative predicted strength. These identifications, along with wavelength, transition, incident strength and observed strength, are detailed in Table 4.7. The majority of the flux is contained within two line blends at ~ 19 Å and ~ 22 Å. The first of these line blends is dominated by O VIII with some O VII. The second of these blends is composed of the He-like triplet of O VII at 21.6 Å, 21.8 Å and 22.1 Å. Unfortunately our resolution at this wavelength is not high enough to compare the relative strengths of the triplet transitions in the data and conduct an analysis such as in Vedder et al. (1986) on equilibrium conditions. A major feature is observed at ~ 44 Å. This blend is composed primarily of Si XII with some Si XI emission. A feature that is not well fit is the emission line seen in the data at ~ 26 Å. The model predicts emission from N VII at 24.8 Å, but unfortunately this does not improve the fit to our emission line due to the ~ 1 Å offset. It is quite possible that our wavelength calibration is slightly offset, causing a misalignment between the predicted N VII emission and corresponding model line. The counts longward of ~ 50 Å are most likely noise counts due to their low significance ($< 2\sigma$) as these counts are sitting on a bed of noise with ~ 100 counts / Å. Fortunately a thermal plasma at the best-fit temperature of 0.23 keV does not predict any substantial emission lines in this region, providing further proof of our fit.

Detector 1 generally agrees with this result. The best fit model is an equilibrium plasma model (vequil) with a temperature of 0.25 keV and absorbing column density of 1.3×10^{21} cm^{-2}. This fit was of lower statistical quality ($\chi^2_\nu = 147/97$) than fits for detector 0. This detector experienced a much higher count rate during the discharge event and was generally less stable during laboratory usage. The initial low gain in detector 0 may have actually reduced the amount of damage caused during the discharge event, allowing it to function better after the event had subsided and the gain increased. Therefore the relative agreement between detectors is comforting, but the degraded performance and fit of detector 1 is not surprising.

This result is generally consistent with previous findings. Leahy (2004) find that 21 subregions in the South West limb are best fit with temperatures between 0.17 - 0.21 keV, consistent with our findings. The two component model of Tsunemi et al. (2007) had the softer component at 0.2 keV and near equilibrium conditions, while Uchida et al. (2009a) find the softer component at 0.19 keV. Lastly their follow up study (Uchida et al. 2009b) with 41 observations found an average temperature of 0.23 keV for the softer component, identical to our findings.

These authors also find a harder temperature component, typically $\sim 0.5 - 0.6$ keV in the interior of the remnant. This component is typically necessary out to approximately 80% of the shock radius. Our result indicate that the X-ray emission from the Cygnus Loop is dominated by the softer component at the forward shock front. This is not surprising given the morphology of emission seen in Figure 1.16. However, the noise problems with the GEM detectors from both flights may be degrading our data and hiding more information. Further observations should be conducted with a more reasonable background level to increase our sensitivity to weaker emission features. An increase in resolution would also benefit our analysis by resolving ambiguities in the model parameters.

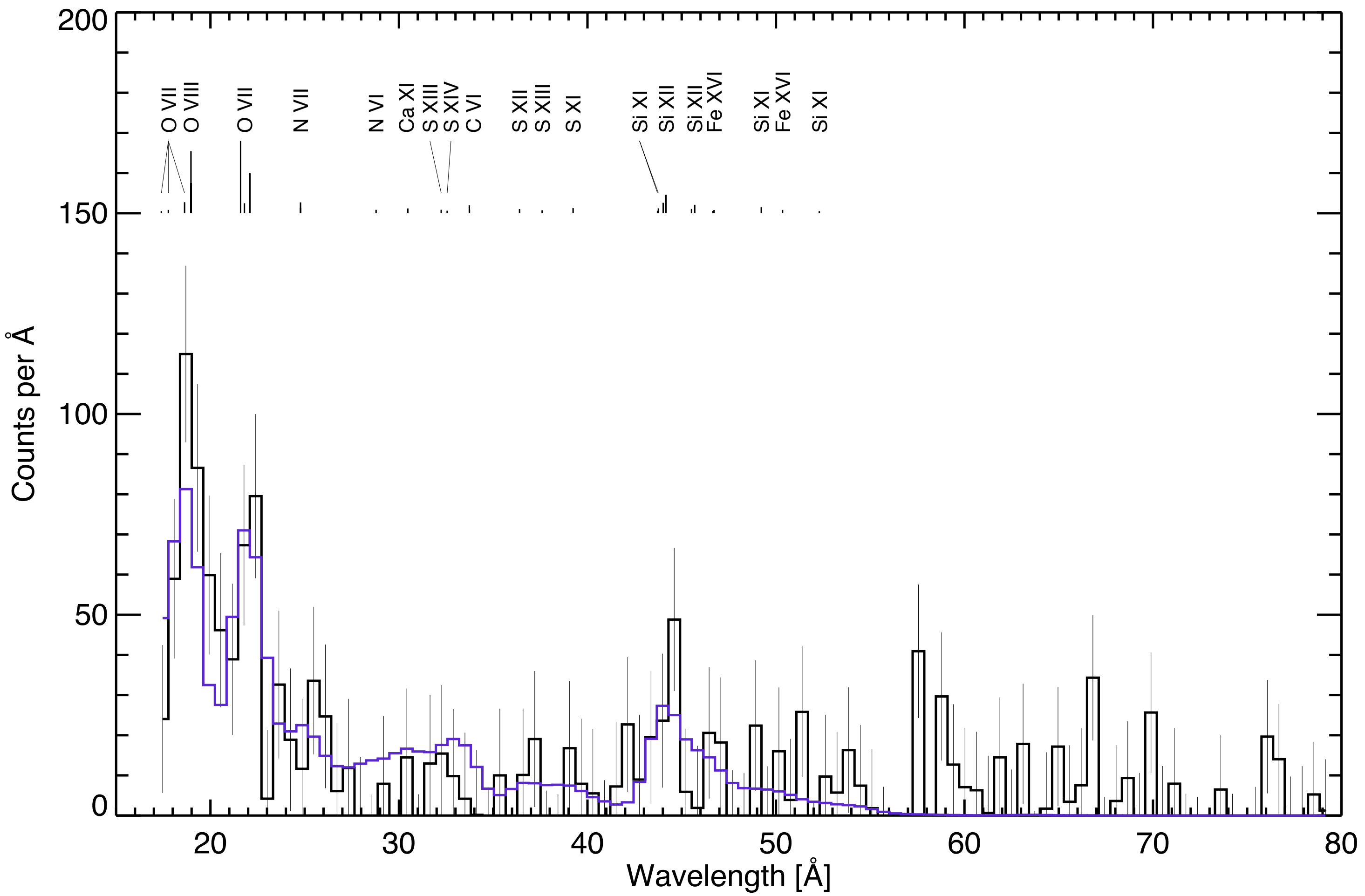

Figure 4.26 The best fit spectrum to EXOS data. A thermal equilibrium model with a temperature of 0.23 keV. The vertical lines above the spectrum indicate major emission lines predicted by the model. The height of the line indicates the strength of the emission after being convolved with the effective area of EXOS at that wavelength. The diagonal lines are simply to clarify the identification. The transition and relative strength of these lines are listed in Table 4.7.

We also compare our results to those from the CyXESS launch (McEntaffer & Cash 2008) to test for consistency. The best-fit model from the CyXESS flight was a thermal equilibrium mekal model at a temperature of 0.14 keV, somewhat lower than the 0.23 keV result found to fit the EXOS data. This comparison is shown in Figure 4.27. The EXOS bandpass is extended to much shorter wavelengths (from 44 Å down to 17 Å). This was done to observe the anticipated oxygen emission lines (see Miyata et al. (2007) and Section 1.4) at energies higher than the CyXESS bandpass. The ability to observe these two ionization states of oxygen (VII and VIII) provides a much more stringent temperature constraint. Measuring the two ionization states provides a direct measure of temperature, rather than relying upon much more sparse elements (such as the Si features fit in the CyXESS data) that result in a much more uncertain fit to the temperature. Given this advantage, the temperature measurement of 0.23 keV is more reliable.

The CyXESS fitting parameters are unable to account for the strength of the observed oxygen emission lines in the EXOS data. The model does reasonably (though not perfectly) fit the line blend at ~ 44 Å seen in both data sets. The EXOS model fits the primary spectral line observed in the CyXESS data set quite well. However the second line (thought to be the He-like O VII triplet seen in second order) is not well-fit. Again this could be due to the uncertainty in our calibrations and lack of high quality calibration sources. The data longward of ~ 50 Å in the CyXESS data is thought to be at least partially caused by detector background noise. This would explain the lack of anticipated counts based on the EXOS model.

The overall count rate is reasonable when comparing EXOS and CyXESS data. The two CyXESS spectral lines have 119 counts in 65 seconds. Extrapolating out to the 340 seconds of useable EXOS observation time gives 622 counts, compared to the 772 counts actually observed (over a more useful bandpass). The noise seen in CyXESS (counts > 50 Å) is observed at a rate of ~ 0.03 counts/s/bin. The noise rate observed over the entire face of the EXOS detectors was ~ 0.30 (a different binsize than utilized in Section 3.3.2). This drastic increase in noise is further proof that the two flights were not seeing a similar unexpected continuum source at longer wavelengths.

The EXOS data confirms the CyXESS finding that the soft X-ray emission is dominated by

Table 4.7. Best fit line identifications based on equilibrium model fits to detector 0

Ion	Wavelength [Å]	Transition	Incident Strength	Observed Strength
O VII	17.396	$1s^2$ - 1s5p	1.000	0.029
O VII	17.768	$1s^2$ - 1s4p	0.858	0.045
O VII	18.627	$1s^2$ - 1s3p	0.552	0.152
O VIII	18.967	1s - 2p	0.417	0.858
O VIII	18.972	1s - 2p	0.152	0.417
O VII	21.601	$1s^2$ - 1s2p [R]	0.113	1.000
O VII	21.804	$1s^2$ - 1s2p [I]	0.067	0.138
O VII	22.098	$1s^2$ - 1s2s [F]	0.064	0.552
N VII	24.779	1s - 2p	0.052	0.150
N VII	24.785	1s - 2p	0.045	0.073
C VI	28.465	1s - 3p	0.039	0.028
C VI	28.466	1s - 3p	0.036	0.013
N VI	28.787	$1s^2$ - 1s2p	0.032	0.047
Ca XI	30.471	$2p^6 - 2p^5 3d$	0.029	0.066
Si XII	31.012	2s - 4p	0.029	0.015
Si XII	32.973	2p - 4d	0.026	0.016
C VI	33.734	1s - 2p	0.019	0.109
C VI	33.740	1s - 2p	0.018	0.052
Si XI	43.763	$2s^2$ - 2s3p	0.017	0.066
Si XII	44.019	2p - 3d	0.013	0.145
Si XII	44.165	2p - 3d	0.012	0.254
Si XII	44.178	2p - 3d	0.012	0.028
Si XII	45.521	2p - 3s	0.011	0.059
Si XII	45.691	2p - 3s	0.008	0.116
Si XI	46.399	2p - 3d	0.007	0.016
Si XI	49.222	2p - 3d	0.007	0.082
Si X	50.524	2p - 3d	0.007	0.016
Si XI	52.298	2p - 3s	0.007	0.029

Note. — Transitions based on Mewe et al. (1985). The incident strength here indicates the strength of the incident emission prior to being convolved with the EXOS effective area curves. The observed strength column represents this strength when convolved with the effective area curves. This last column is the same as the line heights in Figure 4.26.

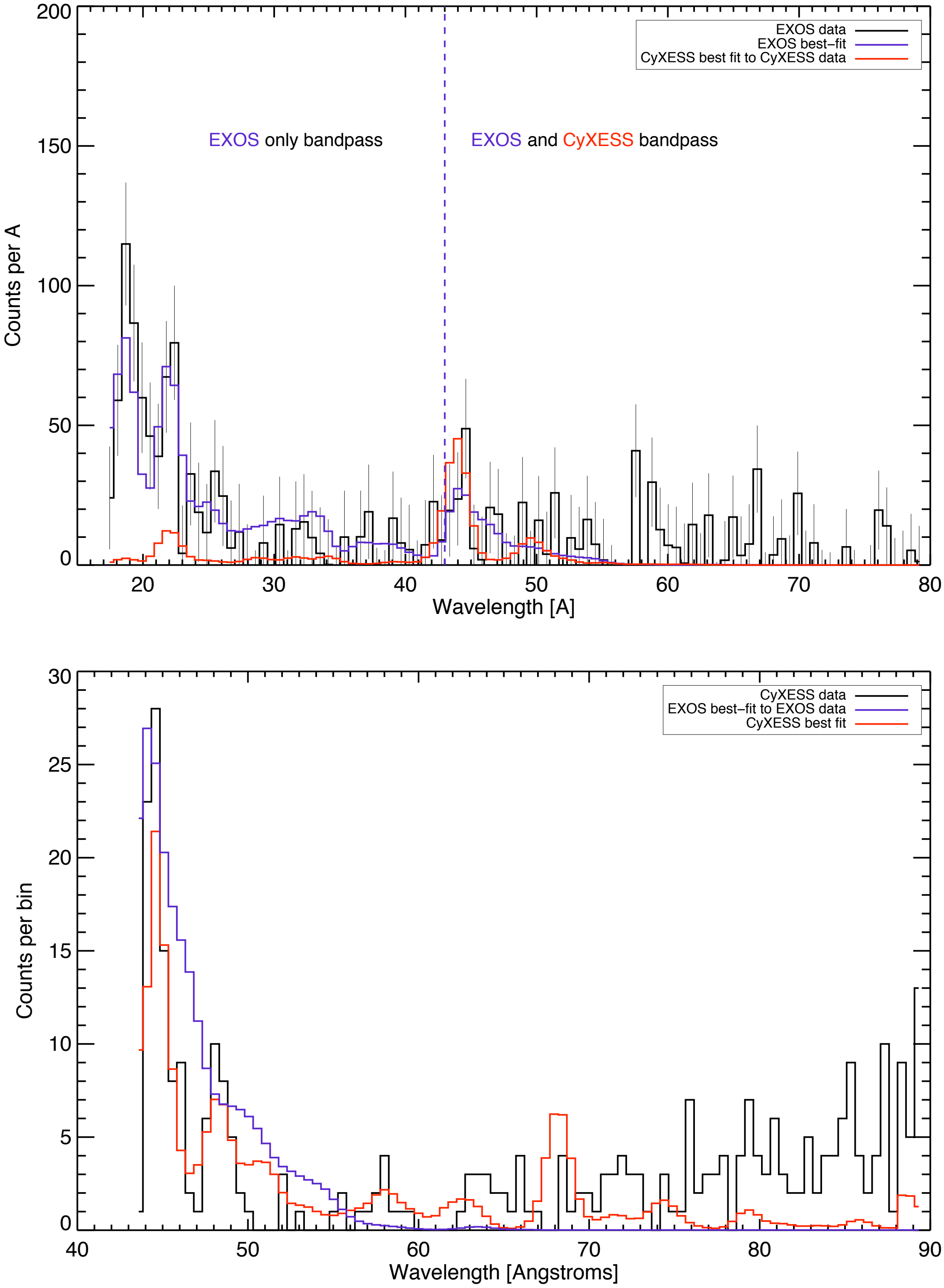

Figure 4.27 Comparison of EXOS and CyXESS data and models **Top** - EXOS data with both the EXOS best fit and the CyXESS best fit, normalized to EXOS flux levels. **Bottom** - CyXESS data with both the CyXESS best fit and the EXOS best fit.

the interaction between the blast wave and the ISM wall. The shifted EXOS bandpass, more stable detectors and more accurate effective area curves find a more reliable temperature value for this softer component.

4.4 Future Work

There are several additional steps that could be taken to improve the payload and provide more detailed analysis for future flights. These steps include vital hardware related improvements as well as interesting, though less vital, steps in the analysis of the flight data. The data were analyzed using the Xspec X-Ray Spectral Fitting Package (Arnaud (1996)) version 12.5.1. Within this package are numerous scientific models developed separately to address a range of astrophysical situations.

Better calibration data is of paramount importance. Specifically, improving our grating efficiency curve (Figure 2.27) by testing at more wavelengths and with an extended source (i.e. the full range of graze angles). The window throughput curve (Figure 2.35) on the GEM detectors should also be verified. These test are challenging as they require a light source that is not only extended in size, but one that is emitting monochromatic light. Currently no X-ray light source in the Rocket Calibration Facilities (RCF) at CASA fulfill either of these two properties. The current X-ray monochrometer would have to be completely redesigned to allow for extended emission and more reliable performance. Given the need to strongly modify the distribution of diffracted orders in the flight data to obtain an acceptable model fit, these calibrations are necessary to better understand our overall system performance.

The current electronics system of the EXOS payload is very susceptible to noise. On the CyXESS flight, the switching action of a single DC-DC power converter put 600 mV AC noise on the pulse height data, rendering both the pulse-height data and the detector ID bit useless. A similar flaw in the electronics could very easily be the cause of our the noise observed on the EXOS flight. Additionally, the stress of two rocket launches and landings (the EXOS landing in particular) has drastically increased the odds of failure in the various flight connectors. Many of the electrical components flew onboard the two ISIS suborbital payloads (Beasley et al. 2004) in addition to the CyXESS and EXOS flights. The multiple modifications to these components required between these four flights may also have lead to unforeseen noise sources. A complete reworking of the payload electronics (though not necessarily the detector electronics) with more modern techniques would greatly increase the chance of success on the next flight.

Additional analysis could also be performed on flight data. This study predominately used the Xspec fitting package. Other packages such as ISIS (Houck & Denicola 2000) and Cloudy (Ferland et al. 1998) were also consulted. Preliminary tests from these packages produced similar results, but further testing could always be performed. This additional testing is not necessary on the EXOS flight data as the major spectral lines were well fit with the Xspec models, the noise degradation makes more detailed analysis highly uncertain, and the initial tests with these other packages produced similar results.

Chapter 5

Conclusion

High resolution X-ray spectroscopy is important to better understand the evolution and energy balance of supernova remnants. Through spectral diagnostics in the soft X-ray bandpass (17-107 Å), we can determine metrics of interest such as temperature, composition and equilibrium state. The Extended X-ray Off-plane Spectrometer (EXOS) payload was designed to accomplish this task on the Cygnus Loop Supernova Remnant. The optical path of the payload is defined by three main components: a wire-grid collimator, off-plane grating arrays and gas electron multiplier detectors. This payload was constructed as an improvement to the CyXESS payload (McEntaffer & Cash 2008). In particular the GEM detectors were modified to use new laser-etched GEM foils. The improved detectors were far more stable in both noise and gain. The EXOS payload was launched from White Sands Missile Range, New Mexico on November 13, 2009 at 7:30 PM, and obtained 340 seconds of useable scientific data. The emission is dominated by O VII and O VIII, including the He-like O VII triplet at ~ 22 Å. Another feature at ~ 45 Å is composed primarily of Si XI and Si XII. The best-fit model to this spectrum is an equilibrium plasma model at a temperature of $\log(\mathrm{T}) = 6.4$ (0.23 keV), likely dominated by the interaction of the initial blast front with the surrounding ISM. This temperature is consistent with previous observations. Some previous observations indicate a need for a second temperature component to account for the material the reverse shock reheats interior to the (softer) forward blast wave. Our ability to observe this component may be limited by the noise level of our detectors. Further observations at this resolution, or higher, are necessary with improved detectors to definitively show the importance of this component.

Bibliography

Arendt, R., Dwek, E., & Leisawitz, D. 1992, The Astrophysical Journal, 400, 562

Arnaud, K. A. 1996, Astronomical Data Analysis Software and Systems V, 101, 17

Aschenbach, B. & Leahy, D. 1999, Astronomy and Astrophysics, 341, 602

Ballet, J. 1989, Astron. Astrophys., 211, 217

Beasley, M., Boone, C., Cunningham, N., Green, J., & Wilkinson, E. 2004, Applied optics, 43, 4633

Benvenuti, P., Dopita, M., & D'Odorico, S. 1980, The Astrophysical Journal, 238, 601

Blair, W. P., Long, K. S., Vancura, O., & Bowers, C. 1991, The Astrophysical, 379, 33

Blair, W. P., Sankrit, R., Raymond, J. C., & Long, K. S. 1999, The Astronomical Journal, 118, 942

Bleeker, J. 1990, Advances in Space Research, 10, 143

Borken, R., Doxsey, R., & Rappaport, S. 1972, The Astrophysical Journal, 178, L115

Borkowski, K. J., Lyerly, W. J., & Reynolds, S. P. 2001, The Astrophysical Journal, 548, 820

Borkowski, K. J., Sarazin, C. L., & Blondin, J. M. 1994, The Astrophysical Journal, 429, 710

Braun, R. & Strom, R. G. 1986, Astronomy and Astrophysics, 164, 208

Cash, W. 1982, Applied Optics, 21, 710

—. 1991, Applied Optics, 30, 1749

Cassam-Chenai, G., Hughes, J. P., Reynoso, E., Badenes, C., & Moffett, D. 2008, The Astrophysical Journal, 680, 1180

Chevalier, R. 1977, Annual Review of Astronomy and Astrophysics, 15, 175

Contini, M. & Shaviv, G. 1982, Astrophysics and Space Science, 85, 203

Danforth, C., Cornett, R., Levenson, N., Blair, W. P., & Stecher, T. 2000, The Astronomical Journal, 119, 2319

Ferland, G. J., Korista, K. T., Verner, D. A., Ferguson, J. W., Kingdon, J. B., & Verner, E. M. 1998, Publications of the Astronomical Society of the Pacific, 110, 761

Fesen, R. & Itoh, H. 1985, The Astrophysical Journal, 295, 43

Fesen, R., Kwitter, K., & Downes, R. 1992, The Astronomical Journal, 104, 719

Gorenstein, P., Harris, B., Gursky, H., & Giacconi, R. 1971a, Nuclear Instruments and Methods, 91, 451

Gorenstein, P., Harris, B., Gursky, H., Giacconi, R., Novick, R., & Vanden Bout, P. 1971b, Science, 172, 369

Graham, J., Wright, G., & Geballe, T. 1991a, The Astrophysical Journal, 372, 21

Graham, J., Wright, G., Hester, J., & Longmore, A. 1991b, The Astronomical Journal, 101, 175

Green, D. A. 2009, Bull. Astr. Soc. India, 45

Greidanus, H. & Strom, R. G. 1992, Astron. Astrophys, 257, 265

Gronenschild, E. 1980, Astronomy and Astrophysics, 85, 66

Gunderson, K., Wilkinson, E., & Green, J. 2000, Proceedings of SPIE, 4013, 421

Hamilton, A., Sarazin, C. L., & Chevalier, R. 1983, The Astrophysical Journal Supplement Series, 51, 115

Hester, J. & Cox, D. 1986, The Astrophysical journal, 300, 675

Hester, J., Raymond, J. C., & Blair, W. P. 1994, The Astrophysical Journal, 420, 721

Houck, J. C. & Denicola, L. 2000, in Astronomical Data Analysis Software and Systems IX (Stanford Research Institute), 591–594

Hughes, J. P., Hayashi, I., & Koyama, K. 1998, The Astrophysical Journal, 505, 732

Hwang, U., Laming, J. M., Badenes, C., Berendse, F., Blondin, J. M., Cioffi, D., Delaney, T., Dewey, D., Fesen, R., Flanagan, K. A., Fryer, C. L., Ghavamian, P., Hughes, J. P., Morse, J., Plucinsky, P. P., Petre, R., & Pohl, M. 2004, The Astrophysical Journal, 615, 117

Hwang, U., Petre, R., Szymkowiak, A. E., & Holt, S. S. 2002, Journal of Astrophysics and Astronomy, 23, 81

Kaplan, D., Gaensler, B., Kulkarni, S., & Slane, P. 2006, The Astrophysical Journal Supplement Series, 163, 344

Katsuda, S., Tsunemi, H., Kimura, M., & Mori, K. 2008, The Astrophysical Journal, 680, 1198

Kirshner, R. P. & Taylor, K. 1976, The Astrophysical Journal, 208, 83

Koyama, K., Petre, R., Gotthelf, E., Hwang, U., Matsuura, M., Ozaki, M., & Holt, S. S. 1995, Nature, 378, 255

Kundu, M. & Becker, R. 1972, The Astronomical Journal, 77, 459

Leahy, D. 2002, The Astronomical Journal, 123, 2689

—. 2004, Monthly Notices of the Royal Astronomical Society, 351, 385

Leahy, D., Fink, R., & Nousek, J. 1990, The Astrophysical Journal, 363, 547

Leahy, D. & Roger, R. 1998, The Astrophysical Journal, 505, 784

Leahy, D., Roger, R., & Ballantyne, D. 1997, The Astronomical Journal, 114, 2081

Levenson, N. & Graham, J. 2001, The Astrophysical Journal, 559, 948

Levenson, N., Graham, J., Aschenbach, B., Blair, W. P., Brinkmann, W., Busser, J., Egger, R., Fesen, R., Hester, J., Kahn, S. M., Klein, R., McKee, C., Petre, R., Pisarski, R., Raymond, J. C., & Snowden, S. L. 1997, The Astrophysical Journal, 484, 304

Levenson, N., Graham, J., Keller, L., & Richter, M. J. 1998, The Astrophysical Journal Supplement Series, 118, 541

Levenson, N., Graham, J., & Snowden, S. L. 1999, The Astrophysical Journal, 526, 874

Levenson, N., Graham, J., & Walters, J. L. 2002, The Astrophysical Journal, 576, 798

Liedahl, D. A., Osterheld, A. L., & Goldstein, W. H. 1995, The Astrophysical Journal, 438, 115

Masai, K. 1994, The Astrophysical Journal, 437, 770

McEntaffer, R. L. & Brantseg, T. 2011, The Astrophysical Journal, submitted

McEntaffer, R. L. & Cash, W. 2008, The Astrophysical Journal, 680, 328

McEntaffer, R. L., Cash, W., Shipley, A., & Schindhelm, E. 2006, Proc. SPIE, 6266, 1

McEntaffer, R. L., Hearty, F. R., Gleeson, B., & Cash, W. 2004a, Proc. SPIE, 5168, 499

McEntaffer, R. L., Murray, N., Holland, A. D., Tutt, J., Barber, S. J., Harriss, R., Schultz, T., Casement, S., Lillie, C. F., Dailey, D., Johnson, T., Danner, R., Cash, W., Zeiger, B., Shipley, A., Page, M., Walton, D., Pool, P., Endicott, J., & Willingale, D. 2010, Proceedings of SPIE, 7732, 77321K

McEntaffer, R. L., Osterman, S., Cash, W., Gilchrist, J., Flamand, J., Touzet, B., Bonnemason, F., & Brach, C. 2004b, Proc. SPIE, 5168, 492

McKee, C. 1974, The Astrophysical Journal, 188, 335

Mewe, R., Gronenschild, E., & Van Den Oord, G. 1985, Astron. Astrophys. Suppl. Ser, 62, 197

Mewe, R., Lemen, J. R., & van Den Oord, G. H. J. 1986, Astronomy and Astrophysics Supplement Series, 65, 511

Minkowski, R. 1958, Reviews of Modern Physics, 30, 1048

Miyata, E., Katsuda, S., Tsunemi, H., Hughes, J. P., Kokubun, M., & Porter, F. S. 2007, PASJ, 59, 163

Miyata, E., Ohta, K., Torii, K., Takeshima, T., Tsunemi, H., Hasegawa, T., & Hashimoto, Y. 2001, The Astrophysical Journal, 550, 1023

Miyata, E. & Tsunemi, H. 2001, The Astrophysical Journal, 552, 624

Miyata, E., Tsunemi, H., Kohmura, T., Suzuki, S., & Kumagai, S. 1998, PASJ, 50, 257

Moffat, P. 1971, Monthly Notices of the Royal Astronomical Society, 153, 401

Neviere, M., Maystre, D., & Hunter, W. R. 1978, Journal of the Optical Society of America, 68, 1106

Osterman, S., McEntaffer, R. L., Cash, W., & Shipley, A. 2004, Proceedings of SPIE, 5488, 302

Raymond, J. C., Davis, M., Gull, T., & Parker, R. 1980, The Astrophysical Journal, 238, 21

Raymond, J. C., Hester, J., Cox, D., Blair, W. P., Fesen, R., & Gull, T. 1988, The Astrophysical Journal, 324, 869

Raymond, J. C. & Smith, B. 1977, The Astrophysical Journal Supplement Series, 35, 419

Reynolds, S. P. 1998, The Astrophysical Journal, 493, 375

Reynolds, S. P., Borkowski, K. J., Hwang, U., Hughes, J. P., Badenes, C., Laming, J. M., & Blondin, J. M. 2007, The Astrophysical Journal, 668, 135

Reynolds, S. P. & Keohane, J. W. 1999, The Astrophysical Journal, 525, 368

Sauvageot, J. L. & Decourchelle, A. 1995, Astronomy and Astrophysics, 296, 201

Schindhelm, E., Burgh, E., Kane, R., Gantner, B., Levine, S., Beasley, M., & Green, J. 2010, SPIE Proceedings, 7732, 773207

Seward, F. D. 1990, The Astrophysical Journal Supplement Series, 73, 781

Shull, P. & Hippelein, H. 1991, The Astrophysical Journal, 383, 714

Simon, F., Azmoun, B., Becker, U., Burns, L., Crary, D., Kearney, K., Keeler, G., Majka, R., Paton, K., Saini, G., Smirnov, N., Surrow, B., & Woody, C. 2007, IEEE Transactions on Nuclear Science, 54, 2646

Straka, W., Dickel, J., Blair, W. P., & Fesen, R. 1986, The Astrophysical Journal, 306, 266

Tamagawa, T., Hayato, A., Abe, K., Iwamoto, S., Nakamura, S., Harayama, A., Iwahashi, T., Makishima, K., Hamagaki, H., & Yamaguchi, Y. 2008, Proc. of SPIE, 7011, 1

Tamagawa, T., Hayato, A., Asami, F., Abe, K., Iwamoto, S., Nakamura, S., Harayama, A., Iwahashi, T., Konami, S., Hamagaki, H., Yamaguchi, Y., Tawara, H., & Makishima, K. 2009, Nuclear Instruments and Methods in Physics Research, 608, 390

Tsunemi, H., Katsuda, S., Nemes, N., & Miller, E. D. 2007, The Astrophysical Journal, 671, 1717

Tsunemi, H., Kimura, M., Uchida, H., Mori, K., & Katsuda, S. 2009, Publications of the Astronomical Society of Japan, 61, S147

Uchida, H., Tsunemi, H., Katsuda, S., Kimura, M., & Kosugi, H. 2009a, Publications of the Astronomical Society of Japan, 61, 301

Uchida, H., Tsunemi, H., Katsuda, S., Kimura, M., Kosugi, H., & Takahashi, H. 2009b, The Astrophysical Journal, 705, 1152

Uyaniker, B., Reich, W., Yar, A., & Fürst, E. 2004, Astronomy, 426, 909

Uyaniker, B., Reich, W., Yar, A., Kothes, R., & Furst, E. 2002, Astronomy and Astrophysics, 389, 61

Vedder, P. W., Canizares, C. R., Markert, T. H., & Pradhan, A. K. 1986, The Astrophysical Journal, 307, 269

Vink, J., Bleeker, J., van Der Heyden, K., Bykov, A., Bamba, A., & Yamazaki, R. 2006, The Astrophysical journal, 648, 33

Warren, J. S., Hughes, J. P., Badenes, C., Ghavamian, P., McKee, C., Moffett, D., Plucinsky, P. P., Rakowski, C., Reynoso, E., & Slane, P. 2005, The Astrophysical Journal, 634, 376

Werner, W. 1977, Applied optics, 16, 2078

Woodgate, B., Stockman, H., & Kirshner, R. P. 1974, The Astrophysical Journal, 188, L79

Zhou, X., Bocchino, F., Miceli, M., Orlando, S., & Chen, Y. 2010, Monthly Notices of the Royal Astronomical Society